IUVO

An Emergency Response Flyer

Final Report

AE3200 Design Synthesis Exercise

Group 28

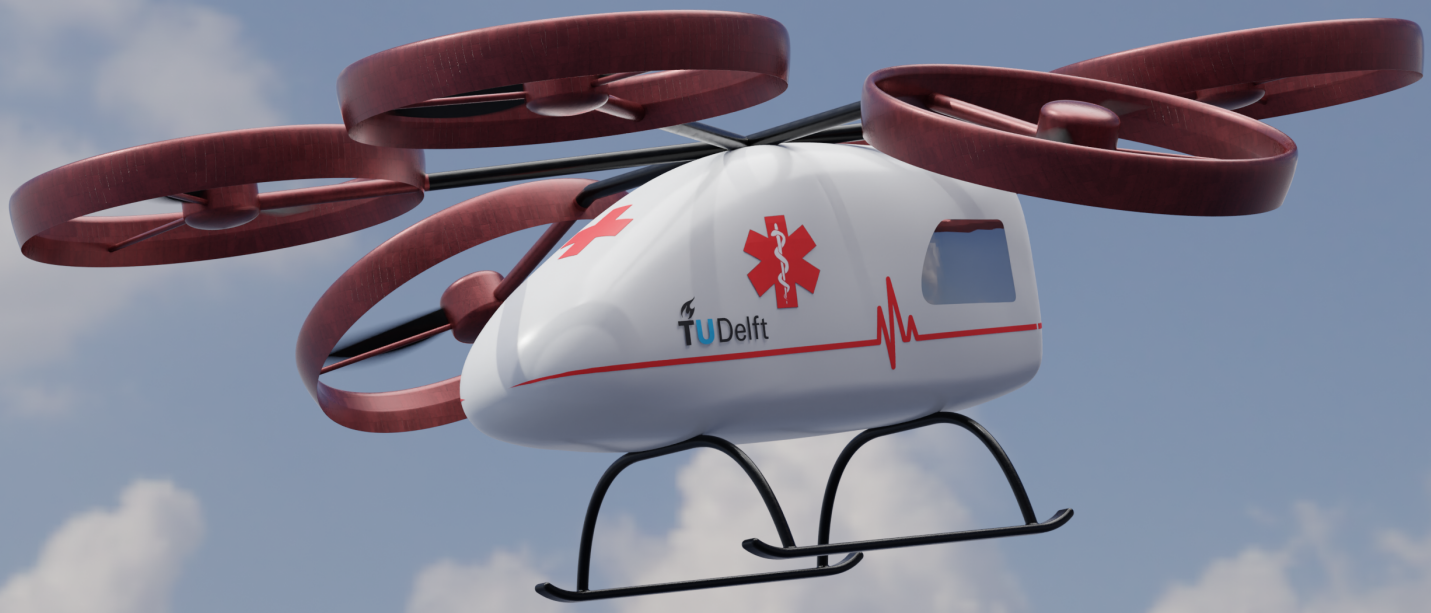

Delft University of Technology

TUDelft

This page intentionally left blank.

IUVO
An Emergency Response Flyer

Final Report

by

Group 28

Student Name	Student Number
Gabriel Gervas Montoya	5562813
Bartłomiej Grochowski	5476445
Buse Kaya	5454026
Jakub Kuleta	5542642
Sara Mouman	5452074
Miłosz Pluciński	5503841
Ioana Raducanu	5558646
Domen Škerlep	5581729
Naomi Stok	5455987
Maciej Szczęśniak	5335937

Tutor:	E. Smeur
External Expert:	M. Priems (Airbus Urban Air Mobility)
Coaches:	P. Georgopoulos and C. Varriale
Project Duration:	April, 2024 - June, 2024
Faculty:	Faculty of Aerospace Engineering, Delft

Cover: Rendered via `https://www.blender.org/features/rendering` by Maciej

TU Delft

Preface

As a group of ten students from Delft University of Technology in the Netherlands, we are proud to present our bachelor's thesis, which comprises a ten-week conceptual design study detailed in this report. In addition to our motivation to complete this final step in our studies, we stand before you as devoted future engineers, dedicated to developing a solution for rapid emergency response to aid society in times of crisis. In recent years, we've all witnessed the devastating impact of natural disasters on our ecosystem, infrastructure, and communities. We acknowledge that many affected by these events cannot be successfully rescued, largely due to the limitations of current response measures. Therefore, we present IUVO as a solution derived from extensive research, design, documentation, and programming.

We would like to take this opportunity to express our appreciation for the involvement and continuous guidance of our tutor Dr. Ewoud J. J. Smeur and coaches Dr. Carmine Varriale and Panos Georgopoulos. Our external expert, Martijn Priems from Airbus Urban Air Mobility, has been with us from the beginning to the end, providing us with valuable advice and support.

And finally, we extend our heartfelt thanks to you, dear reader, for taking the time and effort to explore our project and our journey towards the future of aviation. For many, the sky is the limit, but for us—and all who join us—it is just the beginning.

Group 28
Delft, June 2024

Executive Summary

All around the world, natural disasters disrupt the lives of millions of people with each passing year. The adverse impact of these phenomena is exacerbated in “ambulance deserts”, areas where people in need of aid have to wait for at least 25 minutes for a medical crew to arrive on-site by ambulance [1]. Natural disasters can obstruct infrastructure, further decreasing the feasibility of ground response. Aerial response, led by rescue helicopters, presents a solution but comes with financial constraints for large-scale use, dependence on trained personnel, and limited maneuverability in confined areas. To overcome these limitations and tackle the challenge of rapid emergency response, this project presents IUVO - an autonomous electric Vertical Take-off and Landing (VTOL) vehicle capable of rescuing a single passenger from emergencies.

Project Objectives

Assessing the aerial emergency response missions and requirements reveals certain essential aspects of the design. This unveils the project objective to *“design an emergency response eVTOL able to carry a single person, fly autonomously, and maneuver around obstacles within the budget of 120,000 euros in the span of 10 weeks.”* The vehicle is required to have a range of 30 kilometers to ensure that once deployed, it can reach people in need within a radius of 15 kilometers. It is designed to be transported within US and EU street-legal transport vehicles to the nearest accessible road to the incident for deployment. During its critical range mission, 10 minutes is reserved for hover in case of unsafe landing conditions. Stemming from the vehicle’s mission of bringing people to safety, ensuring operational reliability is a paramount goal in the design process, with a specific focus on integrating redundancy principles. Furthermore, recognizing the correlation between global warming and the increasing frequency of natural disasters, sustainability is prioritized in the design.[1].

Market Analysis

An extensive market analysis first identifies the key stakeholders of the project as well as the strengths and weaknesses of the intended design, followed by an evaluation of the air ambulance market and an examination of competitors. The SWOT analysis of the solution outlines VTOL capability, environmentally friendly design, and low cost as the biggest strengths, whereas relying on battery technology remains a weakness of IUVO, resulting in limited range and payload capabilities.

Currently, the flight rescue market is valued in billions and is expected to continue growing due to its rapid response, remote access capabilities, and ongoing technological advancements regarding the design of air ambulances. At present, the market is dominated by helicopters [2] which are effective but costly solutions. In the near future, the demand within the market is expected to increase shifting towards low-cost, sustainable, short-range aerial vehicles with vertical take-off and landing (VTOL) capabilities, which this project aims to address.

Independently, the eVTOL market is poised for substantial future growth, driven by factors such as escalating traffic congestion, the demand for cleaner fuel alternatives, and heightened interest across various sectors. Within the eVTOL market, the battery-electric segment is expected to dominate, attributed to its environmental benefits, and reduced operational costs, indicating that IUVO will have a strong market positioning. While autonomous systems may not provide an immediate advantage for short-term use, citing passenger trust and regulatory ease as key factors, piloted operations are expected to dominate in the near term. Autonomous systems are recognized for their long-term potential, with public acceptance likely to increase over time.

[1] URL https://www.unep.org/topics/fresh-water/disasters-and-climate-change/climate-change-and-water-related-disasters [cited 02 May 2024]

Configuration Trade-off Results

Stemming from the mission scope and functional requirements, several design options emerge as feasible for achieving the VTOL capabilities of the vehicle. These configurations include multicopter, tiltwing, tiltrotor, and lift & cruise. The options are evaluated in terms of safety, cruise efficiency, maneuverability, mission time, and cost. Given that hover is considered the most demanding flight phase within the vehicle's mission scope, these criteria prioritize the hover capabilities of the configurations. After careful evaluation of the design options, the multicopter configuration distinguishes itself due to its high maneuverability, low cost, exceptional hover performance, and rapid response time. Consequently, the multicopter is chosen to be furthered as the design. For this configuration, the number of rotors has been decided to be 6 as an optimum between redundancy in case of motor failure and vehicle cost. Moreover, to ensure electric propulsion, lithium-ion batteries are chosen for an energy storage system.

Detail Design Approach

The design approach taken to develop IUVO, an optimized hexacopter, focuses on subsystem interfaces and integration to achieve balance and efficiency. Key subsystems, including aerodynamics, propulsion, and energy storage, are thoroughly evaluated. An iterative process refines the design by optimizing RPM and cruise speed to minimize energy consumption. Detailed performance analysis calculates total energy needs, and battery sizing ensures adequate energy supply. The process continues until the weight of the vehicle converges within 2% of the initial estimate, resulting in a well-integrated, efficient emergency response hexacopter.

The aforementioned weight, central to converging on a final design, is estimated using Class II weight relations for critical components. Structural component weights are estimated using historical models and empirical formulas, ensuring accurate calculations for elements like rotors, hubs, fuselage, and landing gear. Battery sizing considers energy conversion efficiencies and future advancements, optimizing the battery weight to meet the required energy with a focus on reliability and technological progress. After numerous iterations, IUVO converges to a maximum takeoff weight (MTOW) of 421 kg, with a battery of 124.5 kg.

Flight Performance Analysis

The flight performance analysis for the multicopter focuses on optimizing design choices to ensure efficiency and robustness in mission performance. The power calculations across different flight phases ensure the vehicle operates within optimal power requirements, particularly highlighting an ideal cruise speed of 33 m/s to maximize efficiency. The cruise phase is the most energy-demanding, consuming approximately half of the total energy due to the 30 km range mission requirement. Therefore, optimizing the design with a focus on the cruise phase proves to be essential. Hovering is also energy-intensive due to the 10-minute loiter time mandated by the mission profile. Additionally, performance analysis shows that the vehicle can complete the mission, including loiter time, in 35 minutes.
Sensitivity analysis reveals how factors like altitude and cruise speed significantly impact performance, guiding design refinements. Overall, the analysis confirms the vehicle's capability to meet mission requirements while maintaining robustness against environmental factors.

Aerodynamic Performance Analysis

The aerodynamic performance analysis focuses on understanding the aerodynamic forces and moments acting on the vehicle during different flight phases and under wind gust conditions. For normal flight conditions, the analysis combines analytical evaluations and CFD simulations to assess aerodynamic loads. The CFD setup, configured in Siemens STAR-CCM+ using the RANS method, ensures detailed simulation of aerodynamic behavior despite certain limitations.

During hover, axial climb/descent, and cruise conditions, the vehicle's drag is estimated considering induced, profile, and parasitic drag components. The analysis highlights the significant role of rotor design and airflow dynamics in optimizing aerodynamic performance.

Wind gust effects are analyzed to evaluate the vehicle's stability and control under extreme conditions, with simulations considering gusts from various directions. The results provide critical data on the

forces and moments the vehicle must withstand, guiding the design of the control subsystem to ensure robustness and reliability in turbulent environments.

Propulsion System Design

The propulsion system design involves determining the size and positioning of the six rotors on the airframe. To improve rotor efficiency and, consequently, decrease their size, rotors are to be ducted and sized using actuator disk theory leading to a rotor size of 1.74 m. Propeller layout is determined bearing in mind obstacle clearance and maneuverability requirements, as well as reducing the structural mass. The edge first configuration is selected and implemented in the design as seen in Figure 1. Vehicle transportation is ensured by a solution of removing all six rotors when retracted.

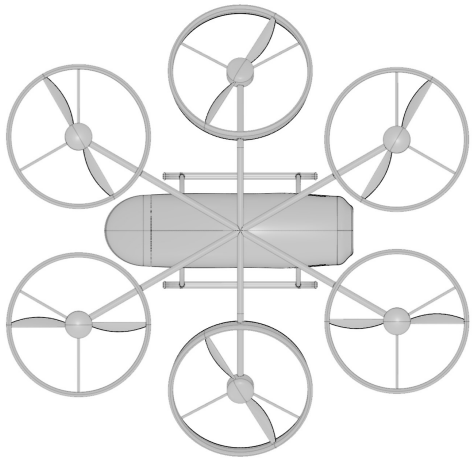

Figure 1: Final Rotor Layout

An analysis is conducted investigating the effects of rotor tilt on controllability in the case of one engine inoperative condition. It is shown that tilting rotors with outward rotation of 33.5 degrees and rotation around the boom axis of 2 degrees is proved to be beneficial for controllability while maintaining 94% of thrust in the vertical direction. Finally, rotor blade geometry is designed using Blade Element Momentum Theory leading to the blade with an efficiency equal to 81.48%.

Stability and Control Characteristics

The analysis of maneuverability and controllability entails the assessment of required and attainable moments set and verifying if all required moments are attainable. The vehicle is designed to be fully maneuverable if any of the rotors fails. The allowable CG range is calculated, where the most constraining scenario of any rotor failure provides an excursion of CG of 5.2 cm in the front-aft axis.

Energy Storage System Design

Having chosen lithium-ion batteries as an energy source, top-level electrical architecture is developed with the use of an Electrical Block Diagram. Two separate systems one operating at high voltage, whereas the other at low voltage, are included for the sake of system redundancy and efficiency. Moreover, battery cells for both low-voltage and high-voltage batteries are arranged in series and in parallel to provide the required voltage and capacity. Cells are organized in modules and packs introducing redundancy in the system and preventing fire spread. Lastly, charging time for batteries is estimated leading to the conclusion that, using commercially available chargers, the vehicle can be charged within 20 minutes.

Thermal Management System

The internal layout is divided into multiple sections to allow for proper temperature management of the battery system (an operational range of 15-35 degrees Celcius is needed despite its high heat dissipation), flight computer, electronics, and passenger cabin. The thermal management system is a

vapor-compression refrigeration system using the EV commonly-used refrigerant HFO-1234yf.

Structural Design and Analysis

In the context of structural design, the team's focus is on the landing gear and the design of the rotor connections. Initially, a thorough investigation of the constraints and requirements associated with these components is performed from the outset. Subsequently, an initial design is developed, incorporating preliminary structural performance calculations. For the landing gear a skid design option is pursued, and for the propeller connection arms extending from the top of the fuselage are developed.

The next step is to determine the suitable material for these structures considering the design as well as the manufacturing aspects. Aluminum 7075-T6 is chosen for the fuselage, structural booms, and propeller ducts. Stainless steel is chosen for the landing gear, and Carbon Fiber Reinforced Polymer (CFRP) laminate for the propeller blades. Later, the structural performance of the design is evaluated against critical load cases using a Finite Element Model (FEM). The outcomes of these simulations confirm that the designs withstand the critical conditions that may occur during mission operations and effectively fulfill the mission requirements.

Controller Design

The multicopter configuration necessitates a robust closed-loop feedback controller for stability and trajectory tracking. The controller ensures autonomy, fault tolerance, and resilience against drag and external disturbances. The control allocation matrix is derived from the squared angular velocities of the rotors, calculating forces and moments to maintain the desired trajectory. The cascaded controller architecture comprises inner loops for stabilization and outer loops for trajectory tracking. PID controllers manage translation and rotation, while motor speeds are optimized using a least-squares optimizing function. The velocity controller calculates the required roll and pitch angles, and the yaw angle is controlled directly.

Aircraft System Characteristics

With critical subsystems designed, the characteristics of other aircraft systems are established. Firstly, the necessary hardware is selected and the fundamental interactions between components are captured in the Hardware Block Diagram. It should be noted that all sensors are chosen in a redundant manner ensuring safe operation. Furthermore, the Software Block Diagram looks into flight software and its architecture capturing distinct processing layers and information exchanged between them. Communication Flow Diagram describes communication links with outside bodies together with information shared between them. Finally, the Data Handling Diagram visualizes how data is handled within the vehicle environment before it is transmitted through the communication subsystem to external bodies.

Cost Analysis

The cost analysis emphasizes both the unit cost and the operational expenses associated with the vehicle. For the analysis of the cost, the Eastlake method for general aviation aircraft is adapted to the eVTOL design. The results indicate that the vehicle is 15% over budget with a total unit cost of € 138k. With this unit cost, the vehicle remains highly competitive within the market, making it financially feasible to pursue. In the context of operational cost same conclusions are reached. With a single mission cost of € 80 without transport and € 116 with 30 kilometers of one-way ground transport, the design demonstrates its cost-effectiveness.

Technical Risk Assessment

Designing a novel vehicle involves numerous risk considerations. In the scope of risk management, the design addresses various risks, including those influenced or caused by passengers, object identification, maneuvering, system failures, structural integrity, electronics and energy storage, flight performance, and power, environmental and weather conditions, and operational and logistical challenges. Through migration and contingency strategies, 18 risks at or above moderate risk magnitude turn to two moderate risk magnitude risk levels. These migration and contingency strategies include increasing

design margins, using different materials, avoiding mechanisms, separating dangerous components, and adding redundancies, therefore, ensuring aircraft safe operation. The analysis reveals that through meticulous design efforts, IUVO emerges as a reliable and robust vehicle ready for operation.

Sustainability Approach

As aforementioned, sustainability remains at the core of the design. Through the three pillars of sustainability, negative environmental, social, and economic impacts can be limited. The sustainability of the vehicle is evaluated through the decisions made in disciplines such as Power & Propulsion, Material & Structures, Control, Stability & Autonomy, and Aerodynamics. The leading contributors to environmental and social sustainability are materials, structures, and power & propulsion. Economic sustainability is influenced by all disciplines as they all come together to meet the market goals.

Furthermore, a life cycle assessment is performed accounting for the material extraction, manufacturing, transportation, and end-of-life phases of the vehicle. This results in a total net to CO_2 emission of 3396.489 kg across its entire lifetime.

Future Development of the Project

Concluding the detailed feasibility assessment of an optimized hexacopter design for emergency response, the project enters into the next phase of product development. This phase begins with further detailed design, followed by prototype manufacturing and testing, ultimately leading to the aircraft's certification. After complying with certification requirements, the product is ready to be produced and enter the commercial market. Customer support is provided throughout product operation including end-of-life schemes. Lastly, after market entry, team efforts are diverted to the assessment of the possibility of further improvements to the vehicle.

Production Plan

The production plan focuses on selecting manufacturing methods for different components, as well as the assembly of parts. The structure is divided into structural divisions of fuselage, landing gear, rotor booms, rotor blades, and rotor ducts. Each structure is manufactured differently based on its geometry and material. The fuselage is made using bending and rubber forming, structural booms through extrusion, and rotor structures with rubber forming and extrusion. The landing gear is manufactured from stainless steel rods by bending and welding. The rotor blades, made out of CFRP laminates, are produced using Resin Transfer Molding (RTM). The assembly line approach increases production efficiency by manufacturing components concurrently and assembling them in a logical order, incorporating quality checks and lean manufacturing to minimize waste and enhance sustainability.

Operations and Logistics

The vehicle lifecycle includes various operations such as storing, charging, transporting, maintaining, and dismantling, occurring at either the storage location, mission location, or end-of-life location. Charging uses a C-rate of 3 when done on-site or during transport (20 minutes) and a C-rate of 1 when done at the storage location (60 minutes). Transportation requires the truck to be operable on both EU and US roads and looking at the environmental sustainability, an electric truck is preferred. Logistics around the mission involves boarding, deboarding, safety, and comfort of the passenger. After each mission, an inspection is performed and after 100 flight hours, thorough maintenance is performed.

To ensure that the systems perform the mission as designed, the RAMS characteristics are analyzed. The overall reliability is 0.74668 for 100 hours; the availability of the vehicle is maximized by minimizing deployment time, charging time, and loiter time; the maintainability is expected to be high; the probability of failure is reduced by introducing contingencies and redundant designs.

Final Design

In the final step, the design is verified against the requirements, demonstrating compliance with all stakeholder constraints and demands, except for the one regarding unit cost. Further consultations with the client reveal that the estimated unit cost of the design is still viable for further investigation of

the solution.

The autonomous electric hexacopter provided by the design delivers a novel alternative for emergency responses. It is notable for its exceptional maneuverability and on-the-fly path planning, as it can rescue a single passenger in a variety of weather and landing scenarios. With all the aforementioned, the final values of the design can be found in the table below.

Table 1: Final Design Parameters

Parameter	Value
MTOM [kg]	421
Payload Capacity [PAX]	1
Range [km]	30
Cruise Altitude [m]	300
Cruise Speed [km/h]	120
Critical Mission Time [min]	35
Charging Time [min]	20
Unit Cost [€]	138169
Operational Cost [€]	80

Parameter	Value
Number of Rotors/Motors [-]	6
Rotor Diameter [m]	1.74
Peak Motor Power [kW]	133
Maximum Thrust [kN]	7.34
Battery Capacity [kWh]	29.4
Vehicle Width [m]	5.8
Vehicle Length [m]	6.0
Vehicle Height [m]	2.1

Contents

Nomenclature

Abbreviations

Abbreviation	Definition
A&P	Airframe and Powerplant
AFS	Attainable Force Set
AI	Artificial Intelligence
AMS	Attainable Moment Set
AR	Augmented Reality
ATC	Air Traffic Control
BEM	Blade Element Momentum Theory
BoL	Beginning of Life
CAGR	Compound Annual Growth Rate
CCCV	Constant Current Constant Volume
CER	Cost Estimating Relationships
CFD	Computational Fluid Dynamics
CFR	Code of Federal Regulations
CFRP	Carbon Fibre Reinforced Polymer
CG	Center of Gravity
DL	Disk Loading
DoD	Depth of Discharge
DSE	Design Synthesis Exercise
EASA	European Union Aviation Safety Agency
EMS	Emergency Medical Services
EoL	End-of-Life
ESC	Electronic Speed Controller
EU	European Union
FAA	Federal Aviation Administration
FEM	Finite Element Method
GAO	Government Accountability Office
GWP	Global Warming Potential
HV	High Voltage
IoT	Internet of Things

Abbreviation	Definition
ISA	International Standard Atmosphere
KTAS	Knots True Airspeed
L/D	Lift-to-Drag Ratio
LV	Low Voltage
MTBF	Mean Time Between Failures
MTOM	Maximum Take-Off Mass
MTOW	Maximum Take-Off Weight
MTTR	Mean Time To Repair
NACA	National Advisory Committee for Aeronautics
NASA	National Aeronautics and Space Administration
NDT	Non-Destructive Testing
PID	Proportional - Integral - Derivative
RAMS	Reliability, Availability, Maintainability and Safety
RFS	Required Force Set
RMS	Required Moment Set
RPM	Revolutions Per Minute
RTM	Resin Transfer Molding
SAR	Search and Rescue
SDG	Sustainability Development Goals
SOC	State Of Charge
SOH	State of Health
SWOT	Strenghts, Weaknessess, Opportunities and Threats
TAS	True Airspeed
TBO	Time Between Overhauls
TR	Technical Risk
TU	Technical Universtiy
UAM	Urban Air Mobility
UN	United Nation
US	United States
VTOL	Vertical Take-Off and Landing

Symbols

Symbol	Definition	Unit
A	Area	[m^2]
a	Axial interference factor	[-]
a'	Rotational interference factor	[-]
C	Cost	[€]
c	Specific heat capacity	[J/kg K]
c_b	Blade chord	[m]
C_{cell}	Cell capacity	[Ah]
C_d	Drag coefficient	[-]
C_{D0}	Zero-lift drag coefficient	[-]

Symbol	Definition	Unit
C_l	Lift coefficient	[-]
C_{P0}	Profile power coefficient	[-]
C_{Pi}	Induced power coefficient	[-]
C_{Pp}	Parasitic power coefficient	[-]
C_T	Thrust coefficient	[-]
D	Drag	[N]
d	Diameter	[m]
DL	Disk loading	[kg/m^2]
e	Coefficient of restitution	[-]
E_{req}	Required energy	[Wh]
E_{sp}	Specific energy	[Wh/kg]
E_{tot}	Total energy	[Wh]
F	Momentum loss factor	[-]
F	Force	[N]
f	Equivalent flat plate area	[ft^2]
g	Gravitational constant	[m/s^2]
GW	Gross weight	[lb]
h	Altitude	[m]
I	Current	[A]
I_1	Integral for nondimensional thrust coefficient	[-]
I_2	Integral for nondimensional thrust coefficient	[-]
J_1	Integral for nondimensional power coefficient	[-]
J_2	Integral for nondimensional power coefficient	[-]
L	Lift	[N]
l_f	Fuselage length	[m]
M	Moment	[Nm]
m_{batt}	Battery mass	[kg]
n	Load factor	[-]
n_b	Number of blades	[-]
N_p	Number of cells in parallel	[-]
n_r	Number of rotors	[-]
N_s	Number of cells in series	[-]
P	Power	[W]
P_c	Climb power	[W]
P_c	Nondimensional power coefficient	[-]
P_{cr}	Cruise power	[W]
P_D	Power due to drag	[W]
P_d	Descent power	[W]
P_h	Hover power	[w]
P_m	Motor power	[W]
Q	Heat	[J]
R	Range	[m]
R	Radius	[m]
R	Electrical resistance	[Ω]
r	Local radius	[m]
SoC_{end}	End state of charge	[-]
S_{w_f}	Wetted surface area fuselage	[m^2]
T	Thrust	[N]
T	Temperature	[K]
t	Time	[s]
T_c	Nondimensional thrust coefficient	[-]
t_c	Climb time	[s]
t_{cr}	Cruise time	[s]
t_d	Descent time	[s]
t_h	Hover time	[s]
T_r	Thrust per rotor	[N]
u	Vertical gust speed	[m/s]
U_{sp}	Volumetric energy density	[Wh/l]
V	Velocity	[m/s]

Symbol	Definition	Unit
V_{batt}	Battery volume	[l]
V_{cell}	Cell voltage	[V]
V_c	Climb speed	[m/s]
V_d	Descent speed	[m/s]
V_{float}	Float Volume	[m^3]
v_h	Induced velocity in hover	[m/s]
v_i	Different induced velocity	[m/s]
V_{req}	Required voltage	[V]
V_{tip}	Tip speed	[m/s]
V_w	Wind speed	[m/s]
V_∞	Free stream airspeed	[m/s]
W	Weight	[N]
w	Local flow speed	[m/s]
α	Angle of attack	[deg]
β	Blade twist	[deg]
ϵ	Energy density	[Wh/kg]
ε	Drag-to-lift ratio	[-]
ζ	Displacement velocity vector	[-]
η	Efficiency	[-]
θ	Pitch angle	[rad]
θ	Rotation angle	[rad]
θ_i	Rotor outward tilt angle	[rad]
κ	Induced power correction factor	[-]
λ	Inflow rate	[-]
μ	Advance ratio	[-]
μ_{fric}	Friction coefficient	[-]
ν	Kinematic viscosity	[m^2/s]
$\boldsymbol{\nu}$	Forces and moments vector	[N and Nm]
ξ	Nondimensional radius	[-]
ξ_i	Rotation coefficient	[-]
ρ	Density	[kg/m^3]
σ	Solidity ratio	[-]
τ	Torque	[Nm]
τ_m	Motor time constant	[-]
ϕ	Flow angle	[rad]
ϕ	Roll angle	[rad]
ϕ_i	Rotor sidewise tilt angle	[rad]
ϕ_t	Flow angle at tip	[rad]
ψ	Yaw angle	[rad]
Ω	Angular velocity	[rad/s]

1 | Introduction

Climate change has significantly increased the frequency of natural disasters worldwide, necessitating prompt and effective emergency responses[1]. Existing solutions, such as rescue helicopters, come with a set of limitations concerning financial restrictions over large-scale use, dependency on trained personnel, and limited maneuverability in confined areas [3]. To address these limitations, IUVO presents a novel design for the market; a multidisciplinary design of an electrical 30 km range vertical takeoff and landing (eVTOL) single-passenger emergency response flyer.This report aims to present the characteristics and performance of the final design. This multidisciplinary design evaluates the compliance of the design to the requirements outlined in the baseline stage of the design, for a multitude of rescue missions.

The report follows the (sub-)system design of the vehicle towards compliance. In Chapter 2 and 3 the need for the project is first introduced. The functional steps performed before and within this phase in terms of accomplishing its mission are then shown in Chapter 4, 5 and 6. Chapter 8 and 7 provide the most general characteristics of the vehicle, such as MTOW, Power and Gust Loading, and verify these fundamentals. In Chapter 9, a CFD of the model is set up to calculate the drags it experiences. Afterwards in Chapter 10 and 11, the propulsion system is set up and through it the vehicle's stability and controllability are modeled. The battery characteristics and the thermal control needed as a result of the batteries are evaluated in Chapter 12 and 13. The design of fundamentally loaded subsystems is done in Chapter 14, as well as assigning them materials and evaluating their structural performance. To carry out the mission, several hardware components work together with software components to handle all the data for a safe mission. Diagrams related to this, as well as system characteristics like internal layout, are shown in Chapter 17. After the input and output of the vehicle control have been decided, a controller is designed in Chapter 16.

Between Chapter 18 and Chapter 24, non-technical aspects are evaluated; this includes a cost analysis, technical resource budget, technical risk assessment, sustainability approach, future development of the project, production plan and operations and logistics. In Chapter 25, the adherence of the designed aircraft to the requirements is evaluated and discussed as to show compliance with the initial need. Lastly, in Chapter 26, a final conclusion is taken and recommendations are given for similar design processes.

2 | Project Objectives

Natural disasters profoundly impact millions of lives around the globe each year, causing serious damage to both people and infrastructure[1]. Ground response, especially in developing countries with insufficient public framework, has restricted accessibility for all first responders[2]. Natural disasters can obstruct ground infrastructure, further decreasing the feasibility of this approach. Aerial response, led by rescue helicopters, presents a solution but comes with financial constraints for large-scale use, dependence on trained personnel, and limited maneuverability in confined areas [3]. These limitations narrow their applicability across a wider spectrum of disasters and may potentially impede accessibility for all individuals in need.

To overcome these limitations and tackle the challenge of rapid response to natural disasters, this project presents IUVO, an autonomous eVTOL emergency response flyer that will rescue an individual in distress faster than on-ground emergency services. The vehicle features advanced maneuverability with on-the-fly path planning for a range of 30 kilometers, at an altitude of 300 meters, targeting a unit cost of around €120,000. It can be transported within US and EU street-legal transport vehicles to

[1]URL https://www.unep.org/topics/fresh-water/disasters-and-climate-change/climate-change-and-water-related-disasters [cited 02 May 2024]

[1]URL https://ecologicalthreatregister.org/ [cited 02 May 2024]

[2]URL https://ourworldindata.org/natural-disasters [cited 03 May 2024]

the nearest accessible road to the incident for deployment. Ensuring safety is a paramount goal in the design process, specifically focusing on integrating redundancy principles.

A mission need statement has been established to guide the decisions made throughout the project toward a common goal.

Mission Need Statement

Provide an autonomous emergency response flyer to rescue a single passenger.

The following project objective statement is developed to implement the mission need statement.

Project Objective Statement

Design an emergency response eVTOL able to carry a single person, fly autonomously, and maneuver around obstacles within the budget of 120,000 euros in the span of 10 weeks.

Throughout this chapter, the project objectives will be further elaborated upon. In Section 2.1, stakeholder requirements will be presented, highlighting key requirements from which the aforementioned project objectives stem. Later in Section 2.2, the project objectives and mission profile will be elaborated to satisfy the stakeholder requirements.

2.1. Stakeholder Requirements

Multiple parties share a vested interest in the project's outcomes or influence its execution. Some stakeholders, including the customers (CLNT), passengers/users (PSGR), the general public (GP), environmental groups (EG), and Emergency Medical Services (EMS), impose requirements and constraints on the design, influencing the overall design space. These requirements and constraints outline what stakeholders expect from the finished product. Therefore, efforts should be directed to comply with the requirements to deliver a product that satisfies all parties involved.

In this regard, some stakeholders and their respective requirements are more critical and influential than others. To account for these distinctions, the stakeholders' positions and power are further studied in the market analysis Section 3.1. Additionally, the requirements are categorized under the following definitions:

- ***Essential***: they have minimal impact on the overall design but are essential for the mission scope.
- ***Driving***: they drive the mission's general design.
- ***Key***: they are a subgroup of driving requirements that are of primary importance for the customer, dictating the mission objective.

All the stakeholder requirements are presented in Table 2.1, with identifiers that denote from which stakeholder the requirements originate. The design's compliance with these requirements is verified later in Chapter 25.

Table 2.1: Stakeholder Requirements

ID	Requirement	Type
STK-CLNT-1	The vehicle shall be able to land on a 3.3 m by 3.3 m platform.	Driving
STK-CLNT-2	The vehicle shall be able to maneuver around obstacles.	Key
STK-CLNT-3	The vehicle shall be able to fly through 8.5 m horizontal and 9.1 m vertical spaces.	Driving
STK-CLNT-4	The vehicle shall be fully autonomous.	Key
STK-CLNT-5	The vehicle shall have on-the-fly path planning.	Key
STK-CLNT-6	The vehicle shall have a safety-critical design.	Key
STK-CLNT-7	The vehicle shall have an electric propulsion system.	Key
STK-CLNT-8	The vehicle shall be able to land on dry sand.	Driving
STK-CLNT-9	The vehicle shall be able to land on a hard surface at a 12-degree angle.	Driving
STK-CLNT-10	The vehicle shall be able to land in half a meter of water.	Driving

Continued on next page

Table 2.1: *Continued from previous page*

ID	Requirement	Type
STK-CLNT-11	The vehicle shall have a minimum altitude ceiling of 1000 m.	Essential
STK-CLNT-12	The vehicle shall have a range of 30 km.	Key
STK-CLNT-13	The vehicle shall be able to carry a payload of 94.5 kg.	Key
STK-CLNT-14	The vehicle shall be able to take off and land vertically.	Key
STK-CLNT-15	The vehicle shall fit on a US and EU street-legal ground transport vehicle.	Key
STK-CLNT-18	The vehicle shall be deployable in 30 minutes by 2 persons.	Essential
STK-CLNT-19	The vehicle shall be able to withstand wind of 6 bft.	Driving
STK-CLNT-20	The cost of the vehicle shall be less than 120,000 euros.	Key
STK-CLNT-21	The development of the vehicle design shall not take more than 10 weeks.	Essential
STK-CLNT-23	The vehicle shall be operative under adverse weather conditions.	Driving
STK-CLNT-30	The vehicle shall be able to save at least 6 people without recharge while maintaining its maximum range.	Key
STK-CLNT-31	The vehicle shall have an additional 10-minute loiter time capability at the hover phase during its range mission.	Key
STK-GP-1	The vehicle shall not disturb the public.	Essential
STK-PSGR-1	The vehicle shall ensure passenger comfort.	Driving
STK-PSGR-2	The vehicle shall be easily accessible for boarding and disembarking.	Driving
STK-EG-1	The vehicle shall have minimal environmental impact.	Driving
STK-EMS-2	The vehicle shall report its state, payload status and flight path continuously to the EMS.	Driving

The design team further breaks down these stakeholder requirements to develop mission and subsystem requirements. These encompass all necessary criteria for the product to effectively fulfill its mission scope. This chapter will refrain from introducing these requirements to maintain clarity and conciseness. For the remainder of the report, they are referenced with identifiers such as *STK-GP-1-MIS-1-SYS-1* denoting the higher-level requirement from which they originate.

2.2. Mission Profiles

To analyze the vehicle's performance under various flight conditions, mission profiles depicted in Figure 2.1 have been developed. These profiles, aligned with mission objectives and requirements, encompass three distinct flight phases: vertical take-off, cruise, and vertical landing. An assumption is made at this stage that all the phases are performed steadily, such that no accelerations are experienced.

The first three mission profiles shown in Figure 2.1 are adapted from the rulebook of the GoAERO competition [4]. The Productivity Mission encompasses the need for rescuing in total 6 passengers within a 2.4 km radius, on one battery charge, as derived from *STK-CLNT-30*. The Adversity Mission encompasses the need to land under various conditions as dictated in requirements *STK-CLNT-8*, *STK-CLNT-9*, and *STK-CLNT-10*. As proof of compliance, this is to be demonstrated in a single mission, however, the landing capabilities highlighted are present in all mission profiles. The Maneuverability Mission presents the ability to clear the obstacles under the requirement *STK-CLNT-2*.

The last two mission profiles are defined as the regular operations of the vehicle. The Altitude Mission considers the requirement *STK-CLNT-11*, ensuring that the service ceiling is set at 1000 m. The Range Mission ensures compatibility with the requirement *STK-CLNT-12* with the cruising altitude set to 300 m, as this is the minimum cruising altitude to satisfy clearance specified by EASA [5], and includes a 10-minute-long loiter (hover) phase in case of unsafe landing conditions, complying with *STK-CLNT-31*.

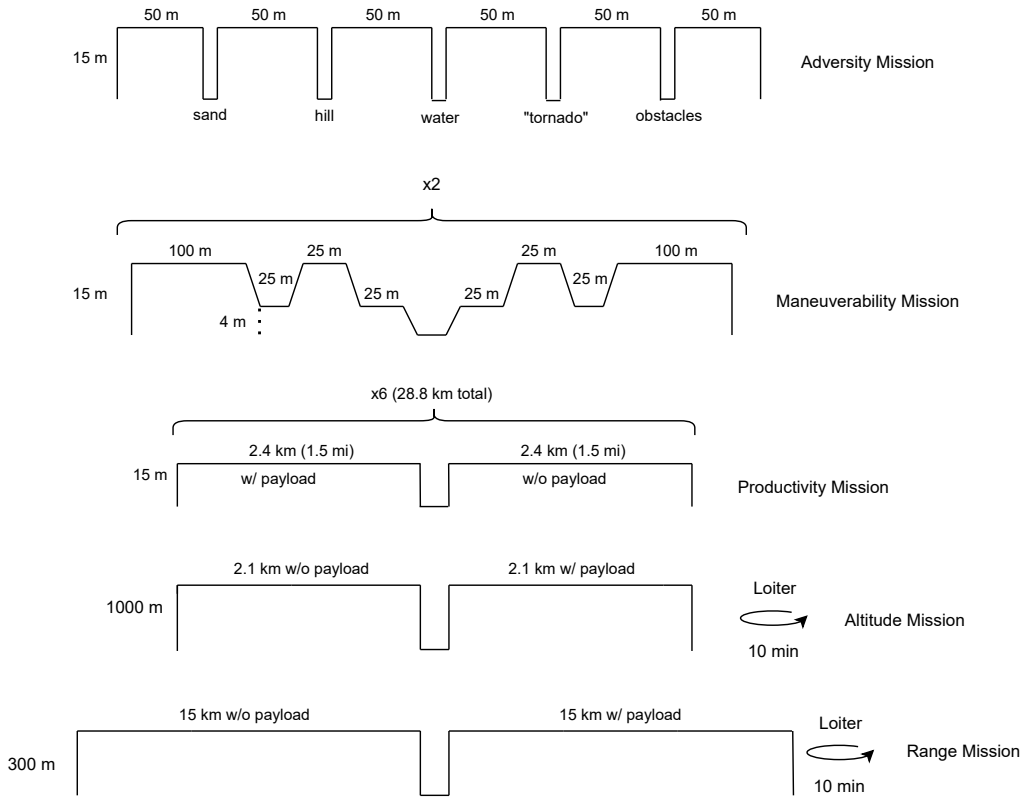

Figure 2.1: Mission Profiles

By being able to perform all the described missions, the design shows compliance with the imposed functional requirements. A critical mission profile is not established for the design. This is a result of the versatility of the design, which needs to fulfill various requirements in different missions. Thus, for example, the Range and Productivity Missions are critical for the range requirement, while the Adversity Mission is critical for the landing gear and sensor design. The focus is however on the former missions, as they most resemble the regular operations of the vehicle.

3 | Market Analysis

The objective of the Market Analysis is to provide a comprehensive understanding of the competitive landscape, including the cost dynamics and volume metrics within the market of aerial emergency response. This analysis is grounded in an evaluation of the current market for similar products and services, alongside a thorough assessment of the value added by introducing the innovative solution intended by Group 28's project objective.

Firstly, in Section 3.1 main stakeholders involved in the project are identified and analyzed for their interests and influence. Subsequently, in Section 3.2 a SWOT analysis is performed on the product, which is used to identify the characteristics of the design relevant to its market positioning. Then, Section 3.3 presents a thorough market analysis that examines the demand within the existing market for the product, as well as its expected growth. The competitive analysis that follows in Section 3.4 examines the potential competitors for the product and their market trends, focusing on Helicopters and eVTOL aircraft. Finally, in Section 3.5, the business model of the vehicle is identified and key requirements and objectives stemming from the market analyses are presented, aiming to enhance the product's market positioning and future potential.

3.1. Stakeholder Analysis

The stakeholder analysis identifies the interest and power of parties that influence project decisions or are affected by the project outcomes. Once their positions regarding the project are evaluated on a scale of 1-10, the appropriate involvement strategies for the stakeholder groups are established. This is visualized on an Influence-Interest map for stakeholders, as found in Figure 3.1. The main stakeholders relevant to the GoAERO rescue flyer design project are the following:

Table 3.1: Stakeholder Analysis

Stakeholder Group	Description	Interest [1-10]	Power [1-10]
Project Team	Group of individuals responsible for planning, executing, and managing the project.	10	10
Customers and Users	Individuals or entities who purchase, operate, and utilize the vehicle.	10	8
General Public	All people in a community or society possibly influenced by the product.	6	4
External Experts	Specialists who provide knowledge or advice to the project.	8	8
TU Delft	Academic institution that organizes the execution of the project.	8	8
Emergency Medical Services (EMS)	Providers of urgent medical care and transport for people experiencing acute health crises.	5	2
Competitors	Air ambulance services, Search and Rescue Helicopter, eVTOL companies	3	2
Regulatory and Certification Authorities	Aviation Authorities, Safety Regulation Bodies	3	7
Business Partners	Suppliers and Vendors, Technology Partners, Distribution Partners	5	6
Investors	Angel investors, Venture capitalists, Banks and Financial institutions	7	5
Environmental Groups	Organizations that advocate for protecting nature and addressing environmental issues.	4	1

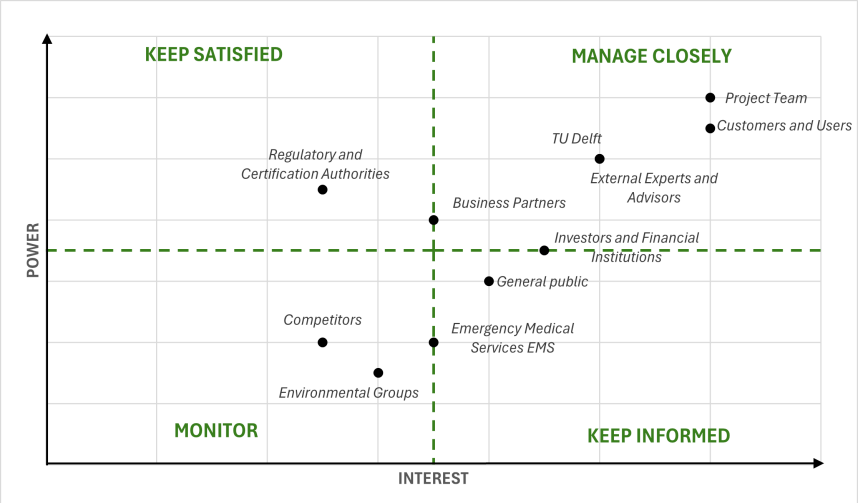

Figure 3.1: Stakeholder Influence-Interest Map

When approaching stakeholders from various groups, it is essential to adopt a tailored strategy that aligns with their needs and expectations. For stakeholders that fall under the “manage closely” category, such as key decision-makers and high-impact influencers, direct engagement and regular communication are crucial. This involves understanding their interests and addressing concerns promptly.

To address this, the team organizes weekly meetings with external experts, advisors, and customers. Daily contact is maintained with university staff who share an interest in the project to ensure the work progresses in the correct direction and delivers high-quality results.

For stakeholders in the “keep satisfied” category, who are not influenced by the project directly but have considerable impact, providing regular updates to ensure their involvement in critical decisions is critical. To ensure this, monthly meetings are organized to personally share project progress with each stakeholder group in their relevant domains. Stakeholders in the “keep informed” group, which include those who have a moderate level of influence, benefit from clear communication regarding how their needs are being addressed and how they can benefit from the project’s outcomes. To ensure this, the team publishes monthly progress reports and conducts regular press update presentations. For the stakeholders to be “monitored”, efforts are focused on continuously analyzing their demands and positions as the project progresses.

Following this stakeholder management policy fosters constructive relationships and ensures alignment toward project goals.

3.2. Product SWOT Analysis

To identify the core competencies and differentiators of the product, recognize limitations and risks, and establish an overall strategic alignment, a SWOT (Strengths, Weaknesses, Opportunities, and Threats) analysis is performed. The results of the analysis are illustrated in Figure 3.2 with detailed explanations of the points discussed thereafter.

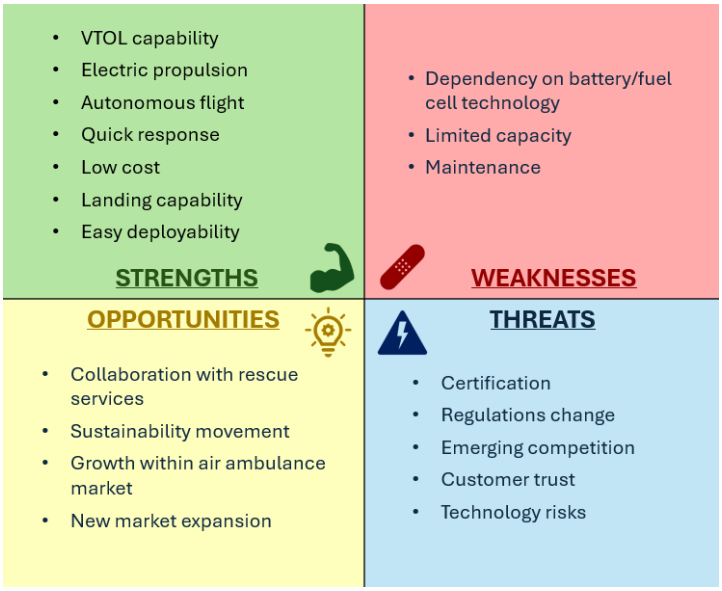

Figure 3.2: SWOT Analysis of the Emergency Response Flyer.

The flyer boasts several key strengths that enhance its effectiveness in emergency rescue operations. Its VTOL capability allows it to take off and land at any location, eliminating the need for a runway. Powered by electric propulsion, it operates with minimal environmental impact. Autonomous flight capabilities reduce human error and enhance safety during operations, particularly in high-risk situations. The flyer’s quick response capability enables swift deployment to inaccessible emergency sites, improving response times compared to conventional methods. Additionally, its lower unit cost relative to traditional air ambulance helicopters makes it a cost-effective solution. The flyer’s versatility is further underscored by its landing capabilities on water, dry sand, and unprepared platforms. The vehicle can be deployed easily by two people in under 30 minutes which enhances its rapid response capabilities. These strengths collectively position the flyer as a promising innovation in the field of emergency medical services and disaster response.

Moreover, there are several opportunities for the product. Collaboration with rescue services facilitates the integration of the flyer within existing networks, enhancing operational efficiency and reach. The global sustainability movement presents an opportunity as environmental awareness increases, poten-

tially favoring the flyer's eco-friendly design over conventional solutions. The expanding air ambulance market, driven by the benefits of rapid medical assistance, accelerates the adoption of innovative solutions like the flyer, which promises enhanced response capabilities. Additionally, the prospect of new market expansions remains a critical opportunity for the development of the project.

Nevertheless, it is acknowledged that the proposed concept has associated weaknesses and threats, prompting proactive preparation and mitigation strategies. The dependency on battery/fuel cell technology means that the range and endurance of the vehicle are highly reliant on current energy storage solutions. Additionally, its limited capacity to carry only one person restricts its utility in scenarios requiring the transportation of multiple individuals, such as a doctor accompanying a patient. Moreover, the flyer's maintenance needs may differ due to its unconventional solutions, potentially necessitating unique maintenance schedules compared to conventional aircraft.

In terms of risks, certification emerges as a significant concern, involving adherence to stringent regulations that can be challenging to meet, particularly in the context of autonomous flight. Moreover, these regulations are subject to change, adding complexity to the design process and requiring continuous adaptation. Evolving regulations may impose new constraints on the design, necessitating ongoing adjustments. Given the expected growth of the aerial response market and high demand for eVTOL, competition is expected to emerge, which pressures the design to stand out to have high market shares. Furthermore, building customer trust for innovative solutions is a considerable threat as it requires time and effort. Finally, technology risks are relevant as they accompany the implementation of innovative solutions, carrying the potential for malfunction and detrimental consequences. These weaknesses and threats underscore the need for vigilant management and strategic planning to navigate challenges in the market landscape.

It is concluded that the vehicle's most prominent strengths lie in its VTOL capability, environment-friendly design, and low cost. These are counterbalanced by the limited range and payload capabilities of the vehicle. Opportunities lie in the market demand for novel, sustainable, and autonomous VTOL solutions. Nevertheless, threats concerning technological risks associated with the pursuit of innovation, regulatory uncertainties, and lack of customer trust need to be mitigated.

3.3. Target Market Assessment

A market analysis is performed for the air ambulance services since it is the market in which the prospective clients for the product operate. The search and rescue market is taken to be a subset of the air ambulance services [6]. The information is obtained from the free extract of detailed market analysis reports, performed by various information companies, summarized in Table 3.2. They all consider a similar array of countries, the main players distributed through the continents, which are taken to represent the global market.

Table 3.2: Air Ambulance Service Market Estimations

Market Analysis Reports	Current Value [$B]	Expected Value [$B]	Compound Annual Growth Rate (CAGR)
Mordor Intelligence [7]	6.97 (2024)	10.80 (2029)	9.15%
SkyQuest [8]	17.4 (2023)	43.08 (2031)	10.6%
Emergen Research [9]	14.63 (2022)	39.17 (2032)	10.3%
Fortune Business Insights [6]	7 (2024)	11.46 (2032)	9%

Segmentation of the market is made through service operator (Hospital-based, Independent, Government), aircraft type (Fixed-Wing, Rotary-Wing), service type (Domestic, International), and geography (continents, which can be subdivided into countries). North America dominates the market, with Europe and Asia Pacific expected to be the fastest-growing segment. The rotary-wing aircraft is the current market leader, however, the fixed-wing segment's revenue is anticipated to grow at a steady rate given its long range and superior ability to operate in adverse weather conditions.

Market drivers are the incorporation of sophisticated medical equipment, fast response, reaching otherwise inaccessible areas, advances in the design of air ambulances as well as the aging population and

increased prevalence of cardiovascular disorders. A major factor contributing to the expected growth is the expansion of air ambulance software suppliers, particularly meteorological software providers.

Moreover, the restraining factors of the market are identified to be the lack of insurance coverage in many regions, and more importantly, the high operating costs involved. This latter one englobes operation, maintenance, and costs required for meeting aviation regulations. This impedes new competition from entering the market and slows down the market growth. From this restraint, the objective of minimizing the operational cost of the product should be considered.

Based on this assessment, the air ambulance services market is currently experiencing robust growth and is valued in the billions, with projections indicating a CAGR of around 9% to 10% into the early 2030s. While helicopters currently dominate the market, there is a noticeable gap for low-cost, sustainable, short-range aerial vehicles with vertical take-off and landing (VTOL) capabilities, which this project aims to address.

3.4. Competitive Analysis

To analyze the possible solutions that could fill the observed market gap, a competitive analysis is performed. This includes identifying the current and future competitors. It should be noted that due to the novelty of the project and its objective of enhancing current aerial rescue methods, there is currently no existing competition that matches the intended product specifications for the project in terms of eVTOL technology, cost efficiency, and operational range, and as such there is no existing market segment for it. Accordingly, an approach is established to perform a market analysis of two different existing markets, which combined would result in an accurate representation of the market segment that the product will create.

As identified by the industry market analysis, the existing Air ambulance market is dominated by rotary wing aircraft (Helicopter), and hence a market analysis is performed for *the helicopter market*, focusing on the subset used for ambulance, search, and rescue missions. Additionally, the similarity between functionalities and constraints between the proposed design and the existing eVTOL models led to the consideration and analysis of the current *market for eVTOL aircraft*. Therefore, integrating the analysis of competitors across both markets will yield a robust estimation of the future market segment for the developed product.

3.4.1. Helicopter Market

To perform a competitive analysis of the helicopter market, the approach taken involves identifying the general market trend, the market share distribution, and researching the leading models' functionalities and costs.

The global helicopter market size was valued at USD 56.87 billion in 2022 & is projected to grow from USD 58.87 billion in 2023 to USD 76.16 billion in 2030, showing a CAGR of 3.7%. Technological advancements such as Hybrid propulsion systems, Big Data, and Artificial intelligence, are the main drivers for the market growth. Additionally, rising demand for Military, and air ambulance services drives the market growth. Conversely, it is identified that the restraining factors of the helicopter market are the delivery delays and setbacks, as well as the aforementioned high operational and maintenance costs [2].

The market is segmented by type (Military, Civil & Commercial) with the latter expected to achieve market dominance, by weight (Light, Medium, Heavy) with light expected to grow and achieve market dominance, and by application (Emergency Medical Service, Corporate service, Defence among others) with the first of these, Emergency Medical Service or Ambulance services, has an 11.15% market share and is expected to dominate the market. In terms of Geography, North America holds the largest market share, followed by Europe. The Asia-Pacific region is expected to grow substantially [2].

In terms of competition, the market is very consolidated, with few companies comprising most of the market share. They include Airbus (France), Leonardo S.p.A. (Italy), Sikorsky Aircraft Corporation (US), Bell Helicopter Textron Inc. (US), Russian Helicopters JSC (Russia), Boeing (US), Kawasaki Heavy Industries (Japan), and Hindustan Aeronautics Limited (India) [10]. The market share of each is illustrated in Figure 3.3:

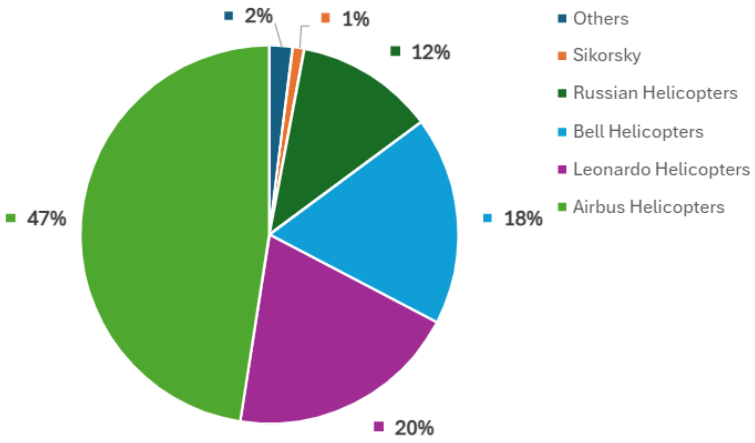

Figure 3.3: Market Share of the Leading Helicopter Manufacturers Worldwide in 2020 [10].

Additionally, the research conducted to identify the most commonly used helicopter models in air ambulance services and search and rescue operations, revealed that H135 ($5.7 Million [11]), H145 ($9.7 Million [12]), AW189 SAR ($15 Million [13]), S-92 SAR ($27 Million [14]), S-70i SAR ($15 Million [15]) models were the most commonly utilized.

The price of said helicopters ranges between around USD 6 million to USD 27 Million. These models, follow a general trend, of long-range (varying around 550 km), large size and payload capabilities (ability to carry around 6-10 passengers), and high cost.

3.4.2. eVTOL Market

This section first explains the importance of the eVTOL market, followed by an analysis of its future potential. The analysis covers both an overall perspective and segmented categories, including usage scenarios, propulsion types, lift technologies, ranges, modes of operation, and regions.

As presented in Section 3.3 the market analysis of the air ambulance industry indicates that the demand for aerial emergency response is starting to shift towards more sustainable, maneuverable, and less costly options. While the helicopter market remains relevant for assessing the current state of air medical services, stemming from the shift in demand and the requirements for the project, analyzing the eVTOL market is of crucial importance.

Currently, eVTOL development remains very costly and unable to satisfy the increasing demand for more affordable aerial rescue vehicles. However, the eVTOL market is relatively new, and it is estimated that production costs will decrease over time due to the development of necessary infrastructure, advancements in materials with better properties, and improvements in manufacturing methods. Thus it is reasonable to assume that the eVTOL market currently lies in the introduction phase of a product life cycle and that it will reach the start of the growth phase by 2030. Thus, these vehicles remain highly promising and are expected to compete with helicopters, offering the market enhanced maneuverability, sustainability, and cost characteristics.

The growing interest in urban air mobility has prompted many leading aerospace companies to explore the feasibility of developing VTOL projects. To assess their profitability, numerous market reports and analyses have recently been released by various consultancy organizations. For instance, BIS Research estimates that by 2035, the VTOL market will achieve a valuation of 1.9 billion US dollars [16]. Conversely, NASA has engaged McKinsey & Company and Crown Consulting to conduct concurrent studies. McKinsey estimates that the market value for Air Taxis (short-distance UAM) could escalate to as much as 500 billion US dollars [17]. Similarly, projections by IDTechEx [18] and Deloitte [19] suggest that the global market could expand to approximately 14.7 and 17.7 billion US dollars by 2040, respectively. Additionally, Reports and Data [20] have documented a potential market size of 7.9 billion US dollars by 2030. According to Fortune Business Insights, the market, currently valued at USD 1.11 billion in 2020, is projected to rise to USD 23.21 billion by 2028, showing a CAGR of 23.13% during the forecast period [21].

As can be seen from these predictions, the market potential for eVTOLs is set to increase substantially, promising considerable profits in the future. Overall, the eVTOL market is experiencing a consistent growth trajectory, driven by advancements in technology and increased investments across various sectors. Fortune Business Insights lists rising traffic congestion, the need for cleaner fuels, and rising interest from various sectors, which is shown in increased investments, as the main factors that will drive the eVTOL market in the future [21]. On the contrary, lack of infrastructure and strict certification requirements are listed as the main factors that could hamper the market growth.

Within the eVTOL market, the battery-electric segment is expected to dominate, attributed to its environmental benefits, and reduced operational costs [21]. The IMARC report aligns with these findings, noting a substantial market share for the battery-electric segment due to its zero-emission operations and quieter performance compared to traditional combustion engines (IMARC). This means that selecting the battery-electric driven power system during the design process is favorable for the financial plan of the project.

In terms of applications, the eVTOL market serves commercial, military, and emergency medical services (EMS). Commercial applications, especially air taxis and delivery drones, dominate the eVTOL usage scenarios, propelled by the ongoing development and urban air mobility solutions. While this sector is expected to lead the market, it is followed by promising growth in emergency medical services (EMS) and military applications (Fortune Business Insights). The growth of the EMS segment is evidenced by the increasing use of eVTOLs in air ambulance services during the COVID-19 pandemic [22].

Considering the VTOL technology, the market has been segmented into vectored thrust, lift & cruise, and multi-rotor sectors. Vectored thrust, encompassing trans-wing, tilt-rotor, tilt-wing, and vectored jet aircraft, commands the largest market share among the three categories. Its superior maneuverability makes it ideal for a wide range of applications, especially in addressing various natural disasters and emergencies for this project scope. Moreover, its demonstrated effectiveness and longstanding implementation in traditional aircraft build confidence among manufacturers and operators, reinforcing its position in the market [23].

Concerning the mode of operation, the market is divided into piloted, autonomous, and semi-autonomous categories. Analysis varies between forecasters. Fortune Business Insights reports that the semi-autonomous division is projected to capture the largest market share due to increased investments from governmental bodies and manufacturers in the research and development of semi-autonomous eVTOL aircraft [21]. They also forecast that the autonomous division will experience the most rapid growth during the forecast period, driven by the expanding integration of artificial intelligence (AI), the Internet of Things (IoT), and Augmented Reality (AR) into eVTOL technology.

Conversely, Markets and Markets list the piloted operation as the segment with the fastest growth [23]. They note that while autonomous systems have potential for the future, piloted operations provide several benefits that can be attributed to their expansion. Passengers often feel more secure and trustful when human pilots are involved, especially in the early phases of eVTOL implementation. According to them addressing safety concerns and regulatory compliance becomes more streamlined with human oversight. Moreover, seamless integration with existing airspace infrastructure and air traffic management systems simplifies the regulatory framework and accelerates market acceptance.

Based on this, it can be deduced that in the near future, the piloted segment will still dominate the eVTOL market. Considering the autonomy requirement for the designed flyer, it is not expected that it would hold a large eVTOL market share in the short term. Public acceptance of the product is expected to be low initially but is projected to grow exponentially in the future. For short-term applications, remotely piloted usage is considered to have potential.

Geographically, the current global market for VTOL aircraft is segmented into various regional markets, including North America, Europe, Asia Pacific, and the rest of the world. North America is expected to lead the market in the future due to the significant presence of major industry companies like Joby Aviation, Bell Textron Inc., and Kitty Hawk, coupled with substantial investments from the U.S. government in VTOL technology [21]. Europe is predicted to experience notable growth, influenced by several cities participating in the Urban Air Mobility (UAM) Initiative under the European Innovation Partnership on Smart Cities and Communities. This prompts a strategy to initially position the eVTOL in the North

American and European markets. After successfully implementing the product in these markets, the reach could be expanded into other markets [21]. Especially the Asia Pacific region, with increased urbanization and investments in urban air mobility by companies such as Ehang, should be considered a critical market with several opportunities.

3.4.3. New Markets

While the product itself will influence the existing markets, its added value also lies within the potentially new markets that might emerge. The introduction of a new autonomous eVTOL aircraft could spawn a variety of innovative markets, which would each present specific needs and opportunities.

In urban environments, the product could serve as a private personal rapid transit system for urban commuters, offering a fast alternative to avoid city traffic. This market would pose strict regulation barriers but has immense potential. For remote areas, the products' capability to access hard-to-reach locations makes it valuable for delivering essential goods and services, such as emergency medical supplies and food. Additionally, the precision and stability it portrays are perfect for infrastructure inspection and maintenance tasks in both urban and rural settings, allowing safer and more frequent inspections of infrastructures like bridges and power lines. On a similar line of argumentation, the product could spread into military markets in the field of remote sensing and observation. Its potential for use in entertainment, such as aerial racing events, opens up a wide range of opportunities that mix technology and sport. Finally, it is worth reiterating that each of these markets is derived from the unique capabilities of the eVTOL to address specific challenges in different industries.

3.5. Business Model and Requirements

Although not analyzed in depth at this stage, the business model for the vehicle is based on the approach of current aircraft manufacturers[1]. Customers order vehicles tailored to their specific needs, leveraging a pull-market strategy where production begins only after an order is placed. This approach ensures efficient use of resources and timely delivery, aligning with lean manufacturing principles. By reducing inventory and focusing on customer demand, it is possible to better meet market needs and maintain high standards of quality and efficiency. Additionally, rigorous after-market services like maintenance, repair, and parts supply improve customer satisfaction and long-term value by ensuring operational reliability and extending the lifespan of the vehicles.

Based on the insights gathered from the SWOT analysis and the market analysis, several objectives can be identified to improve the product's market positioning and enhance its future market potential. The objectives listed below should guide the design process:

1. The potential customers shall be closely involved during the design process, prototyping, and testing. This will ensure that the design meets the customer's needs and incorporation of feedback.
2. The design of the flyer should be in accordance with EASA and FAA regulations, as they regulate the larger markets. This will ensure that the product is safe for use in their airspace, increasing public acceptance.
3. The operational cost of the flyer for each mission, composed of operation, maintenance, and regulation shall be minimized.
4. The operational life of the vehicle should be maximized to ensure increased profitability.
5. From the geographic perspective, the product shall target the North American and European markets when it is first introduced, later to be extended to the Asia-Pacific market.
6. The vehicle shall be designed so that it can be developed into a family of products. Having modular architecture allows for covering a wide range of use cases.

Stemming from some of these objectives, the following requirement is generated:

1. The vehicle shall fit on a US and EU street-legal ground transport vehicle.

[1] URL `https://www.technofunc.com/index.php/domain-knowledge/aerospace-industry/item/aerospace-industry-the-business-model` cited 10 May 2024

4 | Functional Analysis

This chapter thoroughly examines the fundamental operations and capabilities essential for the GoAERO vehicle's mission. Through a systematic breakdown of its functionalities, the analysis encompasses the essential components and operations necessary for fulfilling the vehicle's mission objectives effectively. These mission objectives span from design and development to retirement with an emphasis placed on mission operations, as the fundamental drivers of the design.

The functional analysis discusses and analyzes the aircraft's life across five main phases, each of which is broken down in detail. The analysis of aircraft operations, Phase 4, centers on the mission cycle, beginning with pre-flight procedures and ending with post-flight activities. It considers the functions associated with performing the range mission as the nominal flight. These functions are quite standard for all short-range VTOL aircraft, with deviations due to the autonomous nature of the vehicle. The top-level functional flow is straightforward: transportation of the vehicle to the site, deployment of the vehicle, fly to rescue location, board of the payload, return to base, and transportation of the vehicle back to storage, in that sequence.

Two diagrams are presented to visualize the functional analysis conducted. The Functional Flow Diagram (FFD) on pages 13-14 illustrates the temporal sequence of the functions, while the Functional Breakdown Structure (FBS) illustrates the hierarchical relationship among all functions defined within the mission scope of GoAERO and is shown on page 15. In both diagrams, tasks are allocated to the subsystems responsible for executing them. Thus, the diagrams are used to aid the generation of subsystem requirements.

In the FBS additional functions have been included, such as continuous functions of aircraft and dealing with emergencies, which are not introduced as a part of the nominal mission. This is because emergency response operations are inherently different from the regular flow of the nominal mission.

Additionally in the FFD, at times, functions run in parallel. In such cases, the use of an AND connector is made. These are most common in 'child' functions, the 'parent' of which is a continuous function. It is also common to see functions that split into several alternative paths. These functions are implemented using an OR connector.

Functional Flow Diagram

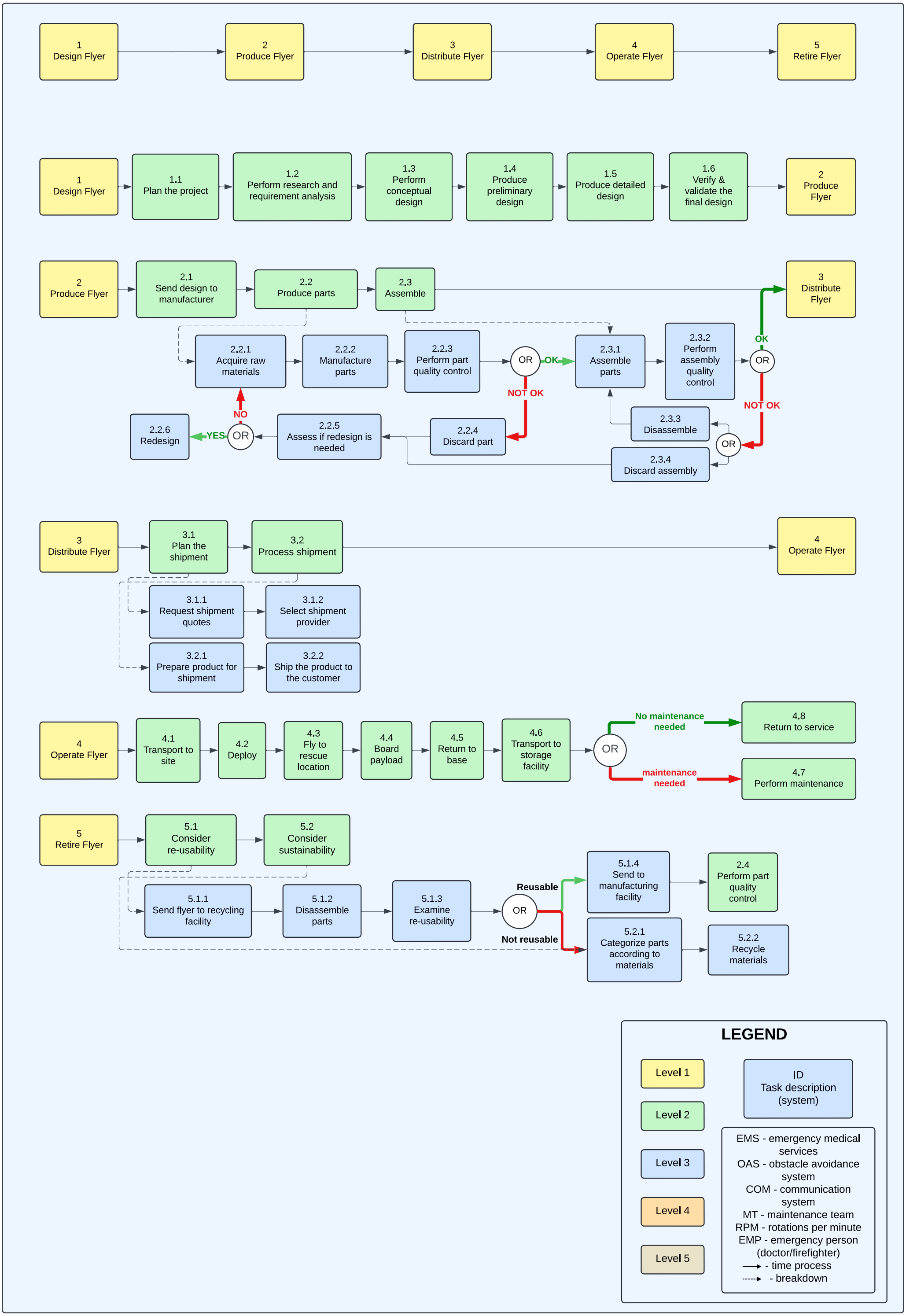

Functional Flow Diagram - Continued

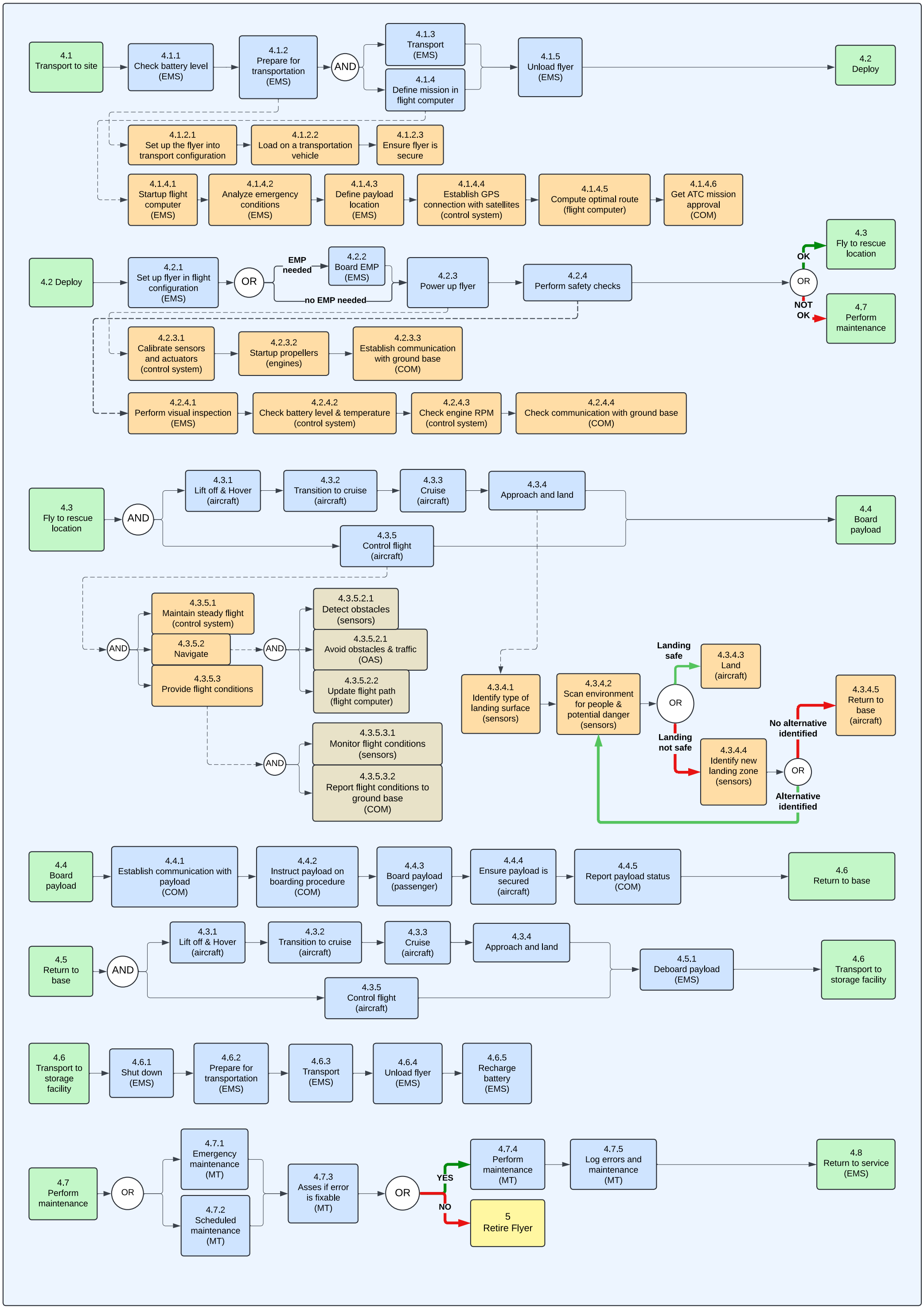

Functional Breakdown Structure

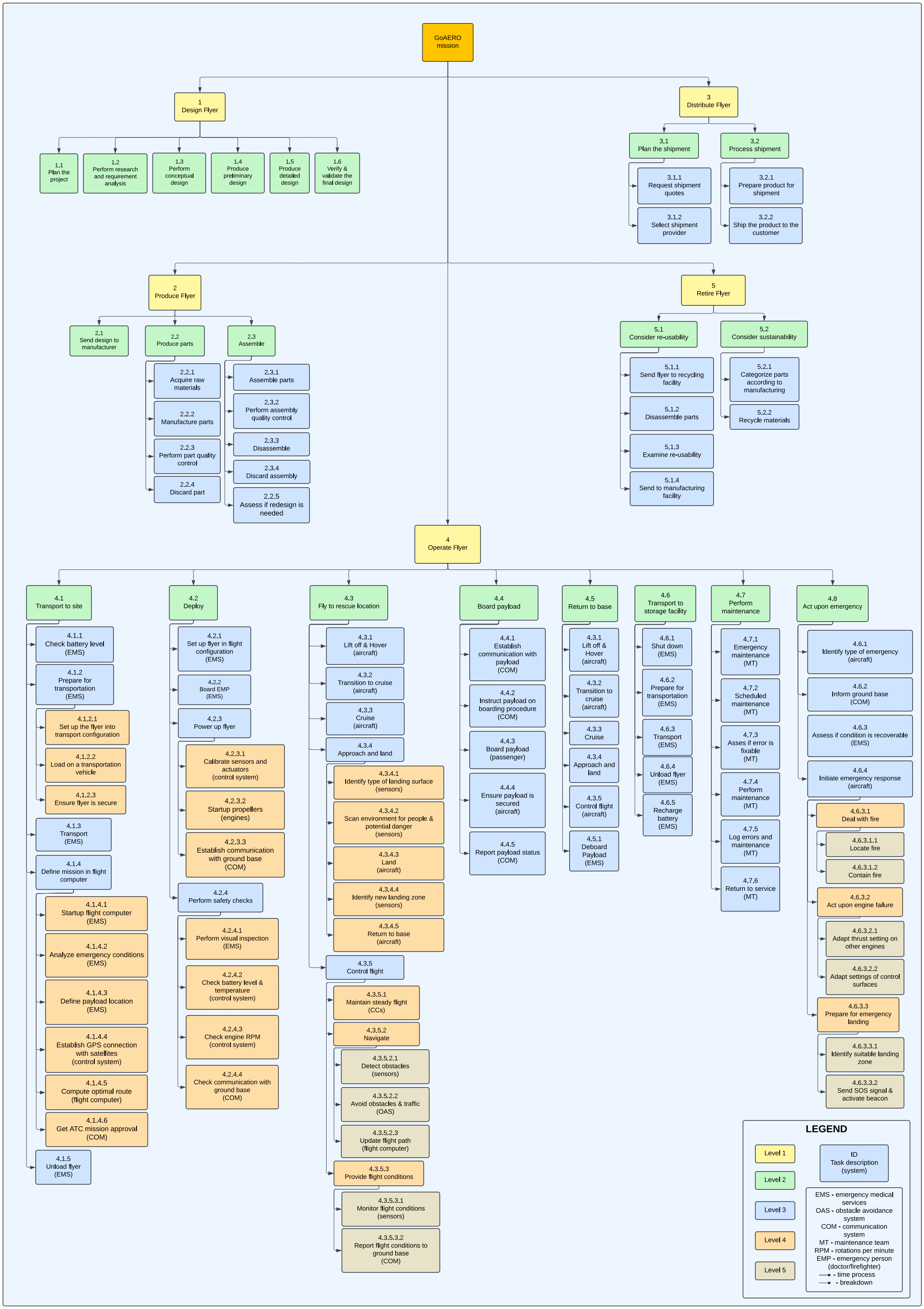

5 | Configuration Trade-off Results

Stemming from the mission scope and functional requirements, several design options emerge as feasible for achieving the VTOL capabilities of the vehicle. These configurations include multicopter, tiltwing, tiltrotor, and lift & cruise, sketches of which are shown in Figure 5.1.

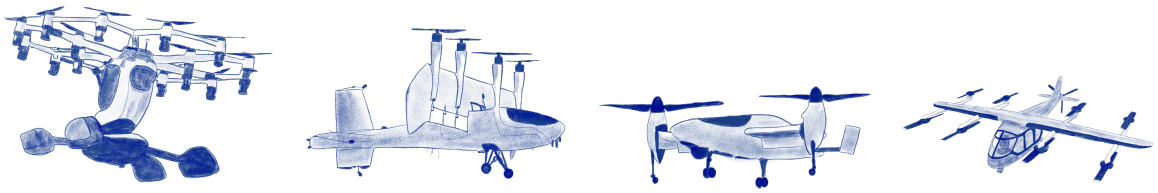

(a) Multicopter[1] **(b)** Tiltwing[2] **(c)** Tiltrotor[3] **(d)** Lift and Cruise[4]

Figure 5.1: Concept Sketches of eVTOL Configurations Selected for Trade-Off

A rigorous trade-off analysis is conducted to determine the optimal VTOL configuration for the mission scope at hand within the constraints of stakeholder requirements and market analysis. Five criteria are identified for this trade-off: mission time, maneuverability, cruise efficiency, safety, and cost. Depending on how much they drive the performance of the vehicle regarding the mission, the weights of each selection criterion are derived. In this regard, it is noted that hovering is the most intensive stage of the mission, especially considering the loiter aspect of the range mission. Thus, hover is considered critical for the assessment of maneuverability and safety.

The results of the analysis distinguish the multicopter solution as the winning configuration for its impressive maneuverability and hover performance, low unit cost, and rapid response time, all while satisfying the safety requirements. While the vehicle exhibits lower cruise efficiency, this aspect is not critical for the mission profile, which does not demand extended cruise periods given its short range. Therefore, this performance limitation does not detract significantly from the suitability of the design option for the mission context.

Following the determination of the winning configuration, the subsequent step involves conducting subsystem trade-offs. Two critical subsystems are considered at this stage which are the energy storage system and propulsion system. For energy storage, batteries emerge as the ideal solution due to cost-effectiveness, technical risk management, and considerations of complexity. Within the battery options, lithium-ion, lithium-sulfur, and solid-state are considered. Despite the promising advantages of other options, lithium-ion batteries are selected due to their current market availability.

The propulsion system considers the number of rotors, 4, 6, and 8, and their layout on the airframe. Existing research on achieving controllability for quadcopters with one engine inoperative operation highlights significant challenges, therefore the four-rotor configuration is considered unsafe, especially given the size of the vehicle and its intended human payload. Having 8 rotors is ideal for ensuring maneuverability and safety; however, the increased costs associated drive the unit cost of the vehicle beyond feasibility. Moreover, to facilitate easy boarding of the payload and address stability concerns, the hexacopter configuration with high fuselage-mounted rotors is chosen for further investigation.

In the subsequent sections of this report, a detailed design is developed based on the conclusions reached from this trade-off analysis, focusing on pursuing the hexacopter configuration.

[1] Adapted from `https://www.engadget.com/2018-12-12-lift-aircraft-passenger-drone-flights.html`

[2] Adapted from `https://www.dufour.aero/post/certified-tilt-wing-aircraft`

[3] Adapted from `https://www.flightglobal.com/new-search-for-vtol-uavs-may-resurrect-bell-tiltrotor/119404.article`

[4] Adapted from `https://www.researchgate.net/figure/Schematic-of-the-NASA-Lift-Cruise-reference-vehicle-concept_fig1_353539418`

6 | Design Approach

In this chapter, the structure of the design approach followed will be described, detailing the various subsystems analyzed and the methods used to arrive at the final converged design for the project. In Section 6.1 the critical subsystem of the vehicle and their interfaces are evaluated. These subsystems are meticulously assessed by the design team throughout the report. Later, in Section 6.2, the procedure followed to integrate these subsystems allowing for a converged design is described.

6.1. Subsystem Interfaces

In the design efforts of an optimized hexacopter for rapid emergency response, several critical subsystems are identified. Group 28 aims to comprehensively address all these subsystems to ensure complete system functionality that meets the project objectives. These subsystems include aerodynamics, propulsion, energy storage, thermal management, flight control, sensors, actuators, and structures illustrated in Figure 6.1. To capture, as well as aid in visualizing, interfaces between the subsystems, the N^2 chart, presented in Appendix A, is created. The N^2 chart represents the design departments using blue diagonal blocks. While the horizontal blocks are the outputs of the subsystem considered in the row, the vertical blocks are inputs to the subsystem considered in the column. These interfaces undergo thorough assessment throughout the design process, ensuring that subsystems are designed in compliance with others.

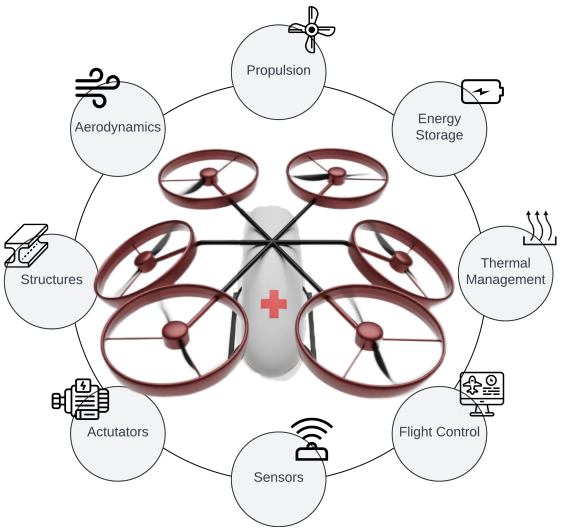

Figure 6.1: Subsystems for the eVTOL Design

6.2. Design Integration

Design integration is a crucial phase in engineering, where achieving a converged maximum take-off weight is essential. A model is created to refine the design iteratively to ensure all components work together without exceeding weight limits, affecting performance and efficiency. The program begins by giving an initial weight as input, specifically the value obtained from the Class I Weight Estimation. To optimize the vehicle's performance, two nested loops are employed, iterating through different values of RPM and cruise speed, with the goal of identifying the combination that results in the lowest total energy consumption.

To find the energy consumption, a detailed performance analysis is conducted. This analysis computes the power required for various flight phases: vertical climb, cruise, hover, and vertical descent. The total energy consumption for the mission is then calculated by summing the energy required for each phase. More detailed information can be found in Chapter 7.

Upon completion of the nested loops, the program identifies the optimal combination of RPM and cruise speed, along with the corresponding energy consumption. The next step is to determine the battery mass. This is achieved by calculating the battery fraction where the energy required for the mission

matches the energy available from the battery.

Following, a Class II weight estimation is performed. This step involves identifying the weights of specific components. The new maximum take-off weight (MTOW) is then determined by summing the component weights, battery mass, and payload mass. A detailed description of the methodology used is given in Chapter 8.

The optimization process checks if the new total weight converges to within 2% of the original weight. If convergence is achieved, the optimization process is complete. If not, the entire process restarts with the initial weight set to the newly calculated weight from the previous iteration. This iterative process continues until the weight convergence criterion is met. The optimization process is illustrated in the flowchart shown in Figure 6.2.

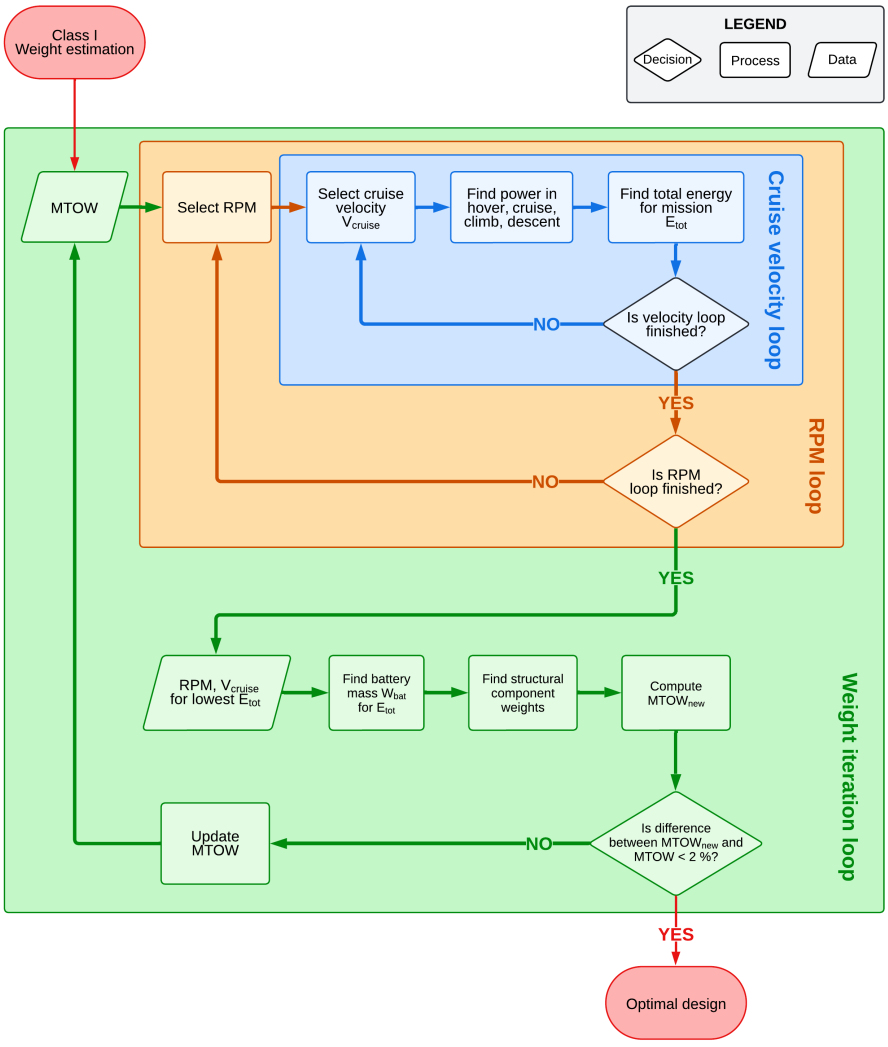

Figure 6.2: Schematic Representation of Design Optimization Code Logic

The convergence of the optimization loop to the final weight is depicted in Figure 6.3. This figure demonstrates the weight's convergence as the number of iterations increases, ultimately achieving a final maximum takeoff weight of 421 kg.

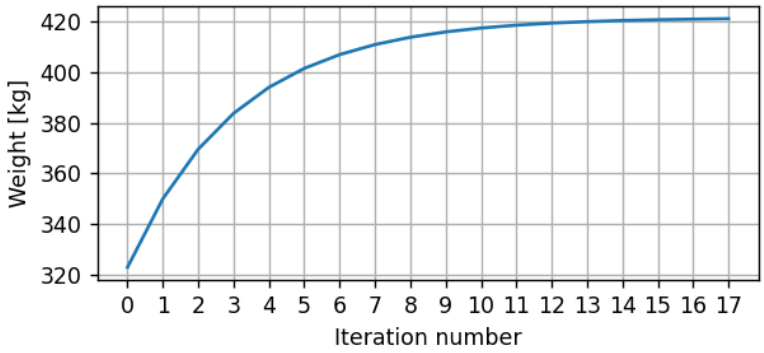

Figure 6.3: Diagram of weight iteration

7 | Flight Performance Analysis

Predicting the flight performance of a vehicle is crucial for efficient design, enabling the optimization of key factors such as power consumption, energy usage, and achievable range.
In Section 7.1, the rotor characteristics are calculated; the power calculations are given in Section 7.2, followed then by the energy calculations in Section 7.3. A payload-range diagram is constructed in Section 7.4, with the final results present in Section 7.5. Finally, sensitivity analysis and verification and validation are carried out respectively in Section 7.6 and Section 7.7.

7.1. Rotor Characteristics

To calculate the power required for the various flight phases, first specific parameters related to the rotors have to be computed. Firstly, the total disk area (A) is found based on the ratio between the mass (W_{MTOW}) and the disk loading (DL) of 25 kg/m^2, which falls in the range of possible values for multirotors [24, 25]; from the total area can then be derived the rotor diameter (d) and the tip speed (V_{tip}).

$$A = \frac{W_{MTOW}}{DL} \quad (7.1) \qquad d = 2\sqrt{\frac{A}{\pi \cdot n_r}} \quad (7.2) \qquad V_{tip} = \frac{RPM \cdot 2 \cdot \pi}{60} \cdot \frac{d}{2} \quad (7.3)$$

Following, the thrust (T) to be delivered is computed, as well as the thrust coefficient (C_T) and the blade solidity (σ), which denotes the ratio of the lifting area of the blades to the area of the rotor. Due to the use of ducted rotors instead of open ones, the thrust production is increased by approximately 18%, represented by the factor η_{thrust} [24, 25]. Additionally, due to the tilt of rotors, there is a loss of 5.1 % in the thrust, as explained Section 10.3, which is represented by the factor η_{tilt} The parameters mentioned are thus calculated in the following way [26]:

$$T = \frac{W_{MTOW} \cdot g}{\eta_{thrust} \cdot \eta_{tilt}} \quad (7.4) \qquad C_T = \frac{T}{\rho \cdot A \cdot V_{tip}^2} \quad (7.5) \qquad \sigma = \frac{n_b \cdot c_b}{\pi \cdot r} \quad (7.6),$$

where n_b is the number of blades, c is the average blade chord, r is the radius of the rotor, which is half of the diameter given in Equation 7.2 and ρ is the air density. More information on the number of blades and the blade chord is given in Section 10.4.

7.2. Power Calculations

To analyze the performance of the vehicle, the power required to accomplish the mission is calculated for each of the flight phases: hover, cruise, climb, and descent. All of the calculations will follow the theory present in [26].

7.2.1. Power in Hover

In hover, the power required can be decomposed into the induced power and the profile power, which can be found by calculating their respective power coefficients:

$$C_{P_i} = \frac{\kappa \cdot C_T^{\frac{3}{2}}}{\sqrt{2}} \quad (7.7) \qquad C_{P_0} = \frac{\sigma \cdot C_{D_0}}{8}. \quad (7.8)$$

The induced power, based on the momentum theory, accounts for both the power needed to lift the vehicle and for various non-ideal yet physical phenomena, including nonuniform inflow, tip losses, wake swirl, suboptimal wake contraction, and the finite number of blades. These nonideal losses are reflected in the induced power correction factor κ. Accounting for the losses the value of kappa is increased from 1 (ideal) to a value of 1.15 [26]. The profile coefficient accounts for the profile drag and viscous drag losses of the rotors. For this, the profile drag coefficient of the rotor C_{D_0} is set to a common value of 0.01. [26].
Finally, the power in hover (P_h) is simply found in the following way:

$$P_h = (C_{P_i} + C_{P_0}) \cdot \rho \cdot A \cdot V_{tip}^3 \quad (7.9)$$

7.2.2. Power in Climb

In the climb phase, the climb velocity impacts the induced velocity at the rotor, therefore affecting the induced power as well. Thus, the ratio between power in climb (P_c) and hover, as well as the induced velocity (v_h) in hover, are given in the equations below:

$$\frac{P_c}{P_h} = \frac{V_c + v_i}{v_h} = \frac{V_c}{v_h} + \frac{v_i}{v_h} \quad (7.10) \qquad v_h = \sqrt{\frac{T}{2\rho A}}, \quad (7.11)$$

where V_c is the climb speed and v_i is the different induced velocity in climb. The two terms on the right-hand side of Equation 7.10 represent respectively the energy expended to alter the potential energy of the vehicle and the energy exerted on the air by the rotors. Using the relationship in Equation 7.12, the power ratio can be rewritten as shown in Equation 7.13:

$$\frac{v_i}{v_h} = -\frac{V_c}{2v_h} + \sqrt{\left(\frac{V_c}{2v_h}\right)^2 + 1} \quad (7.12) \qquad \frac{P_c}{P_h} = \frac{V_c}{2v_h} + \sqrt{\left(\frac{V_c}{2v_h}\right)^2 + 1} \quad (7.13)$$

7.2.3. Power in Cruise

To find the power required for the cruise phase, a similar approach as for the hover power calculations will be followed. The cruise power can be calculated with the following equation:

$$P_{cr} = \left(C_{P_i} + C_{P_0} + C_{P_p}\right) \rho A V_{tip}^3, \quad (7.14)$$

where C_{P_i}, C_{P_0}, and C_{P_p} are the induced, profile, and parasitic power coefficients respectively. Compared to hover, the extra parasitic power loss term is introduced to account for the viscous shear effects and flow separation on the airframe and rotor hubs. It can be calculated with the parasitic power coefficient:

$$C_{P_p} = \frac{1}{2}\frac{f}{A}\mu^3 \quad (7.15) \qquad f = 0.0327 GW^{0.8903} \quad (7.16) \qquad \mu = \frac{V_\infty \cos\alpha}{V_{tip}} \quad (7.17),$$

where f is the equivalent flat plate area, A is the total disk area, μ is the advance ratio, GW is the gross weight, α is the angle of attack and V_∞ is the free stream airspeed. The flat plate area f can be found with equation 7.16 [27], in which the flat plate area (in ft^2) is represented as a function of the gross weight (in lb).

The profile power coefficient C_{P_0} can be computed using Equation 7.18. This term accounts for the profile drag losses of the rotating rotor blades.

$$C_{P_0} = \frac{\sigma \cdot C_{D_0}}{8}\left(1 + 4\mu^2 + \frac{5}{8}\mu^4\right) \quad (7.18)$$

Compared to the profile power coefficient in hover, the extra term in the parenthesis is introduced, which

is a function of the advance ratio. The $4\mu^2$ accounts for the effects of radial flow (flow of air moving in the radial direction over the surface of the rotor), while the $\frac{5}{8}\mu^4$ accounts for the so-called reverse flow effects. The latter is illustrated in Figure 7.1. At higher advance ratios, the blade sections on the retreating side of the disk operate with the trailing edge into the relative wind. This causes the sectional drag contribution of the reverse flow region to act in the opposite direction.

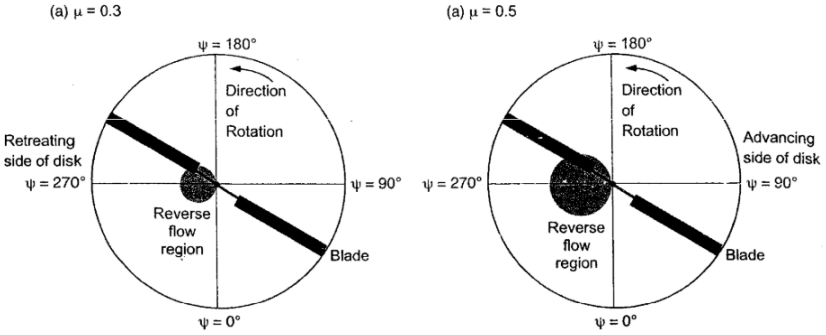

Figure 7.1: Reverse Flow of Advancing Rotor [26]

Lastly, the induced power coefficient is computed using Equation 7.19, where λ is the inflow rate, calculated with Equation 7.20.

$$C_{P_i} = \frac{\kappa \cdot C_T^2}{2\sqrt{\lambda^2 + \mu^2}} \tag{7.19}$$

$$\lambda = \mu \tan \alpha + \frac{C_T}{2\sqrt{\mu^2 + \lambda^2}} \tag{7.20}$$

Compared to the induced coefficient in hover, the extra term is added which represents the additional dependence on the forward speed and angle of attack of the vehicle.

To be able to compute the power coefficients, knowledge of the values of α and λ is required. The angle of attack can be found using the following relationship:

$$\alpha = \arctan\left(\frac{D}{W}\right) = \arctan\left(\frac{P_D}{WV_\infty}\right) \tag{7.21}$$

$$P_D = C_{P_p} \cdot \rho A V_{tip}^3, \tag{7.22}$$

where D is the drag, W is the weight of the vehicle and P_D is the power due to drag, calculated using the parasitic power coefficients. As it's not possible to find the inflow rate analytically with Equation 7.20, a numerical solution is employed to find the result at which both the left and right sides of the equations match. Finally, the power during the cruise can be calculated using Equation 7.14.
The variation of the different components based on the airspeed is visualized in Figure 7.2.

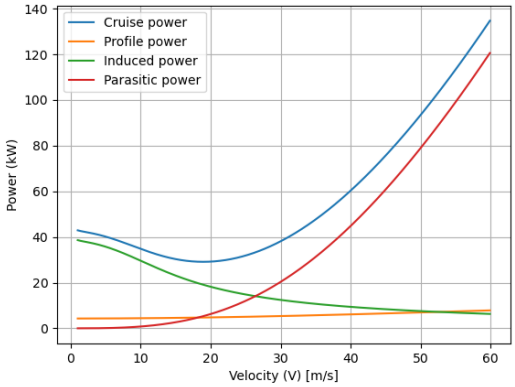

Figure 7.2: Cruise power diagram

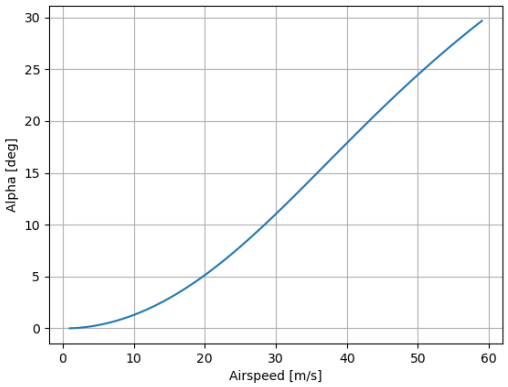

Figure 7.3: Variation of angle of attack with airspeed

As expected, at low speeds the dominant power component is the induced power. At higher speeds, the parasitic power becomes the most influential component, as it increases with the cube of the speed. The angle of attack is related to the parasitic drag of the vehicle; therefore, as drag increases with speed, so does the angle of attack, as illustrated in Figure 7.3.

7.2.4. Power in Descent

Up until now, momentum theory has been applied to compute the power required in the other phases. However, momentum theory becomes invalid in the region $-2 \leq \frac{V_d}{v_h} \leq 0$, since "the flow can take on two possible directions and a well-defined slipstream ceases to exist" [26]. Due to the low descent speed of 2.5 m/s, the ratio between descent speed and induced hover speed falls in the invalid region. However, the power can still be calculated with the use of velocity curves established empirically with data collected from flight tests. Thus, a continuous approximation of the induced velocity is given [26]:

$$\frac{v_i}{v_h} = \kappa + k_1 \left(\frac{V_d}{v_h}\right)^1 + k_2 \left(\frac{V_d}{v_h}\right)^2 + k_3 \left(\frac{V_d}{v_h}\right)^3 + k_4 \left(\frac{V_d}{v_h}\right)^4 \tag{7.23}$$

where $k_1 = -1.125$,$k_2 = -1.372$, $k_3 = -1.718$ and $k_4 = -0.655$.

Once the induced velocity is calculated, the power in descent can be computed with the following equation [26]:

$$P_d = P_h \left(\frac{V_d}{v_h} + \frac{v_i}{v_h}\right) \tag{7.24}$$

7.2.5. Altitude Ceiling

As the altitude increases, the density decreases; since the power is proportional to the air density, with higher altitude, the power available decreases, resulting in higher power required. For the optimization of the design, a cruise altitude of 300 m is considered; however, the vehicle should still be able to operate at its altitude ceiling of 1000 m, therefore the change in power with varying altitudes is investigated, with the results shown in Figure 7.4, where the ground altitude is assumed to be at sea level.

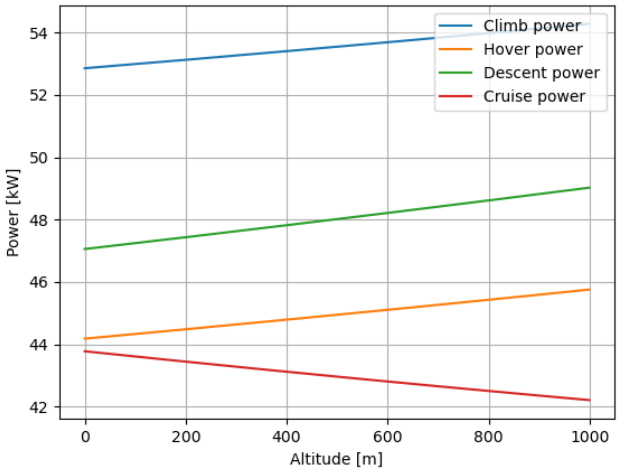

Figure 7.4: Change in Power Required Due to Altitude

As anticipated, the power required increases for all flight phases except for the cruise. As previously discussed, higher altitudes correspond to lower air density, which reduces the number of air molecules per unit volume and consequently lowers parasitic drag. Therefore, the power required for a cruise decreases with altitude. In contrast, the other flight phases do not benefit as significantly from reduced parasitic drag, since it is not as prominent a factor due to the lower airspeeds in these phases; therefore the decrease in available thrust at higher altitudes is not offset by the lower drag.
Additionally, it can be observed that across the range of altitudes considered, the various power values show minimal variation, with a maximum difference of 2 kW. This suggests that power requirements are not highly sensitive to changes in altitude. The primary variable influencing power requirements is the corresponding speed specific to each flight phase. In cruise, this is represented by airspeed, as depicted in Figure 7.2. For the climb and descent phases, it correlates with their respective ascent and descent speeds, while in hover, it is the rotor tip speed.

7.2.6. Maximum Power

When selecting the motors for the vehicle, it is essential to ensure they can provide sufficient total power to sustain flight under various conditions. To achieve this, a maximum load factor n of 2 is considered when initially calculating the thrust required for flight:

$$n = \frac{T}{W} \tag{7.25}$$

Although the critical mission profile assumes a maximum altitude of 300 m, the vehicle must be capable of flying at an altitude of 1000 m, according to requirement *STK-CLNT-11*. At higher altitudes, air density decreases, which reduces the available power since power is proportional to air density. Therefore, it is crucial to ensure that the motors can deliver adequate power to meet the requirements at this higher altitude.

To determine the maximum power needed, the power requirements for each flight phase are recalculated, incorporating the load factor and reduced air density. It should also be noted that when climbing to the service ceiling, the climb speed starts with a value of 3.4 m/s and then decreases to 0.5 m/s when the altitude ceiling is about to be reached[1]. Among all flight phases, the maximum power required is identified. Although climbing typically demands more power, the significantly reduced climb speed results in a lower power requirement compared to hovering. Consequently, the hover power is found to be the highest.

7.3. Energy Calculations

Having obtained the values for the power required for the different segments of the mission, it is now possible to calculate the total energy that the vehicle expends when completing one leg of the most critical mission profile, shown in Figure 2.1.

The total energy can be found using the following equation:

$$E_{tot_{oneway}} = P_h t_h + P_c t_c + P_{cr} t_{cr} + P_d t_d, \tag{7.26}$$

where t_h, t_c,t_{cr},t_d are respectively the hover, climb, cruise and descent times. The methodology required to obtain the different power values is explained in Section 7.2. The total loiter (hover) time is 10 minutes, which translates to 5 minutes when calculating the energy for a one-way trip. During the climb and descent phases, the multicopter operates at respective speeds of V_c = 3.4 and V_d = 4, covering the same distance corresponding to the flight altitude (h = 300 m). Consequently, the time for the climb and descent phase can be determined using the general equation:

$$t = \frac{h}{V} \tag{7.27}$$

When considering cruise time, two scenarios need to be examined: flight with and without wind conditions. For the scenario without wind, the cruise time can be easily calculated using the formula:

$$t_{cr} = \frac{R}{V_{cr}} \tag{7.28}$$

where R is the range of a one-way trip (15 km) and V_{cr} is the cruise speed.

In the presence of wind, the effective flight velocity changes depending on the vehicle's direction relative to the wind. The critical scenario, which expends the most energy, involves flying without the payload with a tailwind to the rescue location and returning with the payload against a headwind, assuming that the wind direction does not change during the mission. The time required for these two conditions is calculated as follows:

$$t_{cr_{payload}} = \frac{R}{V_{cr} - V_w} \tag{7.29}$$

$$t_{cr_{nopayload}} = \frac{R}{V_{cr} + V_w} \tag{7.30}$$

[1] URL https://www.eaa.org/eaa/news-and-publications/eaa-news-and-aviation-news/bits-and-pieces-newsletter/09-13-2016-aviation-word-service-ceiling [cited 19 June 2024]

where V_w is the wind speed which is 13.89 m/s as per the requirement *STK-CLNT-19 (Key): The vehicle shall be able to withstand wind of 6 bft*.

Finally, the total energy used to complete the entire mission is the sum of the energy required for flying with and without the payload. These can be calculated using Equation 7.26.

The variation of the total energy required based on the cruise speed is visualized in Figure 7.5. As can be seen, the cruise speed increases and the energy consumption decreases as the cruise time becomes lower; a minimum is reached at a speed of 45 m/s, thus this is the optimal cruise speed. It can be noted that the diagram does not start at 0 speed, this is due to the fact that when computing the energy requirements, the flight scenario in wind conditions is considered. For the vehicle to be able to fly, it must have a speed higher than that of the wind (13.89 m/s), therefore that is why the graph starts at a speed of 14 m/s.

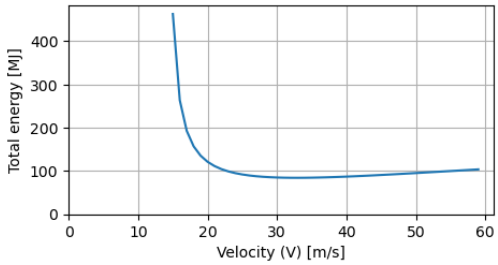

Figure 7.5: Graph of energy as a function of cruise speed

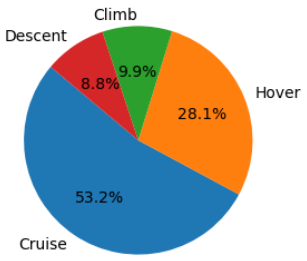

Figure 7.6: Energy split based on flight phases

In Figure 7.6, the distribution of total energy across flight phases is depicted. As expected, the cruise phase demands the most energy (53.2%), given its extended duration covering a total range of 30 km. Following this is the hover phase, consuming a large amount of energy as well (28.1%), as it constitutes nearly one-third of the total mission time due to a 10-minute loiter period in the mission profile. On the other hand, the climb and descent phases require comparatively less energy, accounting for 9.9% and 8.8%, respectively. Descent has lower power consumption and higher speed compared to climb (4 m/s for descent, 3.4 m/s for climb), resulting in a shorter duration and lower energy consumption. However, the difference in these values is minimal, explaining the small variation in percentages.

7.4. Payload-Range Diagram

With the total energy available calculated, it is possible to create a payload-range diagram, showing the change of the maximum achievable range based on the payload mass, which is shown in Figure 7.7. It has to be noted that the range presented includes flying to and back from the emergency location. It should be noted that the above results assume that the battery state of charge at the end of the mission is 20% and 10 min of loiter is reserved for safety reasons and possible avoidance maneuvers.

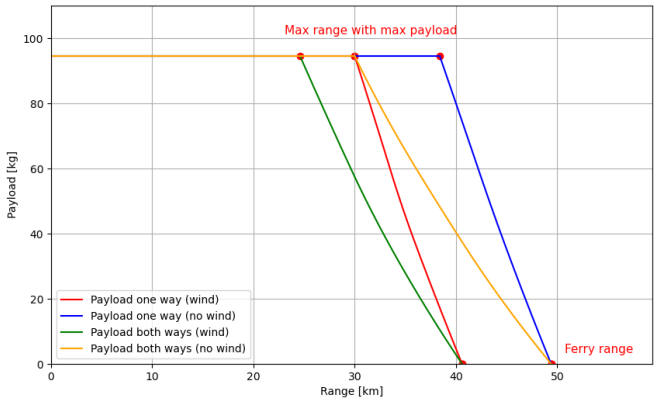

Figure 7.7: Payload-Range Diagram

As can be seen from the figure, there are four possible mission scenarios. The first and second scenarios include carrying the payload only one way. This enables rescuing the passenger from the emergency location, which is what the vehicle has been designed for. The maximum range achievable in this

scenario with a full payload and maximum wind conditions is 30 km. In case of non-windy conditions, this range extends to 38.4 km. The third and fourth scenarios include carrying the payload both ways. This would help in the case where the rescued person is identified pre-flight to be severely injured and thus unable to board the vehicle on its own. Consequently, a medic could use the vehicle to fly to the emergency location and help with boarding the injured person. A secondary pickup is then needed to retrieve the medic. This scenario reduces the maximum range achievable with the maximum payload to 24.6 km in windy conditions and 30 km in non-windy conditions.

By decreasing the payload, the range is increased until the ferry range, which represents the maximum range that the vehicle is able to achieve for the critical mission profile (range mission). The curve shape is consistent with the adapted Brequet's range equation for electric aircraft, where the range is inversely proportional to the payload weight [28]. Windy conditions scenarios converge to one ferry range at 40.6 km. In non-windy conditions, the vehicle is able to fly 49.4 km when carrying no payload.

Compared to the payload range diagram for a conventional aircraft, the vehicle does not use any fuel, therefore no range can be gained in that respect. The battery weight, which is the energy source for this eVTOL, cannot be changed for different operations, as the battery used will be specific to the vehicle and its weight does not vary during the mission.

7.5. Final Results

Upon completion of the calculations presented in the previous sections, the final results are presented in the following tables:

Table 7.1: Final Results of the Flight Performance Analysis

Parameter	Value	Unit
W_{MTOW}	421.0	kg
V_{cr}	33	m/s
RPM	1200	-
A	14.22	m^2
d	1.74	m
n_b	2	-
c_b	0.11	m

Parameter	Value	Unit
α	13.14	deg
P_h	44.6	kW
P_c	53.3	kW
P_d	47.6	kW
P_{cr}	43.3	kW
P_{max}	133.7	kW
E_{tot}	84.7	MJ

7.6. Sensitivity Analysis

After completing the primary calculations, conducting a sensitivity analysis is crucial. This analysis helps determine critical variables that exert the most significant influence on the outcomes and allows for the identification of sources of uncertainty. Understanding the variability of results can give a better idea of the reliability of the model. The main values that are investigated are the range and the mass.

7.6.1. Range

The achievable range of the flyer depends on several factors, such as the payload mass, as illustrated in Figure 7.7. Another critical factor is the cruise altitude, which, as discussed in Subsection 7.2.5, generally decreases the power available. Additionally, with a higher altitude, the mission time increases, as a higher time is spent on climb and descent, where they are assumed to be completely vertical without any forward speed. Consequently, more energy is consumed for covering the same distance, limited by the battery capacity, resulting in a reduced maximum range, as shown in Figure 7.8. This figure illustrates the range variations under flight conditions with and without wind. When wind is present, it is assumed that the aircraft is flying with a tailwind when going to the rescue location and with a headwind when flying back to base with the payload. Sensitivity analysis reveals altitude's significant impact, with the range decreasing by 85% from sea level to 1000 m altitude.

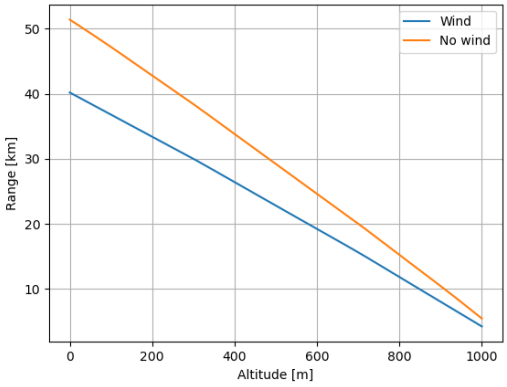

Figure 7.8: Change in Range Due to Cruise Altitude

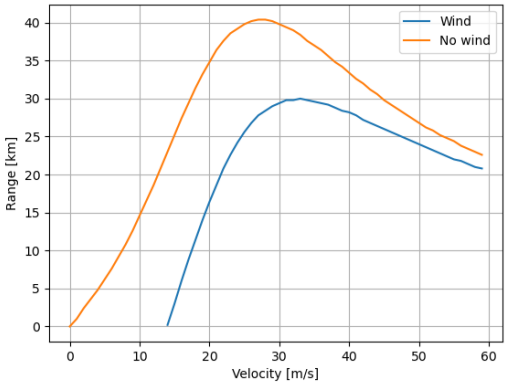

Figure 7.9: Change in Range Due to Cruise Speed

Next, the relationship between range and cruise speed is examined, as illustrated in Figure 7.9. At lower speeds, although power requirements may be reduced, the longer cruise duration leads to higher energy consumption, ultimately limiting the achievable range. As cruise speed increases, optimal speeds of 28 m/s and 33 m/s are respectively achieved for flight without and with wind. At these speeds, the balance between cruise speed and power consumption is optimized; despite higher power consumption, the vehicle's faster flight results in lower overall energy consumption. Beyond these speeds, however, the increased power demand outweighs the benefits of higher speeds, leading to higher energy consumption and consequently reduced range. From the results, it can be determined that the range is highly sensitive to the cruise speed as well.

Finally, as the multicopter should be able to operate in windy conditions, an analysis is conducted on how the range varies with different wind magnitudes and directions, as shown in Figure 7.10. Negative wind values indicate tailwinds when carrying the payload and headwinds when without it; the opposite applies to positive winds. The most energy-intensive scenario occurs with headwinds while carrying the payload, as illustrated in the figure where, at wind speeds of equal magnitude, the range achieved is lower under positive wind conditions. At low tailwinds (-3m/s), a higher range is achieved than when there is no wind. Contrary to expectations, the presence of a tailwind during the payload-carrying flight reduces energy consumption, compensating for the increased energy expenditure when flying against a headwind without a payload, as the headwind is not strong enough to significantly raise the total energy consumption. Across the range of winds considered, the range exhibits a change in magnitude of 42%, highlighting its significant sensitivity to wind speed.

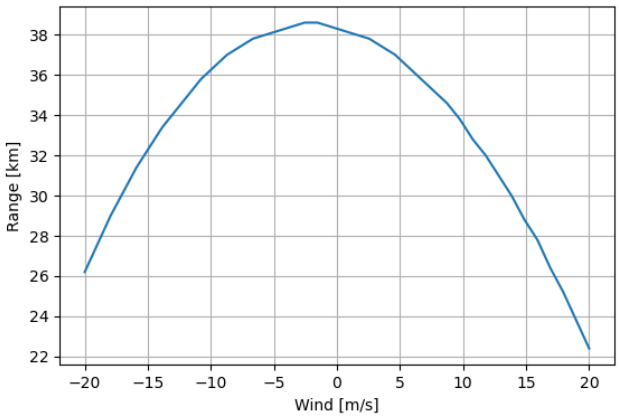

Figure 7.10: Change in Range Due to Wind Speed

7.6.2. Design Sensitivity

As explained in Chapter 6, the final design parameters are obtained through multiple iterations, each time carrying new performance analyses to evaluate the new designs until convergence is achieved. As the design optimization is highly reliant on the performance analyses, a sensitivity analysis is carried out on how the main characteristics of the final design changed based on the main input parameters of the performance analysis, them being the cruise speed, the cruise altitude, and the rotational speed

of the rotors.

Cruise Speed

To achieve the lowest energy consumption, the flyer must operate at the optimal cruise speed of 33 m/s. To evaluate the design's sensitivity to variations in cruise speed, this optimal speed is adjusted by up to ±30%. As shown in Table 7.2, the mass is relatively sensitive, increasing significantly as the optimal speed is altered. The rotor size also exhibits sensitivity, though to a lesser extent. On the other hand, the maximum power, total time, and total energy are highly sensitive to speed variations. Notably, while a lower cruise speed reduces maximum power compared to a higher speed, it leads to much higher total time and energy consumption, resulting in a less efficient design.

Table 7.2: Design Sensitivity to Cruise Speed

Vcr	Mass	Diameter	Max power	Total time	Total energy
-30%	25.09%	11.83%	28.03%	66.91%	52.36%
-20%	6.43%	3.16%	7.08%	32.84%	13.49%
-10%	1.06%	0.53%	1.17%	12.98%	2.28%
10%	0.89%	0.44%	0.97%	-9.16%	1.93%
20%	6.15%	3.03%	17.18%	-15.98%	10.19%
30%	15.55%	7.49%	48.16%	-21.24%	24.49%

Altitude

During the mission, the vehicle may need to change its cruise altitude due to unforeseen conditions, making it crucial to assess the design's sensitivity to altitude variations. Once again, the cruise altitude is varied by $\pm$ 30%. As can be seen in Table 7.3, all the parameters show low sensitivity to altitude change. With a lower altitude, as expected a lower design mass can be achieved, due to the lower power requirements and energy consumption. The opposite happens when the altitude increases, when all the parameters increase, with total energy showing the highest sensitivity.

Table 7.3: Design Sensitivity to Altitude

Altitude	Mass	Diameter	Max power	Total time	Total energy
-30%	-0.03%	-0.01%	-0.27%	-4.20%	-5.58%
-20%	-1.08%	-0.54%	-1.34%	-2.80%	-4.90%
-10%	-0.54%	-0.27%	-0.67%	-1.40%	-2.46%
10%	2.00%	1.00%	2.28%	1.40%	4.22%
20%	4.16%	2.06%	4.73%	2.80%	8.72%
30%	6.48%	3.19%	7.38%	4.20%	13.53%

Rotational Speed

During the design iterations, the optimal RPM of the rotors is computed, resulting in 1200 rpm. Generally, having a lower rotational speed can provide marginal improvements for the maximum power required and total energy required, as shown in Table 7.4. However, in terms of mass and rotor size, the changes are negligible. A lower RPM is not selected as it would result in an inefficient rotor blade, with a too large average chord, for more information in Section 10.4. The same cannot be said when the rotational speed is increased, as the parameters show a much higher sensitivity.

Table 7.4: Design Sensitivity to Rotational Speed

RPM	Mass	Diameter	Max power	Total time	Total energy
-30.00%	0.17%	0.09%	-6.08%	0.00%	-5.74%
-20.00%	-0.29%	-0.14%	-4.93%	0.00%	-4.67%
-10.00%	-0.29%	-0.14%	-2.88%	0.00%	-2.72%
10.00%	2.14%	1.06%	5.63%	0.00%	5.51%
20.00%	5.91%	2.91%	14.27%	0.00%	14.02%
30.00%	12.30%	5.97%	27.97%	0.00%	27.60%

7.7. Verification and Validation

To prove that the model used for the performance analysis is reliable, the program has to be verified to ensure the correctness of the code as well as validated, to show that the model can provide results that match the reality.

7.7.1. Verification

To verify the model, different types of testing are carried out.

Unit testing

The performance analysis model is mainly constituted by the FlightPerformance class, which is itself made up of many functions. Each function is tested independently providing the inputs required and comparing the results obtained by the code with the values calculated by hand using the analytical models. An overview of the unit test results can be observed in the table below:

Table 7.5: Unit testing results

Unit Test	Inputs	Output	Difference
Rotor_characteristics	W_{MTOW}, RPM, ρ	T, d, V_{tip}, A, C_T, σ, v_h	0.0%
Hover_power	C_T, σ, ρ, A, V_{tip}	P_h	0.0%
Cruise_power	σ, μ, ρ, A, v_{tip}, f	P_{cr}	0.0%
Climb_power	P_h, V_c, v_h	P_c	0.0%
Descent_power	V_d,v_h, P_h	P_d	0.0%
Solve_alpha	V, v_{tip}, σ, f, A, ρ, W_{MTOW}	α	0.0%
Solve_lambda	μ, α, C_T	λ	0.0%
Total_energy	t_h, h, V_c, V_d, P_h, P_c, P_d, P_{cr}	E_{tot}	0.0%

As demonstrated, all unit tests are successful, showing no differences between the expected values and the actual code outputs. For the unit tests of *solve_lambda*, the numerical solution is verified by comparing both sides of the equations, resulting in no discrepancies. Additionally, the convergence of the solution is confirmed through graphical representations, as shown in the figure below.

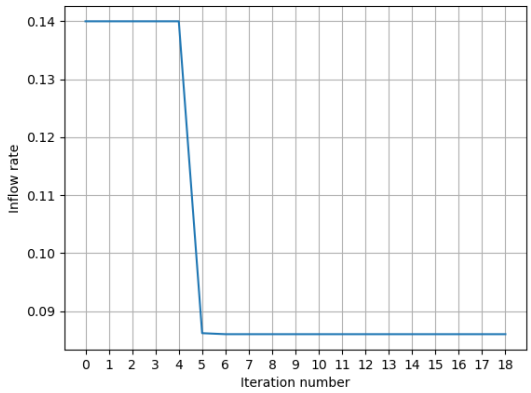

Figure 7.11: Convergence of inflow rate

Boundary Value Analysis

To check the robustness of the model, boundary testing is performed to investigate the behavior of the code with values that are on the edge of the boundary. The main variables tested are mass, density, and speed, as they significantly impact the results. Three types of boundary tests are conducted: setting these factors to 0, assigning them negative values, and using very large values. When set to 0, division by 0 occurs, resulting in code failure. When negative values are used, impossible results are expected, such as negative energy. For very large values, the code is still expected to run, but the results should have impossibly high values. As shown in the table below, all tests pass, demonstrating the expected behavior.

Table 7.6: Boundary testing results

Boundary test	Expected result	Test result
V = ρ = W_{MTOW} = 0	Code failure	Passed
Negative V, ρ, W_{MTOW}	Code failure	Passed
Very large V, ρ, W_{MTOW}	Code works, with results of high magnitude	Passed

Convergence Analysis

For the weight iteration, the optimal design is obtained by looping through different possible speeds to find the optimal cruise speed. An analysis can be carried out to check whether the total mass converges when the step size of the speed is changed to smaller values. As can be seen in the figure below, the final weight is not highly impacted by the step size, converging to the same values.

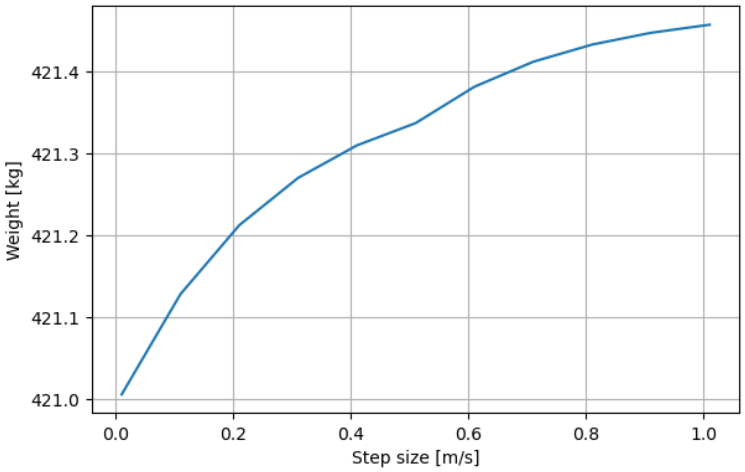

Figure 7.12: Convergence of maximum take-off weight

Integration Testing

Finally, the verification of the code is completed by ensuring all modules of the program work together correctly and produce the expected outputs. Each module is checked for correct input and output handling, expected order of code execution, and error handling.

The system testing is successful, with all values matching the hand-calculated results within a tolerance of 1%. This tolerance is considered acceptable, as hand calculations use fewer significant figures than the program, potentially causing minor discrepancies between the test and code results. The final results are given in the following table:

Table 7.7: Integration Testing Results

Module\Test	Input Handling	Output Handling	Difference	Order of Execution
Rotor_characteristics	Correct	Correct	<1%	Correct
Hover_power	Correct	Correct	<1%	Correct
Cruise_power	Correct	Correct	<1%	Correct
Climb_power	Correct	Correct	<1%	Correct
Descent_power	Correct	Correct	<1%	Correct
Solve_alpha	Correct	Correct	<1%	Correct
Solve_lambda	Correct	Correct	<1%	Correct
Total_energy	Correct	Correct	<1%	Correct

7.7.2. Validation

Once the model verification is completed, the validation process follows. Validation ensures that the program produces results that accurately reflect real-world scenarios. This is achieved by comparing model results with empirical data.

Different techniques can be used to validate the model:

- **Experience**: consists of the validation of the model by comparing it with similar models applied in analogous circumstances.
- **Analysis**: consists of demonstrating the inherent accuracy and integration of model components, often supported by comparison with real-world data. This involves scrutinizing individual components of the model and assessing their reliability to real-world phenomena.
- **Comparison**: consists of validating model results by comparing them with independent models known to be correct or utilizing real test data, such as flight test data from similar aircraft. This comparative approach helps verify the consistency and reliability of the model outputs against real data.

At this design stage, proper validation is challenging due to the limited availability of flight data and characteristics of electric multicopters. However, in future phases, a prototype flyer could be built, and flight test data could be used for validation. Currently, the validation is limited to comparing the code results with those in [27] by using the same inputs, and this comparison is successful despite its limitations. Further validation of the final design is given in Section 25.2.

8 | Class II Weight Estimation

This chapter presents a more detailed weight estimation of the vehicle by components. Firstly, structural component mass is evaluated in Section 8.1 which is followed by battery sizing in Section 8.2. Finally, all results are summarized in Section 8.3. It should be noted that the formulas take into account various parameters such as thrust, power, gross weight, and specific dimensions. Note that thrust per rotor is given in Newtons (N) and motor power is given in kilowatts (kW). All other measurements are provided in imperial units.

8.1. Structural Component Weights

Based on the power calculations and the preliminary fuselage sizing, equations presented in Table 8.1 have been used to perform the more accurate weight estimation of structural components of the multicopter. The equations are based on the approach from [27], which uses the weight models that have been extracted from historical correlations and prior studies of electric rotorcraft [29, 30, 31]. Extra hubs component is computed to account for the high-speed loading with the fixed-pitch rotors, which leads to heavier hubs as given by [31], which has been verified by [32].

Table 8.1: Structural Component Weights

Component	Formula	Variable Definition and Units
Rotors + Hubs	$W_{\text{rotors\_hubs}} = \left(\frac{2.20462}{1000}\right)\left(\left(\frac{7200}{500}\right)(1.5 \cdot T_r - 300) + 800\right) \cdot n_r$	T_r: thrust per rotor (N) n_r: number of rotors
Extra Hubs (multicopter)	$W_{\text{hub}} = 0.0037\,(n_b)^{0.28} R^{1.5} V_{tip}^{0.43} \cdot \left(0.01742 n_b^{0.66} c_b R^{1.3} V_{tip}^{0.67} + g\left(\frac{\pi R^4}{R^2}\right)^{0.5}\right)^{0.55} \cdot n_r$	n_b: number of rotor blades R: radius (ft) V_{tip}: tip velocity (ft/s) c_b: blade chord (ft) g: gravitational acceleration (ft/s²) n_r: number of rotors
Battery	$W_{\text{batt}} = \frac{E_{req}}{\epsilon \cdot \eta_{\text{pt}} \cdot \eta_{\text{r}} \cdot (1 - \text{SoC}_{\text{end}}) \cdot 3600}$	E_{req}: energy required (J) ϵ: energy density (Wh/kg) η_{pt}: powertrain efficiency η_{r}: rotor efficiency SoC_{end}: End State of Charge
Motor	$W_{\text{motor}} = 2.20462\left(\frac{58}{990}(\tau - 10) + 2\right) \cdot n_r$	τ: torque (Nm) n_r: number of rotors
Motor Controller	$W_{\text{motor\_controller}} = 2.20462\left(\frac{49.9}{398}(P_m - 2) + 0.1\right) \cdot n_r$	P_m: power of the motor (kW) n_r: number of rotors
Fuselage	$W_{\text{fuselage}} = 6.9\left(\frac{GW}{1000}\right)^{0.49} l_f^{0.61} S_{w_f}^{0.25}$	GW: gross weight (lb) l_f: length of the fuselage (ft) S_{w_f}: wetted surface area of fuselage (ft²)
Landing Gear	$W_{\text{landing\_gear}} = GW \cdot 0.095$	GW: gross weight (lb)
Flight Controls	$W_{\text{flight\_controls}} = 11.5\left(\frac{GW}{1000}\right)^{0.40}$	GW: gross weight (lb)
Furnishings	$W_{\text{furnishings}} = 13\left(\frac{GW}{1000}\right)^{1.3}$	GW: gross weight (lb)

8.2. Battery Sizing

This section presents the procedure for obtaining a class II battery weight estimation. First, the efficiency of energy conversion will be presented, followed by the procedure of obtaining the battery weight.

8.2.1. Efficiency of Energy Conversion

This section describes the efficiency of all the subsystems that are involved in the energy conversion from the battery to the actual thrust provided by the rotors. This has to be done in order to estimate the energy losses and thus the actual energy available.

Due to the strict certification process, which according to the U.S. Government Accountability Office (GAO) and the Federal Aviation Administration (FAA) can take from 5 to 9 years [33, 34], it is expected that the entry into service for this eVTOL will be at the earliest in about 10 years. Volocopter aims to achieve certification and launch commercial services by 2024, having started its development in the early 2010s [35]. This means that predictions for advancements in technology can be taken into account during the design. Nevertheless, in order to be conservative, predictions will be analyzed based on the credibility of the estimation procedure and authors. If deemed that the estimates are very ambitious, averages between current and predicted values will be taken to avoid under-designing the eVTOL.

Firstly, the current value of the energy density ε at BoL (Beginning of Life) is $250\,\mathrm{Wh/kg}$, consistent with the current battery performance available in the market [36]. It is predicted that by 2026, the cell-specific energy could reach $300\,\mathrm{Wh/kg}$ at BoL (without casing) [27], therefore this value is selected for our design process.

Secondly, Equation 8.1 shows two different efficiencies that are involved in the energy transfer process, propulsive efficiency η_{rotor} and powertrain efficiency $\eta_{powertrain}$, which is then further broken down into storage, electric cables, and electric motor efficiencies.

$$\eta_{conv} = \eta_{rotor} \cdot \eta_{powertrain} = \eta_{rotor} \cdot \eta_{storage} \cdot \eta_{cables} \cdot \eta_{elec.motor} \tag{8.1}$$

The values for all of these vary slightly across different sources. The main reason for this is that due to constant technological advancements, improvements to the subsystems can be made, increasing their efficiency. For 2035, which corresponds to our predicted service entry timeframe, [37] gives the predicted estimates: $\eta_{rotor} = 0.98$, $\eta_{storage} = 0.97$, $\eta_{cables} = 0.99$, $\eta_{elec.motor} = 0.98$. Compared to the current values, the deviations can be observed in $\eta_{rotor} = 0.80$ [27, 38] and $\eta_{elec.motor} = 0.90$ [39]. In order to be conservative and avoid underdesign, the average between the current and future values is taken in all subsequent calculations. The final values for propulsive and powertrain efficiency index are presented in Table 8.2.

Table 8.2: Energy Conversion Efficiency

$\boldsymbol{\eta_{rotor}}$	$\boldsymbol{\eta_{powertrain}}$	$\boldsymbol{\epsilon}(Wh/kg)$
0.89	0.90	300

8.2.2. Battery Weight

This section presents the procedure for obtaining the battery weight using the efficiencies presented earlier. Instead of using a set battery fraction as done in preliminary sizing, the mass of the battery was obtained by looping through different battery fractions and finding the optimal solution that matches the required energy. The total required energy is obtained from Equation 7.26. The energy available from the battery mass is calculated using Equation 8.2. As a rationale check, the obtained fraction from this procedure should be within the specified range from 25% to 35% of the MTOW [40].

$$E_a = \epsilon * m_{batt} * \eta_{powertrain} * \eta_{rotor} * (1 - SoC_{end}) * 3600, \tag{8.2}$$

where m_{batt} is the battery mass, ϵ is the specific energy of the battery, $\eta_{powertrain}$ is the powertrain efficiency, η_{rotor} is the rotor efficiency, batt_frac is the battery weight as a percentage of MTOW and SoC_{end} is the state of charge at the end of mission, set at 20%. Using this approach, the battery fraction is 0.29.

8.3. Updated Weight Results

This section presents the updated weights of all the components. Following the optimization loop explained in Chapter 6, the new MTOM of the eVTOL is **421 kg**. Using the approaches of the last two chapters, respective component weights are then computed. Figure 8.1 presents the weight of all the components as a percentage of the MTOW. It has to be noted that the motor weight includes both the motor and motor controller. Likewise, the battery weight includes both the battery itself and the extra low-voltage battery. The sizing of the battery subsystem will be explained in detail in Section 12.2.

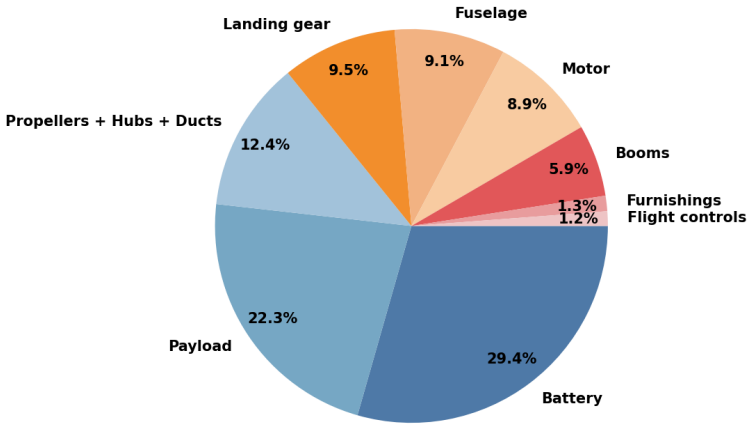

Figure 8.1: Component Weights

9 | Aerodynamic Performance Analysis

This section will present the aerodynamic analysis of the selected design. Section 9.1 will present the aerodynamic forces of the eVTOL in normal flight conditions for each mission phase separately. Section 9.2 will present the gust loading diagram, followed by the evaluation of the aerodynamic forces and moments that are acting on the vehicle when subjected to the wind gusts in Section 9.3.

9.1. Aerodynamic Forces

This section will assess the aerodynamic loads that are imposed on the vehicle during the normal flight condition. Subsection 9.1.1 first describes the setup of CFD simulations which are used as a validation tool. For each flight phase, the analytical evaluation is presented in Subsection 9.1.2. In Subsection 9.1.3, the parasitic drag is also compared to the one evaluated by the CFD simulations.

9.1.1. CFD Setup

The CFD simulation is set up in Siemens STAR-CCM+ software, using the Reynolds Averaged Navier-Stokes (RANS) method. This approach produces time-averaged and iteration-averaged results, reducing computational demands. However, It does come at the cost of reduced detail by taking the steady-state assumption. As a result, the radii of vortices can vary up to 35 percent with time-averaged results compared to transient results due to vortex meandering and local velocity fluctuations [41]. Additionally, velocity fields are smoothed, which can result in deviations in circulation and vortex core size. A comparison between RANS and more accurate LES (Large Eddy Simulation) is shown in Figure 9.1. Despite these limitations, CFD remains the best available tool, but it is essential to note the importance of careful interpretation of its results. Even when using LES method and using the finest mesh possible cannot guarantee perfect accuracy, as all CFD models have inherent approximations.

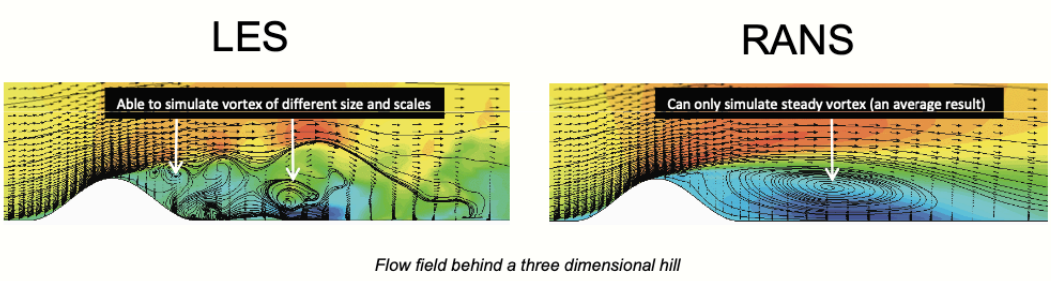

Figure 9.1: Comparison Between LES and RANS

The simulation is configured as a virtual wind tunnel, with the entire aircraft model imported directly there. To save computational time, only half of the aircraft is placed in the wind tunnel (Refer to Figure 9.2), with symmetry used to extrapolate the results. The simulation uses K-Omega turbulence, with an under-relaxation factor starting at 0.5 and linearly increasing to 0.8 over the first 500 iterations to prevent oscillations or divergence. The simulations run for a total of 1800 iterations.

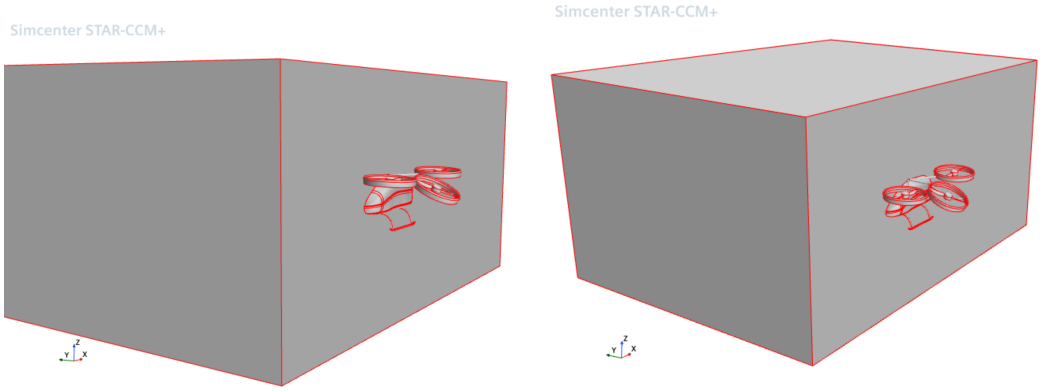

Figure 9.2: CFD Setup in Star-CCM+ Showing the Wind Tunnel and the Aircraft Model

To achieve more accurate results, an adaptive mesh refinement (AMR) is implemented in the simulation. AMR dynamically refines the mesh in regions of high turbulence or sensitivity during the runtime of simulation, unlike standard volume refinement regions that must be defined beforehand. AMR will not coarsen the original mesh, however, and thus a rather coarse starting mesh is required. While this increases overall runtime, it results in better resolution in critical areas, such as regions of high turbulence.

Verification

An important part of verifying the CFD results is checking the residuals of the simulation to evaluate its convergence. As shown in Figure 9.3, the flow components residuals (X,Y,Z momentum) are in the range of 10^{-4}, which indicates an acceptable level of convergence. The residuals also plateau after iteration 1200, implying that a steady-state solution has been reached. The Sdr (Specific Dissipation Rate) residual, is a convergence metric for the specific dissipation rate equation in turbulence modeling. The higher Sdr residual might indicate areas of complex turbulence dynamics or regions needing further refinement. The Sdr is also reduced by 3 orders of magnitude which is considered sufficient. In addition, simulations run with the alternative K-Epsilon turbulence model showed less than 3% variation compared to the results of the K-Omega model, which gives an extra level of confidence in the results and is deemed very good considering the short timeframe for development and refinement of these simulations. Overall, these values demonstrate good numerical accuracy and stability of the solution. The residuals also level off and do not show erratic and oscillatory behavior (except for the iterations 500 - 1100 where Adaptive Mesh Refinement criteria are triggered, where the mesh changes and such behavior is normal).

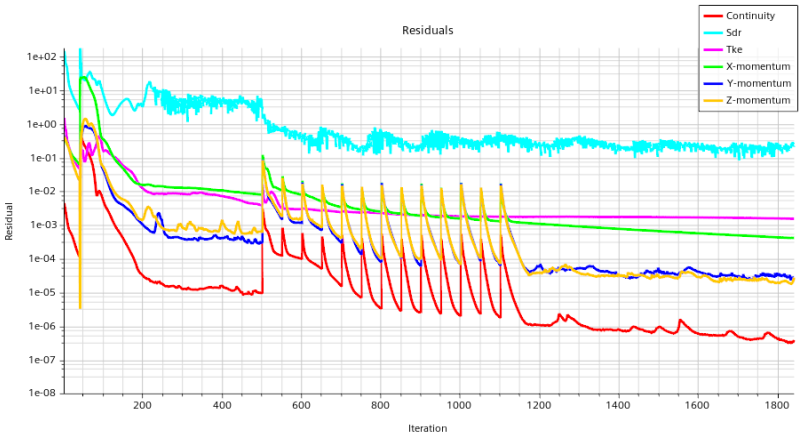

Figure 9.3: Plot with CFD Residuals. Note the oscillatory behavior when the Adaptive Mesh Refinement starts at iteration 500.

9.1.2. Class II drag estimation

This section will present the class II drag estimation. Each mission phase has been analyzed separately due to the significant changes in the direction of the incoming flow during these phases. First, the analytical procedure is presented for each phase, followed by the resulting plots. Lastly, the results are validated using the CFD simulations.

Based on the analytical approach from [26], the drag is split into three components, namely the induced, profile, and parasitic drag. Induced drag arises from the effects of nonuniform inflow, tip losses, wake swirl, suboptimal wake contraction, and the finite number of blades. Profile drag includes the separation of the boundary layer from the surface of propellers, and the wake created by that separation. The parasitic drag includes the skin friction drag of the entire vehicle.

Profile drag is acting only on the propeller blades. Since these rotate this form of drag does not directly cause a backward directed force. However, it does increase the torque and power that the motor has to provide to rotate the propeller blades.

Table 9.2 presents how each of these drag forms is calculated for each phase separately. It has to be noted that this approach coincides with the power calculations in Section 7.2. In the equations, ρ is the density, c_{d_0} is the profile drag coefficient of the rotor, A is the total disk area given in Equation 7.1, C_T is the thrust coefficient given in Equation 7.4, μ is the advance ratio given in Equation 7.17, λ is the inflow rate given in Equation 7.20 and f is the equivalent horizontal flat plate drag area given by Equation 7.16. Other newly introduced variables are presented in the table, where f_{ver} has been computed with Equation 9.1, where A_{top} is the top view area and A_{front} is the front view area of the vehicle.

$$f_{ver} = f\frac{A_{top}}{A_{front}} \tag{9.1}$$

Table 9.1: Drag Calculation

Mission Phase	Induced Drag D_i	Profile Drag D_0	Parasitic Drag D_p	Variable Definition
Hover	$\frac{1.15C_T^2}{\sqrt{2}}\rho A V_{tip_h}^2$	$\frac{\sigma c_{d_0}}{8}\frac{1}{2}\rho S V_{tip_h}^2$	/	V_{tip_h}: Tip speed in hover (m/s)
Axial climb/ descent	$\frac{1.15C_T^2}{\sqrt{2}}\rho A V_{tip_a}^2$	$\frac{\sigma c_{d_0}}{8}\frac{1}{2}\rho S V_{tip_a}^2$	$f_{ver}\frac{1}{2}\rho V_{climb}^2$	V_{tip_a}: Tip speed in axial flight (m/s) f_{ver}: Equivalent vertical flat plate drag area
Cruise	$\frac{1.15C_T^2}{2\sqrt{\lambda^2+\mu^2}}\rho A V_{tip_c}^2$	$\frac{\sigma c_{d_0}}{8}\frac{1}{2}\rho S V_{tip_c}^2(1+2\mu+\frac{\mu^3}{2})$	$f\frac{1}{2}\rho V_{cruise}^2$	V_{tip_c}: Tip speed in cruise (m/s) f: Equivalent horizontal flat plate drag area

With these calculations, one can compute the drag estimations for each of the phases for the climb speed of $V_{climb} = 3.4$ m/s and cruise speed of $V_{cruise} = 33$ m/s.

Table 9.2: Drag Calculation Results

Mission Phase	Induced Drag D_i [N]	Profile Drag D_0 [N]	Parasitic Drag D_p [N]	Total drag [N]
Hover	405.8	33.6	/	439.4
Axial climb/ descent	382.6	37.8	23.9	444.3
Cruise	94.2	52.6	863.6	1010.4

In order to examine how the different types of drag vary with velocity, the drag curves have been computed for all the different possible speeds. In axial climb, the drag dependency has been examined with respect to the climb velocity, which is shown in Figure 9.4. In order to compute this an iterative solver has been implemented, which first computes the power required for each climb velocity and then computes the corresponding RPM setting and tip velocity. This updated tip velocity is then used in drag estimation based on formulas in Table 9.2.

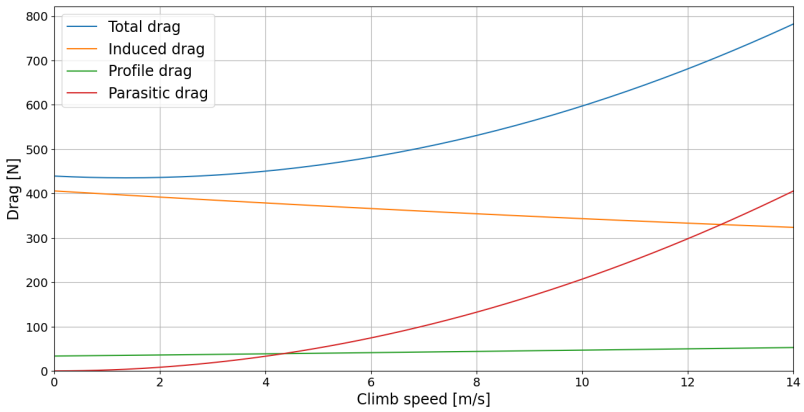

Figure 9.4: Drag in axial climb

The same approach has been used for the cruise phase, with the only difference being that the drag dependency has been examined with respect to the cruise velocity. This is shown in Figure 9.5.

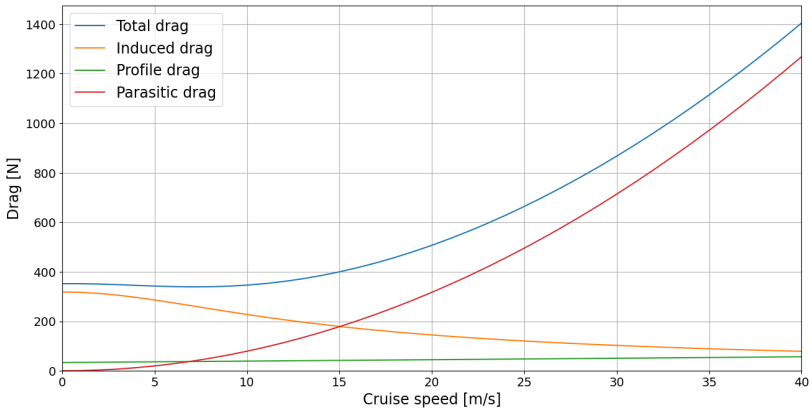

Figure 9.5: Drag in cruise

The shape of these curves shows the expected behavior, where the induced drag decreases with increased velocity, whereas the parasitic drag increases. The profile drag shows little dependency on the speeds, which is expected as it is proportional to the tip speed, which only slightly increases with increasing cruise speed. It has to be noted that the total drag at zero cruise velocity does not exactly coincide with the total drag at zero climb speed. This is attributed to the difference in drag formulation of each mission phase, where cruise formulas assume slightly better efficiency.

Lastly, based on the iterative solver it is useful to compute the variation of the hover drag based on the RPM setting. This is shown in Figure 9.6. While RPM is set for hovering with MTOW, in case of different payload, the RPM changes which in fact also affects the total drag in hover condition.

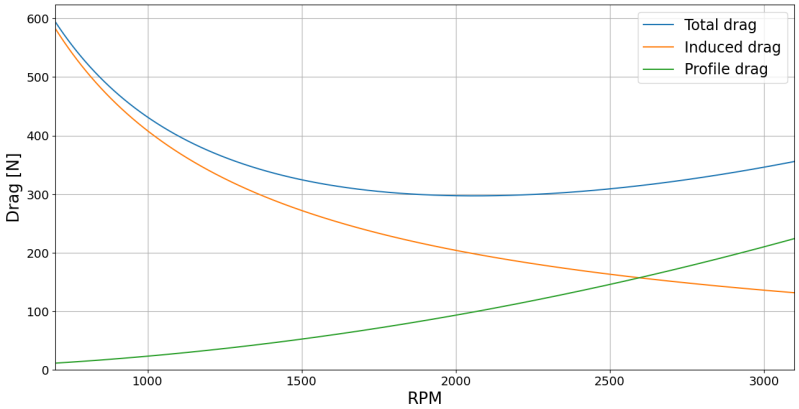

Figure 9.6: The variation of hover drag with RPM

9.1.3. Comparison with CFD simulations

The above results have been compared to the ones obtained from CFD simulations to assess the validity of the estimations. Since the rotation of the propellers is not considered in the CFD simulations, they are only used to compare the parasitic drag estimations. It has to be noted that the mesh could be refined in the CFD simulations, therefore it is expected that the CFD simulations overestimate the parasitic drag. Due to the time and computational constraints, the CFD has been run only for the optimal cruise velocity of 33 m/s. Table 9.3 shows the comparison of the parasitic drag estimation using these two methods.

Table 9.3: Comparison of parasitic drag estimation

Mission Phase	Analytical Approach D_p [N]	CFD Simulation D_p [N]
Axial Climb/Descent	23.9	26.6
Cruise	863.6	1357.2

It can be observed that the CFD simulations indeed overestimate the drag by about 30%. Nevertheless, based on the mesh refinement this is in line with the expectations. The magnitude of the values is therefore close enough to confirm the validity of the estimated analytical values.

9.2. Gust Loading

Flight conditions can vary greatly due to different phenomena, one of them being gusts. It is important to ensure that the vehicle can sustain higher loading due to gusts; to analyze the change in loading, a gust load diagram is constructed.
According to the certification specifications for small rotorcraft (CS-27) [42], the vehicle should be able to sustain vertical gusts (u) of 9.1 m/s.

To build the diagram, the change in the angle of attack ($\Delta\alpha$) due to the gust can be found, which allows also for the computation of the change in thrust (ΔT):

$$\Delta\alpha = \tan^{-1}\left(\frac{u}{V_\infty}\right) \tag{9.2}$$

$$\Delta T = \frac{T}{\cos(\alpha + \Delta\alpha)} - \frac{T}{\cos(\alpha)} \tag{9.3}$$

Finally, the gust loading can be found:

$$n = 1 + \Delta n = 1 + \frac{\Delta T}{W} \tag{9.4}$$

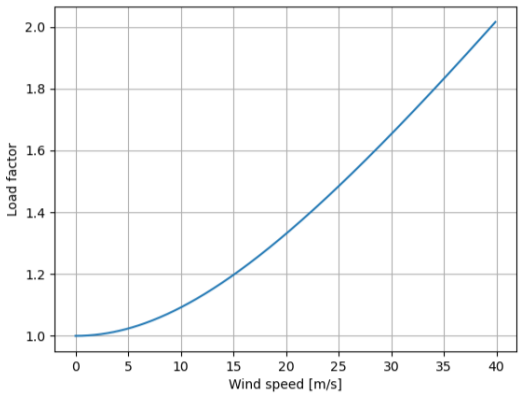

Figure 9.7: Gust load diagram

To construct the gust load diagram, changes in loading for different speeds are calculated, as shown in Figure 9.7. The diagram indicates that the load factor remains below 2 up to gusts of 40 m/s. The maximum gust the vehicle is expected to encounter is 9.1 m/s, corresponding to a load factor of 1.1. This load factor is significantly lower than the maximum load factor of 2 used in the power calculations; therefore, gusts are not critical for the design.

9.3. Aerodynamic Analysis of Wind Gust Effects

This section will present how the aerodynamic effects of wind gusts are computed. The result of this section, namely the required moment set (RMS), will serve as input to the design of the control subsystem for comparison with the Attainable Moment Set (AMS) in Section 11.1.

Similarly to the previous section, the gust effects were modeled using the Computational Fluid Dynamics (CFD) simulation. Based on the requirement *STK-CLNT-19* the vehicle needs to be able to sustain wind corresponding to 6 Beaufort scale or 13.8 m/s. Additionally, to model the gust, the CS27.341 Gust Loads regulation for small rotor-craft specifies that the vehicle should be able to sustain a gust of a maximum of 9.1 m/s. Therefore the maximum speed of the wind acting on our vehicle in hover condition is 22.3 m/s.

5 different cases were analyzed with this wind velocity, depending on the direction of the gust: 1. front, 2. back, 3, top, 4. bottom, 5. side. These are shown in Figure 9.8. For each of these cases, the CFD simulation is first run with zero angle of attack towards the wind. Using the aerodynamic force obtained, the new angle of attack is then computed. The second run of simulations is then done using this updated angle of attack. This ensures that the CFD simulations take into account the initial control response of the vehicle to the gust.

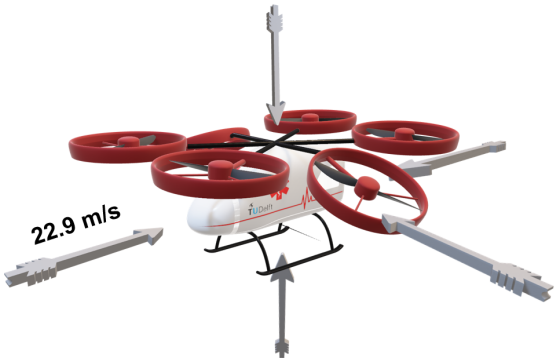

Figure 9.8: Critical cases of gust directions

For each of the 5 cases, CFD simulations gave the following relevant outputs: Lift, Drag, and location of center of pressure. The Centre of pressure specifies the point where the equivalent lift and drag forces act. By defining the aerodynamic force vector F_{aero} as the vector containing lift and drag components and the moment arm r_{arm} as the vector between the center of gravity and center of pressure, moments

around the c.g. caused by the gusts are computed using Equation 9.5.

$$\vec{M}_{\text{gust}} = \vec{r}_{\text{arm}} \times \vec{F}_{\text{aero}} \tag{9.5}$$

This can be done for each of the 5 cases, from which the maximum forces and moments due to gusts around each axis can be computed for each case. The resulting forces are shown in Table 9.4, whereas the resulting moments are shown in Table 9.5. In each of the tables, the maximum absolute values are colored yellow. The coordinate system used is displayed in Figure 9.9.

Figure 9.9: Coordinate system used for gust directions

Table 9.4: Aerodynamic Forces

Case	Force in X (N)	Force in Y (N)	Force in Z (N)
Front Gust	-653.3	0.0	-67.8
Tail Gust	643.6	0.0	-50.1
Top Gust	47.0	0.0	-1207.7
Bottom Gust	-54.8	0.0	1221.8
Side Gust	0.0	1990.9	-100.7

Table 9.5: Aerodynamic Moments

Case	Moment around X-axis (Nm)	Moment around Y-axis (Nm)	Moment around Z-axis (Nm)
Front Gust	0.0	-81.6	-0.0
Tail Gust	0.0	60.6	-0.0
Top Gust	-0.0	-41.9	0.0
Bottom Gust	0.0	-30.7	0.0
Side Gust	1081.0	41.3	816.3

These required force and moment sets (RMS) will be used in Section 11.3.

10 | Propulsion System Design

The propulsion subsystem design for the IUVO project focuses on establishing a rotor configuration that prioritizes high maneuverability within specified design constraints. Additionally, to meet rigorous performance requirements, custom rotor blades are meticulously designed to optimize efficiency and accommodate a diverse range of thrust levels. This chapter provides a comprehensive overview of the design process, starting with the detailed exploration of rotor configurations in Section 10.1, followed by an in-depth analysis of their generated forces and moments, Section 10.2, optimization of the rotor tilt angles in Section 10.3, and finishing with a discussion on rotor blade design in Section 10.4.

10.1. Rotor Position and Sizing

Based on the conclusions drawn from the trade-off analysis conducted for VTOL configurations presented in Chapter 5, the hexacopter configuration, as a fine balance between maneuverability, safety, and cost, is chosen for further study in the propulsion system design. The mounting of the propulsion system is only assessed for, low and high, fuselage-mounted design options, with the latter preferred considering the ease of payload boarding, to comply with *STK-PSGR-2*.

Three critical aspects influence the rotor placement and sizing decision: dimensional constraints, maneuverability, and safety. The dimensional constraints stem from the stakeholder requirements *STK-CLNT-3* and *STK-CLNT-15*. The requirement to maneuver within obstacles constrains the deployed

state of the vehicle and therefore dictates rotor placement. A deployed width of 5.5 meters is pursued to comply with the requirement to maneuver within an 8.5-meter obstacle with a 3-meter clearance. The design space influenced by the latter requirement, to comply with transportation constraints, is investigated in Subsection 10.1.3.

10.1.1. Rotor Sizing

The rotors are sized using actuator disk theory, which assumes incompressible flow and neglects swirl and viscous effects from the rotor blades. Despite these simplifications, this method allows for efficient evaluation of preliminary performance [43].

The disk loading of 25 kg/m^2 is assumed for multi-copter configuration based on the comparable reference aircraft [24, 25]. The assumption is made that each rotor has the same size and that the overall disk loading remains constant. The rotor diameter is subsequently computed using Equation 7.1 and 7.2.

Rotor Type

Using the calculated rotor diameter, several design options are established regarding rotor layout. It is noted that with the current disk loading and power requirement, fitting the rotors within the contained space for the deployed state is challenging. Thus, to reduce the rotor size required, the option of using ducted rotors is explored. Ducted rotors offer several benefits over open rotors, including increased efficiency, reduced noise, improved safety, better performance in confined spaces, higher static thrust, and improved low-speed performance [44]. The efficiency gain of the ducted rotor can be quantified by an increased thrust of 18.46% as presented in [45]. This can be carried forward to calculate the hovering power required, as given in the equations below [46].

$$P_{duct} = \frac{T_h^{3/2}}{2\sqrt{\rho \cdot n_r \cdot A_{rotor}}} \cdot \frac{1}{\eta_{hover}}, \qquad (10.1)$$

$$P_{open} = \frac{T_h^{3/2}}{\sqrt{2 \cdot \rho \cdot n_r \cdot A_{rotor}}} \cdot \frac{1}{\eta_{hover}}, \qquad (10.2)$$

where A_{rotor} is the area of a single rotor, T_h is the hovering thrust required which is assumed to be equal to MTOW, and n_r is the number of rotors, ρ is the air density assuming sea level ISA conditions, η_{hover} is the hovering efficiency, assumed to be 0.8 for both open and ducted rotors. Note that the power calculated here is the average power required in hover, and the peak power required is considerably higher. However, for the sake of the rotor layout discussion, only the average power is considered.

The average power required for ducted rotors resulting from these calculations is 17% less, compared to the hover power required when open rotors are used. The rotors are sized assuming the same amount of power is available to both open and ducted rotors resulting in a serious reduction of diameter. This makes compliance with *STK-CLNT-3* more achievable for the ducted option.

To evaluate the total power saving that comes from the usage of ducted rotors, the drag penalty of the duct during the cruise is estimated. Studies show that the duct length of 10% of the rotor's diameter already significantly increases the thrust output [47]. Thus, the duct frontal surface area is estimated using Equation 10.3, with t_{rotor} assumed to be $0.1 \cdot D_{rotor}$.

The drag of the duct is estimated as a drag of a half cylinder with reference area A_{duct} at sea level conditions and cruise speed, given by Equation 10.4, where C_d is the drag coefficient of a half cylinder, equal to 0.42 [48].

$$A_{duct} = t_{rotor} \cdot D_{rotor} \qquad (10.3)$$

$$D = \frac{1}{2}\rho V^2 A_{duct} C_d \qquad (10.4)$$

The extra power required due to this drag is calculated by multiplying drag with cruise velocity. The usage of ducts requires an additional 4.13 kW of power, which is considerably lower than the 25 kW ducted rotor saves during hover. Thus, ducted propulsion is chosen for implementation in the design.

10.1.2. Rotor Layout

Based on the ducted rotor diameter derived from the multidisciplinary design optimization framework discussed in Chapter 6, two different rotor layouts are investigated. These include an edge-first layout with propellers attached on the side of the vehicle and a vertex-first layout with the propellers equally spaced around the fuselage, illustrated in Figure 10.1 and 10.2 respectively.

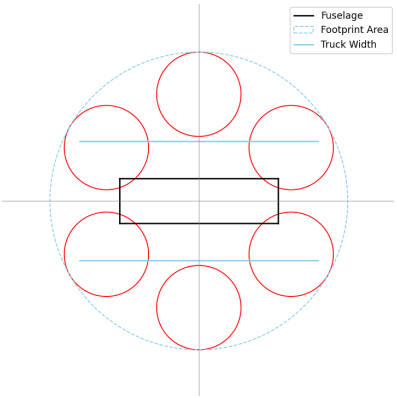

Figure 10.1: Edge First Layout of Rotors of a Hexacopter

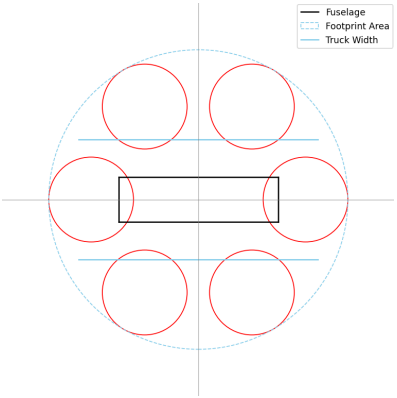

Figure 10.2: Vertex First Layout of Rotors of a Hexacopter

High-fuselage-mounted vertex first layout is found to have a slightly lower Attainable Moment Set margin for the most critical motor failure compared to the edge first configuration. The configurations are compared in cruise (in hover they are equivalent) by changing the direction of the aerodynamic moment, which is determined by the velocity vector. Hence, the team decided to pursue an edge-first configuration.

Numerous iterations are undertaken before arriving at the final rotor layout. The duct edges are initially positioned in a circular arrangement around the fuselage, with a diameter of 5.5 meters. This configuration enables large moment arms, thereby enhancing one-engine inoperative control, while also meeting the sizing constraints. Considerations of structural design and maneuverability within obstacles lead to an updated placement of the rotors, positioning them closer to the fuselage. This arrangement is optimal, as it provides significant benefits in terms of weight savings, structural performance, and increased clearance without compromising controllability. With the aforementioned maximum width requirement derived from *STK-CLNT-3* the rotors are placed around the fuselage as visualized in Figure 10.3. The final positions of the rotor hubs relative to the center of the fuselage, with positive x pointing to the nose, and positive y pointing to the left (such that positive z is pointing up), are summarized in Table 10.1.

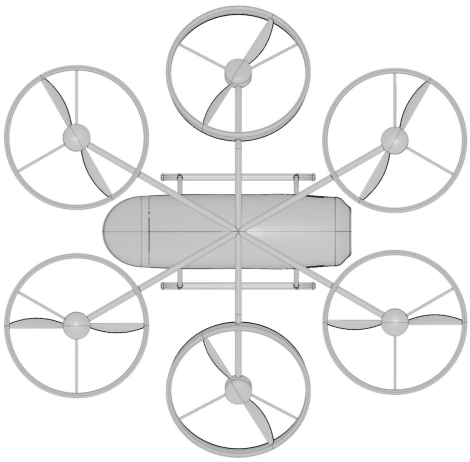

Figure 10.3: Final Rotor Layout

Table 10.1: Rotor Locations

Rotor ID	1	2	3	4	5	6
x position [m]	1.95	0.00	-1.95	-1.95	0.00	1.95
y position [m]	-1.13	-1.90	-1.13	1.13	1.90	1.13

10.1.3. Vehicle Transportation

Due to the number of rotors and their size, vehicle width exceeds the one available in the truck which is equal to 2.4 m. In order to visualize the issue, a top view of the vehicle, as well as an angled side view, are presented on Figure 10.5 and Figure 10.4 respectively. In both figures, the purple box indicates the dimensions of the transport vehicle. As transportability of the emergency flyer is a design driving

requirement (*STK-CLNT-15*), different scenarios are evaluated.

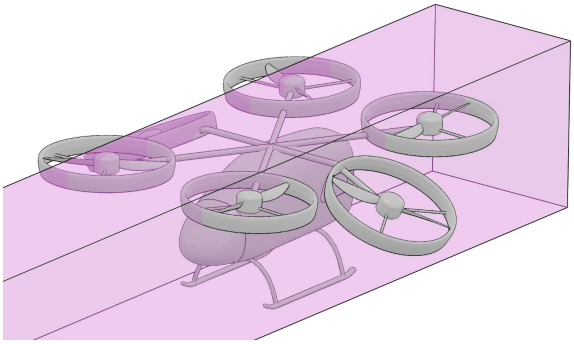

Figure 10.4: Angled Side View of the Vehicle Within the Truck (Purple Box)

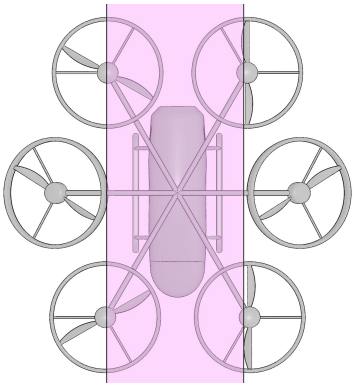

Figure 10.5: Top View of the Vehicle Within the Truck (Purple Box)

Firstly, some rotation mechanisms are considered for the booms to make the vehicle fit in the truck. One option is to rotate around an axis going through the attachment point so that they are stored on top of each other. Nevertheless, this solution comes with complex, heavy mechanisms that weaken the point with the highest stress concentrations in the structure. Moreover, due to the tilt introduced to the ducts, booms would have to be separated vertically by an even higher distance making the solution unfeasible. Another option is to introduce mechanisms allowing for retracting the booms vertically downwards. Despite the fact that this solution is feasible for two booms that are perpendicular to the center line of the fuselage, it is unfeasible for the other four as just folding them downwards would cause a collision with the fuselage before retracting them to a satisfactory extent. In order to counteract that issue, multiple rotation mechanisms would need to be introduced enabling rotor ducts to be placed along the fuselage. However, tilt angles further complicate the design of such mechanisms.

Bearing this consideration in mind together with risks associated with the possible failure of each mechanism making the vehicle inoperable, it is decided that the use of mechanisms should be avoided. This brings the solution of removing booms with ducts from the fuselage and storing them separately in the truck. However, such an approach hinders complying with deployability by 2 people within 30 minutes (*STK-CLNT-18*). In order to counteract that, a fast-release solution is going to be incorporated into the design. Further structural design of the deployment mechanism is beyond the time frame available to the team, and, consequently, is considered in the later design stages.

10.2. Forces and Moments

In order to sustain hover as well as perform a level cruise to a destination, the sum of forces and moments acting on the vehicle should be equal to zero. In the sections below, the ability of the chosen multirotor configuration to generate forces and moments needed to achieve the equilibrium is analyzed.

10.2.1. Control Allocation

With the rotor thrust established beforehand, and set rotor placement, the analysis of vehicle forces and moment can be made. Due to the rotor arm with respect to the CG, the rotors generate additional moments. Moreover, due to the rotor angular acceleration and drag acting on the propellers, a torque is generated that acts on the aircraft. As both rotor thrusts and torques are proportional to the square of angular velocity, a linear relation can be established between the rotor speed, and forces and moments generated by the aircraft in its body frame. The forces and moments acting on the aircraft are denoted by $\boldsymbol{\nu}$, and are given by:

$$\boldsymbol{\nu} = \begin{bmatrix} F_x & F_y & F_z & M_x & M_y & M_z \end{bmatrix}^T \tag{10.5}$$

The aircraft has 6 rotors, each of which can be controlled independently. The control inputs of the motor plant are the squared angular velocities of the rotors, which can be controlled directly using the Electronic Speed Controllers. The control inputs are constrained by the maximum angular velocity the

motors can provide.

$$\boldsymbol{u} = \begin{bmatrix} u_1 & \dots & u_6 \end{bmatrix}^T = \begin{bmatrix} \omega_1^2 & \dots & \omega_6^2 \end{bmatrix}^T \tag{10.6}$$

The control inputs are mapped to the forces and moments acting on the aircraft in the aircraft body frame, using a control allocation matrix $\boldsymbol{B}$. The control allocation matrix is a 6×6 matrix that maps the squared angular velocities of the rotors to the forces and moments acting on the aircraft and is derived using the rotor placement, tilt, and rotor characteristics. It is constructed from thrust and moment parts as follows:

$$\boldsymbol{B} = \begin{bmatrix} \boldsymbol{T} \\ \boldsymbol{M} \end{bmatrix}, \tag{10.7}$$

and its construction begins with a thrust unit vector matrix $\hat{\boldsymbol{V}}_T$:

$$\begin{aligned} \hat{\boldsymbol{V}}_T &= \begin{bmatrix} \hat{\boldsymbol{v}}_{T,1} & \dots & \hat{\boldsymbol{v}}_{T,6} \end{bmatrix}, \text{ where} \\ \hat{\boldsymbol{v}}_{T,i} &= \begin{bmatrix} v_{x,i} & v_{y,i} & v_{z,i} \end{bmatrix}^T, \end{aligned} \tag{10.8}$$

with the subscript i indicating the rotor index. Then, the thrust element of the $\boldsymbol{B}$ matrix is calculated by:

$$\boldsymbol{T} = k_{\text{motor}} \cdot \hat{\boldsymbol{V}}_{\boldsymbol{T}}, \tag{10.9}$$

with $k_{\text{motor}} = \frac{T_{max}}{\omega_{max}^2}$. To obtain the $\boldsymbol{M}$ matrix element, a similar equation is used:

$$\boldsymbol{M} = k_{\text{motor}} \cdot \boldsymbol{R} + k_{\text{torque}} \cdot \boldsymbol{Q}, \tag{10.10}$$

where the k_{motor} remains the same, and $k_{\text{torque}} = \frac{\tau_{max}}{\omega_{max}^2}$. Then, the moment arm matrix $\boldsymbol{R} = \begin{bmatrix} \boldsymbol{r_1} & \dots & \boldsymbol{r_6} \end{bmatrix}$ is obtained, with each moment arm vector obtained by the cross product of the rotor position vector and the thrust unit vector:

$$\boldsymbol{r}_i = \begin{bmatrix} r_{x,i} & r_{y,i} & r_{z,i} \end{bmatrix}^T \times \hat{\boldsymbol{v}}_{T,i}. \tag{10.11}$$

Lastly, the rotor torque matrix $\boldsymbol{Q} = \begin{bmatrix} \xi_1 \hat{\boldsymbol{v}}_{T,1} & \dots & \xi_6 \hat{\boldsymbol{v}}_{T,6} \end{bmatrix}$ is obtained with thrust unit vectors, and rotation coefficient ξ_i:

$$\xi_i = \begin{cases} 1 & \text{if rotating clockwise} \\ -1 & \text{if rotating counterclockwise.} \end{cases} \tag{10.12}$$

The resulting control allocation matrix $\boldsymbol{B}$ can be used to obtain the forces and moments vector ν by multiplication with the rotor squared angular velocity vector $\boldsymbol{u}$ as follows:

$$\boldsymbol{\nu} = \boldsymbol{B}\boldsymbol{u}. \tag{10.13}$$

10.2.2. Attainable Force and Moment Set

To evaluate the controllability of the vehicle, the Attainable Moment Set (AMS) and Attainable Force Set (AFS) can be determined, based on the control allocation matrix $\boldsymbol{B}$ [49]. AMS and AFS are sets of all possible moments and forces that the vehicle can generate, respectively, in the body frame of reference. Both sets can be visualized on a graph as a convex hull, using the `convhulln` function in MATLAB. To obtain the points defining the AMS and AFS, the following set of input rotor speeds containing all possible 2^6 combinations of each rotor operating at either zero or maximum speed can be constructed, by using the Kronecker product:

$$\begin{aligned} \boldsymbol{U} &= \begin{bmatrix} \boldsymbol{u}_1 \dots \boldsymbol{u}_{64} \end{bmatrix} \\ &= \boldsymbol{b} \otimes \boldsymbol{b} \otimes \boldsymbol{b} \otimes \boldsymbol{b} \otimes \boldsymbol{b} \otimes \boldsymbol{b}, \text{ where} \\ \boldsymbol{b} &= \begin{bmatrix} 0 & \omega_{max}^2 \end{bmatrix}^T \end{aligned} \tag{10.14}$$

Then, by multiplying the input rotor speeds set $\boldsymbol{U}$ with the control allocation matrix $\boldsymbol{B}$, a set of 2^6 $\boldsymbol{\nu}$ vectors, in the form of a matrix $\boldsymbol{N}$, is obtained. The convex hull of this set is a set of all possible $\boldsymbol{\nu}$

vectors. By splitting the convex hull into forces and moments parts, the AMS and AFS are obtained.

To check whether a specific combination of forces and moments $\boldsymbol{nu}$ is attainable, it can be checked if it belongs to the convex set using the following procedure. Firstly, the faces of the hull are obtained, defined by a set of vertices $\begin{bmatrix}\boldsymbol{p}_1 & \boldsymbol{p}_2 & \boldsymbol{p}_3\end{bmatrix}$. Next, a vector perpendicular to a face can be determined by constructing two vectors in the plane of the face, namely:

$$\begin{aligned}\boldsymbol{p}_1 - \boldsymbol{p}_2 \\ \boldsymbol{p}_2 - \boldsymbol{p}_3\end{aligned} \tag{10.15}$$

Subsequently, a vector perpendicular (normal) $\boldsymbol{n}$ to the face can be constructed by computing the cross-product of the two in-plane vectors:

$$\boldsymbol{n} = (\boldsymbol{p}_1 - \boldsymbol{p}_2) \times (\boldsymbol{p}_2 - \boldsymbol{p_3}). \tag{10.16}$$

It is also normalized to perform margin calculation in the later stage of the analysis:

$$\hat{\boldsymbol{n}} = \frac{\boldsymbol{n}}{|\boldsymbol{n}|}. \tag{10.17}$$

Now, the vector from the centroid of the vertices ($\boldsymbol{p_{cen}}$) to any of the vertices defining a face can be constructed:

$$\boldsymbol{c} = \boldsymbol{p}_1 - \boldsymbol{p}_{cen}. \tag{10.18}$$

Then, if the normal vector can be oriented such that it points outwards the convex hull by checking if the currently calculated normal vector meets the following criterion:

$$\hat{\boldsymbol{n}} \cdot \boldsymbol{c} > 0. \tag{10.19}$$

If the criterion is met, the vectors do not point in opposite directions, hence the normal vector is the correct one. If it is not met then:

$$\hat{\boldsymbol{n}} \leftarrow (-\hat{\boldsymbol{n}})$$

Having constructed the normal vectors to the faces of the convex hull pointing outwards, it can be seen that if the point is inside the hull, it needs to be closer to the centroid of the hull than the plane defined by the face, for each of the faces. This condition is both necessary and sufficient. To perform this procedure, firstly a vector is constructed pointing from the given design point (p_x) (point corresponding to the moments acting on the vehicle) to any of the points defining the face:

$$\boldsymbol{e} = \boldsymbol{p}_1 - \boldsymbol{p}_x \tag{10.20}$$

Then, the distance of the point to the plane of the face can be computed as an orthogonal projection of the $\boldsymbol{e}$ vector onto the unit vector normal to the surface. If this distance is positive, then the point lies on the same side of the plane as the origin:

$$\boldsymbol{e} \cdot \boldsymbol{n} > 0 \tag{10.21}$$

If this condition is not met, then the point is outside the attainable set, hence corresponding moments or forces cannot be achieved by the vehicle. If this condition is met for each face (plane), then the point is inside the hull.
In particular, in the case of hover stability, the following total moments and forces have to be attainable (body-fixed reference frame for pitch angle $\theta = 0$):

$$\boldsymbol{\nu} = \begin{bmatrix}0 & 0 & MTOM \cdot g & 0 & 0 & 0\end{bmatrix}^T, \tag{10.22}$$

As they represent the forces and moments needed to counteract external forces and moments that act on the vehicle in undisturbed hover.

Hence, both defined force and moment states need to be inside the convex hull defining the attainable forces and moments.

10.3. Rotor Tilt

The simplest design of multicopter rotor positioning is to align them such that the entire thrust is pointing upwards (in the positive z direction). However, analysis of the AMS upon rotor failure shows that the vehicle loses controllability due to the inability to maintain the ν vector shown in Equation 10.22. Thus, tilt to the rotors is introduced and optimized, as it is proven to be able to solve this issue [50].

Two possible rotations are used to describe the rotor orientation: rotation around the arm (ϕ_i) and inwards/outwards rotation (θ_i). The assumption of symmetry around the center point is used to constrain the set of possible unit vector combinations. Then it can be seen, that for the current engine layout, motors 2 and 5 can only be rotated inwards or outwards, to generate zero net moments and force in the x-y plane. For motors 1, 3, 4, and 6, it is possible to introduce the ϕ_i tilt angle such that the four motors do not produce side forces and moments.

As external forces can be counteracted by either tilting the drone (external forces in the X and Y directions) or increasing the RPM of the motors (external force in the Z direction), the focus of the tilt angles optimization is to maximize the ability to counteract the external moments.

Then the following tasks are performed to conduct the optimization.

To retain symmetry, rotation by angle ϕ_i is not applied to motors 2 and 5. Moreover, it is found during optimization that applying the inwards/outwards rotation θ_i to motors 1, 3, 4, and 6 does not give additional benefit compared to only applying this rotation to motors 2 and 5. Therefore, the final optimization setup consists of θ_i rotation of motors 2 and 5 and ϕ rotation of motors 1, 3, 4, and 6.

As the next step, a 161×161 grid of θ_i and ϕ_i values ranging from $-80°$ to $80°$ is created to represent the possible pairs of tilt angles.

Then, the distance from the trim point to the nearest face of the convex hull is proposed as a potential measure to quantify how efficient a particular tilt angle combination is at retaining stability in the case of engine failure.

For each possible pair $\begin{bmatrix}\theta_i & \phi_i\end{bmatrix}$ the smallest Euclidean distance is computed for each six possible engine failures. Then the lowest distance is chosen out of all six values, from now on this distance will be referred to as the AMS margin. It represents the ability of the given configuration to maintain stability in case of engine failure.

Finally, an additional constraint is added, namely, for a given configuration the force equilibrium in hover has to be attainable, hence point $\begin{bmatrix}0 & 0 & MTOM \cdot g\end{bmatrix}^T$ has to be inside the Attainable Force Set convex hull. This constraint mainly limits the values of the tilt angles from above, as in case of engine failure too high tilt angles might result in the lack of available thrust in the Z direction to counteract the gravitational force. The results of the optimization can be seen below in Figure 10.7:

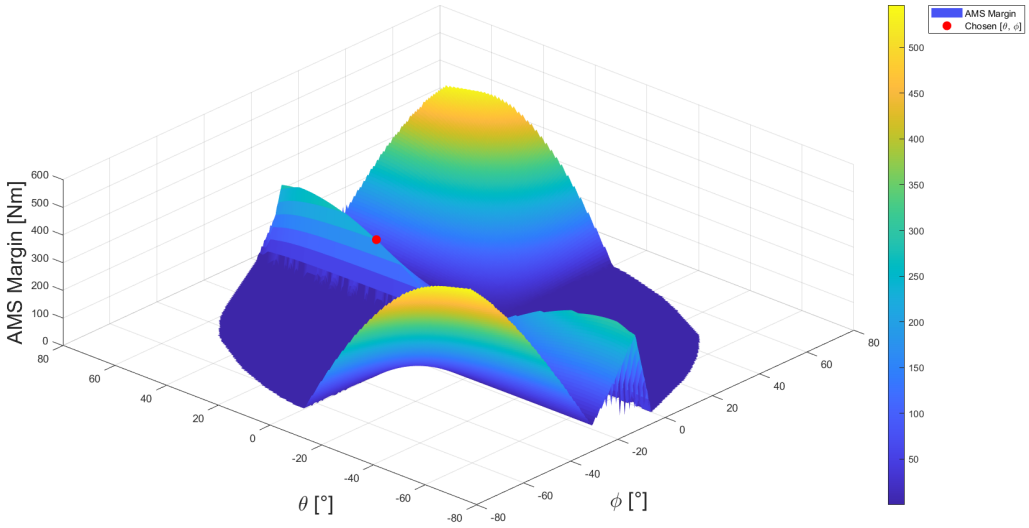

Figure 10.6: Surface Plot of the Minimum Distance to the Attainable Moment Set Boundary as a Function of Tilt Angles, With the Chosen Design Point (red) (grid spacing of $0.5°$).

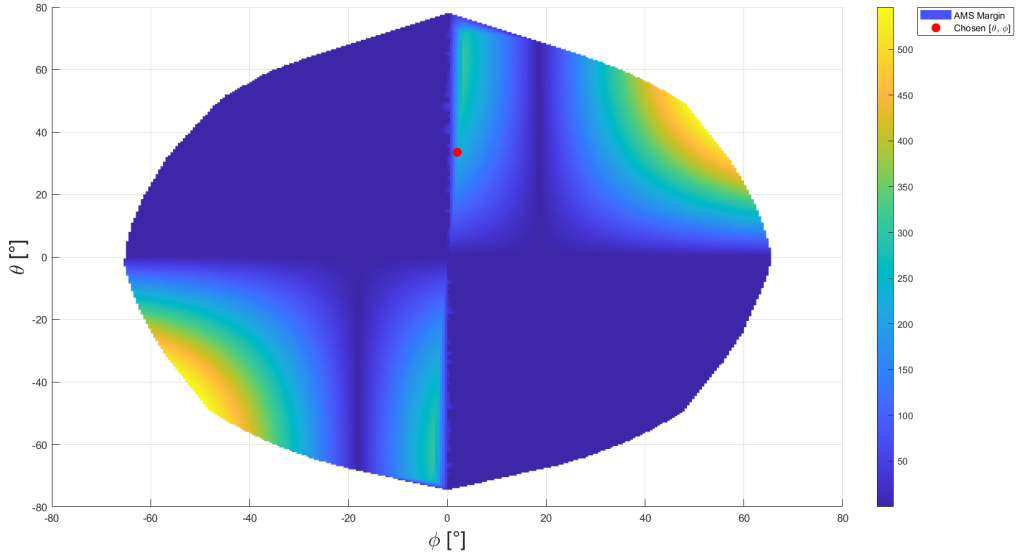

Figure 10.7: Top View of the Surface Plot of the Minimum Distance to the Attainable Moment Set Boundary as a Function of Tilt Angles, With the Chosen Design Point (red) (grid spacing of $0.5°$).

To choose the optimal tilt angles, the trade-off between the AMS margin computed before and thrust loss in the Z direction due to tilting is performed:

$$T_z = T_{engine} \cdot (4 \cdot \cos\phi_i + 2 \cdot \cos\theta_i) \tag{10.23}$$

Hence the factor F by which the thrust is increased compared to the case of no tilting is:

$$F = \frac{6}{(4 \cdot \cos\phi_i + 2 \cdot \cos\theta_i)} \tag{10.24}$$

It can be seen, that for a given tilt angle setup, tilting the rotor around the axis of the arm (ϕ) has a higher influence on the loss of vertical thrust than tilting outwards by the angle (θ). Looking at the Figure 10.6, a ridge along $\phi = \pm 2°$ represents a relatively high AMS margin, moreover, picking a point from that ridge results in smaller vertical thrust losses than high θ, high ϕ configuration.

Then, after selecting the $\phi = \pm 2°$ ridge as the set of possible pairs taken into account for analysis. Then, analyzing the ridge, it can be seen that for $[\theta, \phi] = [33.5°, 2°]$ the AMS margin starts to decrease with increasing θ:

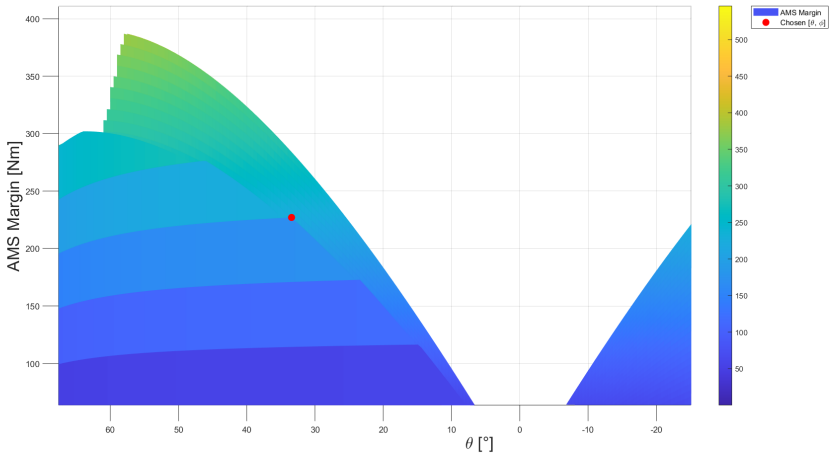

Figure 10.8: High-AMS Margin Ridge in the Moment Space Mapped to $\phi_i = 2°$ plane with the Marked Design Point (red) (grid spacing of $0.5°$).

Therefore, this point is chosen as the optimal tilt angle configuration, taking into account controllability in case of one-engine out and vertical thrust losses due to tilting. This choice is based on the aim to choose a low ϕ solution that guarantees lower thrust loss, as well as on the point that represents the decrease of the AMS Margin derivative on the ridge, as shown in Figure 10.8 It can be seen For the final configuration $\begin{bmatrix}\theta_i & \phi_i\end{bmatrix} = \begin{bmatrix}34° & 2°\end{bmatrix}$ the thrust increases by a factor of 6.1% according to Equation 10.24.

With the finalized rotor positions and tilts, the external propulsion system layout is visualized below in Figure 10.9:

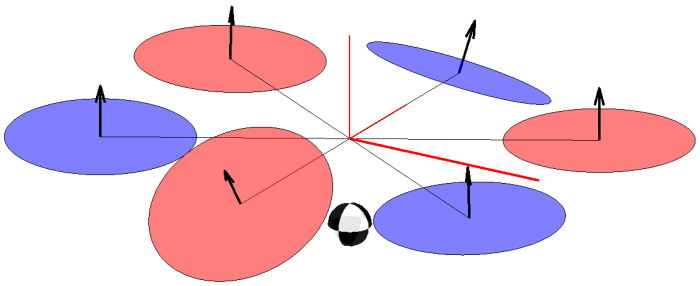

Figure 10.9: Final external layout of the propulsion system with indicated thrust unit vectors.

In the figure, the rotors are visualized as red or blue discs, with red indicating clockwise rotation, and blue indicating counterclockwise rotation. The thrust unit vectors are visualized as well, and the coordinate system is shown by the red lines. The nominal CG location, established using the CAD model is represented as a 3-D symbol as well.

10.4. Rotor Blade Design

The design of the rotor blades is determined based on the Blade Element Momentum Theory (BEM). This theory is a combination of the Blade Element Theory and the Momentum Theory. It divides each blade into several radial stations which are then analyzed as a 2D airfoil and the aerodynamic forces are calculated. These forces are then integrated along the entire length of the blade and over one complete rotation of the rotor and added together to determine the forces and moments of the full rotor.

10.4.1. Procedure

The procedure used is the one described in *Design of Optimum Propellers* by Adkins and Liebeck [51]. Their method modifies Larrabee's approach [52] by removing the small angle approximation and

adjusting some other assumptions which only apply to light loading.

Figure 10.10 shows the velocities acting on the airfoil and their angles at radial station r. w is the local effective velocity and it is composed of a velocity perpendicular to the disc plane and one parallel to the disc plane. The perpendicular component is $V(1+a)$, where V is the freestream velocity and a is the axial interference factor. The parallel component is $\Omega r(1-a')$, where Ω is the angular velocity, r is the local radius of the station and a' is the rotational interference factor. β, the blade twist, is defined as the angle between the disc plane and the chord, ϕ is the angle between w and the disc plane, α is the local angle of attack and is defined as the angle between the chord and the local effective velocity.

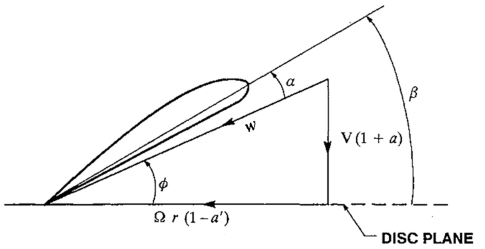

Figure 10.10: Flow Geometry for Radial Station r [51]

First, an initial estimate for the displacement velocity vector, ζ, is determined to be 0.1. Next, the momentum loss factor is calculated using Equation 10.25 where n_b is the number of blades, ξ is the non-dimensional radius, and ϕ_t is the flow angle at the tip which is calculated using Equation 10.26 with λ the tip speed ratio.

$$F = \frac{2}{\pi}\arccos\left(e^{-\frac{n_b}{2}\frac{(1-\xi)}{\sin(\phi_t)}}\right) \qquad (10.25) \qquad \tan(\phi_t) = \lambda\left(1+\frac{\zeta}{2}\right) \qquad (10.26)$$

The Betz condition for minimum energy loss is $r\tan(\phi) = \text{constant}$. Since the flow angle at the tip is known, the flow angle throughout the blade is determined using Equation 10.27.

$$\tan(\phi) = \frac{\tan(\phi_t)}{\xi} \qquad (10.27)$$

The next step is to determine the blade geometry. For this, the product of the local flow speed times the local chord, wc, is determined using the equation below where $G = F\sin(\phi)\cos(\phi)$, V the freestream velocity, R the rotor radius and C_l the local lift coefficient.

$$wc_b = \frac{4\pi\lambda G V R\zeta}{C_l n_b} \qquad (10.28)$$

To determine C_l, first, an airfoil is chosen. For this project, the NACA 4412 airfoil is selected. In order to minimize drag losses, the drag-to-lift ratio, ε, needs to be minimized. Hence, using different C_l values, the Reynolds number is determined using $Re = \frac{wc_b}{\nu}$ where ν is the kinematic viscosity. Then, the corresponding drag coefficient, C_d, and angle of attack, α are determined. The C_l with the lowest ε is selected. This procedure is repeated for each station.

From Figure 10.10, it can be seen that $w = \frac{V(1+a)}{\sin(\phi)}$, with the interference factor defined as $a = \frac{\zeta}{2}\cos^2(\phi)(1-\varepsilon\tan(\phi))$. The local chord, c_b, can then be computed using Equation 10.29. Furthermore, the blade twist is determined using Equation 10.30.

$$c_b = \frac{wc_b}{w} \qquad (10.29) \qquad \beta = \alpha + \phi \qquad (10.30)$$

Using Figure 10.11, the circulation equation for thrust is defined as in Equation 10.31. The nondimensional thrust coefficient, T_C, is defined in Equation 10.32 where T is the thrust and ρ is the density.

$$T' = L'\cos(\phi) - D'\sin(\phi) = L'\cos(\phi)(1-\varepsilon\tan(\phi)) \qquad (10.31) \qquad T_c = \frac{2T}{\rho V^2\pi R^2} \qquad (10.32)$$

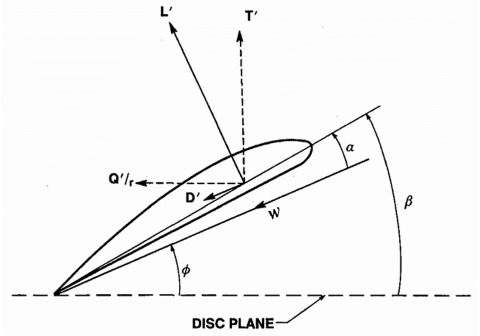

Figure 10.11: Force Diagram for a Blade Element [51]

Combining the above equations gives $T'_c = I'_1\zeta - I'_2\zeta^2$ where $I'_1 = 4\xi G(1 - \varepsilon\tan(\phi))$ and $I'_2 = \lambda\left(\frac{I'_1}{2\xi}\right)\left(1 + \frac{\varepsilon}{\tan(\phi)}\right)\sin(\phi)\cos(\phi)$. Finally, by rewriting this equation to Equation 10.33, the updated displacement velocity ratio can be computed.

$$\zeta = \frac{I_1}{2I_2} - \sqrt{\frac{I_1}{2I_2}^2 - \frac{T_c}{I_2}} \tag{10.33}$$

This procedure is iterated until the difference between the updated and the input ζ is smaller than 0.1%.

Next, J_1 and J_2 are determined using Equation 10.34 and 10.35 where $J'_1 = 4\xi G\left(1 + \frac{\varepsilon}{\tan(\phi)}\right)$ and $J'_2 = \left(\frac{J'_1}{2}\right)(1 - \varepsilon\tan(\phi))\cos^2(\phi)$.

$$J_1 = \int_{\varepsilon_0}^{1} J'_1 d\xi \tag{10.34}$$

$$J_2 = \int_{\varepsilon_0}^{1} J'_2 d\xi \tag{10.35}$$

Using these variables, the non-dimensional power coefficient is calculated using Equation 10.36.

$$P_c = J_1\zeta + J_2\zeta^2 \tag{10.36}$$

Finally, the rotor efficiency, T_c/P_c, is computed.

10.4.2. Tool

To apply this procedure, the tool *Python-BEM* designed by M. Smrekar is used[1]. As this tool does not calculate the rotor efficiency, it is slightly modified to implement this calculation. The inputs used in the tool are shown in Table 10.2.

Table 10.2: Input Values used for the Tool

Parameter	Value
Hub radius [m]	0.1737
Tip radius [m]	0.8684
Number of blades	2
Airfoil	NACA 4412
RPM	1200
Velocity [m/s]	33
Thrust per rotor [N]	611.765

The rotor diameter, RPM, velocity and total thrust are already computed in Section 7.5. To determine the hub radius, a hub-to-tip ratio of 0.2 is used. The tip radius is half of the diameter. The number of blades used is 2 as this is less complex, has a lower weight and a lower cost compared to 3 blades. The airfoil used for the blade is NACA 4412 as this airfoil is widely used in similar applications. Finally, the thrust per rotor is calculated by dividing the total thrust by the number of rotors. As the theory, and,

[1] URL `https://github.com/mihasm/Python-BEM/` [cited 10-06-2024]

therefore, the tool, is designed for rotors without a duct, a correction factor is needed to account for the duct. According to [45], using a duct results in an increase in thrust of 18.46%. Therefore, the total thrust is corrected using this factor. This results in a corrected thrust of 611.765 N per rotor.

Verification and Validation

To verify the tool, multiple tests are performed. Table 10.3 shows the functions verified and the tests used. As can be seen, all tests passed, hence, the tool is verified.

Table 10.3: Tests Performed for Verification of the Tool

Function	Test	Result
Airfoil geometry	Compare airfoil geometry coordinates with the ones on `http://airfoiltools.com/`	Pass
Lift and drag curves	Compare graphs with the ones on `http://airfoiltools.com/`	Pass
Reading input values	Compare printed input values with values inputted	Pass
Iteration formulas	Compare the values calculated in the first iteration with hand-calculated values	Pass
Convergence criteria	Check if iteration continues if criteria are not met and stops when criteria is met	Pass
Rotor efficiency	Compare with hand calculation	Pass

To validate the tool, the output is compared with reference data. The results are shown in Table 10.4. As can be seen, the difference between the data sets is minimal, hence, the tool is considered validated.

Table 10.4: Difference between Reference Data Set and Output Data Set

Output	Difference
Radius R	0.00%
Chord c_b	3.96%
Blade Twist β	4.20%
Flow Angle ϕ	3.63%

10.4.3. Result

The spanwise distribution of the chord and the twist is shown in Figure 10.12. The propeller efficiency of this blade is 0.8148. Figure 10.13 shows the computed rotor blade design.

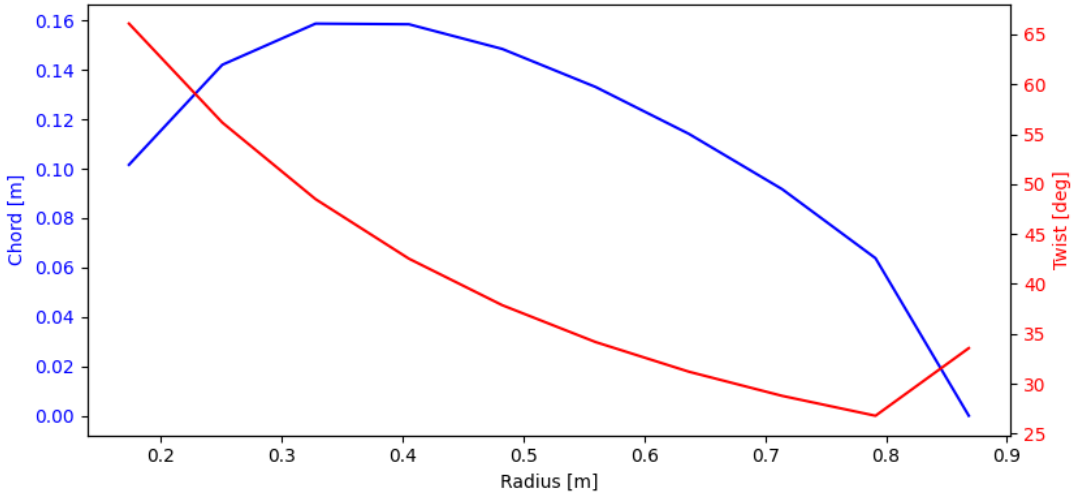

Figure 10.12: Spanwise Distribution of Chord and Twist

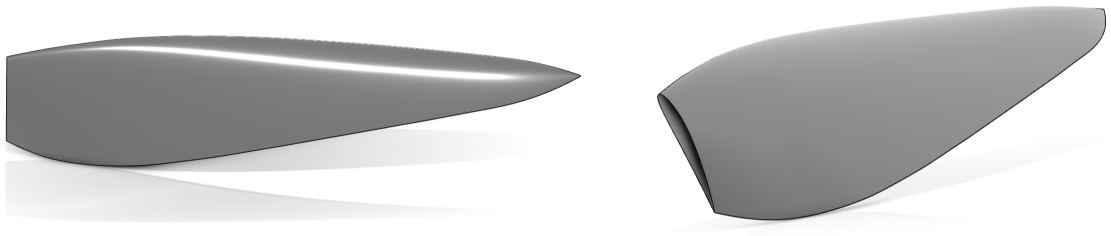

Figure 10.13: Rotor Blade Design

11 | Stability and Control Characteristics

In Chapter 10, the external layout of the rotors is established, together with its associated effect on aircraft forces and moments. Furthermore, the control allocation matrix $\boldsymbol{B}$, and the Attainable Force/-Moment Sets are derived there. This chapter describes the further analysis of said concepts and their effect on the stability and control characteristics. First, the AMS and AFS are compared to the Required Moment and Required Force set, showcasing the ability to generate necessary responses. Then, the analysis of rotor failure and its influence on the AMS/AFS is presented. Then, sensitivity analysis is conducted to conclude with the allowable CG excursion for full controllability and stability.

11.1. Analysis of the Attainable Moment Set

The derived Attainable Moment Set contains a lot of information about the controllability of a multicopter. Thus, this section explores this concept to present the control dynamics of the vehicle.

As described in Section 10.2, the AMS and AFS are convex hulls derived from all the possible combinations of rotor speeds. By splitting the resulting $\boldsymbol{N}$ matrix into force and moment components, the convex hulls are obtained. These hulls, being 3-dimensional, can be visualized with a surface plot, where L is the rolling moment around the x-axis, M is the pitching moment around the y-axis, and N is the yawing moment around the z-axis:

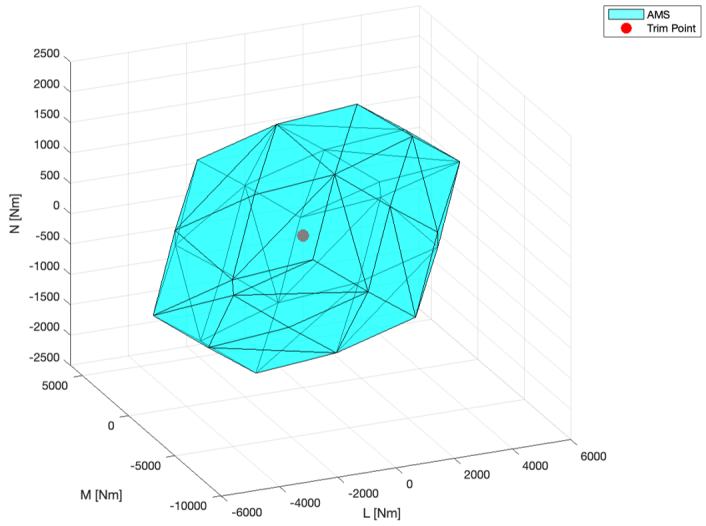

Figure 11.1: Attainable Moment Set visualized with a surface plot.

As seen in Figure 11.1, the AMS has an irregular shape, with scaling in all 3 directions in the same order of magnitude. The trim point (point for force and moment equilibrium), being $\begin{bmatrix}0 & 0 & 0\end{bmatrix}^T$, is also

in close proximity to the centroid of the AMS, thus giving freedom in generating the moments in all of the directions. A more detailed analysis can be made by examining the surface plots on their 2-D planes:

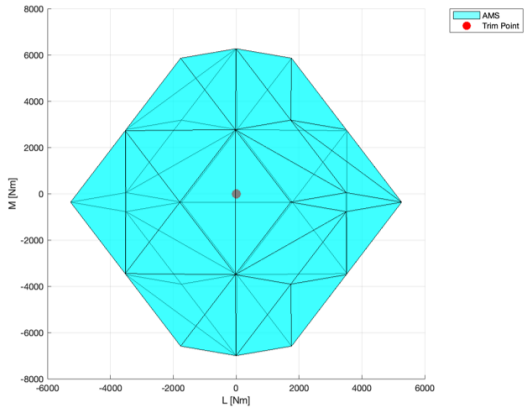

Figure 11.2: AMS visualized on the L-M plane.

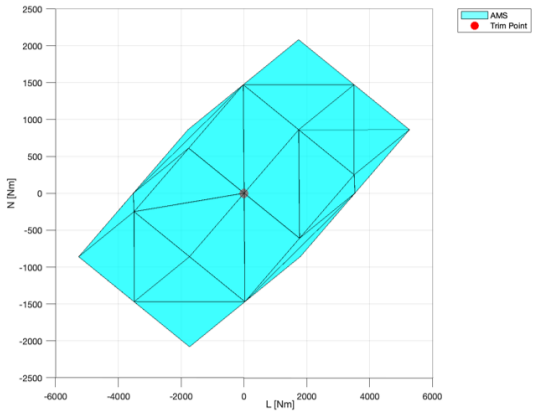

Figure 11.3: AMS visualized on the L-N plane.

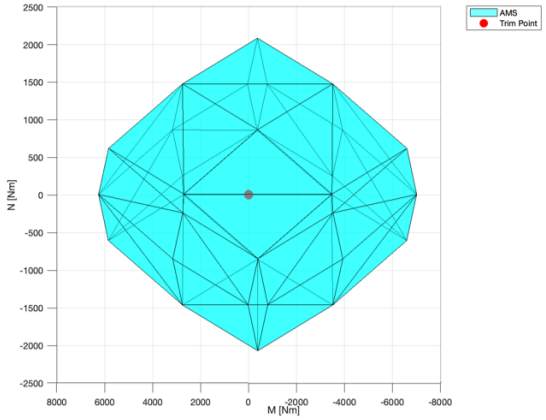

Figure 11.4: AMS visualized on the M-N plane.

Figure 11.2 shows that the AMS has symmetries in the L-M plane around both L and M axes, however not all of them are centered around the trim point. This means that for the aircraft to obtain the maximum possible rolling moment, the resulting pitch would be non-zero. This is the result of the introduced rotor tilt, as the torque generated due to rotor rotation influences the pitching moment as well. In contrast, the maximum possible pitching moment does not produce an additional rolling moment.

In Figure 11.3, it can be seen that the AMS projection on the L-N plane is not symmetrical about any of these axes. This is a result of the choice of classical hexacopter configuration, as described in [50], and a particular order of rotor rotation direction. This also means that neither maximum rolling or yawing moment can be generated without additional complementary moment in this plane.

Lastly, the AMS presented in the M-N plane in Figure 11.4 again shows symmetry in the presented axes. Similarly to the L-M plane, the maximum attainable yawing moment results in an additional pitching moment. This is not the case for the reverse situation.

11.2. One Motor Out Stability

To ensure the design is fault-tolerant, the AMS is also analyzed for each motor inoperative. This set is obtained in an identical way to the one described in Section 10.2, however, the row corresponding to the failed motor is set to 0 for all of the cases, effectively reducing the number of considered combinations to 2^5.

The following AMS curves with marked trim points are constructed for each possible engine failure:

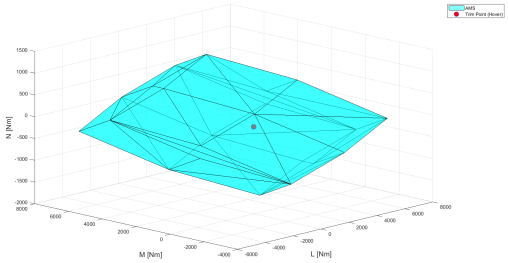

Figure 11.5: AMS for the First Engine Out.

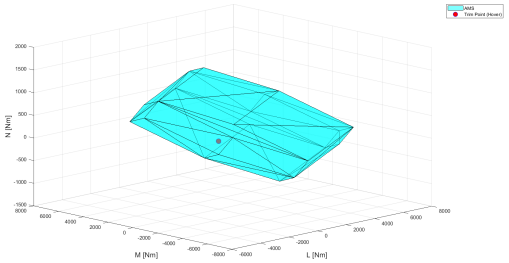

Figure 11.6: AMS for the Second Engine out.

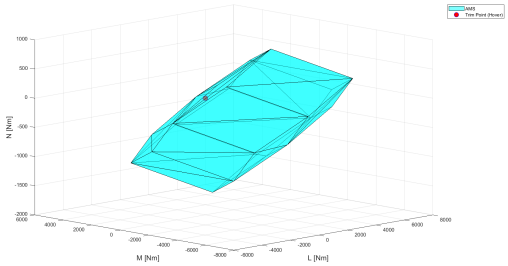

Figure 11.7: AMS for the Third Engine Out.

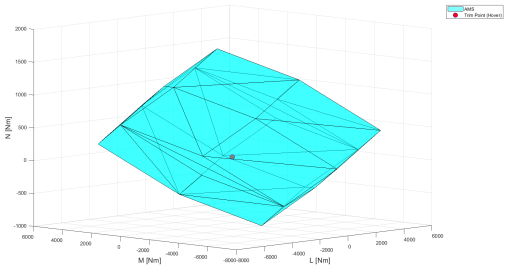

Figure 11.8: AMS for the Fourth Engine Out with a marked trim point.

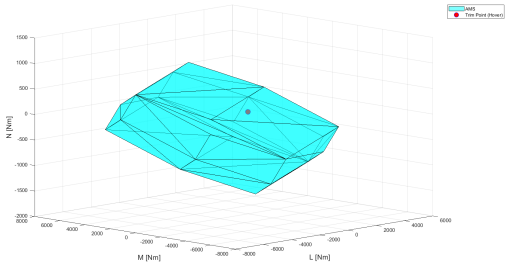

Figure 11.9: AMS for the Fifth Engine Out with the marked trim point.

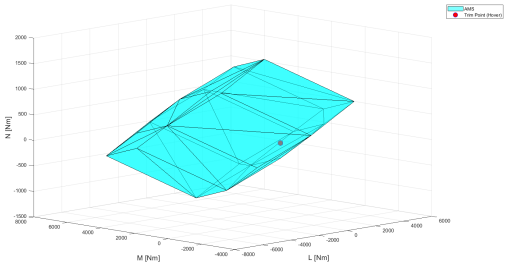

Figure 11.10: AMS for the Sixth Engine Out with the marked trim point.

11.3. Required Moment Set (RMS)

The required Moment Set (RMS) and Required Force Set (RFS) can be introduced to represent respectively the set of all possible moments and forces that can act on the vehicle due to aerodynamic loading during the flight regime. Those sets consist of three-dimensional points L, M, N in case of moments and F_x, F_y, F_z in case of forces. To counteract the aforementioned disturbances (possible moments in the L, M, N space and forces in the X, Y, Z space), it can clearly be seen that RMS needs to be fully enclosed by AMS, and RFS has to be fully enclosed by AFS:

$$\begin{aligned} RMS \subset AMS \\ RFS \subset AFS \end{aligned} \tag{11.1}$$

For convex sets (all mentioned sets are convex), to determine if the required moment and force sets are fully the available moment and force sets, it can be shown that all points (vertices) defining the required sets are inside the available sets. Required and available moment and force sets occupy a three-dimensional subspace of the moment set:

$$RMS, RFS, AMS, AFS \in \mathbb{R}^3 \tag{11.2}$$

Therefore, those sets can be visualized as volumes shown in Figure 11.11. However, the AFS and RFS comparison is not analyzed, as compared to moments, forces in the x-y plane are generated mainly by tilting the entire vehicle in the desired direction, which causes the change of the direction of the total thrust vector. To construct RMS, maximum possible moments due to aerodynamic loading in each direction are computed in Section 9.3. Then, they are represented as five vertices in the moment space (the maximum magnitudes in each axis are presented in Table 9.5, and the convex hull can be constructed (at least four non-coplanar points are needed for that):

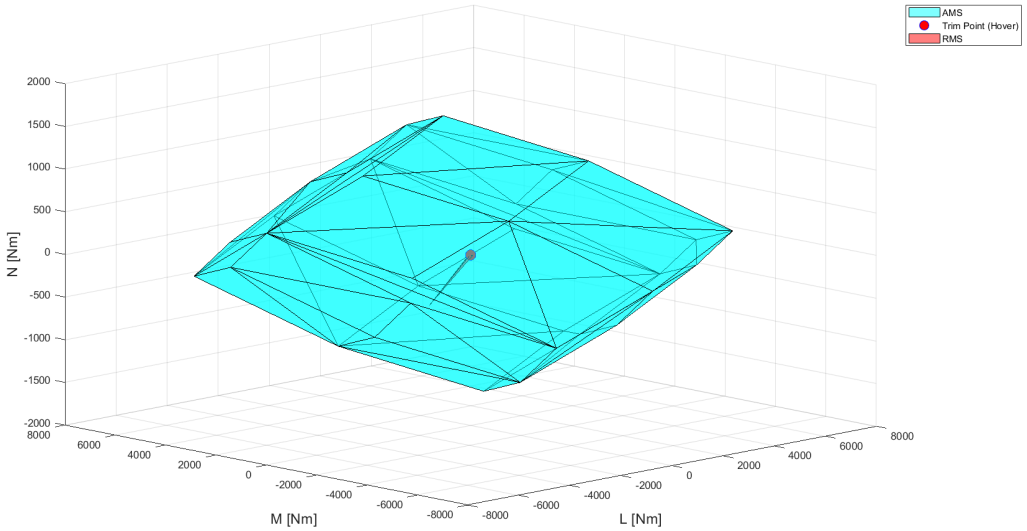

Figure 11.11: Attainable Moment Set, Required Moment Set, and Zero-Moment Point Plotted in the Moment Space for All Engines Operative

As can be seen on the Figure 11.11, RMS is fully enclosed by AMS, hence according to the criteria presented in Equation 11.1 the vehicle is able to counteract the disturbance moments.

11.4. Verification

Multiple checks are performed to test the correctness of the optimization algorithm.

Firstly, the discretization is modified from a coarser to a finer grid to check if the optimization is convergent, meaning if the result becomes more precise with finer discretization, but not significantly changing (the change should not be bigger than the grid spacing $\Delta\theta, \Delta\phi$ before changing the grid). The grid spacing is increased from ($0.5°$ to $1°$), and no divergence is observed (the optimization result changed from $[33.5, 2]$ to $[34, 2]$).

Secondly, additional check is performed, namely, the tilt angles (θ, ϕ) should meet both of those inequalities:

$$\begin{aligned} 4 \cdot \cos(\phi) + \cos(\theta) &> 3 \\ 3 \cdot \cos(\phi) + 2 \cdot \cos(\theta) &> 3 \end{aligned} \tag{11.3}$$

which represents the ability to generate vertical thrust in case of one engine failure (the first inequality corresponds to the failure of engine 2 or 5, and the second inequality corresponds to the failure of engines 1, 3, 4, and 6). As can be seen in the Figure 10.7, the angles are indeed constrained from above and the set should be similar to the theoretical possible set:

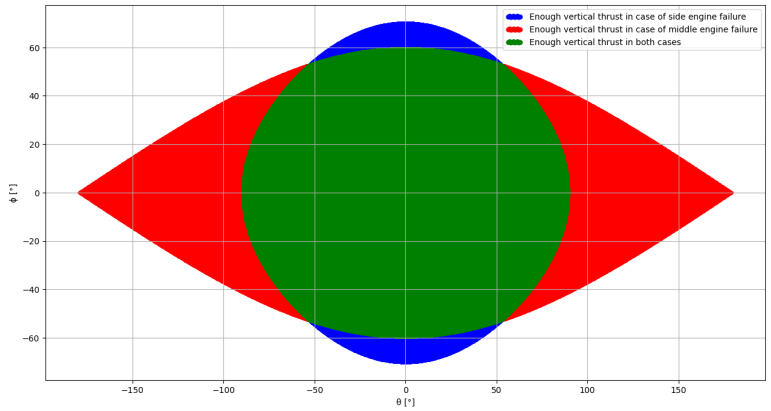

Figure 11.12: Set of all possible tilt angles for one engine inoperative condition that meets the condition Equation 11.3.

As can be seen, the available tilt angles set based on the vertical thrust in Figure 11.12 coincide with the available set in Figure 10.7. This provides additional physics-based confirmation of the optimization

method's correctness.

11.5. Sensitivity Analysis

Sensitivity is checked with respect to the variables that influence the process, namely k_{yaw}, k_{motor}, ω_{max} and rotor positions (while still retaining symmetry): arm length for rotors 2 and 5 ($l_{2,5}$), the magnitude of the x coordinate of the side rotors ($l_{x_{1,3,4,6}}$) and the magnitude of the Y coordinate of the side rotors ($l_{y_{1,3,4,6}}$). are varied by $\pm 10\%$ and the new optimal point is found (the initial value is $[\theta, \phi, \text{AMS margin}] = [34, 2, 227]$):

Table 11.1: Optimal Tilt Angles and the Corresponding AMS Margin After Changing the Selected Variables by $\pm 10\%$

	k_{yaw}	k_{motor}	ω_{max}	$l_{2,5}$	$l_{x_{1,3,4,6}}$	$l_{y_{1,3,4,6}}$
+10%	[27, 2, 225]	[44, 2, 249]	[34, 2, 274]	[36, 2, 229]	[42, 2, 244]	[33, 2, 230]
-10%	[45, 2, 227]	[27, 2, 202]	[34, 2, 184]	[32, 2, 223]	[27, 2, 209]	[35, 2, 223]

Firstly, it is noticed that the high AMS margin ridge does not shift from its initial location $\phi_i = 2°$ after changing the parameters. Furthermore, the maximum value on the $\phi_i = 2°$ does shift after changing the parameters, and the corresponding maximum AMS margin also changes, as can be seen in Table 11.1. Then, the result's sensitivity to k_{yaw} is analyzed in greater detail, as this variable is computed using simplified assumptions, and the real value may most significantly differ from the estimation. To check the sensitivity, both optimal θ and corresponding AMS margin are computed after altering k_{yaw} by $-40\%, -30\%, -20\%, -10\%, 0\%, 10\%, 20\%, 30\%, 40\%$ respectively:

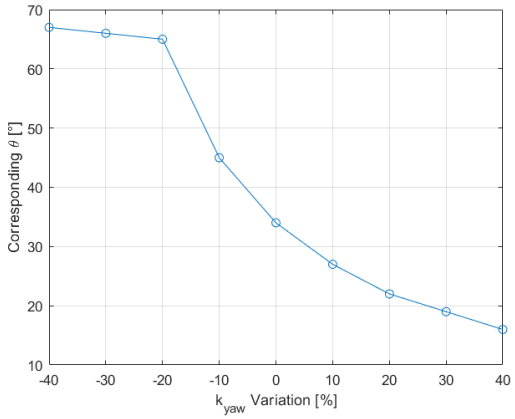

Figure 11.13: Optimal θ as a function of k_{yaw} percentage change from original value.

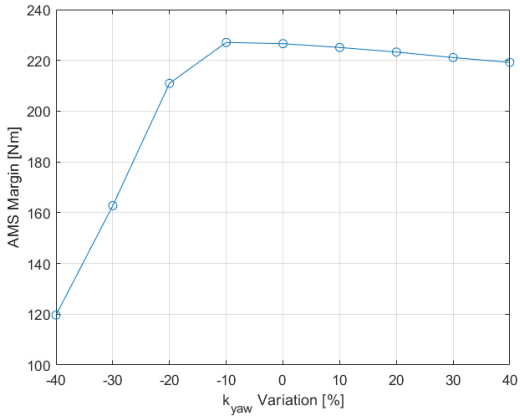

Figure 11.14: Optimal AMS margin as a function of k_{yaw} percentage change from original value.

As can be seen from the figures above, if the actual value of k_{yaw} is more than 10% lower than the assumed one, the AMS margin decreases significantly and the θ angle increases significantly (which translates directly into vertical thrust losses). However, even for -40% k_{yaw} change the AMS margin is still significantly higher than zero (120 $N \cdot m$), and the corresponding $\theta = 67°$ results in the loss of vertical thrust equal to around 20% (see Equation 10.22), which is considerably higher than the maximum possible loss of 33% (derived from the maximum thrust being two times higher than the required thrust and assuming one engine failure).

11.6. CG Excursion

As the IUVO is designed for saving the passengers, the payload mass, and thus the CG location can change between missions. That is why an investigation of the controllability characteristics is done for the changing CG location at MTOM.

A change of the location of the CG changes the moment arm vector $\boldsymbol{r}_i$ of each rotor, and thus the control allocation matrix $\boldsymbol{B}$. That means that the AMS changes as well with changing CG location. The analysis of the allowable CG excursion relies on ensuring that the trim point $\boldsymbol{\nu}$ is inside the AMS and AFS. A grid of realistic CG positions, which are inside the fuselage, is set. Then, each point on the grid is analyzed by calculating the AMS, and checking if the point is inside the convex hull, as described in Section 10.2. Moreover, if the CG is indeed valid, the same approach is set for checking if $\boldsymbol{\nu}$ is in the

AMS and AFS, even if any of the rotors fails. The result of the said analysis is shown in Figure 11.15.

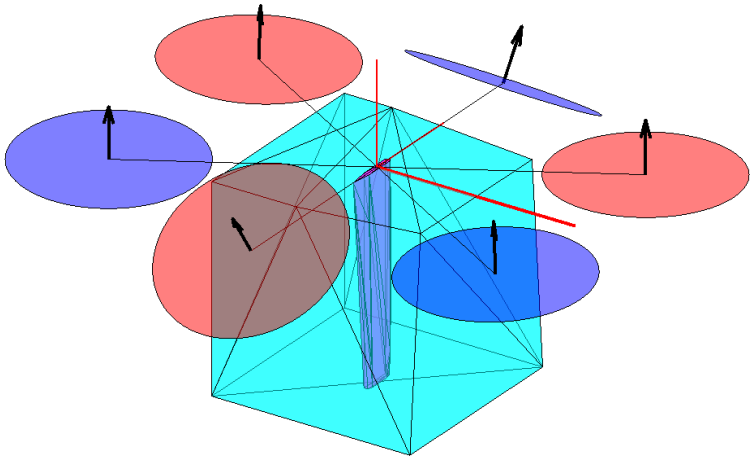

Figure 11.15: Allowable CG range for controllability.

In the figure, the light blue surface represents the CG range with all motors operative. As it can be seen, due to the broad range of the AMS, the allowable CG excursion covers the entire fuselage and thus does not pose a problem for controllability. On the other hand, fault-tolerant CG excursion (in case any of the rotors fails) is highly limited, as visualized by the dark blue surface. Namely, the maximum front/aft CG shift w.r.t. the rotor mounting point is ± 2.6 cm, and the allowable lateral CG shift is ± 16 cm, in the cross-section of the nominal z-location of the CG.

12 | Energy Storage System Design

In order to comply with *STK-CLNT-7: The vehicle shall have an electric propulsion system.*, an energy source not requiring combustion must be selected. During the configuration trade-off, described in Chapter 5, lithium-ion batteries are selected as the energy source for the vehicle owing to their low cost, reduced complexity and high availability in the market compared to other battery types or hydrogen fuel cells. The characteristics of lithium-ion batteries can be found in Table 12.1.

Table 12.1: Lithium-Ion Performance Characteristics

Battery type	Specific Energy [Wh/kg]	Volumetric Energy Density [Wh/l]	Specific Power [W/kg]	Cost [$/kg]	Cycle life [# of cycles]
Lithium-ion	300 [36]	500 [53]	1000 [54]	113[1]	1000[2]

This chapter elaborates on the design of the energy storage architecture and sizing methodology. Firstly, the selection of the energy storage option is explained followed by the description of the general layout. Then, the sizing procedure for the power supply is presented and the final layout is determined.

12.1. Electrical Block Diagram

The electrical subsystem concerns the power components present in the aircraft. The architecture contains energy sources, energy-consuming components, and interconnections between them. The system is divided into a high-voltage loop powering motors and a low-voltage loop supplying power to onboard electronics, as presented on Figure 12.1. Each system is equipped with an independent energy supply and is protected from overvoltages and overcurrents by battery management systems and fuses. Furthermore, the Battery Eliminator Circuit allows for reducing voltage provided from high-voltage battery to the one required by onboard electronics creating an alternative low-voltage power supply in case of low-voltage battery failure.

[1] URL https://about.bnef.com/blog/lithium-ion-battery-pack-prices-hit-record-low-of-139-kwh [cited 17 May 2024]

[2] URL https://www.doitpoms.ac.uk/tlplib/batteries/batteries_lithium.php [cited 17 May 2024]

The high-voltage battery directly powers the electronic speed controllers (ESCs), which monitor and regulate the current supplied to the electronic motors to control their rotational speed. The low-voltage battery directly supplies power to the flight computer and communication transceivers, while the sensors are powered through the flight computer.

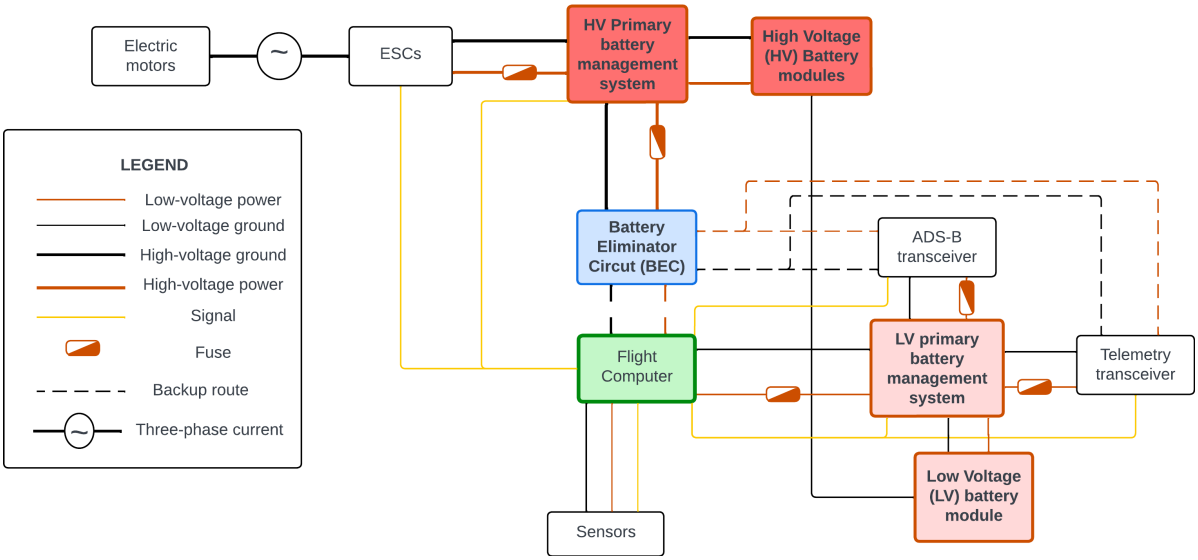

Figure 12.1: Electrical System Block Diagram

12.2. Battery Sizing

This section aims to describe the adopted battery sizing methodology concerning battery cell packaging. Firstly, the theory behind connecting cells in series and parallel is explained. Subsequently, high-voltage sizing and packaging are performed. With the design of the high-voltage system complete, the focus shifts to the low-voltage system, starting with power allocation to electronic components, followed by the battery sizing.

Cells in Series and Parallel

Lithium-ion batteries are composed of cells that can be characterized by the nominal voltage equal to $V_{cell} = 3.6V$ and the capacity of $C_{cell} = 3.2Ah$ [55]. In order to achieve higher voltage and capacity leading to higher energy stored, cells have to be connected both in series and in parallel. Connecting batteries in series, as presented on Figure 12.2, results in the equivalent voltage being the sum of individual cells, whereas equivalent capacity remains equal to the capacity of the individual cell. On the other hand, connecting batteries in parallel, as shown on Figure 12.3, keeps the equivalent voltage at the level of the individual cell while equivalent capacity becomes the sum of the capacities of individual cells.

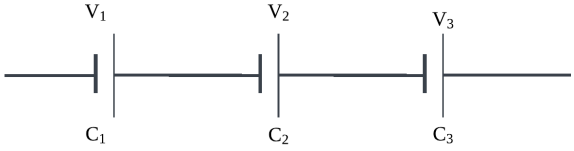

Figure 12.2: Batteries in Series

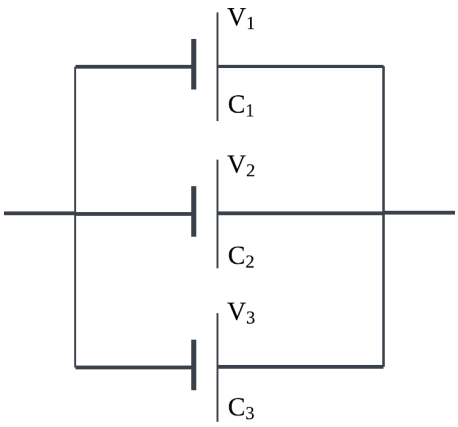

Figure 12.3: Batteries in Parallel

Having these things considered, it is possible to calculate the needed number of cells in series (N_s) and parallel (N_p) for the mission, according to the following equations:

$$N_s = \frac{V_{req}}{V_{cell}}, \qquad N_p = \frac{E_{req}}{V_{req} \cdot C_{cell}}, \tag{12.1}$$

where E_{req} stands for the required energy to be stored on board, and V_{req} is the required voltage.

High-voltage Battery Sizing and Packaging

Based on the calculations done in Chapter 7, the energy that has to be stored in the battery amounts to 29396.60 Wh and, consequently, the required battery mass (m_{batt}) is equal to 122.58 kg. Therefore, battery volume (V_{batt}) can be computed as follows:

$$V_{batt} = m_{batt} \cdot \frac{\varepsilon}{U_{sp}}, \tag{12.2}$$

where ε stands for specific energy and U_{sp} for volumetric energy density. Using this formula, the battery volume amounts to 58.793 liters.

Subsequently, the high-voltage battery packaging can be established using Equation 12.1, where the voltage required by the electric motors is set to be 350 V. These calculations lead to 98 cells in series and 28 cells in parallel, with the number of cells rounded up to the nearest integer. In total 2744 cells are packaged for the high-voltage battery.

In order to ensure fire safety and redundancy in the design, cells are grouped into packs of 11 in series and 7 in parallel, commonly referred to as 11s-7p battery pack. Cells are separated by heat sinks preventing overheating and easing thermal management within the battery pack. Moreover, each cell is equipped with its slave battery management system that is connected to the package master battery management system monitoring temperature, state of charge (SOC), and state of health (SOH). Additionally, these management systems guarantee cells are discharging equally.

Nine packages are arranged into a module ensuring the required voltage is provided. There are four modules, connected in parallel, boosting battery capacity to the required level. These modules ensure that in the extreme scenario of an emergency, even with one module inoperative and only 20% state of charge remaining in the other three modules, it is sufficient to safely land. The energy required for a single landing is 1035 kWh as discussed in Section 7.3. Additionally, accounting for ten minutes of hover time to search for an emergency landing space, which requires 6584 kWh, the total required energy for safely landing amounts to 7619 kWh. The combined reserve energy of the three modules

totals 17637 kWh, which is more than sufficient to perform this maneuver. Furthermore, all master battery management systems are connected to the primary battery management system which keeps the system working within its safe operation range.

Moreover, modules and packs are to be thermally insulated from each other to prevent fire from spreading from one pack to the other causing further failure. All the technical data about the system is summarized in Table 12.2, with the high-voltage battery system layout presented on Figure 12.4.

Table 12.2: High-voltage Battery System Characteristics

Parameter	Value
Required voltage [V]	350
Required energy [Wh]	29396.6
Cell voltage [V]	3.6
Cell capacity [Ah]	3.2
Cells in series	98
Number of packs in module	9
Cells in series in pack	11
Required capacity [Ah]	83.99
Cells in parallel	28
Number of modules	4
Cells in parallel in a pack	7

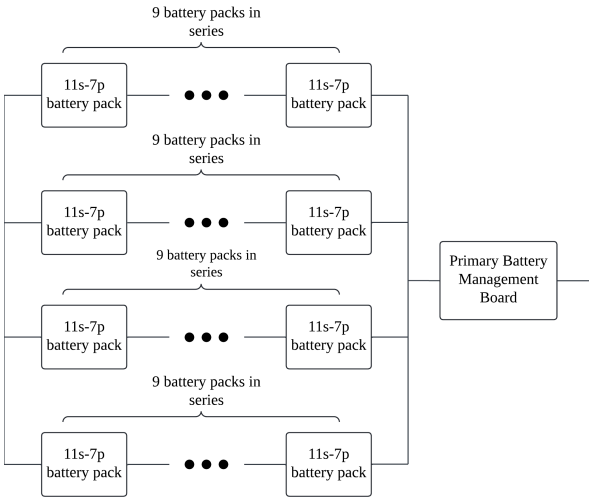

Figure 12.4: High-voltage Battery System Layout

Low-voltage Battery Sizing and Packaging

The low-voltage battery system is designed to power all electronic components except motors and electronic speed controllers, as explained in Figure 12.1. Due to the early stage of the design, the power required is roughly estimated for the flight computer and all other avionic instruments grouped [56]. Their power consumption is outlined in Table 12.3. To account for exceeding power consumption of considered components or other components, a contingency power consumption labeled as “Other” in Table 12.3 is introduced.

To determine the battery size and packaging, the required energy, that has to be stored in the battery, for low-voltage components (E_{LV}) is computed using the following equation:

$$E_{LV} = \frac{P_{LV} \cdot t}{DoD}, \tag{12.3}$$

where P_{LV} stands for power consumption of low-voltage components, t for the operational time of the system which is set to be one hour and 15 minutes, and DoD for Depth of Discharge being equal to 0.8 as previously discussed in Subsection 8.2.2. This calculation leads to the energy required amounting to 560.25 Wh.

The same procedure as for the high-voltage system is followed to determine the number of cells in series and parallel. As the voltage required by flight instruments is equal to 28 V [56], 8 cells are needed to be placed in series to provide it. To supply enough energy, 7 cells must be connected in parallel. Due to the small number of cells in total, it is decided to put them all in one pack and introduce redundancy in the system through the use of Battery Circuit Eliminator as explained in Section 12.1.

Lastly, it is important to note that, similarly, each cell is governed by its slave battery management system that is connected to the master battery management battery system ensuring adequate operational conditions for the battery. Moreover, cells are separated by heat sinks to preserve adequate heat exchange.

All the technical data about the system is summarized in Table 12.4.

Table 12.3: Power Consumption per Component in Low-voltage System [56].

Component	Power consumption [W]
Avionics	253
Flight computer	177
Other	336

Table 12.4: Low-voltage Battery System Characteristics

Parameter	Value
Power required [W]	766
Energy required [Wh]	560.62
Required voltage [V]	28
Cell voltage [V]	3.6
Cell capacity [Ah]	3.2
Cells in series	8
Number of packs in module	1
Cells in series in pack	8
Required capacity [Ah]	20.02
Cells in parallel	7
Number of modules	1
Number of cells in parallel in a pack	7

12.3. Charging Time

The charging time of a battery influences the turn-around time and utility of a vehicle. Therefore, from an operational standpoint, charging time should be minimized to maximize the use of the vehicle. Alas, charging fast has an adverse effect on the cycle life of the battery as well as on its state of health [57].

The charging time can be computed using the following equation[3]:

$$Charging\ time\ [\text{hr}] = \frac{Battery\ capacity\ [\text{Ah}]}{Charging\ current\ [\text{A}]} = \frac{Battery\ energy\ [\text{Wh}]}{Charging\ power\ [\text{W}]}. \tag{12.4}$$

Given the following relation, it can be concluded that the charging time of the specific battery uniquely depends on the charging current. The higher the current, the lower the charging time is. To ensure optimal charging of the battery, charging current of the magnitude being not less than 10% of the battery capacity shall be used along with the Constant Current Constant Volume (CCCV) scheme [57]. It is advised to charge batteries with a C-rate of 1 meaning the battery is charged within 1 hour to its full capacity.[4]

Table 12.5 presents the charging time with the associated required current for the high-voltage system, whereas Table 12.6 for the low-voltage system. Given commercially available chargers for electric cars, the vehicle can be charged within 20 minutes if needed, ensuring adequate cooling.[5] Nevertheless, if there is no time constraint, charging at the C-rate close to 1 should be done.

Table 12.5: Charging Time With Associated C-Rate and Required Current to Charge High-voltage Battery System

Charging C-rate	Equivalent Charging Time [min]	Required current [A]
1C	60	83.99
0.75C	90	55.99
0.5C	120	42.00
1.5C	40	125.99
2C	30	167.98
3C	20	251.97

Table 12.6: Charging Time With Associated C-Rate and Required Current to Charge Low-voltage Battery System

Charging C-rate	Equivalent Charging Time [min]	Required current [A]
1C	60	20.02
0.75C	9	13.35
0.5C	120	10.01
1.5C	40	30.03
2C	30	40.04
3C	20	60.07

[3]URL `https://ethcircuits.com/battery-charging-time-battery-charging-current/` [cited 23 June 2024]
[4]URL `https://batteryuniversity.com/article/bu-409-charging-lithium-ion` [cited 14 June 2024]
[5]URL `https://evbox.com/en/ev-chargers/fast-charger` [cited 14 June 2024]

13 | Thermal Management System

Thermal control is a crucial aspect of mission operations, particularly for the electronics and battery packs. The heat generated during battery discharge, charge, and self-discharge poses a serious threat to safe operation, as lithium-ion batteries can combust when overheating [58]. Additionally, proper cooling measures are essential for extending the battery's cycle and calendar life, as well as ensuring its efficient use [59]. To maintain the system components within their optimal temperature range, a thermal management system has been developed. This chapter aims to introduce the thermal management system and provide a detailed overview of its development process. In Section 13.1, the calculation of heat generation and temperature changes due to batteries is presented, along with the discussion of methods for dissipating this heat. Subsequently, the thermal management solution is presented.

13.1. Battery Heat Generation

The battery packs are the main source of heat within the VTOL, with research indicating a heat generation rate of 17 mW/cm3 for the LixC/LiNiO2 cell and 11.2 mW/cm3 for the LixC/75% LiCoO2, 25% LiNiO2 cell[59]. As mentioned earlier, this heat must be dissipated to prevent thermal runaway and the development of thermal gradients and hot spots. These conditions significantly accelerate the degradation of the electrolyte, anode, cathode, and separator of the battery and cause operational risks [58].

Heat production in batteries can occur through two primary mechanisms. Primarily, internal resistance, also known as Ohmic Loss, generates heat as a result of the electrical resistance within the battery during charge and discharge cycles. Moreover, chemical losses contribute to heat production due to irreversible chemical reactions that occur within the battery during operation. Quantifying chemical losses can be challenging, and typically, thermal management systems focus on mitigating Ohmic Loss through active and passive strategies such as managing terminal welding spots, metal foils, wires, and connectors, and creating cooling loops.

For safety in case of battery physical failure, along with combustion, the battery is divided into multiple packs. The exact layout is aforementioned in Chapter 12. Calculating the power that is dissipated due to Ohmic Losses by each battery pack is performed using Equation 13.1, which is then utilized to compute the heat dissipation. Subsequently, temperature raises are quantified using Equation 13.2.

$$P_{cell} = R \cdot I^2 \tag{13.1}$$

$$Q = m \cdot c \cdot \Delta T \tag{13.2}$$

With P_{cell} representing the power dissipation within a cell, where R denotes the electrical resistance and I is the current flowing through the cell. Equation 13.2 describes Q, the heat generation from temperature changes within the battery. Here, m denotes the mass of the battery components, c signifies the specific heat capacity of the battery materials, and ΔT denotes the temperature difference.

Assuming a cell resistance of 0.005 ohms, voltage of 3.6 V, and capacity of 3.2 Ah per cell as stemming from Table 12.2, a power loss of 0.3 W is calculated per cell. With the battery system modules established in Chapter 12 consisting of 28 cells in parallel and 98 in series, 825 W of total power is lost due to cell resistances. Over a mission duration of 35 minutes with an 80% depth of discharge, this translates to 1.7 MJ of heat.

Batteries have optimal operating temperatures, and these must be adhered to for the full operation range both during charging and discharge. Lithium-ion batteries have to be maintained between 15-35 °C to operate optimally [58]. The total heat loss aforementioned corresponds to a temperature increase of 35 Kelvins, which underlines the necessity of a thermal management system to mitigate the resulting temperature increase. These calculations are validated based on research indicating a heat generation rate of 17 mW/cm3 for the size of the battery system under consideration, resulting in a temperature rise of 42 Kelvin.

13.2. Battery Unit Thermal Dissipation Design

Following requirement *STK-CLNT-23-MIS-2: The vehicle shall operate within -50 to 50 degrees Celsius temperature range*, along with the battery needing to be between 15 and 35 degrees Celsius for optimal use [60], whilst adding 35 to 45 degrees Celsius, both a heating as well as a cooling system is needed. For the thermal management of the battery packs, electric cars are taken for inspiration. The battery is then accompanied by both a refrigerant plate as well as an electric heater[1].

The refrigerant plate should have a cooler or refrigerant flowing through some tubing on top of the battery working on the basis of conduction. The principle on which the cooling plate should be designed can be observed through the review of the two competing battery cold plates, seen in Figure 13.1 and Figure 13.2.

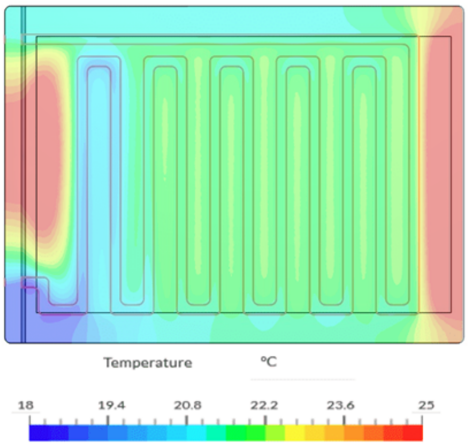

Figure 13.1: Thermal analysis of the original tried and tested cold plate (v1). The inlet is at the bottom left and the outlet can be seen top left.[2]

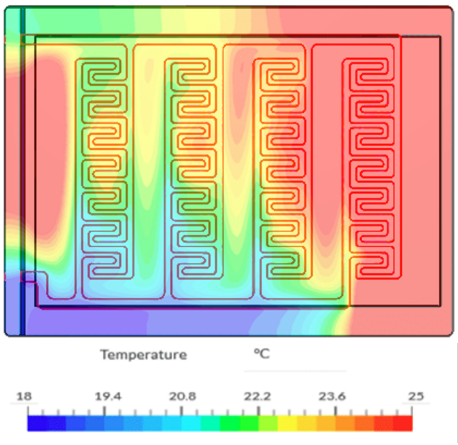

Figure 13.2: Thermal analysis of the new design (v2) with increased surface area for heat transfer[2]. The inlet is at the bottom left and the outlet can be seen top left.

The new design, from Figure 13.2, has an increased surface area compared to the original design and therefore has a larger heat exchange area. Despite the sufficient heat exchange area, there is inconsistent velocity flow through the tubing, as a result of preferred pathways through the many splits of the tubing. The inconsistent velocity flow causes v2 to have poorer thermal performance. To create an efficient cooling plate, the splitting points, width and amount of the tubing should be considered. The width/amount of tubing and velocity in the tubing should be evaluated together. If the width/amount increases, the velocity decreases hence allowing for less warmth to be carried away in the same time. The difference between the battery and refrigerant temperature is less too and this leads to less heat exchange.

As aforementioned, not only refrigerant plate but also an electric heater should be used. The electric heater should be controlled, either through the coordination with an electric thermostat or by using a mechanical thermostat with a mechanical actuator to turn the heater on. In the automotive industry, usually a mechanical wax thermostatic element is used [3] and due to its simplicity this is also the one that shall be used for the eVTOL's thermal regulation.

13.3. Computational Unit and Electronics Thermal Dissipation

The battery unit is not the only entity that dissipates heat, electronics and the computational unit also do. Since electronics are known to dissipate significantly less heat than the battery unit, a different approach can be taken. Heat sinks are commonly used for the thermal management of the computational unit and other electronics.

[1] URL https://www.hella.com/techworld/uk/Technical/Car-air-conditioning/Thermal-management-in-electric-and-hybrid-vehicles-1725/ [cited 05 June 2024]

[2] URL https://www.simscale.com/blog/simulating-optimizing-electric-vehicle-battery-cold-plate/ [cited 18 June 2024]

[3] URL https://en.wikipedia.org/wiki/Wax_thermostatic_element [cited 18 June 2024]

Heat sinks work on the basis of conductive heat transfer, from the device through a thermal interface material into the heat sink base and towards the thermal fins[4]. The fin sizing influences both the fragility of the heat sink as well as its effectiveness. The effectiveness is a direct result of conduction as the area that will be exposed to passing refrigerant or surrounding air is cooled. This allows for a passive heat dissipation solution.

13.4. Refrigerant

The cooling system needs a cooling gas or liquid. This is usually water, air or a refrigerant throughout the system. This should not only be done for the battery, computer and electronics but also for the comfort of the passenger. As a consequence of *STK-CLNT-23-MIS-2*, the outside air is unreliable in temperature and since *STK-CLNT-23-MIS-1* even mentions smoke in the air it is also not reliable in quality. Based on this and the better thermal capabilities of refrigerants compared to water, it is decided that the thermal management system will be based on refrigerants. The size and weight benefits of compressor-based systems as applied by most refrigerants are beneficial to the application.

There exist many chemical compositions, each with its own advantages and disadvantages. One great disadvantage of many refrigerants, that were popular in the creation of conventional cars, is the harm it does in terms of environmental sustainability; many worsened the state of the ozone layer[5]. Previously commonly-used and efficient refrigerants were banned and new regulations gave the need for the use of new refrigerants.

The competing new options, especially the promising ones like R-290 (Propane), R-600a (Isobutane), R-717 (Ammonia), R-1234yf HFO-1234yf (2,3,3,3-Tetrafluoropropene) and R-744 (Carbon dioxide), have strict requirements for safety as they must be compressed, are flammable, toxic, corrosive or asphyxiating.[6] Despite its flammability and need to be compressed, HFO-1234yf (2,3,3,3-Tetrafluoropropene) has been increasingly implemented in newer models of vehicles[5]. The flammability of HFO-1234yf is a point of contention against its use, however since SAE International performed a fault tree analysis procedure and concluded there would be no ignition under any normal conditions it is deemed safe [61]. Therefore HFO-1234yf is used as the refrigerant of the system.

13.4.1. General Layout of Vehicle's Thermal Management

All aforementioned components must come together in the eVTOL design. The placements are further explained in Chapter 15, however the thermal management within the layout is shown in Figure 13.3.

[4] URL `https://www.3erp.com/blog/what-are-heat-sinks-and-how-are-they-made/` [cited 18 June 2024]

[5] URL `https://www.cbac.com/media-center/blog/2024/may/everything-you-need-to-know-about-car-ac-refrige/` [cited 05 June 2024]

[6] URL `https://en.wikipedia.org/wiki/Refrigerant` [cited 05 June 2024]

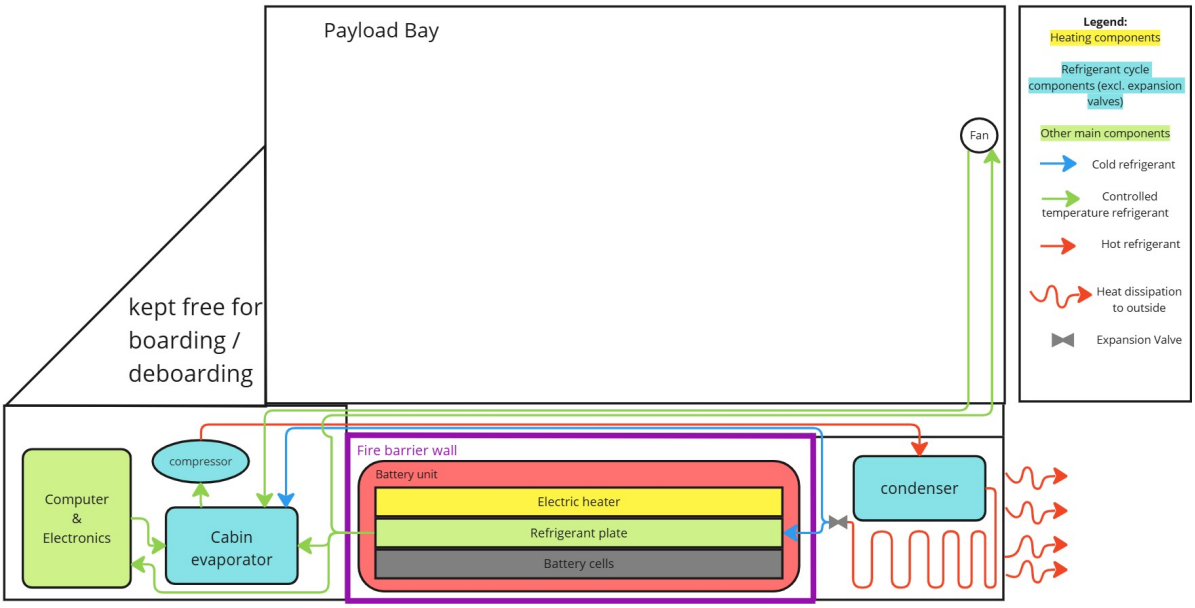

Figure 13.3: Thermal Management Loop

The side view of the fuselage, shown with the nosecone on the left in Figure 13.3, is divided into several sections. The payload bay section contains the passenger and a fan, in front of it towards the nose cone there is empty space for boarding and deboarding. The flight computer, electronics, battery and thermal management components are all placed at the bottom of the fuselage; the components are separated into two different sections divided by the battery section. The battery section, isolated with a fire barrier wall, includes the battery unit.

To provide appropriate cooling the refrigerants run in loops cooling the heating components. The refrigerant (HFO-1234yf) is stored until the eVTOL starts running. Generally thermal loops starts flowing as a cold liquid/vapor mixture to the evaporator, where it is turned into a saturated/subcooled cold vapor. At the compressor, it goes from low pressure to high presure hence leading to superheated vapor. After the condenser, it is turned into saturated/subcooled hot liquid, where you shall reject the heat to cool quickly. Lastly, it goes through expansion devices that turns it back into a liquid/vapor cold mixture.

When the battery unit is booted up, the thermostatic unit starts measuring its needs. Starting from the expansion valves again, the hot liquid has just become a cold liquid/vapor mixture. Based on the temperatures the batteries are experiencing, the pressure is increased or decreased to control its temperature.[7] In case the refrigerant plate is too cool for the battery cells, the electric heater is turned on and the refrigerant can be heated to the desired level.

After flowing through the batteries to maintain them between the range of 15 and 35 degrees Celcius, the refrigerant goes to other parts that need temperature control. It flows to the fan in the payload bay to cool/heat the passenger, the electronics and the flight computer. Generally, these elements are not as hot and after the batteries, the refrigerant should already be heated to a comfortable temperature passively due to the battery heat exchange. After cooling/heating those elements, the refrigerant goes to the evaporator where it is turned into a vapor. This is brought to the compressor, where the heat is dissipated to the outside. Afterwards, it is carried to the expansion valves cooling the refrigerant again and leading it to the battery unit or the cabin evaporator for the short route.

14 | Structural Design and Analysis

The external and internal structural design is more complex than only sizing. Although all structures must be designed and analysed in terms of loading and fatigue, especially the landing gear and rotor booms carry high loads. These are first designed, in Section 14.1 and Section 14.2 respectively. The

[7] URL `https://refrigeranthq.com/r-1234yf-refrigerant-pt-chart/` [cited 18 June 2024]

loads necessitate the use an adequate material. The material characteristics are examined and then assigned appropriately to the fuselage, structural booms, rotors and landing gear in Section 14.3. To evaluate the combination of material and design with the required load cases, a simulation is set up. This simulation encompasses the structural analysis of important subsystems in Section 14.4.

14.1. Landing Gear Structural Design

The landing gear is a critical component that accommodates various landing conditions essential for the vehicle's design. All the possible design options, skids, legs, wheels and floats, that comply with these requirements are presented in Figure 14.1.

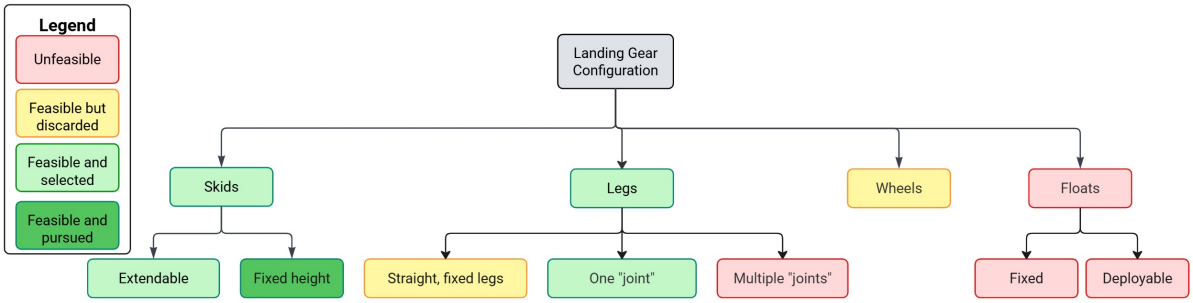

Figure 14.1: Landing Gear Design Option Tree

Skids, legs and floats all have sub-classifications. For the skids, considering the landing needs to accommodate slopes, there is a possibility of not making conventional skids but adding hydraulics to make either part, either one side or front/back, of the skid extendable. Legs are an innovative approach to landing; they must be specified by how many designed bending points, and joints, they have. Straight, fixed legs are the least complex and cheapest option. However, depending on the landing surface, they shall deflect easier based

14.1.1. Design Constraints

The design option tree conveys multiple components ranging in feasibility and performance capabilities. The feasibility of the design is entirely dependent on the mission. Within the requirements some mission characteristics are stipulated which limit the design options of the landing gear. The requirements STK-CLNT-8-MIS-3, STK-CLNT-9-MIS-3, STK-CLNT-10-MIS-3, STK-CLNT-19-MIS-2 mention landing operations regarding no damage to onboard systems and payloads in sand, 0.5 [m] water, 12 ° slope and 6bft wind speeds respectively. The sand requirement was specified to be not a requirement within the landing gear design but more so for the usage of sensors when sand is blown up. Therefore the sand requirement is not considered separately, but is briefly mentioned in the initial elimination.

First, considering these requirements and the performance capabilities a primary elimination shall be made. Afterwards, design decisions for the chosen configuration are made following first the water requirement, then the slope requirements, including sliding and tipping over in regular and windy conditions, and lastly the impact requirement. Since the design choices fit and meet requirements the final landing gear shall then be elaborated upon, based on the feasibility.

Initial Elimination

For the aforementioned critical landing configurations, skids are deemed more suitable compared to other feasible option. They are therefore the ones that shall be analyzed further in regard to feasibility in this mission. Only if this is not met shall other options be considered again. The lack of all other options shall be briefly discussed here.

Wheels are generally used due to easy movement as a result of their rolling capabilities. The rolling property of the wheels, in the missions specified, does not have benefits beyond the logistical removal of the vehicle out of the truck. They will even limit the possibility of expansion of missions, like landing on dry sand [1]. An advantage that wheels are however also known for apart from their rolling capabilities is the friction they provide. The friction of the wheels and their size is good against slipping. Despite

[1] URL `https://aviation.stackexchange.com/questions/7934/what-are-the-risks-in-landing-on-a-beach-vs-shallow-waters` [cited 07 June 2024]

the benefits of the wheels such as the movement out of the truck and surface friction, their cost and weight lead to the disregarding of the option.

Floats operate on the concept of buoyancy, where the things influencing the necessary float volume (V_{float}) are the weight that must float (m) and the density of the substance it must float on (ρ)

$$\rho g V_{float} = mg \tag{14.1}$$

To make a vehicle of 421 kg float at least a volume of 0.42 m^3 is necessary under the float line. The float line must prevent tipping over at all times and therefore additional volume shall be necessary during the design process s.t. landing on water shall be possible. Although the volume does not pose unfeasible restrictions on the design, it is overachieving in the water requirement whilst less reliable and less versatile. As a consequence, float landing gear is disregarded.

In the comparison between legs and skids, legs are an innovative design especially designed for versatile areas whilst skids have the advantage of being well-researched and having better distribution of stresses [2]. Some legs are also designed for extending mission possibilities such as landing on snow or other soft surfaces. For skids to extend their mission capabilities additional components, most commonly bear paws, must be equipped. The main constraint for choosing skids over legs is financial. Unless conventional skids do not work within the mission requirements, skids will be chosen.

Water Landing

As stipulated by *STK-CLN-10: the vehicle shall be able to land in 0.5-meter water*. This requirement is considered in the design of the landing gear, with a minimum height of 0.6 meters enforced on the sizing. This leaves 10 cm between the bottom of the fuselage and maximum water level. By ensuring this clearance, risks considering water damage, apart from rain, are minimized.

Sliding on the Slope

The vehicle should be stationary after landing; to satisfy this both tip over and sliding on the slope should not occur. The sliding condition is displayed in Figure 14.2.

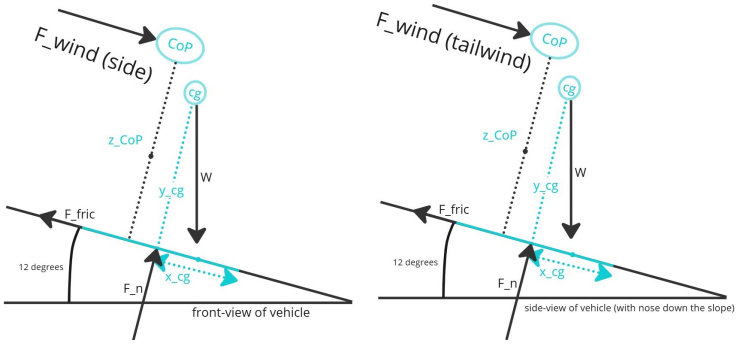

Figure 14.2: Sliding Slope Conditions With Wind Forces From Different Sides

To calculate if the vehicle will slide along the slope the friction force must be found and compared to the weight force along the slope. The friction force is calculated with $F_{fric} = \mu \cdot F_n$, where $F_n = W cos(12°)$. $F_{fric}, F_n, \mu_{fric}$ and $+F_{\text{max wind}}$ are friction force, normal force, friction coefficients and maximum wind/-gust force, obtained from calculations done in Section 9.3, respectively. All wind forces are derived from withstanding a 6bft wind, as described in STK-CLNT-19. If the friction obtained ($\mu_{fric(min)}$) exceeds the surface friction ($\mu_{fric(surface)}$), the vehicle shall slide. To obtain the friction needed to not slide in the situation, Equation 14.2 is used.

$$\mu_{fric(min)} = tan(12°) + F_{\text{max wind}}/(mgcos(12°)) \tag{14.2}$$

For the two conditions shown in Figure 14.2, the wind forces are the differentiating factors. The wind forces are also applied at different Center of Pressures (CoPs), although this has no affect for sliding. Different minimum friction coefficients will be needed from the surface to prevent slipping. The only way

[2] URL `https://news.softpedia.com/news/check-out-darpa-s-new-helicopter-landing-gear-491658.shtml` [cited 24 June 2024]

to adjust this with the design is by either changing the weight or the material of the landing gear. Since neither of those have an effect of the derivation of the maximum wind/gust force that is later calculated in Section 9.3, those values can be used to find the minimum surface friction coefficients acceptable. For the front-view situation, with the side wind, the maximum wind force experienced is 1991N whilst for the side-view situation, with the tailwind, the maximum wind force experienced is 644 N. These forces lead to the minimum surface friction coefficients needed for no slipping of 0.71 and 0.37 respectively.

Based on the requirements in testing competitions, a friction coefficient greater than 0.54 is used [62][4]. To explore possible landing positions on a slope the maximum wind force is calculated. The maximum wind force that is allowed to be experienced, with this friction coefficient, is 1322 N. This leads to the conclusion that with wind forces higher than 1322 N a side-landing on a slope is not acceptable. However nose-down landings, as shown in the front view of Figure 14.2, are always a viable solution to avoid slipping.

Tipping Over on the Slope

Tipping over conditions are most critical on slopes, as the weight contributes to the tipping possibilities. There are four situations considered most critical for tipping over; two describe an angle of attack (alpha) and wind forces, situation a & b, two describe no approach angle but with wind forces, situation c & d. Situation d is the only condition in which the vehicle is evaluated from the front view and not the side view.

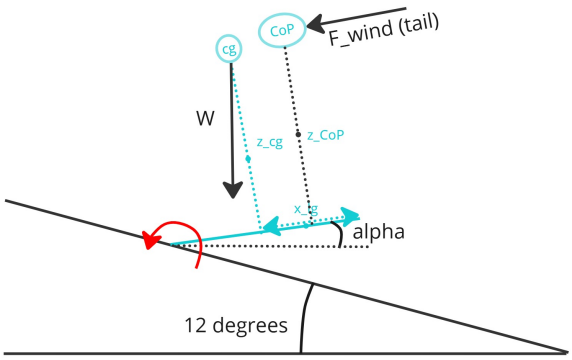

Figure 14.3: (a) Side-view With Tailwind During Approach

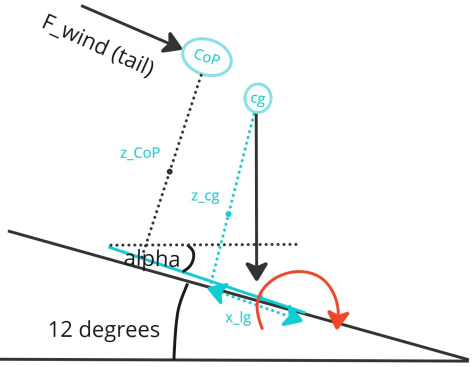

Figure 14.4: (b) Side-view With Tailwind Pushing Down the Slope During Approach

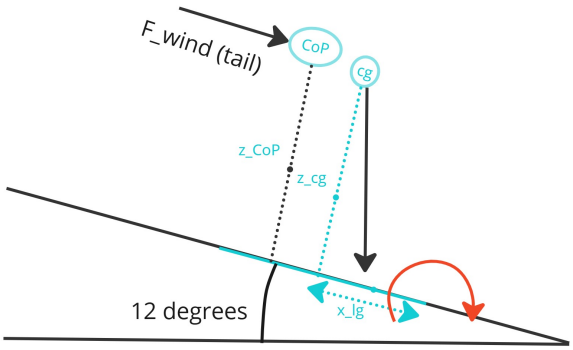

Figure 14.5: (c) Side-view With Tailwind from Stationary

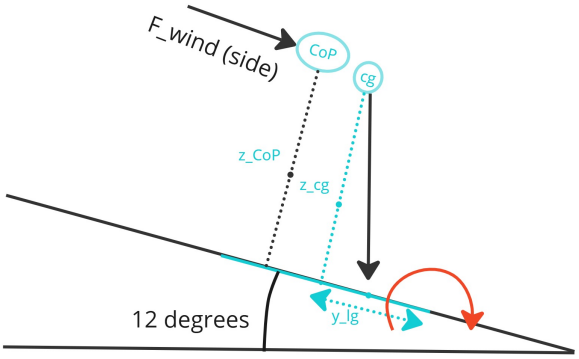

Figure 14.6: (d) Front-view With Side-windfrom Stationary

The maximum approach angle is 13 ° , which is determined in Chapter 11). To determine if the vehicle will tip over Equation 14.3 is created.

$$z_{lg} sin(\alpha) W + F_{\text{max wind}} > x_{lg} cos(\alpha) mg \tag{14.3}$$

If Equation 14.3 is true, the vehicle shall tip over. To evaluate how critical the situations are, a comparison shall be done first. Conditions a and b will prove to have the same resulting x_lg; between conditions b & c, condition b will be more critical than condition c, as it is already partly rotated; condition d is completely separately evaluated. Note that the Centre of Pressure (CoP) are different when

different direction wind are evaluated. Both the wind forces as well as the center of pressure locations in case of wind are obtained and further elaborated in Section 9.3.

Critical condition (b),with tailwind force of 644 [N], leads to a minimum x_lg of 0.54 [m]. The tailwind force has the same value as aforementioned during the sliding condition. Therefore if it is perfectly centered under the cg location, considering the cg range of 8 cm, the landing gear skid length should be at least 1.16 [m].

Critical condition (d), with a side-wind force of 1991 [N], leads to a minimum x_lg of 1.11 [m], therefore if perfectly centered under the cg location then the landing gear width apart should be at least 2.22 [m]. The side-wind force has the same value as aforementioned during the sliding condition. This will however also slip, so considering 1323 [N] the landing gear width becomes 1.66 [m]. These are unusually high compared to on-the-market helicopters whilst the rest of the parameters are not extraordinary. Therefore with wind forces higher than 300 [N], no side-landings shall be performed, like in critical situation d.

Since tailwind can meet wind conditions even on a slope without tipping over or slipping, landing on the 12 ° slope condition can always be met. There can also be forces in other directions than down the slope. The forces needed to lead to tipping over are of the same magnitude as would have been on a flat surface. On flat surfaces the lateral tip over force (caused by side winds) must not exceed 950 [N], longitudinally these wind forces will never be met as it exceeds the maximum winds that occur. These forces are considering the final dimensions shown in Figure 14.7.

Impact

Impact resilience is a critical design aspect, necessitating certification of the landing gear accordingly. Certification requirements ensure the safety of the payload and system in the event of a critical system failure. As the project is concerned with eVTOL design with a hexacopter configuration, EASA-CS-VTOL, and EASE-CS-27-Small Rotorcraft documents are relevant to comply with.

There are several cases to consider to obtain the maximum load on the vehicle. The one critical is from CS 27.725 Limit drop test; the most critical is “The limit drop test must be conducted as follows:(a) The drop height must be – (1) 0.33 m (13 inches) from the lowest point of the landing gear to the ground”[42]. Moreover this condition is made even more critical as a result of considering CS 27.501 Ground loading conditions as well. CS 27.501 necessitates the use of a drop height of 1.5 times that specified in CS 27.725. This is the most critical for certification for landing gear with skids.

Therefore, to comply with this requirement, a drop height of 0.5 meters is considered when determining critical load cases. Considering Elastic collision, coefficient of restitution, e=1. Therefore, velocity of separation and approach will be same. According to Newton’s second law,

$$\text{Impulsive force} = \text{Change in Linear momentum/impact time} = (mv)/t \tag{14.4}$$

The sinking speed (v) is decided on having a dropping height of 0.5 [m], hence leading to 3.13 [m/s] by direct conversion of energy. This translates to a change in linear momentum of 1318.626 [kg m/s], considering an impact time of 0.1 [s]. The impact force is therefore 13186.26 [N]. The design will influence the sizing and material choice, discussed in Section 14.3. This impact force also has a direct effect when introduced in the final element model, found in Figure 14.11.

14.1.2. Final Design

The final design of the landing gear is shown in the Figure 14.7. The vertical beams are welded to the bottom skids and the entire structure is connected to the fuselage with a rigid ring attachment, as explained in Subsection 14.4.2. The final dimensions are summarized in the Table 14.1.

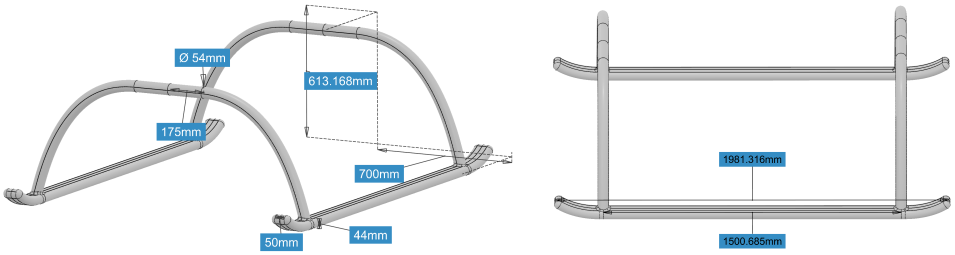

Figure 14.7: Final design of the landing gear.

Table 14.1: Final Landing Gear Sizing.

Type	Dimension [mm]
Outer Tube Diameter	54
Wall Thickness	4
Leg Straight Section Length	175
Total Skid Length	1982
Skid Flat Section Length	1500
Skid Width	50
Skid Height	44
Skid Spacing	1400
Total Landing Gear Height	613

14.2. Rotor Boom Structural Design

Rotor booms are safety-critical structural components. Therefore, their design is of utmost importance. Due to the preliminary nature of the design, a first order sizing method is used. In order to reduce the structural mass, the structure is decided to be thin-walled. Moreover, each boom is modeled separately assuming the following:

1. Boom behaves according to the assumptions of Euler-Bernoulli beam theory.[3]
2. Boom is a cantilever beam clamped at one end with exclusively vertical point load (thrust) located at the other end acting on it.
3. Boom's mass is ignored basing on the fact that it would act as distributed load acting in the opposite direction to thrust vector relieving the bending stress experienced by the structure. Hence, the assumption is a conservative one.
4. Motor, rotor and duct mass is ignored because of the same reasoning as the boom's mass itself.
5. Circular cross-section is assumed to be circular in order to ease the weight comparison.

The vertical deflection (δ) of each boom is going to be considered and calculated according with the equation:

$$\delta = \frac{PL^3}{3EI}, \tag{14.5}$$

where P stands for point load, L for boom length, which is determined beforehand having propulsion and maneuverability considerations in mind, E for Young's modulus, depending on the material choice, of the material and I for area moment of inertia.

In the design process, the team decides that each structural boom should not deflect by more than 5cm. Therefore, having a set deflection, material chosen, defined length and loading case, the only variable free to vary in the design geometry is the area moment of inertia. It depends on sheet thickness (t) and outer radius of the circular profile (R) and can be calculated using the following equation:

$$I = \frac{\pi(R^4 - (R-t)^4)}{4} \approx \pi R^3 t. \tag{14.6}$$

The values of radius and thickness are iterated in order to find an optimum between maximum area moment of inertia and minimum weight without compromising mechanical properties. The safety factor for the thrust load equal to 2 is applied to be on the conservative side in the design. In order to ease

[3]URL `https://web.mit.edu/16.20/homepage/7_SimpleBeamTheory/SimpleBeamTheory_files/module_7_no_solutions.pdf` [cited 19 June 2024]

the manufacturing, the biggest length of the boom is taken to size all of them. The calculations led to booms having sheet thickness of 5 mm and outer radius of 40 mm.

Booms need to be mounted to the fuselage providing multiple load paths in line with principles of safety-critical design. Bearing that in mind, a single attachment is considered an ill-chosen design solution leading to high stress concentrations. In order to counteract that, a mounting hub is introduced that is designed to transfer the load to the fuselage frame in a more distributed manner. The schematics of the mounting hub is presented on Figure 14.8.

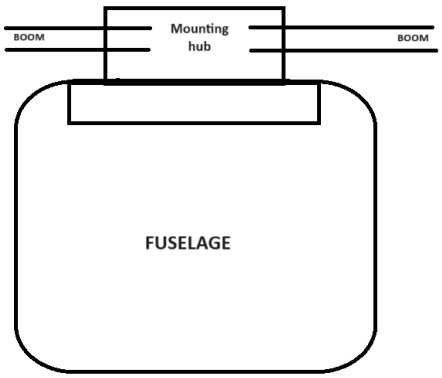

Figure 14.8: Mounting hub for the rotor booms schematics.

14.2.1. Final Design

The final design is presented in Figure 14.9. The booms are connected to the central hub, which is then connected directly to the fuselage's primary structure. Note that the central hub is not fully accurately modeled in the figure. The wall thickness of the boom is 3mm. The coordinates of the boom endpoints with respect to their central point are presented in Table 10.1.

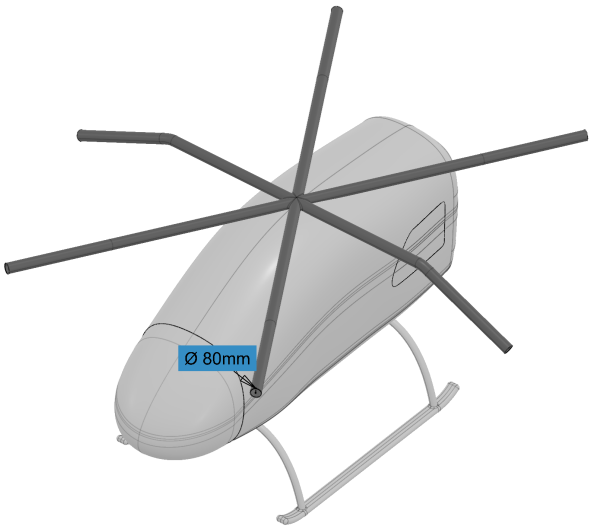

Figure 14.9: Final rotor booms design. Two center booms feature an elbow bent to facilitate a rotor tilt of 33.5 deg

14.3. Material Selection

A crucial part of any design is related to the selection of appropriate materials for the different components. This is even more important when considering aerial vehicles, due to the need for light, high-performing materials. This performance involves many criteria, ranging from the mechanical properties of materials, their cost, and their production processes. As such, the material selection is quite frequently a compromise between these criteria.

The assignment of materials is performed by first selecting several appropriate materials and examining

their properties. They are later matched, depending on their properties, to the different groups of the vehicle, i.e. the fuselage, the structural booms, the rotor hubs and blades, and the landing gear.

14.3.1. Material Examination

For the material selection, the following criteria are taken into account. First, the mechanical properties of each material are considered ensuring it is able to carry the loads subjected to. These correspond to the stiffness (Young's Modulus E), strength (ultimate tensile strength and yield strength), and density. The cost of each material is also taken into account.

Additionally, some qualitative criteria are taken into account as well; these are corrosive resistance to water, corrosion between the materials (including galvanic corrosion interactions between them), compatibility of materials, ease in processing the material, and thermal and electrical characteristics. Finally, in line with the sustainable goals of the project, recyclability is also considered as a criteria.

Once these criteria have been defined, the options for materials that meet them are selected. Due to their predominant and historical use in aircraft, aluminum alloys are the first option considered. Similarly, the specific use of titanium alloys and steel alloys in aircraft makes them sensible options. Finally, in line with more recent trends in aviation, carbon fiber-reinforced composites are also considered for the design. Other common materials were considered, such as wood, polymers, and heavier metals, but they did not combine acceptable values for all the criteria needed, i.e. mechanical properties, weight, corrosion resistance. The summary of the quantitative mechanical properties of the materials is included in Table 14.2, and their qualitative properties are mentioned in their application to the different vehicle parts.

Table 14.2: Mechanical Properties of the Materials Considered for the Design[4,5][63]

Material	Ultimate tensile strength [MPa]	Yield strength [MPa]	Young's Modulus [GPa]	Density [kg/m^3]	Cost [$/kg]
Aluminum 2014-T6	469	331	74	2796	1.80
Aluminum 2024-T4	393	262	74	2768	1.80
Aluminum 7075-T6	538	483	74	2796	1.80
Titatnium-64Al-4v (H.T.)	1082	1048	110	4429	16.50
Stainless steel AISI 630	1105	1000	196	7750	2.70
CFRP Laminate (graphite)	1172	965	152	1550	110

14.3.2. Fuselage

The fuselage is responsible for giving shape to the vehicle, and carry and distribute the loads throughout the entire structure.

With these functions in mind, the materials considered are mainly aluminum alloys. These alloys are light, strong materials that are proven in the aerospace industry, which reduces the risk. The material is relatively easy to process, and allows for creation of stiff, parts with very low thickness, aiding in weight reduction. It is categorized as acceptable in terms of corrosion, deemed sufficient since the fuselage should not be in contact with the water at any point. Within the aluminum alloys, although they are very similar in density and cost, due to their different composition they have different properties and performance.

Aluminum 7075-T6 has a very high strength, making it ideal for handling the high stresses encountered in the fuselage. While it has lower corrosion resistance compared to the other two alloys and is less resistant to fatigue than the 2024-T4 option, its superior toughness and high strength-to-weight ratio outweigh these drawbacks. Consequently, to comply with the high loads the fuselage experiences, confirming that the corrosion and fatigue resistance are valid, the 7075-T6 alloy is selected over the 2024-T4 and 2013-T6 alloys.

Fiber-reinforced composites are also considered, given their low weight, high performance, and match for the fuselage shape. However, they are discarded because of their high cost and low recyclability, both of which do not meet the requirements of the vehicle. Titanium is discarded due to its high cost

[4]URL `https://www.atlassteels.com.au/documents/Atlas_Grade_datasheet_630_rev_May_2008.pdf` [cited 18 June 2024]

[5]URL `https://web.mit.edu/course/3/3.11/www/modules/props.pdf` [cited 18 June 2024]

and high density, which makes it unfeasible to comply with the weight requirement. Finally, stainless steel is discarded because of its high density, making it unable to comply with the weight requirement.

14.3.3. Structural Booms

The structural booms have the function of connecting the rotors to the fuselage, acting as a critical load path between the two. As such, the structure undergoes very high loads, which it must comply with comfortably, given its importance to safety. Additionally, the interactions and compatibility between the materials is also considered. The use of two different materials is feasible if an external fairing is used, including an additional structure to connect them.

Aluminum alloys again represent an ideal candidate due to their lightweight, high strength, and proven reliability in aerospace. They are easy to process and provide acceptable corrosion and fatigue resistance. Similarly to the fuselage, the 7075-T6 is chosen over the other two options due to its superior strength.

When considering composite carbon fiber, it completely satisfies the high strength and low density requirements. However, the high cost of the material makes it unsuitable for a large structure such as the booms. The recyclability concerns are also an issue. Additionally, composite materials behave very differently in tension and compression, showing roughly half the strength (MPa), as cited by [64], showing a much higher brittleness. This does not suit the particular loading case of the booms during flight, causing the top part to be in compression. As such, composite materials are not ideal for the safety-critical structural booms. Lastly, the production process of a composite tube is considerably more complicated than for the other materials considered. Thus, all of these factors led to the rejection of fiber-reinforced composite for the structural booms.

The titanium and stainless steel material options have been discarded due to their high cost and high density. Thus, the material selected for the structural booms is the aluminum alloy 7075-T6.

14.3.4. Rotors

For the rotor group, it is useful to subdivide into two subgroups, analyzing first the rotor structures, and secondly the rotor blades. Firstly, the rotor structures are comprised of the rotor ducts and structural connections. They carry the loads introduced by the thrust of the rotors, and transfer the loads to the structural booms. The aluminum alloy 7075-T6 is an ideal candidate due to its high strength, low weight, ease of processing, acceptable corrosion and fatigue resistance, recyclability, and low cost. Fiber reinforced composites are discarded due to high cost and no recyclability. Finally, titanium and steel are discarded on a density and cost basis. As such aluminum 7075-T6 is chosen for the rotor structures.

The second group, the rotor blades have the function of converting the motor power into thrust. They rotate at very high speeds and are subjected to very high loads. Given these high loads, a very high strength is required.

When considering composite materials, their higher performance is certainly beneficial. The high strength complies with the high loads, and their low weight reduces the load on the engine. Given that the design utilizes custom rotor blades, using composites would not prove a disadvantage in terms of manufacturing since they are suitable for complex shapes.

Aside from this, since the rotor blades comprise a lower percentage of the total vehicle, it would not severely affect the recyclability requirement. On the other hand, the higher cost of the material is a problem, but given the smaller mass, it is still feasible under the budget, also making it feasible in this aspect. There are also some concerns regarding the brittleness of the material and its fragility when hit by an external object since they are exposed to the airflow. To prevent this, a different material is included on the leading edge of the blade, which is the same aluminum 7075-T6. Additionally, these concerns are alleviated by the fact that the rotors are covered and protected by a duct, considerably reducing the probability of hit. Additionally, the safety and control of one engine inoperative condition have been thoroughly calculated and analyzed in Section 10.3. As such, in the event that one of the rotor blades breaks, the vehicle would still be controllable. Aluminum is indeed considered due to its favorable properties, and titanium and stainless steel are again discarded due to their high weight. Thus, even though aluminum is a suitable material for the rotor blades, the added value in the performance of

utilizing carbon fiber is deemed worth the extra cost and reduction in recyclability. As such, the material for the rotor blades is chosen to be carbon fiber composites.

14.3.5. Landing Gear

The landing gear structure must support vehicle weight in combination with high-impact loads in case of a hard landing. This implies the need for the material it is made out of to be high strength, excellent fracture toughness, and good resistance to fatigue loading [65]. Moreover, due to the mission specifics of landing in half a meter of water, material shall be resistant to corrosion. According to Kumar, for helicopter skid landing gear, the most commonly used materials are aluminum alloy 7075-T6 (Al7075-T6), 300M alloy steel and alpha-beta titanium alloy Ti6Al-4V [66]. Nevertheless, due to low corrosion resistance of 300M steel, stainless steel AISI 630 is considered instead. 2xxx aluminum alloy series is discarded because of its strength being below the satisfactory level for crashworthiness and impact resistance [67]. Moreover, despite promising tailorable properties of composites, they are not considered due to their brittle nature and low impact resistance [64].

Having analyzed material properties, gathered in Table 14.2, it can be concluded that despite titanium high performance and low density, its cost is significantly greater than other options. Choosing titanium increases manufacturing cost making cost requirement difficult to meet. Consequently, titanium is deemed to be an unfeasible choice for the design. Al7075-T6 is lighter compared to AISI 630 steel which is characterized by higher strength. Moreover, this steel is characterized with better corrosion resistance than Al7075-T6 alloy. Having this considerations in mind and mission requirements of water landing and crash-worthiness, stainless steel AISI 630 is chosen to be a material for the landing gear.

Due to the fact that the landing gear must be capable of water landing under normal operational conditions, corrosive resistance of materials must be addressed. Adversely to aluminum and titanium, 300M steel is not corrosive resistant.[6] In order to counteract that, protective cadmium or chromium platings must be applied to the steel surface [63].

14.4. Structural Analysis

Aircraft design requires high-accuracy modeling predictions as structural deflections beyond a certain threshold may pose a risk to the structural integrity of the vehicle. Several software packages are employed in industry applications that implement a finite element method (FEM) for solving partial differential equations that model the mechanical behavior of structures. This approach is followed to assess the structural performance of the load-bearing structures at this stage of the design, the landing gear, and rotor booms.

To pursue this, finite element models are developed on Simcenter3D using three-dimensional elements. Assumptions made during modeling are discussed, with their impacts on the model results in Subsection 14.4.1. Simulations are conducted for the identified limit load cases of these structures in Subsection 14.4.2, to obtain nodal displacement, elemental strain, and elemental stress outputs. These results are then compared with the material properties to ensure structural integrity and prevent yielding in Subsection 14.4.3. Furthermore, design updates are implemented accordingly to achieve optimal structural performance and weight characteristics.

14.4.1. Modeling Assumptions

The set of assumptions made for the entire model are shown below:

- STR_AS_01: The structure is loaded in the linear-elastic regime. Plastic deformation can indicate that the material has exceeded its yield strength, leading to a reduction in the overall structural integrity and load-bearing capacity. This can lead to fatigue, crack initiation, and safety risks, making the structure more susceptible to failure under subsequent loads. Therefore, it is assumed that the structure is not subject to stresses beyond the yield stress and the materials are linear elastic. Consequently, the model is insufficient to capture plastic deformation.
- STR_AS_02: The structure can be discretized with finite geometrically simple elements. The choice of element type (e.g., tetrahedral, hexahedral) and the mesh density is assumed to be

[6] URL https://www.sae.org/publications/technical-papers/content/2021-01-0028/ [cited 13 June 2024]

sufficient to capture the stress and strain distribution accurately. The differential equations for the stress and strain are simpler to solve for the idealized finite elements used to model the structure. Consequently, parts of the structure with high curvature will require multiple elements for an accurate approximation. Some details of the geometry will be lost. Very minimal effects are expected for the preliminary design.

- STR_AS_03: Young's modulus of the materials does not vary with temperature differences. Step changes of the Young's Modulus are difficult to quantify and implement in the simulation. This assumption reduces the complexity of the simulation and analysis. However, in reality, Young's Modulus decreases with increasing temperature due to increased thermal vibrations of atoms. This discrepancy is around 5.5% and 13% for a temperature range of $20\,\mathrm{K}$ to $250\,\mathrm{K}$ for steel and aluminum[68]. The simulation neglects this and underestimates the stresses due to the thermal loading.
- STR_AS_04: Metals have the same properties at every point; they are uniform without irregularities. The structure is composed of metals that exhibit macroscopic homogeneous behavior. Material irregularities are difficult and time-consuming to capture. As a result, the simulation results may deviate from reality if the metals have significant imperfections and non-homogeneity.
- STR_AS_05: No manufacturing irregularities are present. The modeled structures are assumed to be manufactured without deficiencies. Manufacturing irregularities are challenging to acknowledge and estimate. Studies argue that finite element models that overlook typical manufacturing errors still show sufficient results [69]. Hence, while some stresses and strains may not be accurate, the effect of this assumption will be minimal for the preliminary design.
- STR_AS_06: Boundary conditions are fully constraining. Accurate representation of boundary conditions, including constraints and loads, is assumed to reflect the actual operational conditions. Real boundary conditions might differ from ideal ones, but this assumption is necessary to avoid unsolvable systems. However, in reality, the supporting structure is assumed to be significantly stiffer than the structure being modeled, and this is likely to be insignificant.
- STR_AS_07: There is perfect bonding between different materials or components, with no slippage or separation at interfaces. This assumption simplifies the analysis by assuming uniform load transfer across interfaces, ensuring that stresses and deformations are distributed uniformly throughout the bonded regions. It facilitates computational efficiency and reduces complexity in modeling while providing a reasonable approximation of structural behavior. This idealization may neglect real-world factors like adhesive variability and environmental impacts, potentially affecting structural accuracy.
- STR_AS_08: Engineering stresses are considered. Engineering stresses use the undeformed area of the cross-section, while true stresses account for Poisson effects that momentarily modify this area. Given the 2D nature of the model, the Poisson effect is overlooked in the simulation. Ignoring the Poisson effects implies that the stresses are underestimated. For steel, this effect is quantified by the Poisson ratio of 0.287, which results in a stress discrepancy of 2.95% when compared to true stresses in a 10 by $10\,\mathrm{mm}$ beam.
- STR_AS_09: The slopes of the deformed beams are small, i.e. the angles remain small. Small angle approximations are used to derive the equations of motion. This makes mathematical expressions simpler and calculations less intensive. For small deflections, the added error is small, being only 1.5% at 10°.

14.4.2. Load Cases

The vehicle along with its subsystems is subject to various loading cases. Among these, some load cases are critical for the load-bearing structures, at this stage of the design these include the landing gear and the rotor booms. In this section, these critical load cases are identified which are considered for the structural analysis of the vehicle.

Landing Gear

For the landing gear structural analysis, the load case elaborated in Equation 14.1.1 is applicable. The total load of 14000 N along with the weight of the vehicle of 4200 N is equally distributed on the surface of the landing skids. The structure is connected to the fuselage through the two parallel arms underneath it with a rigid ring attachment. A similar connection for a helicopter skid is depicted in Figure 14.10. To accurately model this type of connection and the introduction of loads, the FEM is constrained at the

relevant nodes on the structure.

Figure 14.10: Helicopter Skid Ring Connection [7]

The landing gear skids and legs are modeled using CTETRA10 meshes with an element size of 10 millimeters, while the connection rod is modeled using CHEXA8 meshes with an element size of 15 millimeters. The part where the nodes are constrained to model the landing gear fuselage attachments is modeled with CTETRA10 meshes with an element size of 12 millimeters. This mesh sizing enabled the generation of intended structural loading outcomes using the linear solver efficiently within a short period. The meshing of the model as well as the fixed constraints, and the loads are illustrated in Figure 14.11. The red arrows on the structure represent the distributed load split between the two skids. The blue lines at the top of the structure are the fixed constraints simulating the fuselage connection.

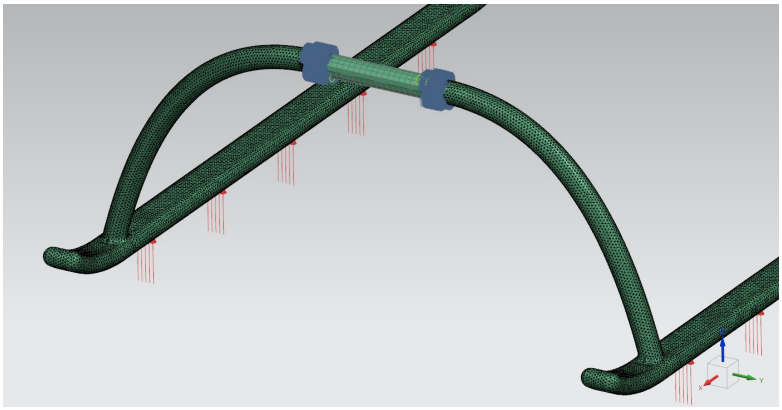

Figure 14.11: Landing Gear Finite Element Model with Constraints and Loads

Rotor Booms

For the structural analysis of the rotor boom, the critical load case is defined as the scenario where each rotor provides the maximum thrust of the system. This is determined to be a total of 8300 N, distributed equally across the rotors. This is introduced to the booms at their connection to the rotor hubs as a distributed load around the boom connection face. Despite the structural design discussions provided in Section 14.2 the model does not depict the intended connection point of the rotor booms to the fuselage. Therefore, the point of contact of the booms to the fuselage is not assessed for structural performance in this analysis. To constrain the model the structure is assumed attached to the fuselage with a fixed constraint on the relevant nodes.

The connection arms are modeled using CHEXA8 meshes with an element size of 10 millimeters, while the connection point is modeled using CTETRA10 meshes with an element size of 6 millimeters. The FEM of the structure is depicted on Figure 14.12. The red arrows on the structure represent the distributed load split between the six arms. The blue lines at the bottom of the center are the fixed constraints simulating the fuselage connection.

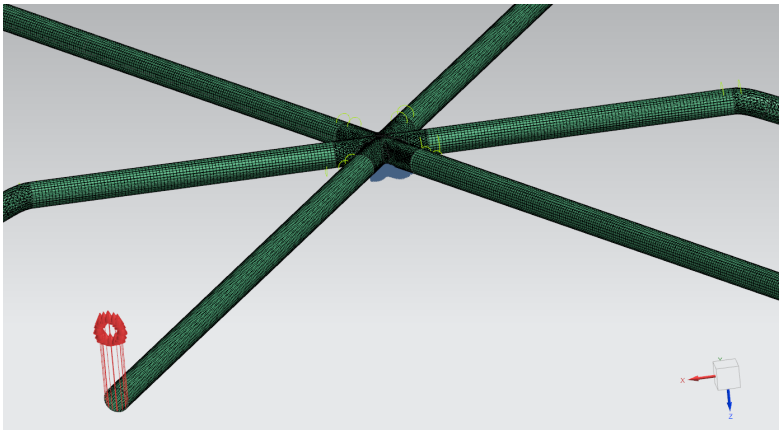

Figure 14.12: Rotor Boom Finite Element Model with Constraints and Loads

14.4.3. Simulation Results

The outcomes of the simulations provide insights into stress distribution and deformation patterns, influencing the structural integrity and performance of the system for the aforementioned load cases. The results highlight the critical load paths for the investigated load cases, offering valuable insights into areas requiring reinforcement. Based on the analysis results, necessary design updates for the structures are identified. In the next phases of the design, these updates should be incorporated to converge to an optimal structural design.

Landing Gear

The landing gear stress results as seen in Figure 14.13 reach a maximum of around 700 MPa close to the notes of load introduction. The peak stress observed is attributed to the method used for modeling the fuselage connections and is not the primary focus of this analysis. For the remaining model, critical loads are observed around the top of the landing gear legs and the connection points to the skids, in the range of 500 MPa. The yield stress of the chosen stainless steel 1000 MPa, is higher than this range indicating that the structure does not fail under critical loading.

When looking at the strains observed it is concluded that the structure is loaded within the linear elastic region of the material. This ensures that the solver results are accurate within the modeling assumption made.

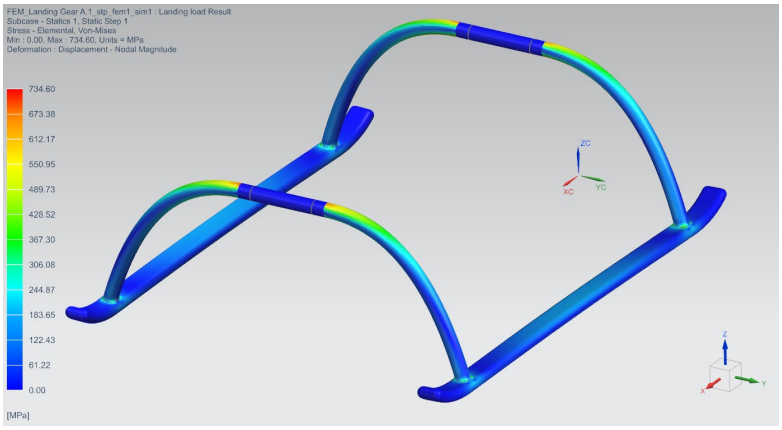

Figure 14.13: Landing Gear Stress Results

With manufacturing considerations in mind, reducing the thickness of certain parts of the skids and landing gear legs, and making it a variable thickness structure is deemed unfeasible. A structural improvement that would aid weight savings is reducing the landing gear leg thickness by a millimeter. This approach allows for some structural loading margin within the design, enhancing overall safety. Observing that the skid connections are highly loaded, the weld line is recommended to be further reinforced to enhance structural integrity in the final iteration.

Rotor Booms

The rotor booms are analyzed with a focus on the arms, neglecting the loading on the connection point as the model does not depict the intended structural design. Along the arms, a maximum stress of 150 MPa is experienced as seen in Figure 14.14. Considering the yield stress of the Aluminum alloy, which is 538 MPa, this loading scenario can be performed without structural failure. The strain results once again confirm that the structure is loaded within the linear elastic region of the material.

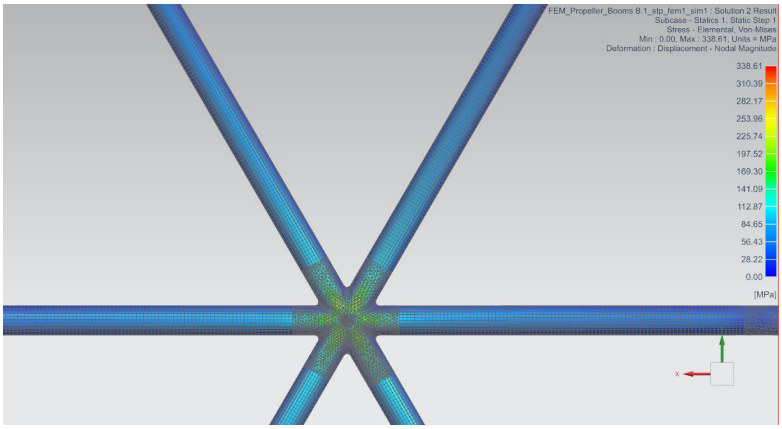

Figure 14.14: Rotor Boom Stress Results

Considering the high margin of loading, a reduction in the thickness of the arms for the rotor booms is recommended. The structural performance of this part is already robust, so additional reinforcements are not necessary.

14.4.4. Limitations and Recommendations

For future studies, load cases such as one engine inoperative landing can also be examined to evaluate the criticality of these scenarios for the structural design. For accurate load introductions in the landing gear modeling, it is essential to model the actual ring along with the landing gear. A note for future iterations is made regarding the connection point of the rotor boom, to gain a thorough understanding of the performance of the structure the connection should be modeled as designed for in Section 14.2. Moreover, an improved design should consider connecting the rotor arms directly to the fuselage reinforced via frames that span across the fuselage.

15 | Internal Layout

Once the external layout is known and sizing is performed, an analysis regarding the internal layout and fitting of the components is performed. This serves the purpose of ensuring that all required components are placed in the correct locations depending on their functions and that it is feasible to include them in a volumetric sense. Since internal components are defined as the items housed inside the fuselage fairing, it will be used as a constraint.

The general outline of the analysis is as follows: First, the volume of the different components is estimated. This is followed by their initial placement within the fuselage. This then leads to the calculation of the combined center of gravity of all internal components. This value is used as a reference, guiding the iterations and relocation of the internal components.

15.1. Component Sizing

Within the fuselage, the items included are the following: battery, sensors & flight computer, passenger, stretcher, structural connections & wiring. Their respective masses are presented in Section 8.3. With this known the next step is estimating their volume.

To estimate the volume of the battery the volumetric energy density is used. This value is specific to battery types and relates the energy capacity of the battery (Wh) to the volume it occupies. The total battery volume for the specific battery used is approximately 59 liters, as presented in Section 12.2.

Regarding the volume taken up by the passenger, to provide a conservative estimation, the average dimensions of a man corresponding to 94.5 kg were used, which correspond to a height of 190 cm, and a width of 50 cm, and depth of 18 cm [70].

Due to the emergency nature of the mission, the passenger is accommodated on a stretcher, which is also used to load him/her into the vehicle. This stretcher has wheels that allow for its extension outside. When extended, its legs can be adjusted in height so that the payload can be comfortably loaded or unloaded, complying with STK-PSGR-2, and folded into a horizontal plank when inside the vehicle. The particular model chosen is produced by RedLeaf, and has a volume of approximately 400 liters [1].

Figure 15.1: RedLeaf Extendable stretcher

The volume of the sensors and the flight computer is estimated by analyzing different off-the-shelf options on the market. For the flight computer, a model compatible with the mission scope of this project, the PX4 Sky-Drones AIRLink, is chosen as a reference. This is a cutting-edge flight controller with autopilot, including an AI mission computer and internet connectivity. It is compatible with the rest of the sensors: accelerometers, gyroscopes, magnetometers, pressure sensors, GNSS, rangefinders, lidars, optical flow sensors, and cameras [2]. In total, it has a volume of 0.23 liters.

The sensors are analyzed individually, and their volumes are then combined into one sensor grouping. The existing volumes for each type of sensor, combined with a safety margin, provide appropriate dimension estimations for the sensors. The radar used as reference is the EchoFlight produced by Echodyne, which is specifically designed to be onboard aerial vehicles to detect small objects, such as commercial drones at a distance of 1 km, and larger objects at a distance of up to 6 km. It has a volume of 0.9 liters [3]. The lidar used as reference is the Zenmuse L1, produced by DJI enterprise. It is used for aerial surveying and could be tailored for the specific applications of the vehicle. It has a volume of 2.85 liters [4] [5]. Finally, the vision camera is taken to occupy a conservative volume of 3 liters.

This concludes the estimation of the most voluminous sensors, which are summarized in Table 15.1. The remaining sensors are not estimated since they do not make as considerable of a volumetric contribution and are to be included at a later stage.

[1] URL https://www.redleaf-medical.net/emergency-stretchers-series/stretcher-for-ambulance/ems-ambulance-stretcher-dimensions.html [cited 03 June 2024]

[2] URL https://docs.px4.io/main/en/flight_controller/airlink.html [cited 03 June 2024]

[3] URL https://www.echodyne.com/radar-solutions/echoflight/ [cited 03 June 2024]

[4] URL https://enterprise.dji.com/zenmuse-l1 [cited 03 June 2024]

[5] URL https://www.dji.com/nl/support/product/zenmuse-l1 [cited 03 June 2024]

Table 15.1: Sensor grouping volume breakdown

Item	Volume [liters]
Flight Computer	0.32
Radar	0.9
Lidar	2.85
Vision Camera	3
Total	**7.1**

This results in a total volume for the sensor group of 7.1 liters. Even though these estimations are rather rudimentary, they give a sense of the order of magnitude of the volume taken by the sensors. The volume is given a general rectangular shape, which holds all components. An extra empty space of almost double the volume is included around the sensor grouping to account for uncertainty. See Figure 15.2.

15.2. Component Placement

The placement of the components is determined based on their functionalities and their estimated contribution to the global center of gravity (c.g.). This is an iterative process, in which components are shifted in all directions to find an optimal location.

In general, all components are placed centered laterally (Y direction), such that their center of gravity does not affect stability in this axis, and symmetry is preserved. Regarding the longitudinal placement (X direction) efforts are made to ensure that the final c.g. lies close to the axis formed by the connection of the rotors. This simplifies considerably the controllability aspects, specifically for the one motor failure event, as explained in Section 11.6. Regarding the vertical placement (Z direction), it is crucial to maintain the passenger clearance, such that there is as much space above him as possible, with the aim of maximizing comfort. Thus, as a general guideline, it is beneficial to keep the c.g. low. This helps with controllability since it creates a longer moment arm between c.g. and rotors. Additionally, it helps with stability on the ground.

Following these guidelines, the sensor grouping is placed near the front of the fuselage, underneath the stretcher. This allows for the camera, radar, and Lidar to face the in-flight direction, which is crucial for object recognition and vehicle autonomy. The passenger bay, which is comprised of the passenger, the stretcher, and a reserved volume for the passenger to feel comfortable, are all placed horizontally slightly towards the back of the vehicle. This thus aligns it with the windows near the rear of the fuselage. However, given that the passenger makes an important contribution to the total weight, it is important to keep it centered and not too far aft. The battery, given its high weight, is located centered, close to the bottom of the fuselage. Given the fact that the chosen battery is composed of modules, as explained in Chapter 12, it is possible to rearrange the volume into any shape. As such, for convenience and comfortable fit, it is arranged into a rectangle of dimensions (1.18x0.5x0.1 m).

Finally, regarding the Structural connections & wiring, given their nature and overall distribution throughout the vehicle, they are expected to take up a low volume [71]. This is accounted for in the margins and free space left within the fuselage. The result of all of these placements can be better visualized and understood in Figure 15.2.

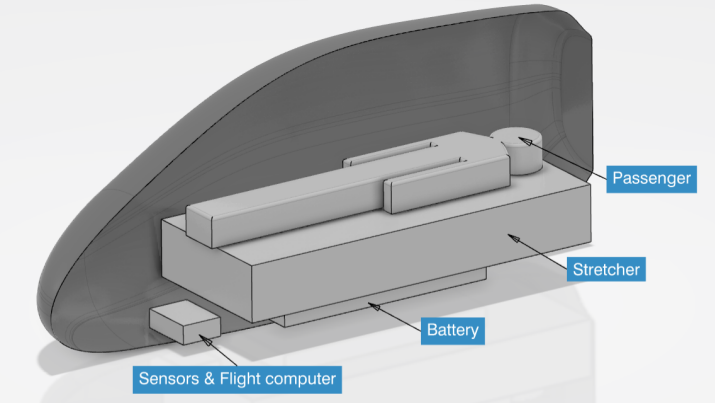

Figure 15.2: Placement of interior layout

15.3. Center of Gravity of the Vehicle

Stemming from the internal placement, the calculation of the global center of gravity is done. Equation 15.1 is used to calculate the c.g. The geometric CGs of the different components obtained from the CAD model are multiplied by their assigned weight, defined in Section 8.3. These values are linearly combined and divided by the sum of the weights.

$$\mathbf{R}_{\text{cg}} = \frac{\sum_{i=1}^{n} W_i \mathbf{r}_i}{\sum_{i=1}^{n} W_i} \tag{15.1}$$

These global values of the c.g. position are then used as the reference for the iterations shifting the battery and passenger location longitudinally (X direction) and recalculating the c.g. such that it lies below the axis line formed by the connection of the propellers. The vertical location of the two is also iterated, aiming to keep the c.g. as low as possible and to maximize the space the passenger has on top of him. Once this adjustment is achieved, the internal layout is finalized.

16 | Controller Design

Due to the wingless design of IUVO, it is naturally not stable and thus needs a carefully designed closed-loop feedback controller. This section describes the design of such a controller for the multicopter. First, the controller design goals are shown in Section 16.1. Then, the architecture of the designed controller is presented and described in Section 16.2. With the established controller, its performance is analyzed in Section 16.3, and the chapter is concluded with a V&V assessment in Section 16.4.

16.1. Control Allocation

To design a controller for the aircraft, it is important to first understand the control inputs available. A multicopter can move by generating certain forces and moments using its rotors. These depend on each rotor's squared angular velocities, as described in Section 10.2. Thus, the derived control allocation matrix B is used in the controller.

By calculating the forces and moments acting on the multicopter, and knowing its inertial properties, the acceleration of the vehicle can be calculated. With the acceleration, the desired trajectory can be tracked using a feedback controller. As the autonomy of the flyer is a key feature, the controller is designed to track a desired trajectory, such that it can work with path planning. Thus, the inputs to the controller of the aircraft position in a global frame and its heading, both of which are controlled with a feedback loop. The controller is designed to be robust to external disturbances, and to be fault-tolerant, such that the aircraft can continue to fly in the presence of rotor failures.

16.2. Controller Architecture

The controller of IUVO is designed to be a cascaded controller, with inner and outer loops. The inner loops are responsible for the stabilization of the aircraft, and the outer loops are responsible for tracking a desired trajectory.

The first cascaded controller is responsible for tracking the position of the aircraft. First, the desired position in the inertia; frame is fed to the position controller, where based on the position error, the Proportional, Integral, Derivative (PID) controllers output a desired velocity, within a limit of $\langle -33, 33 \rangle$ for the velocity in the x direction, $\langle -5, 5 \rangle$ in the y direction, and $\langle -2.5, 2.5 \rangle$ for the climb rate. The desired velocity is fed into the velocity controller, which based on PD controllers outputs the desired acceleration in the inertial frame, within the range of $\langle -5, 5 \rangle$ in the x and y axes, and $\langle -2, 2 \rangle$ for the climb acceleration.

The calculated accelerations are then used in the calculation of the desired attitude. The attitude is specified in the Euler angles, where ϕ is the roll angle, θ is the pitch angle, and ψ is the yaw angle. The following equations are used:

$$\begin{aligned} \theta_{des} &= -atan2\left(-a_x \cos(\psi) - a_y \sin(\psi), -a_z + g\right), \text{ and} \\ \phi_{des} &= -atan2\left(-a_x \sin(\psi) + a_y \cos(\psi)\cos(\theta_{des}), -a_z + g\right), \end{aligned} \tag{16.1}$$

where a is the acceleration in the axis indicated in the subscript. The calculated angles are then saturated to the range $\langle -15°, 15° \rangle$. Together with the desired accelerations derived before, they are used to calculate the necessary thrust in the body z-axis as follows:

$$T_z = \frac{MTOM(a_z + g)}{\cos(\theta_{des})\cos(\phi_{des})} \tag{16.2}$$

Then, the computed pitch and roll angles, together with input yaw angle, are fed into the attitude PID controllers, of which the output is the desired attitude change rate. This is fed to another controller, proportional rate controllers, which output the desired moments. Combined with the desired thrust, they are fed into the motor plant, which calculates the motor rotations and outputs the actual forces and moment acting on the multicopter.

In addition to the forces generated by the rotors, a simple parasitic drag model based on the analysis done in Chapter 9 is implemented. After adding the gravity force, the complete resultant forces and moments acting on the multicopter are fed into an aircraft equations of motion block, which calculates the dynamics of the aircraft, based on its inertial properties. The mass $MTOM = 421\,\mathrm{kg}$ used is obtained from the Class II weight estimation described in Chapter 8, and the Inertia tensor is extracted from the CAD model, and is shown below:

$$\mathbf{I} = \begin{bmatrix} 472.762 & 0.060143 & 0.813414 \\ 0.060143 & 655.531 & -0.163989 \\ 0.813414 & -0.163989 & 794.225 \end{bmatrix} \tag{16.3}$$

The designed controller's block diagram modeled in Simulink is presented in Figure 16.1.

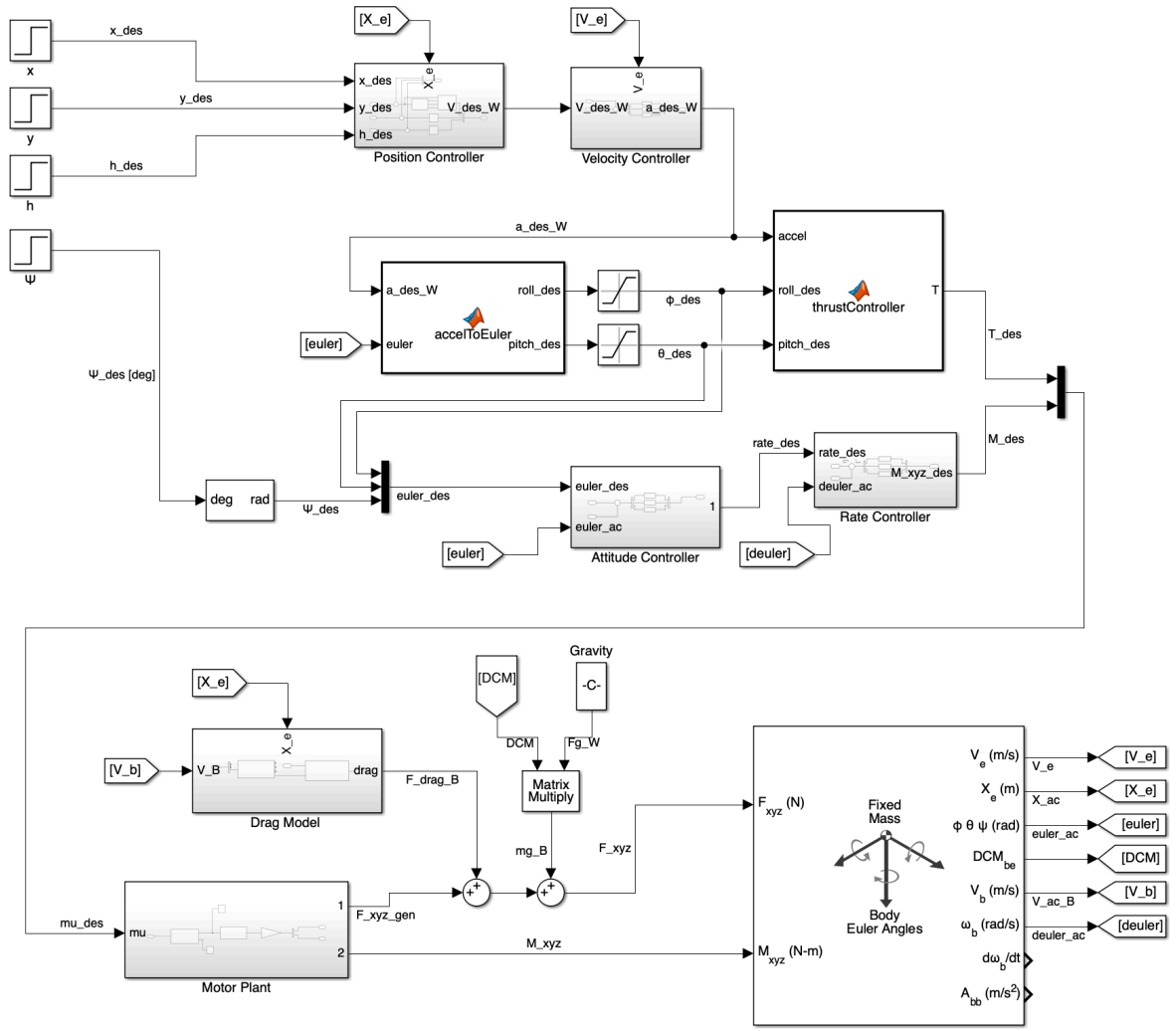

Figure 16.1: Control Block Diagram of the Multicopter.

As seen in the figure, the multicopter controller uses two custom MATLAB functions, `accelToEuler` and `ThrustController`, which implement Equations 16.1 and 16.2, respectively. The remaining controllers are native Simulink PID blocks. The output of the controller sections, the desired $\boldsymbol{\nu}$ vector, is fed into the motor plant model, of which the block diagram is shown in Figure 16.2.

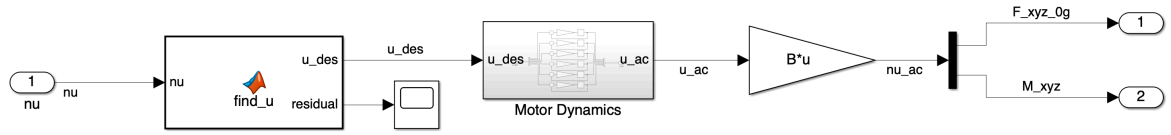

Figure 16.2: Motor Plant Model of the Multicopter.

The motor plant finds the necessary motor rotations by using the `lsqlin` function included in the MATLAB Optimization Toolbox. Implemented in the `find_u` block, it finds the optimal motor rotation vector $\boldsymbol{u}$ for the desired forces and moments $\boldsymbol{\nu}$ based on the control allocation matrix $\boldsymbol{B}$, motor rotations lower and upper bounds, and an initial guess that uses the Moore-Penrose pseudoinverse of $\boldsymbol{B}$. This way, if the desired $\boldsymbol{\nu}$ vector lies outside the Attainable Moment Set and/or Attainable Force Set, the function finds a solution that lies inside the AMS and AFS with the least squared error, and additional outputs the residuals for extra information. Then, the speeds are fed into a motor dynamics model, which is a simple transfer function $H(s) = \frac{1}{\tau_m s+1}$, with $\tau_m = 0.1$ being the motor time constant, that models the response of the motors. The motor model outputs the actual motor speeds, which are then fed back into the control allocation matrix to calculate the actual forces and moments acting on the aircraft by

the rotors.

16.3. Controller Performance

After designing the controller, and tuning the control loops, it is crucial to assess its performance. One way to check the behavior of the controller is to analyze its response to unit step input. The unit step responses are shown in the figures below:

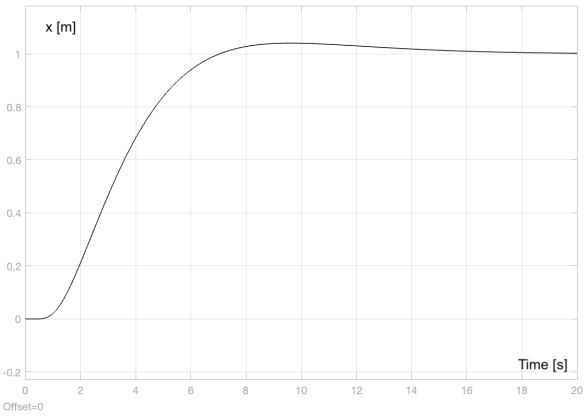

Figure 16.3: Unit step response for the x position.

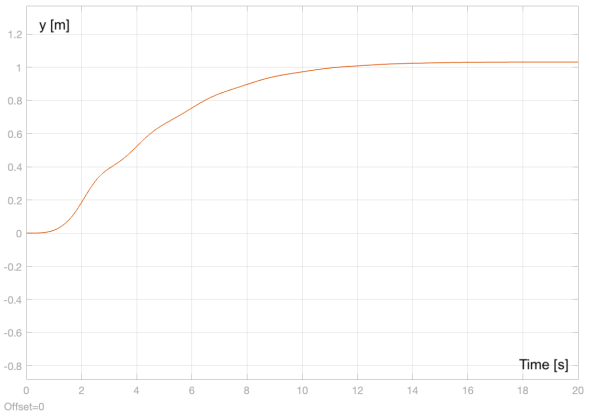

Figure 16.4: Unit step response for the y position.

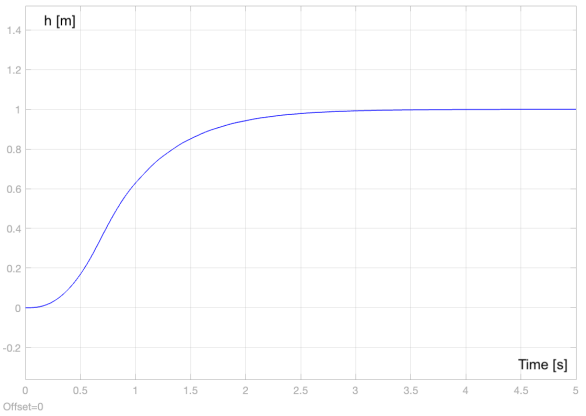

Figure 16.5: Unit step response for the altitude.

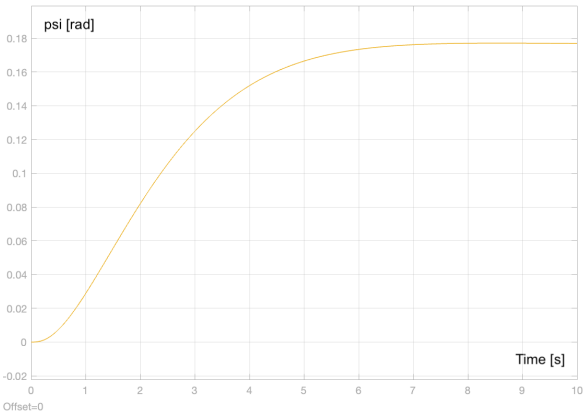

Figure 16.6: Step response for a 10 degree yaw turn.

As seen in the figures, the controller can track the desired position and yaw successfully. The x position tracking response starts after approximately 1 second, and settles down after a slight overshoot after 14 seconds, without a steady-state error. The y position tracking does not settles after around 14 seconds as well, with a smaller overshoot, but a small steady-state error (which slowly reduces over time due to integral action). The altitude controller achieves better performance for small inputs, with a settling time of 3 seconds, minimal response time, and no overshoot. Similarly, the yaw controller has no overshoot and minimal response time and settles in 8 seconds. It is worth noting that none of the responses show non-minimum phase behavior.

It is worth noting that the x and y position controllers have relatively slow settling times. This is a result of tuning the controller for higher input displacements. Due to the saturation of the velocity, the controller is not linear. Thus, different scales of step inputs exhibit different behavior. The step responses that experience the velocity saturations are shown below:

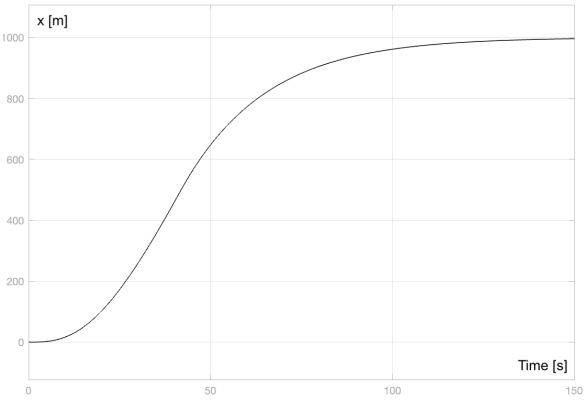

Figure 16.7: Step response for a 1000 m displacement in the x direction.

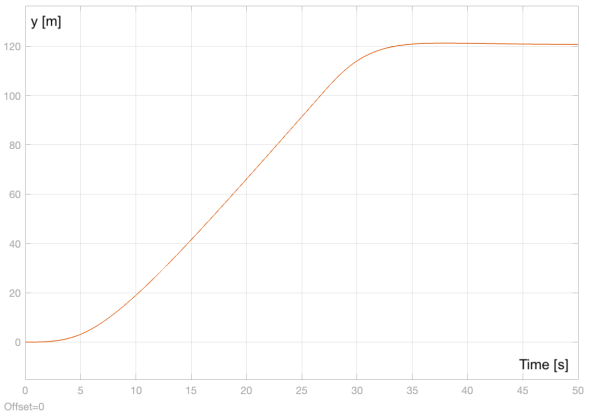

Figure 16.8: Step response for a 120 m displacement in the y direction.

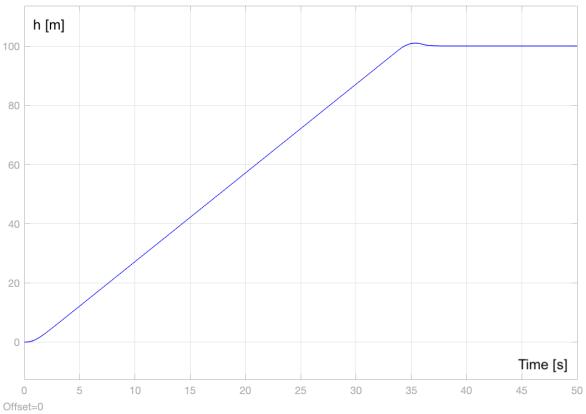

Figure 16.9: Step response for a 100 m altitude change.

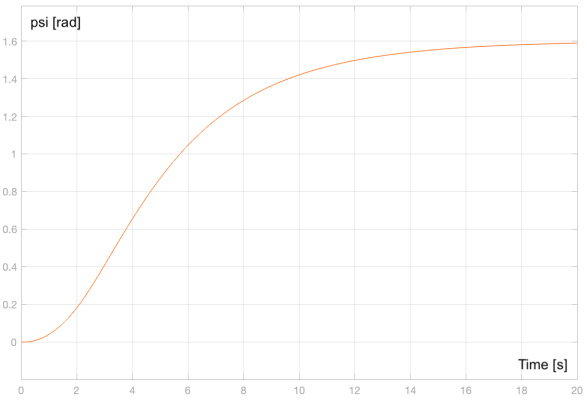

Figure 16.10: Step response for a 90 degree yaw turn.

The step scales are selected such that the controllers start operating in the saturated state. As seen in the figures, the responses are greatly improved for the displacement in the x and y directions. The x position controller does not exhibit overshoot and settles much quicker in the relative sense. The y controller features a slight overshoot but settles even faster. The same can be said for the altitude controller, whereas the yaw controller shows analogous behavior to the small step input. Again, none of the responses show non-minimum phase behavior.

The improved performance is a result of tuning the controller for such inputs. As a result of the saturation-introduced nonlinearity, the optimal PID gains are different for small and large inputs. To improve the performance, a gain scheduler can be implemented, which can switch the gains depending on the inputs. Additionally, the saturation causes a loss of control for the integral term. This is a phenomenon known as wind-up, and it is solved using the clamping method [72].

With the controller implementation in Simulink, it is possible to simulate performing the range mission. The simulated mission is a return flight with a range of 15 km each way, with an added slight repositioning in the y direction to showcase obstacle avoidance capabilities. This simulation can demonstrate that the controller is stable and capable of performing a crucial mission profile and shows how the aircraft operates under high parasitic drag. The resulting trajectories are shown below:

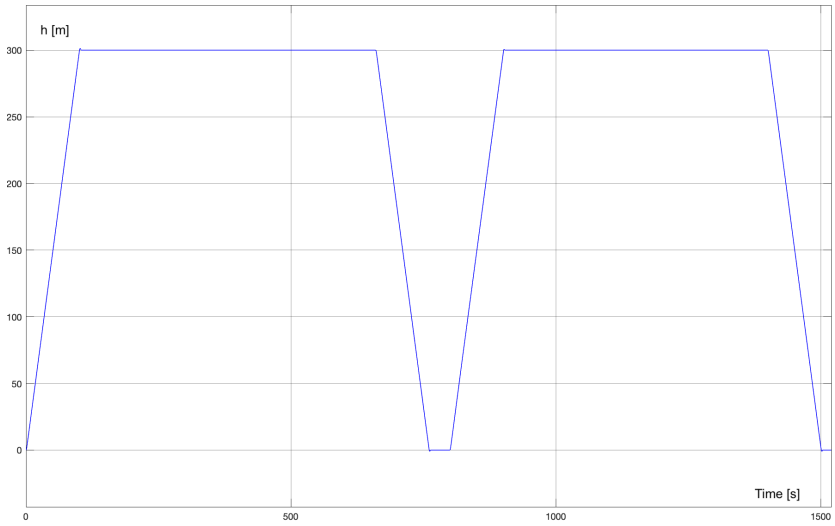

Figure 16.11: Simulated altitude trajectory over time for the range mission.

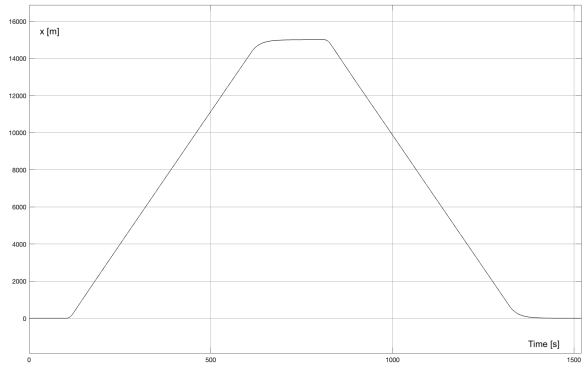

Figure 16.12: Simulated x trajectory over time for the range mission.

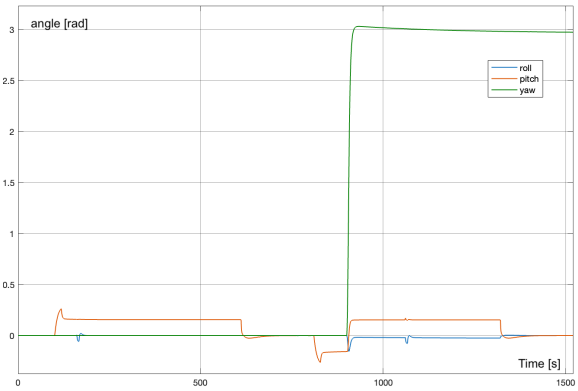

Figure 16.13: Simulated body angles over time for the range mission.

16.4. Verification and Validation

Previous sections analyzed the controller design and performance. As safety is a key design driver of IUVO, an assessment is made of the validity and safety of the model.

In principle, the simulation uses Simulink, which is an industry-standard software for controller design purposes. Thus, the simulation software itself is considered verified and valid. Moreover, the core of the simulation, which is the rigid body dynamics block (`6DOF Fixed Mass Euler Angles`), is an in-built component, thus its implemented equations of motion are considered correct. However, the blocks proceeding with them require additional analysis. For example, the gravity vector acting on the aircraft with motors turned off produces an expected acceleration equal to g. The motor dynamics block for example is analyzed for its response to the input signal, and the phase shift is as expected by the set motor constant.

The `find_u` block, which is the solver for the optimal motor rotations, needs certain considerations. For example, an analysis of the residuals can be made. The residuals present in the range mission are present below:

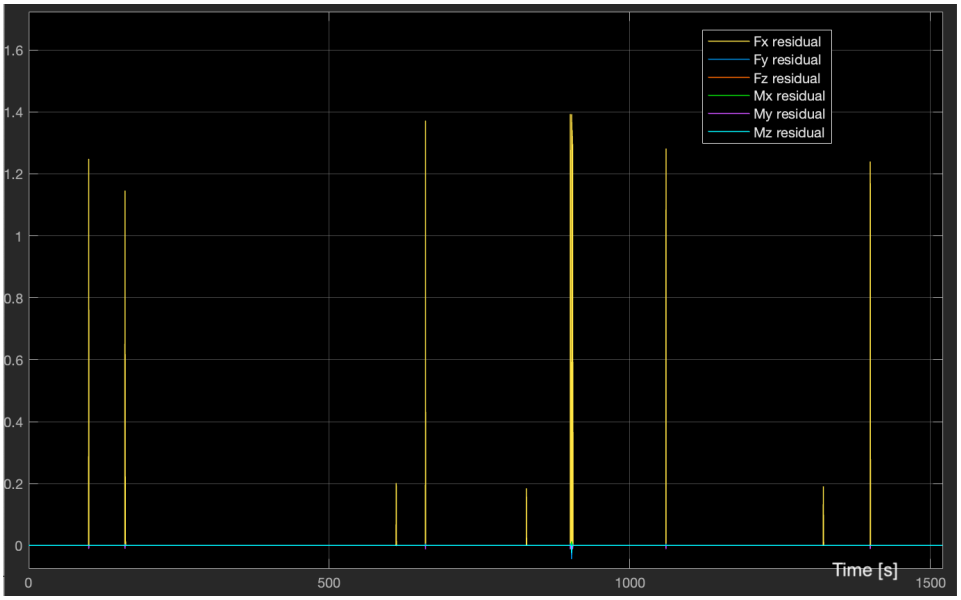

Figure 16.14: Residuals of the motor speed optimizer for the range mission.

In Figure 16.14, it can be seen that the optimizer uses low magnitude over actuation of the vehicle in certain timestamps, but otherwise the solution is usually found with no or minimal residuals. Moreover, the controller is tested in case of any single motor out conditions, and within the allowable CG range calculated in Chapter 11, and due to the used `lsqlin` solution solver, it does not feature any problems. Thus, these tests are deemed sufficient to verify and validate the controller model.

17 | Aircraft System Characteristics

This chapter aims to describe the characteristics of aircraft systems and the interactions between various components. At this early stage of the design process, only the general layout of the systems has been established.

In Section 12.1, the electrical system layout is presented grouping hardware components based on their connection to the power supply. A further description of onboard electronics and their interrelations is provided in Section 17.1. Having determined the hardware, the focus is placed on looking for software capable of achieving the required mission autonomously in Section 17.2. Also, due to the autonomy of the vehicle, communication with the ground station and other bodies must be ensured, adhering to *STK-EMS-2* requirement, which is explored in Section 17.3. Lastly, Section 17.4 evaluates the data handling and flow of information within the vehicle.

17.1. Hardware Block Diagram

In order to aid in creating an overview of the electronics onboard the aircraft, a hardware block diagram is created. The components are classified into the respective subgroups and relations with external parties are captured. In the diagram, arrows represent the flow of signals between components. Double-sided arrows indicate that both components send and receive signals whereas one-sided arrow means that one of the components is a messenger and the other is the receiver.

The central part of the hardware is a flight computer which controls the entire system. It contains different processing units to process visuals separately from critical autopilot processes, ensuring latency and delays in non-critical components do not influence real-time operations. Sensors, described in Table 17.1, gather data from the environment that is sent to the flight computer which processes them further and sends an actuation signal to electronic speed controllers (ESCs) which are derived from *STK-CLNT-2-MIS-2* requirement. Lastly, the ADS-B transceiver fulfills the function of communication with Air Traffic Control (ATC) and other aircraft, whereas the telemetry transceiver is used for communication with the moving ground station. The hardware layout is present in the block diagram shown

in Figure 17.1. Please note that colored blocks are used to indicate hardware tasked with similar functions, i.e. blue box labeled ”Communications” entails two transceivers with the function of data transfer with external parties.

Table 17.1: Sensors With Their Associated Requirements and Assessment of Redundancy

Sensor	Requirement	Redundancy
GNSS	STK-CLNT-5-MIS-1	Yes, 2 sensors are provided
Barometer	STK-CLNT-5-MIS-1	Yes, 2 sensors are provided
IMU (Accelerometer, Magnetometer, Gyroscope)	STK-CLNT-5-MIS-1	Yes, 3 sensors are provided
Vision Camera	STK-CLNT-5-MIS-2 STK-CLNT-3-MIS-2	Yes, LiDAR and Radar
LiDAR sensor		Yes, Vision Camera and Radar
Radar		Yes, LiDAR and Vision Camera
Airspeed Sensor	STK-CLNT-5-MIS-1	Yes, 2 sensors are provided
Ultrasound Water Level Sensor	STK-CLNT-10-MIS-1	Yes, Time-of-Flight multi-zone ranging sensor
Time-of-Flight multi-zone ranging sensor	STK-CLNT-9-MIS-1	Yes, Ultrasound Water Level Sensor

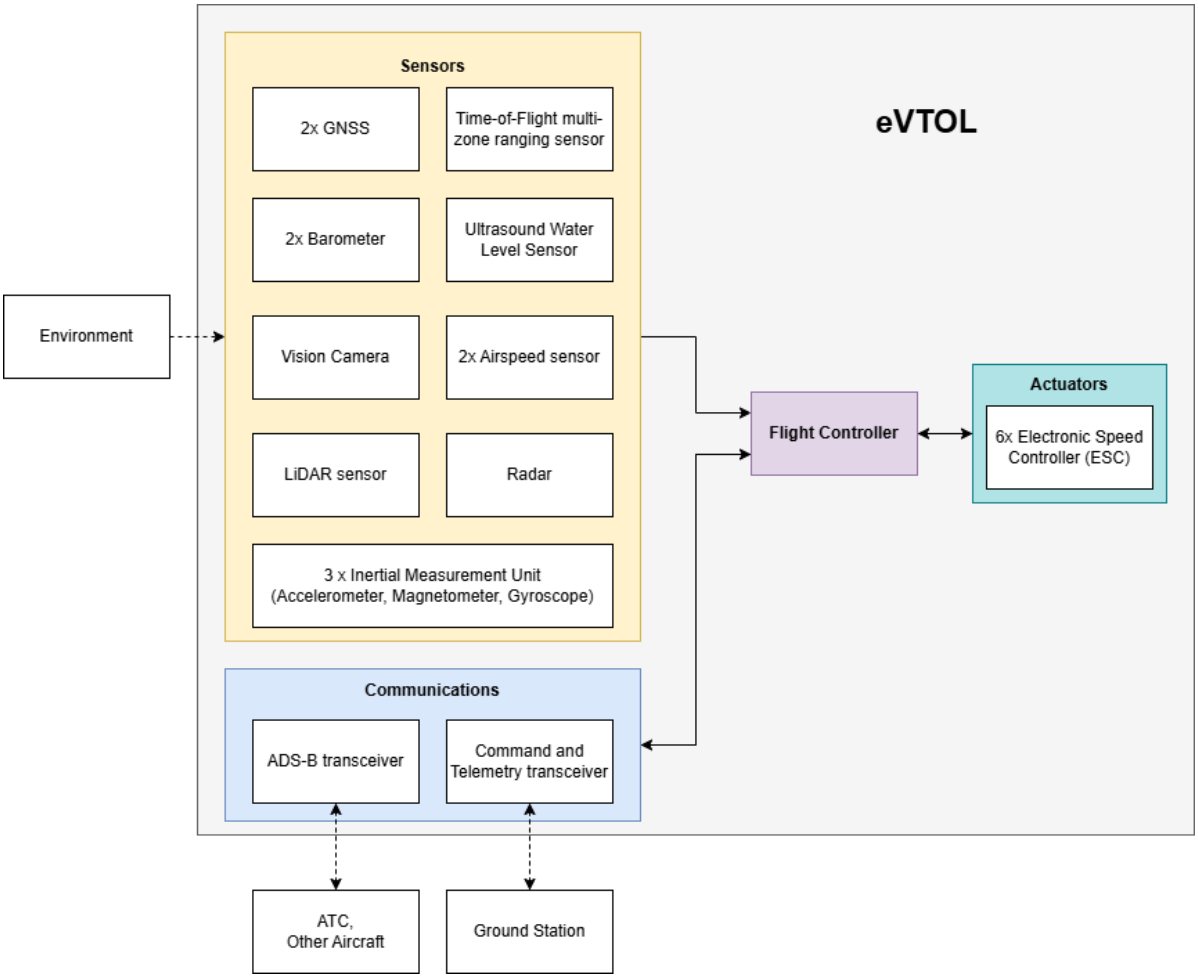

Figure 17.1: Hardware Diagram

17.2. Software Block Diagram

Due to the complexity of the flight software necessary for the operation of autonomous aircraft, it is instrumental to create a diagram that provides an overview of this system. Such an overview serves as a guideline for software engineers writing the code, encompassing different functionalities simultaneously. Despite the software overview given as a whole, it should be noted that some functions, such as image processing, are processed in separate computing units ensuring minimal delay in critical computations.

The flight software is divided into six layers, which comprise multiple modules. To handle the environment data, the Sensor Interface Layer handles the communications between the sensors and the rest

of the code. Then, the Data Processing Layer prepares the raw sensor information for further use. The Navigation and Control Layer uses said data to plan the flight and control it. Then, the output signals are sent to the Motor Control Layer, which interfaces with the electronic speed controllers (ESCs). The Communications Layer handles the data that are sent and received from ATC, other aircraft, or the moving ground station and exchanges it with the Navigation and Control Layer. Finally, the Safety and Redundancy Layer monitors the aircraft's state and handles unsafe situations. The Software Block Diagram is presented in Figure 17.2. In the diagram, the connections between the layers are shown and labeled with the data type exchanged.

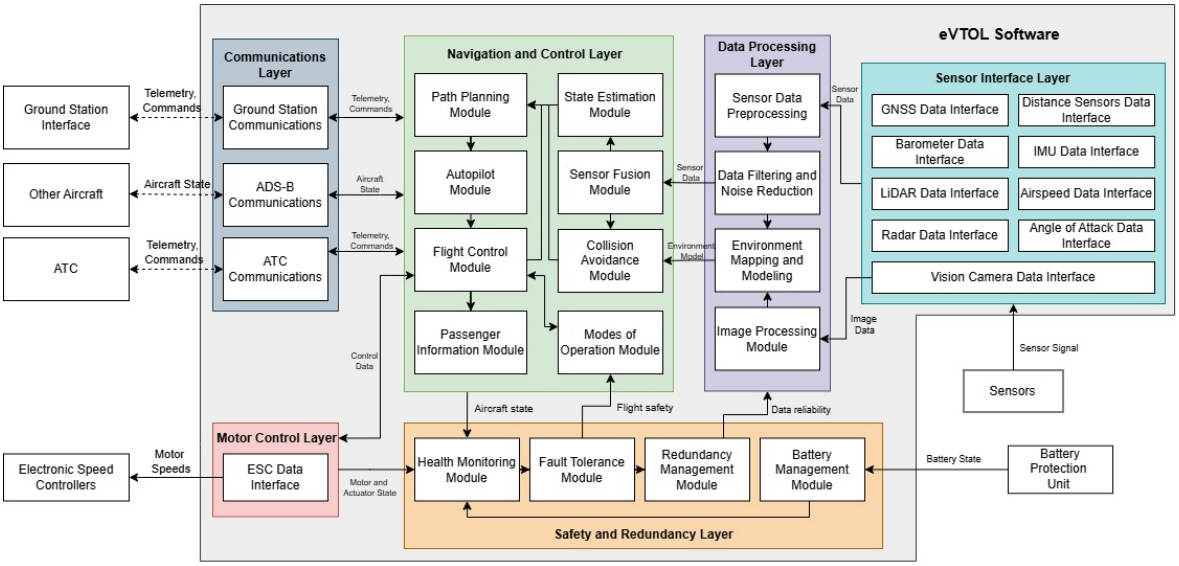

Figure 17.2: Software Block Diagram.

The modules inside the Sensor Interface Layer are device drivers to interact with the sensors, using a yet unknown communication protocol. These drivers then output the data to the Data Processing Layer. It contains the Sensor Data Preprocessing module, which samples the data, and the Data Filtering and Noise Reduction module. Moreover, it includes the Image Processing module which enables the Environment Mapping and Modeling module to create an environment model from the camera imagery, LiDAR, and Radar data.

The Navigation and Control Layer uses the said model to estimate if there is a need for a collision avoidance system to take action. Moreover, it combines the input from multiple sensor-processed data in the Sensor Fusion Module. Then, the combined data are used for estimating the current state of the aircraft, which is used by the autonomy-enabling Path Planning Module. The Autopilot Module determines the necessary heading changes or required altitude to fly, which is then fed to the Flight Control module that computes the required input to the motors and actuators. Additionally, the Modes of Operation module determines whether the aircraft is in the take-off, climb, cruise or hover mode, and the Passenger Information Module provides the necessary information, like remaining mission time, to the passenger in the Payload Bay.

The Communications Layer transmits the data about the aircraft state to other nearby aircraft, ATC, and the moving ground station. The ATC and Ground Station Communications modules also exchange aircraft commands with the Navigation and Control Layer whenever necessary.

Finally, the Safety and Redundancy Layer monitors the health of the overall aircraft, including checking the battery charge level, or the working condition of the motors. Any failures are handled by the Fault Tolerance Module which determines the action needed for safe operations under failure. Lastly, the Redundancy Management Module handles the failure of one of the redundant sensors used.

17.3. Communication Flow Diagram

Communication for autonomous vehicles is crucial for successful mission completion. The most important communication is between the vehicle and the ground station. Through that link, the ground station sends mission parameters such as target location or planned route, as well as other commands. The vehicle updates the ground component with its position, orientation, and velocity. It also transmits battery metrics from the monitoring system, safety warnings, and any visuals on the environment gathered during flight.

Not only is the vehicle in constant communication with the ground station, but it also sends its position, orientation, and velocity to other aircraft and ATC. ATC as a controlling body of the airspace, instructs the vehicle with no-go zones and altered routes avoiding any collisions. Lastly, other aircraft communicate their position, orientation, and velocity to the vehicle as an additional measure in avoiding collisions. All interrelations are captured on Figure 17.3.

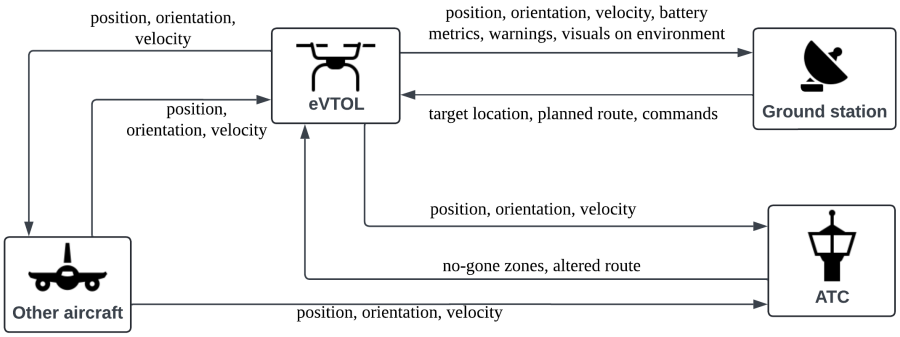

Figure 17.3: Communication Diagram

17.4. Data Handling Diagram

In the previous section, communication between the vehicle and external bodies is laid out. This section focuses on the data links between internal components and the information transferred between them. Figure 17.4 presents the diagram visualizing all the interactions considered. In the figure, arrows indicate the direction of data flow, whereas colored boxes entail hardware components tasked with similar functions, i.e. yellow box labeled ”Sensors” contains all sensors whose function is to collect data about the state of the vehicle and the environment.

As the main processing unit is the flight computer, all data is sent and redistributed through this component. The flight computer comprises a system processing unit, that analyzes the camera imagery and LiDAR data, and a flight controller that runs the low-level and safety-critical embedded code. All other components can be grouped into four categories: sensors, communications, actuators, and energy storage. Sensors are tasked with gathering data about the environment and the state of the vehicle allowing for its control and real-time path planning. This data is processed and sent through communications along with other metrics. Moreover, it serves to determine the magnitude of the PWM signal sent to ESCs controlling motor speed and torque. ESCs, similarly battery management boards, transmit fault signals through the flight computer to a telemetry transceiver that communicates with the ground station. The battery management systems inform the flight computer about the state of health and state of charge of batteries that is further passed to the ground station. Finally, based on sensor data, the flight computer sends information about the state of the vehicle to the telemetry and ADS-B transceivers. The telemetry transceiver transfers information about the target location, planned route, or other commands to the flight computer, whereas the ADS-B transceiver informs the flight computer about no-go zones and altered routes for the sake of collision avoidance.

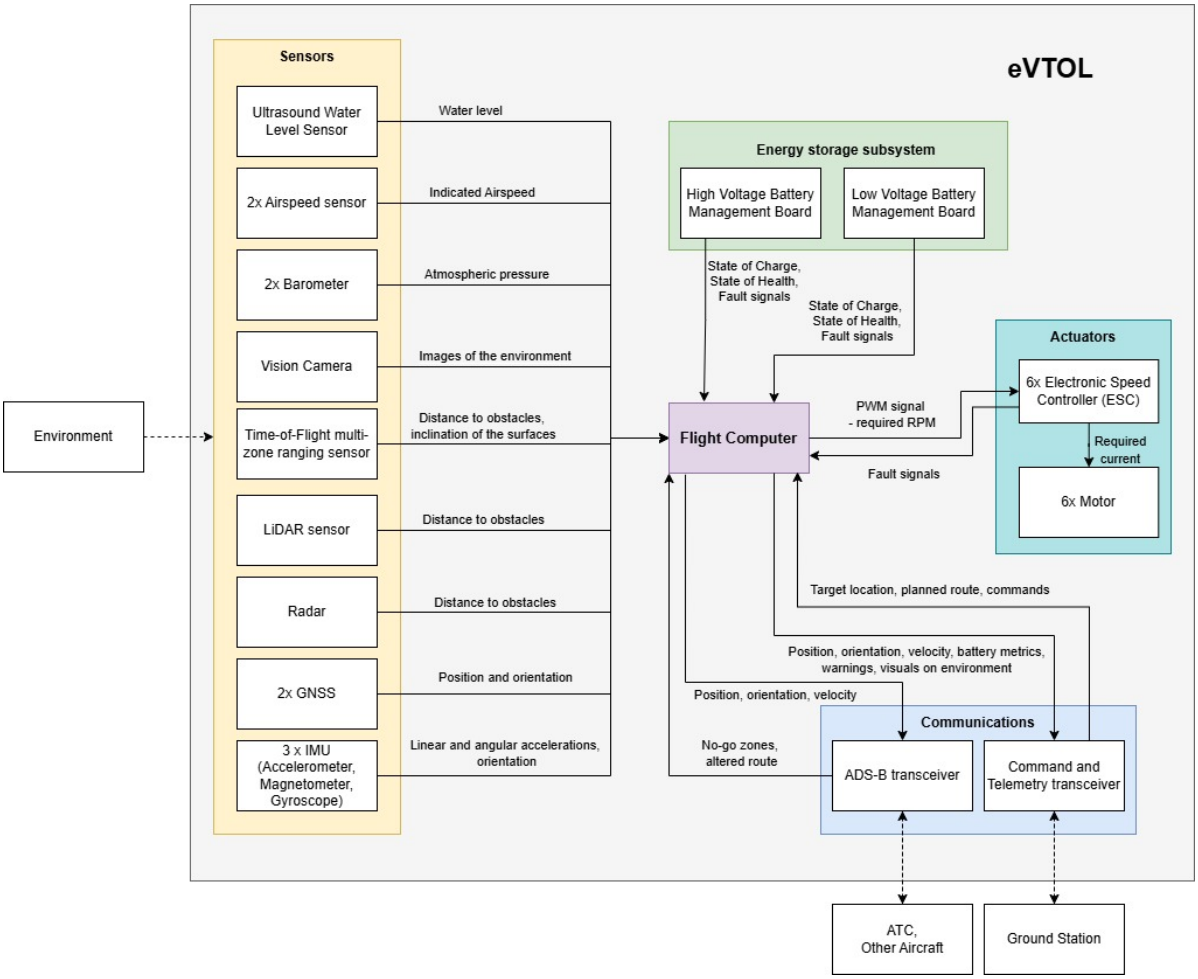

Figure 17.4: Data Handling Diagram

18 | Cost Analysis

This chapter presents the cost analysis conducted to estimate both the unit cost of the design and the operational cost of performing the range mission. In Section 18.1, the unit cost estimation model is presented, along with the relevant assumptions made. Later in Section 18.2 a similar layout evaluates the operational cost of the vehicle. In the cost breakdown diagram below, Figure 18.1 the cost components considered in the estimation are visualized.

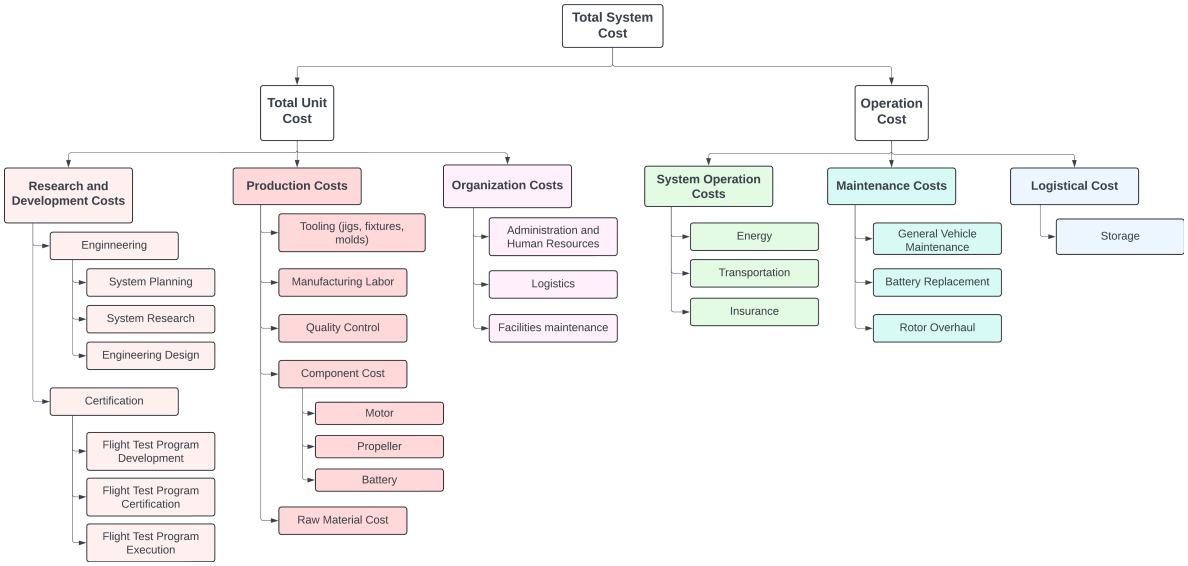

Figure 18.1: Cost Breakdown Diagram

18.1. Scope of Unit Cost Analysis

In this section, the scope of the unit cost analysis is established. The definitions of the cost components considered in the analysis are presented, followed up with the necessary inputs to carry out the procedure as well as the assumptions made.

Cost Breakdown

To analyze the cost of designing and manufacturing the vehicle, the Eastlake method for general aviation aircraft is adapted to eVTOL design, by considering their mission scope and mechanical complexity of them [73]. This method breaks down the total cost into individual components and provides statistical Cost Estimating Relationships (CERs), obtained by multi-variable least-squares regression, to estimate each cost element. These components are grouped into three categories: research and development, production, and organizational costs. The first two categories are evaluated under engineering and certification costs, and component and manufacturing costs respectively.

For costs directly tied to compensating human resources for their efforts, firstly the necessary man-hours required for constructing the design is estimated. These include engineering, tooling, and manufacturing costs, respectively C_{ENG}, C_{TOOL}, and C_{MFG}. Engineering cost entails the design cost associated with the vehicle. It includes the total cost of engineering the aircraft (C_{ENG}) which stems from the estimated engineering man-hours required to design the aircraft and perform the necessary RDT&E (H_{ENG}). The manufacturing cost encompasses all expenses associated with constructing the vehicle. It includes the cost of acquiring the necessary tools for manufacturing, which entails the cost of designing, fabricating, and maintaining tools, fixtures, jigs, molds, and other tools required to build the airplane (C_{TOOL}). Additionally, the total cost of manufacturing labor required to produce the aircraft (C_{MFG}) is considered under this category. The statistical estimation methods used for the estimation of these cost components are as follows:

$$H_{ENG} = 0.0396 \cdot W_{airframe}^{0.791} \cdot V_H^{1.526} \cdot N^{0.183} \cdot F_{CERT} \cdot F_{CF} \cdot F_{COMP} \cdot F_{PRESS} \cdot F_{MECH} \tag{18.1}$$

$$H_{TOOL} = 1.0032 \cdot W_{airframe}^{0.764} \cdot V_H^{0.899} \cdot N^{0.178} \cdot Q_m^{0.066} \cdot F_{TAPER} \cdot F_{CF} \cdot F_{COMP} \cdot F_{PRESS} \cdot F_{MECH} \tag{18.2}$$

$$H_{MFG} = 9.6613 \cdot W_{airframe}^{0.74} \cdot V_H^{0.543} \cdot N^{0.524} \cdot F_{CERT} \cdot F_{CF} \cdot F_{COMP} \cdot F_{MECH} \tag{18.3}$$

Where: W_{airframe} is the weight of the airframe, V_H is the maximum cruising speed, N is the number of units produced, F_{CERT} is a factor accounting for the relevant certification guidelines, F_{CF} is a complexity factor accounting for the flaps, F_{COMP} is a complexity factor accounting for the use of composites, F_{PRESS} is a complexity factor accounting for the cabin pressurization, and F_{MECH} is a complexity factor

accounting for the tilting mechanism.

$$C_{ENG} = 2.0969 \cdot H_{ENG} \cdot R_{ENG} \cdot CPI_{2012}^{2024} \tag{18.4}$$

$$C_{TOOL} = 2.0969 \cdot H_{TOOL} \cdot R_{TOOL} \cdot CPI_{2012}^{2024} \tag{18.5}$$

$$C_{MFG} = 2.0969 \cdot H_{MFG} \cdot R_{MFG} \cdot CPI_{2012}^{2024} \tag{18.6}$$

Where: R_{ENG} is the rate of engineering labor, CPI_{2012}^{2024} is the Consumer Price Index ratio of 2024 to 2012, accounting for inflation, R_{TOOL} is the rate of tooling labor, and R_{MFG} is the rate of manufacturing labor.

Another major component of the manufacturing cost is the cost of acquiring raw materials (aluminum sheets, pre-impregnated composites, landing gear, avionics, etc.) required to fabricate the airplane (C_{MAT}). Furthermore, the cost associated with ensuring quality control in manufacturing (C_{QC}) is part of the total manufacturing cost. This entails the cost of technicians and the equipment required to demonstrate that the product is being manufactured according to quality standards. The following statistical estimation methods are relevant to compute these components.

$$C_{QC} = 0.13 \cdot C_{MFG} \cdot F_{CERT} \cdot F_{COMP} \tag{18.7}$$

$$C_{MAT} = 24.896 \cdot W_{airframe}^{0.689} \cdot V_H^{0.624} \cdot N^{0.792} \cdot CPI_{2012}^{2024} \cdot F_{CERT} \cdot F_{CF} \cdot F_{PRESS} \tag{18.8}$$

The component cost comprises the total expenses for the motors (C_{PP}), rotors (C_{PROP}), battery (C_{BAT}), avionics (C_{AV}), and landing gear (C_{LG}) which are identified as the primary components influencing the overall component cost of eVTOLs. The following statistical estimation methods are relevant, with the powerplant cost adapted for electric motors [74]:

$$C_{PP} = N_{PP}\left(0.0022 \cdot P_{SHP}^3 - 0.4209 \cdot P_{SHP}^2 + 48.6 \cdot P_{SHP} + 1612\right) \text{ [74]} \tag{18.9}$$

$$C_{BAT} = m_{bat} \cdot E_{kg} \cdot C_{BAT_{Wh}} \tag{18.10}$$

Where N_{PP} is the number of motors, P_{SHP} is the shaft horsepower per motor, m_{bat} is the mass of the battery E_{kg} is the energy density of the battery in Wh/kg, $C_{\text{BAT}_{\text{Wh}}}$ is the cost of battery per Wh.

A distinction is made based on the type of rotor designed, whether it has a fixed pitch or constant speed. The following formulas are used for each type, respectively.

$$C_{FIXPROP} = 3145 \cdot N_{PP} \cdot CPI_{2012}^{2024} \tag{18.11}$$

$$C_{CSTPROP} = 209.69 \cdot N_{PP} \cdot CPI_{2012}^{2024} \cdot D_P^2 \cdot \left(\frac{P_{SHP}}{D_P}\right)^{0.12} \tag{18.12}$$

Where D_P is the diameter of the rotor in ft.

The fixed costs for avionics and landing gear price reduction for no retraction mechanism are shown below, as part of the component cost.

$$C_{AV} = 15000 \cdot F_{MECH} \tag{18.13}$$

$$C_{LG} = -7500 \tag{18.14}$$

Lastly, the cost associated with certification is considerable for the vehicle. Under this category, the total cost of completing the development of prototypes and certification flight-test program is considered (C_{FT}).

$$C_{FT} = 0.009646 \cdot W_{airframe}^{1.16} \cdot V_H^{1.3718} \cdot N_P^{1.281} \cdot CPI_{2012}^{2024} \cdot F_{CERT} \cdot F_{MECH} \tag{18.15}$$

$$\tag{18.16}$$

There is also a cost associated with the overheads, administration, logistics, human resources, facilities maintenance personnel, and similar entities required to support the development effort (C_{DEV}). This is regarded separately from the other four categories.

$$C_{DEV} = 0.06458 \cdot W_{airframe}^{0.873} \cdot V_H^{1.89} \cdot N_P^{0.346} \cdot CPI_{2012}^{2024} \cdot F_{CERT} \cdot F_{CF} \cdot F_{COMP} \cdot F_{PRESS} \tag{18.17}$$

Once these cost components are estimated, they are categorized into Non-Recurring Costs (NRC) and Recurring Costs (RC) to establish a total unit cost for each configuration. NRC includes everything regarding R&D and Certification efforts prior to the vehicle's entry into service, while RC includes all costs related to the production of one vehicle: including machinery production hours, material, etc. The unit cost of the vehicle is calculated using the following formulas.

$$C_{NR} = C_{ENG} + C_{DEV} + C_{FT} + C_{TOOL} \tag{18.18}$$

$$C_{UNIT} = \frac{C_{NR} + C_{MFG} + C_{QC} + C_{MAT}}{N} + C_{LG} + C_{AV} + C_{PP} + C_{PROP} + C_{BAT} \tag{18.19}$$

The above estimates are calculated in fiscal year 2024 dollars. To express the cost in euros, the following relation is used based on the currency exchange rate provided by the European Central Bank[1].

$$C_{UNIT}\,[€] = 0.92 \cdot C_{UNIT}\,[\$] \tag{18.20}$$

Estimation Inputs

The main driver of the aircraft's cost is its weight. The heavier the aircraft, the more material is needed to build it. Additionally, heavier aircraft tend to be more complicated to design, tool, and manufacture, and later on test and certify [73]. Thus, almost every cost component includes weight as a factor. The Eastlake method proposes using the weight of the airframe $W_{airframe}$ in pounds as an input, which is the empty weight without engines, avionics, seats, furnishing, or control systems. With the Class II weight estimation, the values of these components are available, allowing for a refined computation of the empty weight.

The next input in the cost estimation is the horizontal speed in cruise V_H, expressed in KTAS. It's a logical input, as higher speeds cause increased loading on the structure. Additionally, for higher speeds, the aircraft needs more precise tolerances and streamlined design, thus driving the cost[2].

To estimate the cost of the electric propulsion (C_{PROP}), the needed parameter is shaft horsepower per motor P_{SHP}, and the number of motors in the configuration N_{PP}. Additionally, the rotor cost depends on the type of rotor (fixed pitch or constant speed), and its diameter D_P expressed in feet. Moreover, the price of the battery is a significant part of the unit cost of an electric aircraft with the mass of the battery a driving input. These values are obtained from the performance analysis calculations in Chapter 7.

Lastly, the estimations use several *complexity factors* throughout the process. These complexity factors are adapted to the context of the cost estimation made for the eVTOLs designed for. As a fixed rotor hexacopter design is pursued the complexity factors regarding winged aircraft configurations and rotor tilting mechanisms are disregarded.

Constants and Assumptions

Several assumptions were made in order to estimate the unit cost of the vehicle. Among these assumptions is the total number of units of the vehicle produced N. In terms of the number of units sold [74] claims that selling below 450 units is not economically feasible due to the high RDT&E costs per aircraft. Since this number is often exceeded for most aircraft models [75], and within the scope of first order estimation, the aim is to manufacture and sell 2000 aircraft. This estimation is based on the

[1] URL `https://www.ecb.europa.eu/stats/policy_and_exchange_rates/html/index.en.html` [cited 16 May 2024]
[2] URL `https://www.australianflying.com.au/latest/cirrus-adds-speed-to-sr22` [cited 22 May 2024]

product's promising market potential and versatility, which increases the likelihood of dual uses. Moreover, it is assumed that 4 prototypes for testing and certifications are going to be built, as proposed by Eastlake. Lastly, the throughput time is assumed to be five years, again as a standard value in the Eastlake method [73].

Given the maximum altitude set in the mission profile, it is assumed that the cabin is not pressurized, which influences the complexity factor associated with cabin pressurization, F_{PRESS}. The estimation also takes into account the certification type of the aircraft, which for all configurations is assumed to be CFR Part 23 (equivalent to EASA CS-23 Small Aircraft). This dictates the complexity factor associated with certification, F_{CERT}.

Additionally, the cost of the aircraft is heavily dependent on the cost of engineering, manufacturing, and tooling labor. The book recommends an engineering hourly rate of 100$. For manufacturing and tooling, the average manufacturing wage in EU countries is considered, assuming production will take place within the EU. An hourly rate of $60 is considered for the latter two aspects respectively.

Furthermore, some assumptions were made to compute component costs for each vehicle. Estimation of the battery cost relies on the assumed energy density of 300 Wh/kg, and the cost of 1040 $/kWh[3]. Likewise, the estimation of the motor cost relies on the assumed number of motors which is 6 as presented in Chapter 10. Lastly, the shaft horsepower per motor is computed following the assumption that the maximum power required in the most power-intensive phase of the mission profile for each configuration is equally distributed between motors.

18.2. Scope of Operational Cost Analysis

In this section, the scope of the operational cost analysis is established. The definitions of the cost components considered in the analysis are presented, followed up with the necessary inputs to carry out the procedure as well as the assumptions made.

Cost Breakdown

To analyze the cost of operating the vehicle, a consistent approach to the unit cost assessment is followed, adapting the Eastlake method for general aviation aircraft to the eVTOL design [73]. Three cost components are identified under the branch of operational costs, system operation, maintenance, and storage costs all calculated annually.

The total cost of maintenance per year is further broken down to general maintenance, C_{AP}, estimated using a statistical relation between the ratio of total flight hours and required general maintenance, battery replacement, and overhaul. Within general maintenance, an additional cost component stems from vehicle inspection, C_{INSP}, which is the expenses incurred for assessing the condition, safety, and compliance of a vehicle with regulatory standards and operational requirements. The battery replacement cost, $C_{B,REP}$, refers to the total expense of purchasing, installing, and disposing of new batteries used in the aircraft's power system. Lastly, overhaul cost, C_{OVER}, refers to the total cost of detailed inspection and repairs for the airplane's rotors, as stipulated by the engine's required time between overhauls per year. The following formulas are used to quantify these cost elements.

$$C_{AP} = F_{MF} \cdot R_{AP} \cdot Q_{FLGT} \tag{18.21}$$

$$C_{B,REP} = \frac{B_m C_{kg} Q_{FLGT}}{F_{cycle} \cdot N_{cycles}} \tag{18.22}$$

$$C_{OVER} = 5 \cdot N_{PP} \cdot Q_{FLGT} \tag{18.23}$$

Where F_{MF} is the ratio of maintenance man-hours to flight hours, R_{AP} is the hourly rate of for a certified Airframe and Powerplant mechanic, Q_{FLGT} is the total annual flight hours, B_m is the mass of the battery, N_{cycles} is the number of discharge cycles, F_{cycle} the number of flight hours per cycle, E_{kg} the specific energy of batteries, and finally, N_{PP} is the number of rotors.

System operation entails energy consumed to fly the mission, transportation, and insurance. Energy consumption cost, $C_{B,ENERY}$ is the expense incurred for the energy required to operate a system or

[3]URL `https://youtu.be/HXx0dXJ47Mo` [cited 22 May 2024]

device. This is calculated based on the amount of energy used and the cost per unit of energy. The transportation cost, C_{TRANS} is estimated based on the maximum distance the vehicle travels on the ground per operation using a conventional petrol truck, assuming it operates in the Netherlands from the ground stations of the existing aerial rescue helicopters, as presented in Section 21.3. This is a conservative estimation because, with the vehicle's target unit cost, it is expected to become popular in the market, leading to more widespread coverage across nations. Additionally, given its short range, this will be the vehicle's ideal use case. Lastly, the cost of insurance, C_{INS} is estimated using a statistical relationship between the cost of the vehicle insured, taken as the unit cost. The following formulas are used to quantify these cost elements.

$$C_{B,ENERY} = DoD \frac{B_m E_{kg} C_{kWh} Q_{FLGT}}{F_{cycle}} \tag{18.24}$$

$$C_{TRANS} = \frac{Total_m}{N} \cdot (2 \cdot D_a vg) \cdot C_{truck} \tag{18.25}$$

$$C_{INS} = 500 + 0.015 \cdot C_{AC} \tag{18.26}$$

Where C_{kWh} is the cost of grid-line energy, DoD is the depth of discharge, $Total_m$ is the total number of missions performed by the fleet, N is the number of units of the vehicle produced, D_{avg} is the average distance traveled on the ground via transport one way for one mission, and C_{truck} is the cost of utilizing a transport truck of the intended dimensions per kilometer traveled.

Once these cost components are estimated, the yearly operation cost of the vehicle is calculated by summing the components. At this stage, a distinction is made between operations that require truck usage and those that are directly deployed from the storage facility. The following formulas are used to quantify the annual operational cost.

$$C_{YEAR} = C_{AP} + C_{STOR} + C_{INS} + C_{INSP} + C_{OVER} + C_{B,ENERGY} + C_{B,REP} \tag{18.27}$$

$$C_{YEAR,TRANS} = C_{YEAR} + C_{TRANS} \tag{18.28}$$

Later, this yearly cost is divided by the annual operation hours of a single vehicle to get the cost per flight hour. A better operational understanding can be achieved from the cost per mission performed, which is estimated subsequently.

$$C_{HR} = \frac{C_{YEAR}}{Q_{FLGT}} \tag{18.29}$$

$$C_{HR,TRANS} = \frac{C_{YEAR,TRANS}}{Q_{FLGT}} \tag{18.30}$$

$$C_{TOTAL_{MISSION}} = C_{HR} \cdot \frac{M_t}{60} \tag{18.31}$$

$$C_{TOTAL_{TRANSPORT}} = C_{HR,TRANS} \cdot \frac{M_t}{60} \tag{18.32}$$

The above estimates are calculated in fiscal year 2024 dollars. To express the cost in euros, the currency exchange rate provided by the European Central Bank is used[4].

Estimation Inputs

The vehicle's number of flight hours per year is a critical input for many of its operational cost components. This input drives the cost of maintenance, as there is a direct correlation between the extent of usage and the maintenance needs of the vehicle. This value is determined by carefully analyzing the market and assessing the total usage of air ambulances globally. With its unit cost and performance capabilities, the vehicle is estimated to be utilized as frequently, if not more so, than air ambulances once established in the market. To make a conservative estimation the number of passengers saved is taken as the current usage of air ambulances globally.

To estimate the cost of the overhaul of the rotors, the number of motors in the configuration N_{PP} is considered. Moreover to estimate the battery replacement cost within maintenance not only the mass of the battery was relevant, but the parameters that dictate its operation. Lastly, for general maintenance

[4]URL `https://www.ecb.europa.eu/stats/policy_and_exchange_rates/html/index.en.html` [cited 16 May 2024]

cost estimation, the hourly rate of a certified Airframe and Powerplant (A&P) mechanic is an input, for which the rate recommended book is taken with the inflation accounted.

Constants and Assumptions

Some assumptions were necessary to provide a reliable estimate of the unit costs. These include the total number of units of the vehicle produced N. For the unit cost analysis, this value is assumed to be 1000, as the annual flight hours are calculated based on the demand for air ambulances. Therefore, the dual-use capabilities of the vehicles are excluded from this analysis and the results only reflect the vehicles used for emergency response. In this regard, the total demand for air ambulances is assumed to be 550,000[5]. This is the total number of passengers saved globally using existing aerial emergency rescue vehicles.

For general maintenance cost estimations, the hourly rate of a certified Airframe and Powerplant (A&P) mechanic is assumed to be $ 50 in 2012, as recommended by the book. The ratio of maintenance man-hours to flight hours is estimated with several complexity factors, those that are only relevant to winged aircraft are disregarded for the estimation. Moreover, the annual vehicle inspection cost is assumed to be $500. These estimations were established in 2012, therefore, an inflation term of $CPI_{2012}^{2024} = 1.32$ is used as aforementioned before.

Battery replacement costs have several input parameters for analysis which are assumed consistently with those introduced in Chapter 12. These include C_B assumed to be $113 in 2024, N_{cycles} set at 1000, E_{kg} measured at 300 Wh/kg, and finally, DoD calculated at 0.8. For energy consumption calculations, the cost of energy is taken as 0.40$ − kWh which is the grid-line price cap in the Netherlands[6].

Additionally, for transportation costs, a kilometer rate of $ 1.6 is used[7]. As a first-order approximation, the transportation distance of 40 kilometers is considered as the average distance traveled on the ground via transport one way for one mission[8]. Finally, the cost of storage per month per vehicle is estimated to be $225 in 2012 as recommended by Eastlake, which adjusts to $500 when accounting for inflation.

18.3. Cost Estimates

The outlined process evaluates the costs associated with the design, taking into account the assumptions made for each cost component. In the context of operational costs, two final values are calculated: one includes the cost of transportation based on the average ground distance traveled, and the other assumes the emergency is within the maximum operational radius. The outcomes of the estimation, rounded to the nearest dollar/euro, are provided in Table 18.1 and Table 18.2.

[5]URL https://www.airambulanceworldwide.com/how-often-are-air-ambulances-used/ [cited 17 June 2024]

[6]URL https://www.government.nl/topics/energy-crisis/cabinet-plans-price-cap-for-gas-and-electricity [cited 16 June 2024]

[7]URL https://www.iru.org/news-resources/newsroom/european-road-freight-rate-benchmark-q4-2023-contract-market-holds-spot-market-plummets [cited 19 June 2024]

[8]URL https://venticare.nl/het-mobiel-medische-team-de-traumahelikopter-wat-voegt-deze-toe-2/ [cited 19 June 2024]

Table 18.1: Unit Cost Assessment

Parameter	Value
C_{ENG} [$]	2,034,763
C_{DEV} [$]	61,570
C_{FT} [$]	62,716,431
C_{TOOL} [$]	2,157,676
C_{MFG} [$]	50,618,423
C_{QC} [$]	6,580,395
C_{MAT} [$]	10,819,067
C_{CERT} [$]	66,970,440
C_{PP} [$]	16,296
C_{PROP} [$]	24,908
C_{BAT} [$]	32,370
$C_{TOTAL_{FIX}}$ [$]	131,793,089
$C_{TOTAL_{UNIT}}$ [$]	148,569
$C_{TOTAL_{UNIT}}$ [€]	138,169

Table 18.2: Operational Cost Assessment

Parameter	Value
C_{AP} [$/year]	4,337
C_{STOR} [$/year]	3,960
C_{INS} [$/year]	2,572
C_{INSP} [$/year]	500
C_{OVER} [$/year]	10,010
$C_{B,ENERG}$ [$/year]	11,952
$C_{B,REP}$ [$/year]	14,068
C_{TRANS} [$/year]	21,450
C_{YEAR} [$/year]	47,400
$C_{YEAR,TRANS}$ [$/year]	68,850
C_{HR} [$/hr]	142
C_{HR} [€/hr]	132
$C_{HR,TRANS}$ [$/hr]	206
$C_{HR,TRANS}$ [€/hr]	192
$C_{TOTAL_{MISSION}}$ [€/mission]	80
$C_{TOTAL_{TRANSPORT}}$ [€/mission]	116

When the unit cost is evaluated based on how well it aligns with requirement *STK-CLNT-20* a discrepancy of 15% is noted. Nevertheless, this does not render the design unfeasible. Discussions with clients reveal that this discrepancy is acceptable for pursuing the design option. The vehicle remains highly competitive in the market with this unit cost as the competition analysis highlights in Chapter 3.

Considering the current aerial emergency response market these results are highly promising. On average the operational cost of helicopters remains around the range of € 600 to € 1000 per flight hour. The design, with an hourly operational cost of € 132, is expected to excel in the market.

18.4. Sensitivity Analysis

In order to assess the sensitivity of the cost estimates to uncertain inputs, a sensitivity analysis is carried out regarding the aforementioned assumptions. In this section, the unit cost estimation model is analyzed first, followed by the operational cost model.

For the analysis of the unit costs, the Class II weight estimation output MTOM and battery weight, cruise speed of the vehicle, number of units produced, and number of prototypes built and tested are deemed the most uncertain inputs. For the assessment, all the inputs are increased by 10%, besides the number of prototypes which is increased by one (25%), and the number of units produced which is decreased by 10% to achieve a positive sensitivity. The analysis evaluates how much the total unit cost changes in percentage as well as in absolute difference as a response to this increase. The results of the analysis are presented in Table 18.3.

Table 18.3: Sensitivity analysis of the unit cost estimation method.

	Input Changed					
	MTOM [+10%]	**Cruise Speed [+10%]**	**Number of Units Produced [-10%]**	**Number of Prototypes [+25%]**	**Rate of Engineering Labor [+10%]**	**Rate of Manufacturing and Tooling Labor [+10%]**
Total Unit Cost Difference [%]	8.46	4.37	0.58	0.001	0.07	2.00
Total Unit Cost Difference [$]	12,575.46	6,492.51	2,970.30	2.47	104.21	2,970.30

The analysis yields a critical relation between the vehicle weight and unit cost. This is expected given the strict relationship an aircraft's weight has with its cost. As mentioned in Section 18.1 the amount of material required to build an aircraft increases with its weight. In addition, the design, tooling, manufacturing, testing, and certification processes for heavier aircraft are typically more complex. Thus,

weight is a factor in almost all cost components and a change in weight is carried forward to the unit cost almost linearly. Furthermore, both cruise speed and rate of manufacturing and tooling labor are identified to be driving inputs of the estimation result. However, the number of units produced, the number of prototypes tested, and the rate of engineering labor remain uncritical. The change in unit cost due to changes in these inputs is strictly less than 1%.

Acknowledging the sensitivity of the cost criterion to MTOM, it is recommended to re-evaluate the unit cost of the vehicle if further iterations of the design are performed at later stages. These iterations may also change the cruise speed of the flyer, necessitating a new estimation of the unit cost for the next design iterations.

For the analysis of the operational costs the cost per mission excluding transportation costs is assessed. Mission time, the ratio between total demand and number of units produced, the price of the battery per kilo, and the number of discharge cycles for one battery are deemed the most uncertain inputs for this estimation. For the assessment, all the inputs are increased by 10%, besides the ratio of demand and units produced which was decreased by 10% to achieve a positive sensitivity. The latter indicates a scenario when there is too little demand for a large number of supply. The results of the analysis are presented in Table 18.4.

Table 18.4: Sensitivity analysis of the operational cost estimation method.

	Input Changed			
	Mission Time [+10%]	**Ratio of Demand and Units produced [-10%]**	**Price of the Battery per kilo [+10%]**	**Number of Discharge Cycles [+10%]**
Total Cost Per Mission Difference [%]	3.02	7.75	2.97	2.52
Total Cost Per Mission Difference [$]	2.43	6.22	2.38	2.02

The results of this analysis indicate that the operational cost is most sensitive to the ratio of demand and units produced, resulting in a change of around 8% of the mission cost. This result is expected as there are only a few components to quantify the mission costs, and most are highly correlated with the annual flight time of a vehicle driven by this ratio. The remaining inputs still show a considerable change in the estimate, deeming that the inputs considered for this sensitivity analysis are critical for the model used.

Recognizing the sensitivity of the model, it is recommended to re-evaluate the operational cost of the vehicle if more clarity regarding these inputs is achieved at any stage of the design.

18.5. Verification and Validation

In addition to the sensitivity analysis, the cost estimation model undergoes verification through unit tests to ensure the absence of negative costs. These tests also replicate sample calculations from the book [73] and compare the results to confirm the accurate implementation of the method. Additionally, an analysis of gradual changes to input values confirms no sudden output fluctuations.

The Eastlake method is considered already validated, as it is established as an industry standard, and originates from methods developed by Cessna. Nevertheless, this method is not designed for eVTOL configurations. Thus, a comparison with the eVTOL database, prices is performed.

In the scope of the unit cost estimation validation, publicly available data regarding vehicle costs is scarce as most competitors are still in the concept or prototype stage. Thus, a comparison with the following models is pursued: Ehand 184, Jetson One, Ryse Recon. It should be noted that the unit price calculated is not equal to the retail price of these vehicles. Thus, validation is considered sufficient at this design stage if the order of magnitude of the prices match. The results are presented in Table 18.5.

Table 18.5: Unit Cost Validation

Vehicle	Retail Cost [k$]	Unit Cost Difference [%]	Unit Cost Difference [k$]	Remarks
IUVO	140-160	-	multicolumn1c|-	Payload mass: 95kg, Cruise Speed: 120km/h, Range: 30km
Jetson One[9,10]	90-110	-33.3	-50	Payload mass: 95kg, Cruise Speed: 100km/h, Range: 32km
Ryse Recon[11]	160-170[12]	10	15	Payload mass: 115kg, Cruise Speed: 65km/h, Range: 40km
Ehang 184[13]	200-300[14]	66.6	100	Payload mass: 100kg, Cruise Speed: 100km/h, Range: 30km

As can be seen from the table the unit cost estimate of the vehicle is within acceptable margins of the retail price estimates of the competitive eVTOLs in development when an order of magnitude assessment is performed. All models, the design is validated against, are octocopters, which justifies the positive difference in unit cost to an extent. Moreover, as discussed earlier, these retail prices are still approximate. In conclusion, the model is sufficiently valid within the scope of establishing a preliminary cost estimate.

As for validating the vehicle's operational cost, a comparison is made with general eVTOL operation assessment in the industry. Extensive research has been conducted on the operations of eVTOLs, with analysis revealing cost predictions around $2.25 per seat-mile[15]. This corresponds to € 1,30 per one kilometer traveled per passenger. These results have been criticized by several researchers, engineers, and enthusiasts. Overall, a concrete conclusion regarding eVTOL operational costs has not been reached[16]. Despite this, with a passenger-kilometer cost of € 2.66 the estimated operational cost of the design is around similar orders of magnitude to these publicly available estimates.

19 | Technical Resource Budgets

In aircraft development, some resources (like mass or power) have a tendency to grow during the development, while driving the product cost [3]. One way to counter this is to set up an initial limit to the resource, that is carefully managed throughout the design process. Then, this limit can be distributed between the subsystems to form a budget. This section describes the said limits imposed. As the budgeting values of production aircraft are seldom publicly available, low-fidelity assumptions and a common sense approach are placed.

Firstly, the budgeted resources are identified. In aerospace projects, it is common to budget mass, energy, and computational power between subsystems [76]. Nevertheless, budgeting computational power is omitted as each subsystem can be equipped with a separate computing unit that satisfies its computational needs. Additionally, it is decided that cost and design time are other resources important to the technical resource budget.

In the initial design phase, resources are budgeted based on the engineering judgment and cross-

[9]URL https://jetson.com/jetson-one&90-110 [cited 24 June 2024]
[10]URL https://jetson.com/news/price-increase-for-new-clients [cited 23 June 2024]
[11]URL https://ryseaerotech.com/ [cited 24 June 2024]
[12]URL https://www.futurefarming.com/tech-in-focus/drones/video-this-mega-drone-puts-farmers-in-the-pilots-seat/ [cited 23 June 2024]
[13]URL https://www.ehang.com/ehangaav/ [cited 24 June 2024]
[14]URL https://www.dronethusiast.com/ehang-184-is-a-manned-uav-you-will-never-get-to-fly/ [cited 23 June 2024]
[15]URL https://www.ainonline.com/news-article/2021-11-15/counting-cost-urban-air-mobility-flights. [cited 15 June 2024]
[16]URL https://venticare.nl/het-mobiel-medische-team-de-traumahelikopter-wat-voegt-deze-toe-2/ [cited 19 June 2024]

references to the existing vehicles, as explained in the Baseline Report [77]. The resulting estimations are provided in Table 19.1.

Table 19.1: Initial Technical Resources Budget Allocation per Subsystem.

Subsystem	Mass		Power		Cost		Design time	
	Fraction of the total	Value [kg]	Fraction of the total	Value [kW]	Fraction of the total	Value [k€]	Fraction of the total	Value [work hours]
Propulsion	0.10	32	0.98	14.70	0.25	30	0.15	420
Payload Bay	0.30	96	0.00	0	0.05	6	0.05	140
Control	0.05	16	0.015	0.23	0.18	21.6	0.3	840
Structure	0.30	96	0.00	0	36	43.2	35	980
Energy Storage	0.20	64	0.00	0	0.15	18	0.1	280
Landing gear	0.05	16	0.005	0.08	0.01	0.6	0.05	140
Total:		320		15		120		2800

In the further design stages, resources are estimated using more refined methods. Mass is budgeted based on the class II weight estimations presented in Chapter 8. Following the calculations from Chapter 12, the estimations of the energy use per subsystem could be derived. As the total cost is the stakeholder requirement, the fractions per subsystem are based on the estimate of combined development and production costs for medium-product series [78]. Finally, the design time fractions are adapted based on the subsystem importance in the design [3]. The total development time is determined as the project man-hours devoted to technical work on the design approximated to be 2/3 of the total project time.

Table 19.2: Technical Resources Budget Allocation per Subsystem

Subsystem	Mass		Power		Cost		Design time	
	Fraction of the total	Value [kg]	Fraction of the total	Value [kW]	Fraction of the total	Value [k€]	Fraction of the total	Value [work hours]
Propulsion	0.26	110	0.98	6.53	0.33	46	0.15	420
Payload Bay	0.24	100	0.00	0	0.05	7	0.05	140
Control	0.02	11	0.02	0.16	0.15	21	0.25	700
Structure	0.09	39	0.00	0	0.20	28	0.25	700
Energy Storage	0.29	123	0.00	0	0.25	35	0.1	280
Landing gear	0.09	40	0.00	0	0.02	3	0.05	140
Total:		421		6.69		138.169		2800

Table 19.2 presents the technical budget for all aspects described beforehand. Due to the preliminary stage of the design implying some uncertainty, the values are estimations that are subject to refinement in the future. The main conclusion from the budget allocation is that the propulsion subsystem is the most energy-hungry subsystem having substantial cost and mass associated with it. A lot of development time is put into the structural design of the vehicle and its control, whereas the energy storage subsystem is costly and heavy despite its relatively short development time.

Moreover, it can noticed that there are many differences between the initial budget (Table 19.1) and latter estimations (Table 19.2). It can be concluded that cost was initially underestimated with a deviation of 12.5%, whereas mass with a deviation of 30%, compared to the latter estimations. On the other hand, power was overestimated by more than 50%. Finally, no changes are experienced in estimations of design time, as the methodology remained the same. All in all, the comparative analysis of the budgets concluded that the results obtained initially are significantly different from the ones obtained with refined methods.

20 | Technical Risk Assessment

In this chapter, the most relevant technical risks (TRs) associated with the autonomous eVTOL emergency response hexacopter are identified. The definitions used to evaluate the probability of occurrence for each risk (P) in an average mission are shown in Table 20.1, as well as the severity of consequences for each risk (C), in Table 20.2.

Table 20.1: Probability of Occurrence in an Average Mission

Score	Probability	Description
1	p<1%	Very Unlikely
2	1%≤p<10%	Unlikely
3	10%≤p<40%	Likely
4	p≥40%	Very likely

Table 20.2: Severity of Consequences

Score	Consequence
1	Minor; Minor effect to mission
2	Moderate; Moderate effect to mission
3	Critical; Significant threat to mission
4	Catastrophic; jeopardizing whole mission

The severity of each risk is computed according to Equation 20.1.

$$\text{Risk} = \text{Probability} \cdot \text{Consequence} \tag{20.1}$$

In Section 20.1, the probability and consequence of each risk are evaluated. Due to the severity of the same risks, mitigation and contingency methods are introduced and elaborated on in Section 20.2. The risks will decrease in consequence and probability level post-mitigation.

20.1. Pre-Mitigation Risks

Each risk is identified and its probability together with the consequence is assessed. Based on its probability and consequence, a color indicating its risk is assigned. The risks are further elaborated on through the risk map in Table 20.4. The summary of all risks can be found in Table 20.3. The risks that are considered fall under the following categories: passenger influencing/caused risks, object-identification/maneuvering risks, system failure risks, structural risks, electronics & energy risks, flight performance & power risks, environment/weather risks, and operational/logistical risks.

Table 20.3: Pre-mitigation Technical Risk (TR) Identification. Each technical risk is described and assigned probability (P), as well as consequence (C).

TR nr	TR Name	Description	P, C
		Passenger influencing/caused risks	
1	Human Injured	Injuries due to impact during landing before boarding, injuries due to maneuvers and landing while inside, personnel injuries during (un)hinging/assembling from the rotors	2, 4
2	Motion Sickness of the Person	Disturbances and maneuver forces and displacements may threaten temporary health (triggered by low-frequency vertical, lateral, angular, rotary motion to which the passenger has not adapted[79])	3, 1
3	C.G. Shift Due to Passenger Movement	Passenger moves (voluntarily standing up or is shifted due to the maneuvers) such that the C.G. location displaces during boarding or flight	4, 2
		Object-Identification/ Maneuvering Risks	
4	Collision with Obstacle During Flight	Scraping wall, roof, trees, etc., completely impacting small objects that appear suddenly, or as a result of it being the best possible flight path (note that misjudgment of path plan is separately mentioned in TR-5)	2, 4
5	Path Planning Failure	Objects are seen but unjustly neglected by the path planning algorithm, objects are not observed during flight (only objects that have been in the vision for long enough to be input into the path planning algorithm, else it is related to TR-4), path planning identifies possible route/landing but it exceeds possibilities (e.g. greater slopes than 12-degrees)	3, 3
6	Control System Failure	Bias/error in state estimation, inaccurate portrayal of the vehicle's situation within the control loop system (due to changed situation or initial mistakes)	2[1], 3
		System Failure Risks	
7	Rotor Failure	One rotor inoperative condition as a result of impact (connection with TR-4) or powertrain failure (connection with TR-8)	3, 4

Continued on next page

[1] Bias/Error is more likely to occur. P and C would be around 4 and 2, but other case is more critical risk in this criteria

Table 20.3: *Continued from previous page*

TR nr	TR Name	Description	P, C
8	Powertrain Failure (HV)	Part of the powertrain (one of the battery systems) fails as a consequence of combustion, exposure to damaging chemical, impact damage, etc.	2, 4
9	Landing Gear Failure	Dimensional problems causing tipping over or scraping of other, no possible landing with auto-rotation or approach angle of attack, take-off causes crashing, natural frequency (resonance) causes interference with rotors	3, 3
10	Motor failure	One of the motor fails resulting in partial loss of thrust.	2,4
		Structural Risks	
11	Structural Failure of the Main Frame	Maximum load factor is exceeded, material/structure has failure related to fatigue or frequent use, load type is incorrectly disregarded or forgotten during design stage	2, 4
12	Structural Degradation Under Weather Requirements	Degradation due to rain, smoke, ash presence or -50 to 50 degrees Celsius temperature range.	2, 3
13	Maximum Load Factor Exceeded for a Structural Component	A maneuver is performed that is safe in any other regards (for passenger and electronics) but not for a component (which is not part of the mainframe)	2, 4
		Electronics & Energy Storage Risks	
14	Sensor Failure	Positioning, acceleration, orientation, angular rate, object detection, airspeed or environment (water, wind, temperature etc.) sensor failure	3, 4
15	Electronic Component Failure (LV)	Transceivers (ADS-B, Telemetry) fail and do not work,	2, 4
16	No Localization Signal for a Prolonged Time	Vehicle passes signal denied environment in relation to GNSS or any other localization signal	3, 3
17	Battery Auto-Ignition / Overheating	Improper thermal management, extreme heats (50 degrees Celcius), a battery comes into contact with auto-ignited battery or burning refrigerant and overheats	2, 4
18	Short Circuit	Electrical short circuit occurs (in regard to exposure to water)	3, 3
		Flight Performance & Power Risks	
19	Running Out of Battery Power During Take-Off/Landing	During the less than 7 seconds of take-off/landing battery power runs out	2, 4
20	Running Out of Battery Power During Cruise	During cruise at cruise altitude of mission being performed battery power runs out	2, 4[2]
21	Payload Exceeds the Design Weight	Passenger exceeds the design payload weight of 94.5 kg and therefore surpasses power taken onboard for the mission and estimations regarding control, the passenger might not fit (comfortably) in the cabin	3[3456], 4
		Environment/Weather Risks	
22	Lightning Strike Damage	Damage to/interferences with electronics/avionics, damage to structure and passenger	1 7[80], 4

Continued on next page

[2]The consequence is greater for lack of battery during cruise than during take-off/landing due to altitude, despite them being catastrophic.

[3]The range of BMI classified as obese is 30<bmi<40 (42.4% of the population), the range morbidly obese is bmi>40 (9.2% of population). As such more than 10% of population weights more than the calculated BMI of 34.7 for a passenger with of average height and with the design weight (94.5 kg)

[4]URL `https://ourworldindata.org/human-height` [cited 13 June 2024]

[5]URL `https://www.who.int/news-room/fact-sheets/detail/obesity-and-overweight` [cited 13 June 2024]

[6]URL `https://www.niddk.nih.gov/health-information/health-statistics/overweight-obesity` [cited 13 June 2024]

[7]URL `https://aerocorner.com/blog/do-planes-get-struck-by-lightning/` [cited 13 June 2024]

Table 20.3: *Continued from previous page*

TR nr	TR Name	Description	P, C
23	Damage During Landing in Difficult Conditions	Damage to structure and passenger caused by slopes less than 12-degree angles, dry sand, sudden small drops after having landed or half a meter of water	4[8], 3
24	Bird Strike	Bird hits any part of the vehicle	3, 3[9]
25	Significant Wind, Turbulence and Gust Causes Instability	Wind, Turbulence and gust instabilities are caused during cruise but especially during hover or landing, therefore allowing for tipping over or incontrollability	3, 3
Operational/Logistical Risks			
26	Too High Noise Emission in Urban Areas	Vibrations or other noise-causing mechanisms (mostly rotor-related) threaten quality of life or health of surpassing area's citizens (as prescribed in the requirements based on health journals)	3, 2
27	Vehicle Cost Exceeding the Budget	Manufacturing, maintenance, material or component costs exceed the technical budget and contingency assignment	4, 2
28	Certification Failure	Flyer is uncertifiable due to unconventional design, mix between similarities and differences to certifiable aircraft causes unclear requirements, amendments are made to the certifications and have not been designed for	3, 3
29	Exceeding Truck Dimensional Requirements	Transportation cannot be done due to exceeding regular truck dimensional requirements for US and EU roads	4, 3
30	Exceeding Allowable Assembly Time	Assembling an/or tilting all the necessary mechanism safely (according to a safety booklet provided post-DSE) to allow for deployment in 30 minutes by two people is not met	4, 2

To aid in identifying the most detrimental risks, the risk impact on the project is visualized on the risk map shown in Table 20.4.

Table 20.4: Pre-Mitigation Technical Risk Map

Consequence \ Probability	1 - Very Unlikely (<1%)	2 - Unlikely (1-10%)	3 - Likely (10-40%)	4 - Very Likely (>40%)
4 - Catastrophic	TR-22	TR-1, TR-4, TR-8, TR-10, TR-11, TR-13, TR-15, TR-17, TR-19, TR-20	TR-7, TR-14, TR-21	
3 - Critical		TR-6, TR-12	TR-5, TR-9, TR-16, TR-18, TR-24, TR-25, TR-28	TR-23, TR-29
2 - Moderate			TR-26	TR-3, TR-27, TR-30
1 - Negligible			TR-2	
Risk Magnitude	Low	Moderate	High	Very High

This map shows that the most detrimental risks (top-right) are related to the safety of the passenger, the aircraft, and generally, the mission. The most vital risks to consider (highest risk value) are human injury during the rescue, collision with an obstacle during flight, running out of battery during flight, sensor failure, rotor failure, and exceeding truck dimensional requirements. They are deemed most consequential and likely as without mitigation/contingency they lead to the project's futility or mission failure.

[8] The high probability without mitigation is due to the fact that the landings required by the mission are harsh (compared to the ones regular missions need to account for).

[9] remote areas are prone to wildlife and vehicle is moving fast (32 m/s)

20.2. Post-Mitigation Risks

Implementing mitigation strategies is intended to shift the risks toward the bottom-left of the risk map, reducing both their likelihood and impact. The possible correction strategies used are:

- **Reduce:** The risk will be reduced by taking actions to reduce the probability of occurrence or the severity of consequences.
- **Transfer:** The risk will be transferred to another party, such as a supplier or insurance company.
- **Accept:** The risk will be (partly) accepted, and no further action will be taken.
- **Avoid:** The risk will be eliminated by completely removing/avoiding the action/component causing the risk.

The strategies are either for mitigation or contingency. Mitigation is done by taking preventative actions, if this is not possible contingencies plan for when the action does occur. Note that different strategies are used in combination as part of risk mitigation/contingency management. In Table 20.5, the mitigation/contingency strategies are elaborated in detail. Most detrimental risks are reduced by introducing redundancies in the system, increasing design margins, using different materials, and, therefore, ensuring aircraft safe operation. It can be noticed that, despite some mitigation strategies implemented, the risk probability or consequence score has not changed for some of the risks. This stems from the fact that each score is awarded for a range of values, as described in Table 20.1. Thus, while the risk probability or consequence is reduced with the mitigation/contingency measure the percentage remains within its initial range, concealing the reduction in it.

Table 20.5: Correction strategies with mitigation and contingency plans for each risk together with associated probability (P) and consequence (C).

TR nr	Correction	Mitigation	Contingency	P,C
Passenger-influencing / passenger-caused risks				
1	Reduce (Ioana)	Verification of obstacle avoidance algorithm/ verify & validate machine vision detection of humans to detect more than 95% of time before coming within 4 m distance; clear audio instructions for the rescued person (e.g. for using of protective gear for the rescued person, like seat belts as they reduce crash-related injuries by half[10]); choose landing location based on probable disturbances (s.t. gust will not influence safe landing); land with a maximum speed s.t. acceleration experienced by the passenger will never be higher than 5g[11]; adding safety instruction for pre-deployment activities, implementing protective rotors/place rotors & their rotation plane out of reach of the passenger	Add part of an emergency kit (part that be self treated to payload bay and design payload bay to prevent further injuries to the rescued person	2, 2
2	Reduce (Sara)	Increase the stability of the aircraft (less oscillations), Incorporate a close control loop (for overcoming drastic effects of instability)	Prepare motion sickness medication for passenger, have laying down or sitting position with glass or opening in the line of sight into the horizon[12]	2, 1
3	Reduce (Sara)	Precise passenger placement in the cabin through seat belt; place the hold close to aircraft C.G.; design for a wide stability range	Adjust control loop such that it can still react to sensor inputs with a displaced C.G.	2, 1
Object-Identification / Maneuvering Risks				

Continued on next page

[10] URL `https://www.hg.org/legal-articles/seatbelts-on-ambulances-to-protect-first-responders-49091` [cited 11 June 2024]

[11] URL `https://mtg-aviation.com/g-forces-human-limit` [cited 13 June 2024]

[12] URL `https://www.webmd.com/first-aid/how-to-beat-motion-sickness` [cited 13 June 2024]

Table 20.5: *Continued from previous page*

TR nr	Correction	Mitigation	Contingency	P,C
4	Reduce (Miłosz)	Employ and verify obstacle avoidance algorithm; recognize obstacles bigger than rotor radius with an accuracy of 95% of the time within the time frame s.t. actions to avoid it can be taken; use reliable sensors	Use a sturdy structure that can withstand light collisions; protect rotors with ducts	2, 3
5	Reduce (Miłosz)	Implement additional flight-planning algorithms for cross-validation if they both then detect different things, take conservative approach	See TR-4	2, 3
6	Reduce (Miłosz)	-	Implement redundancy in the control mechanism; ensure the flyer can operate safely with a complete failure of one control mechanism; Set bigger minimum margins for error in the control algorithm (more conservative flight)	2, 3
System Failure Risks				
7	Reduce (Bartłomiej)	-	Including redundancy for controlled landing in rotor configuration decision (4 coaxial rotors or > 4 rotors, consider permanent or variable tilting) to ensure redundancy; implement and verify control algorithms for asymmetric engine placement in regard to all six DOF; Ensure safe landing with one rotor out (with the use of that control algorithm)	2, 3
8	Reduce (Jakub)	-	Draw power from remaining battery modules or use an emergency backup system that supplies power to flight control and avionics to land safely (see TR-7); design for Autorotation capability; divide the battery into multiple independent systems to ensure redundancy	2, 3
9	Reduce (Gabriel)	Use a durable and fatigue-resistant material; include a safety factor during design	Perform an emergency landing without the landing gear	2, 3
10	Reduce (Bartłomiej)	Tilt the rotors to maintain controllability around all six degrees of freedom; adjust the controller	-	2,2
Structural Risks				
11	Reduce (Maciej)	Perform regular inspection and maintenance using Non-Destructive Testing (NDT); implement safety factors in structural analysis (unless other is specified SF=1.5); use metals instead of composites for the sake of early warning of high loads occurring in the structure	-	1, 4
12	Reduce (Gabriel)	Use anti-corrosive paint; add cleaning against ash or filtering for earlier smoke presence to maintenance booklet, prepare outer design against critical temperature range; add temperature management system for inside the fuselage	-	2, 3

Continued on next page

Table 20.5: *Continued from previous page*

TR nr	Correction	Mitigation	Contingency	P,C
13	Reduce (Gabriel)	Implement safety factors in structural analysis in the design process (unless other is specified SF=1.5)	Employing fail-safe structural design (redundant structural components); use metals instead of composites for the sake of early warning of high loads occurring in the structure	1, 4
Electronics & Energy Storage Risks				
14	Reduce (Jakub)	Multi-sensor Fusion, Redundant sensors, real-time monitoring	Allow for remote control of the aircraft	3, 2
15	Reduce (Jakub)	-	Employ redundancy in the system; use fault detection and monitoring systems to identify electronic failures; maintain an inventory of spare electronic components for quick replacement	2, 3
16	Reduce (Miłosz)	-	Use alternative navigation systems (inertial navigation system, radar, LiDAR, vision-based navigation); use local radio frequency beacons or transmitters installed at known locations within the operating area; implement an advanced autonomous decision-making system capable of adapting to changing environmental conditions and lack of GNSS	3, 2
17	Reduce (Jakub)	Splitting the battery into multiple independent modules for increased redundancy	Have a firewall between passenger/flight computer and batteries	1, 3
18	Reduce (Domen)	Implement water-proof casing	apply parallel circuits, Implement circuit isolation.	2, 2
Flight Performance & Power Risks				
19	Reduce (Naomi)	Include a safety factor when sizing the battery; monitor battery levels and provide real-time alerts	Design to be able to land without battery power (e.g., with a parachute)	2, 4
20	Reduce (Domen)	Include a safety factor when sizing the battery, abort the mission at battery power needed for emergency landing	Design to be able to land without battery power (e.g., with a parachute)	1, 3
21	Reduce/Avoid (Ioana)	Use sufficient safety factors to account for overweight cargo (Reduce); implement weight checks before the flight (Avoid)	Facilitate enough take-off power for rescue (power available margin with respect to the maximum power required during mission); only allow passenger with reduced range (can be an intermediate waiting location during vehicle charging) to establish landing safely	3, 3
Environment / Weather Risks				
22	Avoid / Reduce / Transfer (Jakub)	Avoid flying through clouds (where 96% of lightning strikes occur) (Avoid) [80], have a thick enough exterior to prevent damaging interior (Reduce), protect electronics within an enclosure, apply surge suppression devices (against damaging surges or transients) (Reduce), only buy/obligate manufacturers to have protected-against-lightning verification for their devices(Transfer)	Use conductive material or embed isolating material with conductive layer to safeguard the aircraft's exterior (lower voltages will be present, better grounding capability are observed as the electricity flows in and out of the skin faster[81]), after suspicion or occurrence of lighting strike perform special inspection on its next check	1, 3

Continued on next page

Table 20.5: *Continued from previous page*

TR nr	Correction	Mitigation	Contingency	P,C
23	Reduce (Gabriel)	Develop a control algorithm to ensure the smoothest landing possible, with real-time ground surveying, etc.; include high-quality suspension in the landing gear; design landing gear appropriately (see TR-9 and TR-11)	-	2, 3
24	Avoid / Reduce (Sara)	Avoid flying near parks, nature reserves, wetlands, bird sanctuaries and known migration passages (Avoid), train vision learning to recognize birds far enough that the attainable moment set can avoid the strike (see TR-2) (Reduce	Bird resistant design (reinforced hub, windshield wiper for windows, ducts for rotors), for more see TR-4.	2, 2
25	Avoid / Reduce (Maciej)	Avoid areas behind irregular terrain and man-made obstacles by flying in front of the obstacle or preferably above it (with clearance) if possible (where mechanical turbulence occurs [13])(Avoid), Detect turbulence pattern in clouds (Reduce), account for gust forces in design (be controllable and landable under produced forces and moments) (Reduce)	Do not fly when the wind and gust forces/moments exceed the design gust forces/moments	3, 2
Operational / Logistical Risks				
26	Reduce (Naomi)	Choose different airfoil in new iteration; choose a different number of blades on the rotor in new iteration; increase design flight altitude	Perform noise assessment before reiterating final design and measure noise during validation of the design	2, 2
27	Reduce (Domen)	Implement smaller contingencies (forcing the design team to reconsider costly decisions earlier in the design process); allocate part of the budget as a contingency reserve; adopt cheaper material if both materials are acceptable; avoid complicated/costly mechanisms if not detrimental to the mission (rotating mechanisms in thrusters, hydraulic pistons in landing gear, etc.)	Negotiating the cost limit; relocating funds from other areas of the project; seek additional funding to cover the cost overrun	3,2
28	Reduce (Buse)	Make sure to state all relevant regulations at the beginning of the design process; increase relevant margins; limit amount of hinges/joints	Mediate leniencies regarding regulations derived from other types of airplanes as a result of the differences between them and the design of an eVTOL (not a simple rotorcraft) and an emergency responder. Also, create an not fully autonomous version (e.g. with remote control of the aircraft or redesign for piloted version) to start operations before autonomous system certification	2, 3
29	Reduce (Ioana)	Apply folding or detaching mechanism to booms to rotors, have a customized truck with non-rigid walls (curtains) to limit the need of clearances		2, 3

Continued on next page

[13] URL `https://www.weather.gov/source/zhu/ZHU_Training_Page/turbulence_stuff/turbulence/turbulence.htm` [cited 14 June 2024]

Table 20.5: *Continued from previous page*

TR nr	Correction	Mitigation	Contingency	P,C
30	Reduce (Buse)	Limit amount of mechanisms unless necessary to the mission, train assemblers by highly skilled and specialized mechanics	Mediate the extension of allowable assembly time, or do software checks during transport	3, 2

A new risk map is made using these new scores and post-mitigation effects can be viewed in Table 20.6. From the figure, it is noticeable that the most critical risks were successfully mitigated as they are shifted to the bottom-left corner.

Table 20.6: Post-Mitigation Technical Risk Map

Consequence \ Probability	1 - Very Unlikely (<1%)	2 - Unlikely (1-10%)	3 - Likely (10-40%)	4 - Very Likely (>40%)
4 - Catastrophic	TR-11, TR-13	TR-19		
3 - Critical	TR-17, TR-20, TR-22	TR-4, TR-5, TR-6, TR-7, TR-8, TR-9, TR-12, TR-15, TR-23, TR-28, TR-29	TR-21	
2 - Moderate		TR-1, TR-10, TR-18, TR-24, TR-26	TR-14, TR-16, TR-25, TR-27, TR-30	
1 - Negligible		TR-2, TR-3		
Risk Magnitude	Low	Moderate	High	Very High

21 | Sustainability Approach

During the design of the product, the future of the product and its effect on society should be derived and adverse effects should be minimized. That leads directly to the definition of sustainability: “the ability of a concept to be maintained at a certain rate or level”.[1] For a sustainable development the “concepts” considered are concerning the needs of a current and future generation as described in the United Nation’s (UN) Sustainability Development Goals (SDG)[2] The approaches can be divided into three pillars of environmental, social, and economic sustainability, as shown in Section 21.1. Afterwards, the three pillars of sustainability are assessed within each discipline and the design choices made regarding them are elaborated upon, in Section 21.2.

21.1. The 3 Pillars

For each of these pillars, associated disciplines and SDGs are as follows:

- **Environmental Sustainability**
  Associated disciplines: Aerodynamics, Materials & Structure, Control, Stability & Autonomy, Power & Propulsion
  7. Avoid non-renewable energy sources and limit energy use to cyclic production possibilities[2]
  7. Limit all waste and avoid harmful waste completely[2]
- **Social Sustainability**
  Associated disciplines: Materials & Structure, Power & Propulsion, Control, Stability & Autonomy
  3. “Ensure healthy lives and promote well-being for all at all ages”[2]
  11. “Make cities and human settlements inclusive, safe, resilient and sustainable”[2]
- **Economic Sustainability**
  Associated disciplines: All disciplines

[1] URL `https://www.oed.com/dictionary/sustainability_n?tl=true` [cited 08 May 2024]
[2] URL `https://sdgs.un.org/goals` [cited 01 May 2024]

8. “Promote sustained, inclusive and sustainable economic growth, full and productive employment and decent work for all”[2]

For economic sustainability, the market’s stability and growth must be ensured. This is done in the market analysis as long as the budget is met, in Chapter 3, where future growth is also envisioned through the possibility of expanding the eVTOL’s use cases. Finally, as mentioned in the risk assessment there are mitigation and contingency methods for meeting the budget. These are with limiting costs of especially mechanisms and materials.

21.2. Discipline-related Design Influences

In each of the disciplines design choices influencing the three pillars are made. The decisions range from method choices, to material choices and range from disciplines such as Power & Propulsion to Aerodynamics.

21.2.1. Power & Propulsion

Environmental Sustainability

The energy usage of eVTOLs has little to no adverse effect on current emission levels as the energy is generated through renewable means (such as hydro-electric power plants) [82, 83]. Currently, in the United States of America, the electric grid is not completely renewable; despite that, the use of batteries releases less CO_2 than that of fossil fuels.[3] Due to the not completely green electric grid, it is still helpful for the product’s sustainability contribution to limit energy use. Little hover time, lightweight design and green electrical grid contribute positively to limiting energy use[84]. The lightweight design is further discussed in the discipline of material & structures, in Subsection 21.2.2. Considering or creating a cleaner energy grid is out of the scope of this project, especially since the operational location will determine the energy grid. Regarding hover time, as a result of the short range and cruise speed, hover time is the majority of the mission. This is especially the case for the productivity mission. Despite this fact, high maneuverability affects the hover time, as is further discussed in Subsection 21.2.3.

Without considering the battery, operations have the most environmental impact, then production, then end-of-life; each phase reduces the impact by one order of magnitude[85]. Therefore, the previous paragraph discussing energy levels during operation is of great importance. When battery manufacturing is included, the impact of production increases greatly; battery production becomes the most constraining environmental sustainability aspect. For every kWh of energy produced by a battery, a third of the emissions can be attributed to battery production.

Unfortunately, other energy systems aside from batteries are considered unfeasible. The battery options are Li-ion (Lithium-ion), Li-S (Lithium-Sulfur) and Solid state. Considering production is the most constraining phase, the following aspects were looked at: the use of cycle life, climate change, human toxicity, metal resource depletion and photochemical oxidant formation, following [86]. “Climate change” most likely considers CO_2 emitted, water needed directly, transportation of water to often dry locations, chemicals used, waste incl. toxic created during mining and CO_2 emitted during manufacturing[3]. Despite the other options having promising advantages regarding both performance and sustainability upon further research, Li-ion batteries are the only ones that are feasible and on the market. In case any of the other battery options enter the market, the trade-off must be reconsidered along with the aforementioned environmental aspects, beneficial lessened cost and the social sustainability aspects discussed in the same subsection however in two paragraphs.

Moreover, lithium has limited raw material sources as well as a lack of a circular economy developed, hence depleting resources [87]. Laws and regulations on circular economies will change in 2026 in the European Union[4]. The laws and regulations will not influence the design initially since the product is made for the US market. However, the change in laws and regulations will likely create a positive momentum for research and other laws which cause an easier obtainment of more environmentally sustainable materials in regard to circular economies. These laws will also apply in case the product is introduced later in the European market. Laws and regulations on circular economies will introduce the

[3] URL https://climate.mit.edu/ask-mit/how-much-co2-emitted-manufacturing-batteries [cited 02 May 2024]

[4] URL https://www.amnesty.org/en/latest/news/2022/03/eu-batteries-will-need-to-comply-with-new-human-rights-and-green-rules [cited 01 May 2024]

need for end-of-life procedures as well. In case battery materials can be recycled and possibly used to make new batteries, they have an additional positive trait of lowering production impact.

Social Sustainability

A less obvious, but important aspect of batteries is the social sustainability in regards to human right violations.,[5,3] Once again most lithium-ion batteries do not outperform lithium-sulphur or solid-state batteries in terms of social sustainability when child labor, corruption and forced labor are considered [86]. To allow for improvement in social sustainability, companies should be screened and their transparency rated during acquisition.

21.2.2. Materials & Structures

Environmental Sustainability

As aforementioned little hover time, lightweight design and green electrical grid contribute positively to limiting energy use[84]. The lightweight design derives not only from optimisation, in Chapter 8, but also during the trade-off when the calculated MTOW of the multicopter configuration is significantly lower than for other configurations. Another way to need less energy has been considering different positioning of the booms, by bringing them closer to the fuselage boom less material is to be manufactured and weight is lessened by more than 10 kg (see Section 14.3 and Section 14.2).

For the stages of the life cycle material extraction, manufacturing emissions, as well as emissions during end-of-life, are taken into account. The full analysis can be viewed in Section 21.3. Aside from these emissions, the recyclability possibilities of the materials themselves should also be taken into account. As specified in the requirements, material and component choices should be made with the goal of being able to recycle 90% of the aircraft's weight, as that is the level of recyclability of other aircraft.[6] Especially steel and aluminum already present this capability as they are currently recyclable up to 90 and 95% in the transport industry [88]. Even magnesium recyclability is also on the rise especially in automotive and aerospace industries[89], although it is not used for our design. Carbon fiber, on the other hand, is hard to recycle, actually ending up on landfills, and is, therefore, limited to only the propeller blades [7]. Another less expected effect on environmental sustainability is that recycling saves up to 20 times (between 60-95%) of the energy needed compared to the extraction of those metals from ores whilst preserving the quality [88].

As to not need additional material Non-Destructive Testing (NDT) shall be performed for the structural testing as much as certification and other needs allow.

Social Sustainability

As seen in the aluminum and iron/steel industries, and similar to the aforementioned battery acquisition, material choices can have detrimental effects on the people having to acquire or work on them. Their extraction is again limited to specific regions. Especially with the rise in the demand for materials, industries of e.g. EVs lack to oversee the ethical problems going during the extraction, or even manufacturing of products.

21.2.3. Control, Stability & Autonomy

Environmental Sustainability

Autonomy leads to the design of the vehicle having lower weight as no pilot is needed, consuming less energy per trip and, therefore, also needing a smaller battery than other eVTOLs. For design considerations, the level of precision of the autonomous system leads to efficient flying, reducing waste like noise pollution [90]. The autonomous system should therefore be simulated to quantize how well it can find the optimized safe route.

Furthermore, great controllability leads to high maneuverability. High maneuverability, with ranges of attainable moments found in Chapter 16, allows for the ability to avoid obstacles and land faster while

[5] URL https://www.business-humanrights.org/en/from-us/media-centre/manufacturing-of-electric-vehicle-batteries-riddled-by-human-rights-violations/ [cited 01 May 2024]

[6] URL https://kpmg.com/ie/en/home/insights/2024/03/circularity-in-flight-fs-aviation.html [cited 01 May 2024]

[7] URL https://www.ethicallyengineered.com/is-carbon-fiber-eco-friendly/ [cited 19 June 2024]

doing so. This decreases hover time and therefore energy needed, as aforementioned in Subsection 21.2.1.

Social Sustainability

The primary mission of the emergency response flyer is to transport people to proper equipment and/or out of unsafe areas. This is inherently an improvement in social standards, especially for those in remote areas or areas otherwise unreachable. People in remote, inaccessible areas do not have the same possibilities for healthcare nearby as others have, but can with the implementation of autonomous rescue eVTOLs improve their healthcare possibilities. For transporting civilians or medical professionals, autonomy is important and implemented as it will require no flying skills from the passenger.

The social sustainability aspect is also impacted by the possibilities for landing. Providing healthcare opportunities for people from different locations and backgrounds creates a more inclusive society and brings equal rights. Moreover, social sustainability is improved by increasing the amount of operating vehicles. To increase the number of vehicles, price is limited. Depending on pricing, vehicles can be implemented for the public as ambulances; the social addition of the vehicles is then heightened.

Smaller impacts on social sustainability include passenger comfort and safety from the aforementioned lessened noise pollution and stability/controllability of the eVTOL.

21.2.4. Aerodynamics

Although aerodynamic importance is minimal compared to winged designs, it influences environmental sustainability. Throughout the design phase drag is minimized whilst lift, within reasonable bounds, is optimized. As a result, less thrust is needed and energy is saved. Less energy needed during the mission allows for less energy charging from the grid and a smaller battery (less battery mass).

The main aerodynamic lift is created by the rotor blades. It is therefore important to properly validate its design. The blade design, especially due to the twist, is unique. The main ways to verify/validate rotor blade design are through wind tunnel testing or use of validated CFD software. Depending on the model that needs to fit in the windtunnels, power needed varies. Therefore one of the four prototypes should be on a smaller scale to be able to use a smaller wind tunnel, like the low-speed wind tunnel from TU Delft (525 kW power needed)[8]. The energy needed has an environmental effect; since it is of significant level its use should be limited unless CFD software does not give satisfactory detail.

21.3. Life Cycle Assessment

Electric flight has been a focal point of research for several years, particularly in the context of urban air mobility through VTOL applications. These innovations promise significant time savings and reduced carbon emissions, making them a key area of interest for sustainable transportation solutions. For regional travel, eVTOLs consume 77% less CO2 than average helicopters, 46% less than petrol cars, 44% less than diesel cars. On the other hand, they are less sustainable compared to ground transport alternatives that rely on similar powertrains such as electric cars and trains. [91] This positions eVTOLs in a critical space for ensuring sustainability in transportation, offering significant benefits in reducing global carbon dioxide emissions for use cases where ground transport is not an option, such as aerial emergency response.

In this section, a life cycle assessment evaluates the sustainability of the design beyond its operational aspects, providing a comprehensive assessment of the design's overall sustainability. In effect, the life cycle assessment accounts for the material extraction, manufacturing, transportation step of the operations, and end-of-life phases of the vehicle.

Material Extraction

The first phase is the extraction of the materials. The materials used per component and their mass are shown in Table 21.1.

[8] URL https://www.tudelft.nl/lr/organisatie/afdelingen/flow-physics-and-technology/facilities/low-speed-wind-tunnels/low-turbulence-tunnel [cited 12 June 2024]

Table 21.1: Material and Mass per Component

Component	Material	Mass [kg]
Fuselage	Aluminum 7075	38.56
Structural Booms	Aluminum 7075	25.00
Rotor Ducts	Aluminum 7075	10.00
Rotor Blades	Carbon fiber	6.00
Landing Gear	Stainless Steel AISI630	40.00

Since each material has their own extraction method, their carbon footprint differ. Table 21.2 shows the CO_2 emission for each material when 1 kg is extracted.

Table 21.2: CO_2 Emission and Energy Consumption per Material

	Aluminum 7075	Carbon fiber	Stainless Steel AISI630
CO_2 Emission [kg/kg material]	12.7 [92]	20 [93]	2.21 [94]

Based on the above two tables, this results in a total CO_2 emission of 1142.612 kg for the extraction of the materials required for the vehicle.

Manufacturing

The production of a lithium-ion battery has a CO_2 emission of 73 kg/kWh[9]. As determined in Section 12.2, the energy required for the high voltage battery system is 29.3966 kWh and 0.560625 kWh for the low voltage battery system. This results in a total CO_2 emission of 2186.877 kg for manufacturing the battery.

For the manufacturing of the vehicle, different techniques are used, resulting in different CO_2 emissions. Table 21.3 shows the average CO_2 emission per technique for 1 kg material.

Table 21.3: CO_2 Emission per Manufacturing Technique

Manufacturing Technique	CO_2 Emission [kg/kg material]
Rubber forming	0.143 [95]
Extrusion	0.68[10]
Resin Transfer Molding (RTM)	2.641 [96]

Taking into account all techniques used for each material results in a total CO_2 emission of 67 kg for manufacturing the vehicle. However, it should be noted that factors such as assembling have not been considered for this analysis.

Combining both manufacturing processes results in a total CO_2 emission of 2253.877 kg for the manufacturing phase.

Transportation

The vehicle is transported from the storage facilities to the emergency site using a street-legal transport truck compliant with EU and US regulations. With environmental sustainability goals in mind, preference is given to an electric truck for transportation. However, since this decision is ultimately left to the operator, a life cycle assessment is also conducted encompassing conventional trucks.

To estimate the average distance traveled by ground transport to the disaster zone, the coverage intended by the Netherlands emergency response helicopter ground stations is used as a reference. In the Netherlands, four ground stations span the entire country, with a maximum coverage range of 90 kilometers. Assuming a design-intended coverage radius of 15 kilometers, the maximum ground transportation distance of 75 kilometers is assessed. However, further evaluation of the vehicle's mission and capabilities reveals that having more widespread stations with reduced ground transport requirements is optimal for the product. Thus an average ground transportation of 30 kilometers is established.

According to the International Council on Clean Transportation, urban delivery trucks with a 4x10 axle configuration that relies on petrol emit around 307 gCO2/t-km carbon dioxide while transporting one

[9]URL https://www.changeit.app/blog/2021-03-26-environmental-impact-of-lithium-batteries/ [cited 18 June 2024]

tonne of goods for a kilometer [11]. For the maximum ground transport distance from the ground stations of the existing aerial response vehicles, the total emission for each mission is 46 kilograms. For the average ground transport distance of 30 kilometers, this value reduces to 18 kilograms.

In any case, using electric trucks mitigates the majority of the CO_2 emissions from this phase. Therefore, the team strongly encourages all operators of the vehicle to opt for electric ground transportation.

End-of-Life

As stated before, the recyclability is expected to be 90%. This means, that in the future, less CO_2 needs to be emitted during the material extraction phase.

Conclusion

From this analysis, it is evident that using a petrol truck significantly contributes to the total CO_2 emissions during the transportation phase. Conversely, opting for an electric truck shifts the highest contribution to the total CO_2 emissions to the manufacturing phase. Combining all phases and considering an electric truck is used, results in a total CO_2 emission of 3396.489 kg across its entire lifetime. If operations prefer to use a petrol truck, an additional 20 to 50 kilograms of emissions per mission per vehicle is expected. Assuming that the vehicle performs around 5000 missions across its lifetimes transportation would increase the total CO_2 emission by 100000 kg. Thus the vehicle itself in comparison to other conventional transport options has a low CO_2 emission across its lifetime and to preserve this electric truck transportation is advised for operators.

22 | Future Development of the Project

This chapter aims to describe the actions regarding further product development after the end of DSE. Firstly, the flow chart of the planned activities is created, capturing the logical order of them and their interrelations as described in Section 22.1. Secondly, the timeline is developed and presented as a Gantt chart in Section 22.2.

22.1. Post-DSE Work Flow Diagram

After DSE is finished, the design stage is yet preliminary as high-fidelity tools were not used extensively for aerodynamic, structural, and control design. Therefore, the team efforts are to be focused on performing detailed design of subsystems allowing for developing refined CAD models and control simulation. If the design performance is satisfactory, optimization takes place with additional operational assessments. Finally, compliance with internal and external requirements is verified, followed by the design of autonomous control software.

Once the design is finished, the first prototypes are to be manufactured, requiring preparations of facilities, as well as tools. Also, materials and pre-made parts need to be brought from external suppliers allowing for prototype assembly. Having the prototype finished, its testing can resume. Firstly, subsystem tests are performed, followed by ground tests of the vehicle. Finally, flight testing is carried out, allowing for the start of the long certification process.

After the vehicle is certified, aircraft production starts posing logistical challenges of preparations of tools and facilities, acquisition of material and parts, and assembly of the aircraft. Also, certification is the start of commercial operations including sales and customer assistance, per the business model proposed in Subsection 3.4.3. It is decided to provide customers with several support schemes concerning maintenance, truck service, and customer service. Assistance is also provided with decommissioning the aircraft, proposing recyclable end-of-life solutions, or disposal of recyclable parts in a sustainable manner.

Once an aircraft has entered the market, the market might have changed slightly. Therefore afterwards assessment of other existing solutions is conducted in order to identify innovative improvements to the

[11] URL https://theicct.org/publication/co2-emissions-from-trucks-in-the-eu-an-analysis-of-the-heavy-duty-co2-standards-baseline-data/ [cited 18 June 2024]

design. To decide whether discovered improvements are worth investigating, market analysis is carried out outlying the market gap to be filled.

All activities are summarized and their interrelations are displayed on page 115.

22.2. Post-DSE Gantt Chart

This section focuses on the timeline of activities described in Section 22.1. It should be mentioned that time estimations provided in the section result from the engineering judgment rather than a thorough analysis of a product and its functioning in the market. The Gantt chart is presented on page 116.

Post-DSE Work Flow Diagram

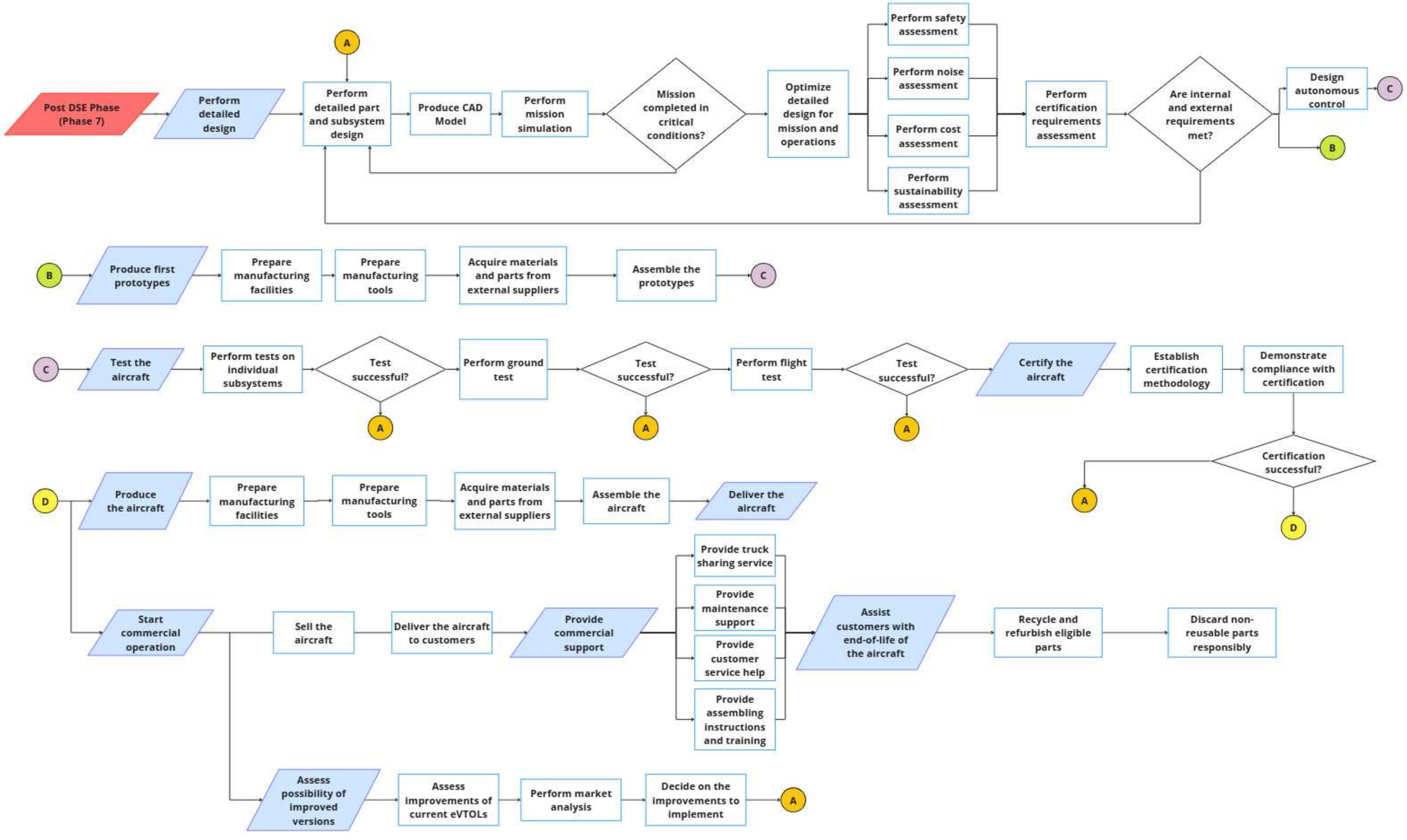

Post-DSE Gantt Chart

ID	Task Mode	Task Name	Duration	Start	Finish	Predecessors
1		**Perform detailed design**	**480 days**	**Tue 18-6-24**	**Mon 20-4-26**	
2		Perform detailed part and subsystem design (incl. CAD modelling)	12 mons	Tue 18-6-24	Mon 19-5-25	
3		Perform mission simulation	12 mons	Tue 20-5-25	Mon 20-4-26	2
4		Optimize detailed design for mission and operations	12 mons	Tue 21-4-26	Mon 22-3-27	1
5		Produce prototypes	300 days	Tue 23-3-27	Mon 15-5-28	4
6		**Test the aircraft**	**360 days**	**Tue 16-5-28**	**Mon 1-10-29**	**5**
7		Perform tests on individual subsystems	6 mons	Tue 16-5-28	Mon 30-10-28	
8		Perform ground test	6 mons	Tue 31-10-28	Mon 16-4-29	7
9		Perform flight test	6 mons	Tue 17-4-29	Mon 1-10-29	8
10		Certify the aircraft	33 mons	Tue 2-10-29	Mon 12-4-32	6
11		Certify the aircraft	0 days	Mon 12-4-32	Mon 12-4-32	10
12		Produce the aircraft	12 mons	Tue 13-4-32	Mon 14-3-33	10
13		**Start commerical operation**	**240 days**	**Tue 13-4-32**	**Mon 14-3-33**	**10**
14		Sell the aircraft	12 mons	Tue 13-4-32	Mon 14-3-33	
15		Deliver the aircraft to customers	0 days	Mon 14-3-33	Mon 14-3-33	14
16		**Provide commercial support**	**2160 days**	**Tue 15-3-33**	**Mon 24-6-41**	**13**
17		Provide customer support	60 mons	Tue 15-3-33	Mon 19-10-37	
18		**Assist customers with end-of-life of the aircraft**	**960 days**	**Tue 20-10-37**	**Mon 24-6-41**	**17**
19		Recycle and refurbish eligible parts	24 mons	Tue 20-10-37	Mon 22-8-39	
20		Discard non-reusable	24 mons	Tue 23-8-39	Mon 24-6-41	19
21		**Assess the possibility of improved versions**	**480 days**	**Tue 25-6-41**	**Mon 27-4-43**	**16**
22		Assess improvements of current eVTOLs	6 mons	Tue 25-6-41	Mon 9-12-41	
23		Perform market analysis	6 mons	Tue 10-12-41	Mon 26-5-42	22
24		Decide on the improvements to implement	12 mons	Tue 27-5-42	Mon 27-4-43	23

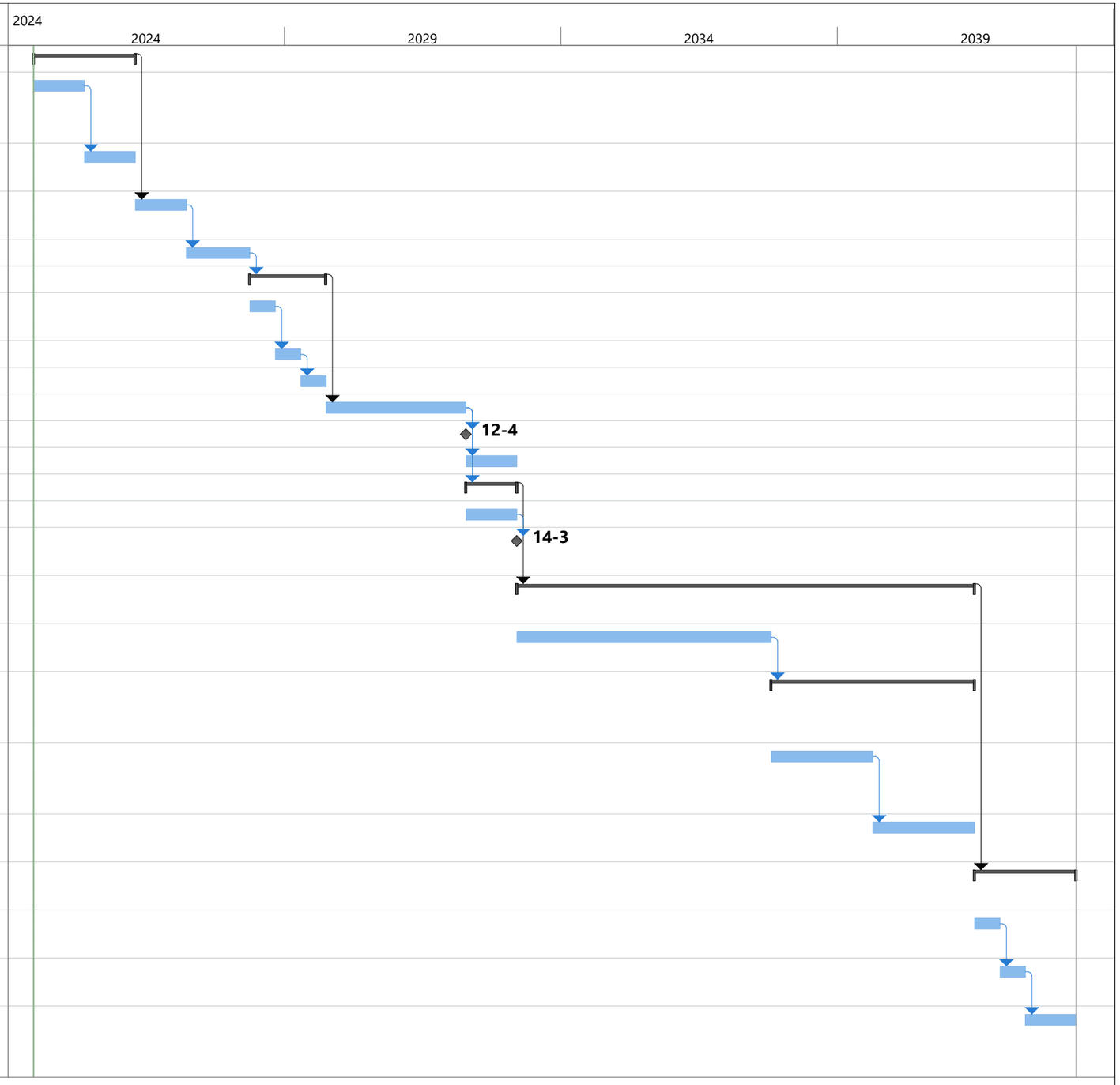

Project: AfterDSE_GoAERO
Date: Wed 19-6-24

Task	Project Summary	Manual Task	Start-only	Deadline
Split	Inactive Task	Duration-only	Finish-only	Progress
Milestone	Inactive Milestone	Manual Summary Rollup	External Tasks	Manual Progress
Summary	Inactive Summary	Manual Summary	External Milestone	

23 | Production Plan

The design of an aerial vehicle is only feasible with appropriate manufacturing and assembly approaches. Therefore, selecting appropriate manufacturing methods for the different components is fundamental. It is also crucial to establish a production approach that allows for the assembly of the vehicle to be subdivided into different intermediate steps. This results in increased production efficiency since multiple parts can be worked on simultaneously, as well as improved accessibility and ease of production, with smaller parts being easier to handle [97].

In the following sections, the choices and arguments for manufacturing methods are presented in Section 23.1, and the general time-ordered assembly of the vehicle in Section 23.2.

23.1. Manufacturing Methods

The processing and manufacturing choice of components depends heavily on the material choice as well as the structural design since not all methods are suitable or optimal for all materials. The geometry and size of the component also determine the type of manufacturing method. Following the breakdown used for the material selection Subsection 21.2.2, the manufacturing choices are argued for the fuselage, the structural booms, the rotor structures, and the rotor blades.

Firstly, the fuselage is made of aluminum 7075-T6, The structure is made up of large thin sheets (skin) and thin-walled reinforcements and stiffeners. The skin can be manufactured by bending or stretch-forming. See Figure 23.1, and Figure 23.2 for a schematic of the processes. Although both can be used to achieve the precise angles and shapes required for aerodynamic performance and have little material waste, bending is selected due to its lower tooling costs[97]. The reinforcements and stiffeners can be manufactured using a sheet metal forming technique like rubber forming [97]. This technique involves placing prepared and cleaned aluminum sheets on a rigid die. A flexible rubber pad is then pressed against the sheet using a hydraulic or mechanical press, forcing the aluminum to conform to the die's shape. The rubber distributes the force evenly, reducing localized stress. See Figure 23.3 for a schematic of the process. Finally, the part is trimmed and inspected for quality and accuracy. The skin and stiffeners are then assembled to form a complete fuselage.

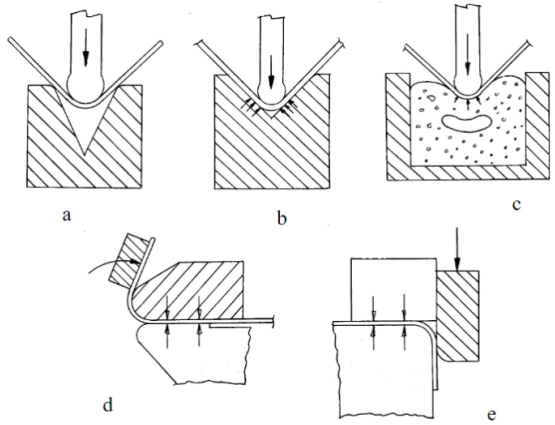

Figure 23.1: Bending Processes [97]

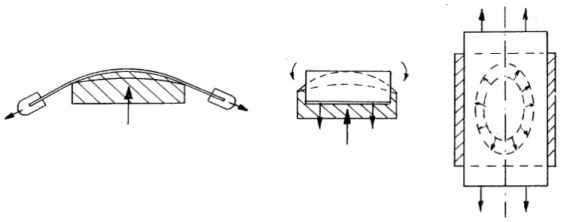

Figure 23.2: Stretch-forming process: front, side, top views [97]

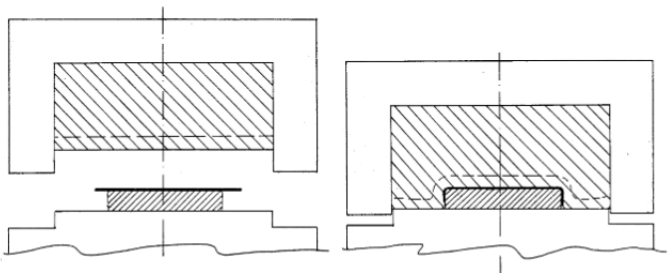

Figure 23.3: Rubber forming process [97]

The structural booms, slender, thin, hollow circular beams, are made of aluminum 7075-T6. This component can be produced through the metal bulk-forming process of extrusion, see schematic in Figure 23.4. It is ideal for producing long, constant cross-sectional components at a relatively low cost and little waste and time. It is suitable for a structural component since the process aligns the grain structure, which enhances its mechanical properties [97].

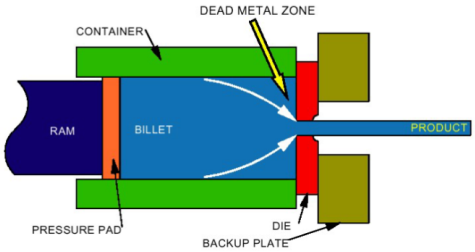

Figure 23.4: Extrusion process [97]

The rotor structures are entirely made of aluminum 7075-T6 but contain different structural materials. These can be divided into the ducts, and the structural rods joining the duct to the rotor blade axis. The ducts have a curvature and can be produced through rubber forming. This technique can accommodate complex shapes and curvature, at a very effective cost. It is important to consider and account for the spring-back inherent to this type of process to ensure the final shape complies with the desired geometry [97]. For the structural rods, the aforementioned extrusion process can also be used since it only requires exchanging the extrusion die to match the new desired cross-section profile.

Regarding the rotor blades, to produce a custom CFRP laminate, the method of Resin Transfer Molding (RTM) is suitable due to its precision and efficiency. The process involves preparing a high-precision mold and laying up dry carbon fiber preforms before clamping the mold. The aluminum leading edge can also be included at this stage, as mentioned in Section 14.3. An epoxy resin can then be injected under pressure to impregnate the fibers and fill the mold cavity. The resin is then cured, solidifying the composite part. After curing, the mold is opened, and the blade undergoes finishing processes like trimming and sanding. See Figure 23.5. RTM ensures high strength, lightweight, and dimensional accuracy, making it ideal for producing complex, high-performance components such as rotor blades [97].

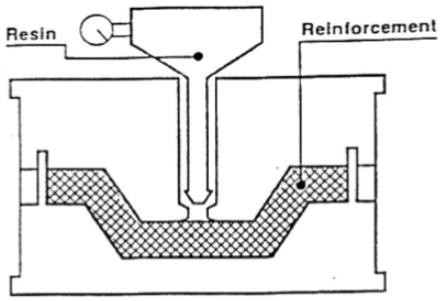

Figure 23.5: Resin Transfer Molding (RTM) process [97]

Finally, the landing gear structure is made up of slender rods made of stainless steel. To produce them, a combination of bending and welding methods is selected. Long tubes of stainless steel are

cut to dimensions and bent in the right geometries to create the landing gear legs and skids, which are then welded together. The process allows for high precision and consistency in producing the required shapes, ensuring structural integrity since the welding and bending maintain the properties of the stainless steel. This is achieved at a relatively low tooling cost and little waste [97].

23.2. Assembly Line

The vehicle's production approach follows an assembly line. It involves producing the different components concurrently and assembling them at specific stations in a logical order. This allows increased production efficiency, reduced labor costs, minimized waste, and scalability for series production.

As a general overview, the assembly process begins with the manufacturing of the fuselage structure, using bending for the skin and rubber forming for the reinforcements and stiffeners. Concurrently, the landing gear is manufactured from stainless steel, through bending and welding of tubes. Once both the fuselage and landing gear are completed, they are attached and riveted together into a sub-assembly. Separately, the rotor structures are produced with the ducts formed through rubber forming and the structural rods created via extrusion. Simultaneously, the structural booms are manufactured using extrusion at a different station and then connected to the rotor structures. Meanwhile, the CFRP rotor blades are produced through Resin Transfer Molding (RTM) and assembled into the rotor structures. Finally, the rotor sub-assembly (structures and blades) is connected to the fuselage sub-assembly (fuselage and landing gear). Once this final step is completed and the general structure of the vehicle is finalized, the different internal components of the vehicle can be introduced and assembled within the structure. These include the batteries, the payload bay, passenger furnishings, the sensors, the wiring, the motors, and the controllers. These are left for the end of the assembly since they should be accessible for maintenance and replacement. Thus the structure must accommodate for their inclusion at a later stage. This process can be visualized in the flowchart Figure 23.6.

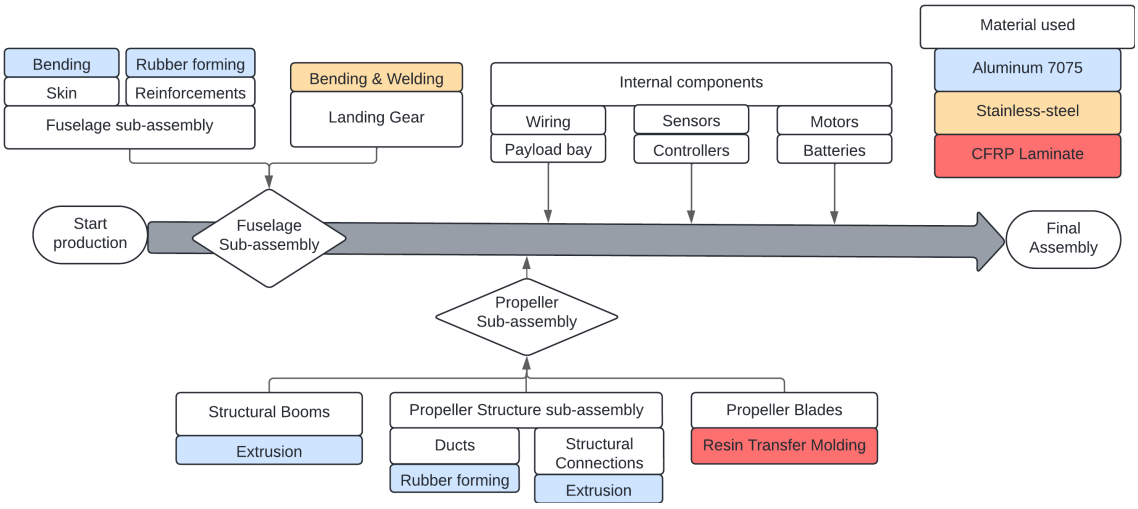

Figure 23.6: Assembly Line Production

At each of these intermediate steps and sub-assemblies, quality checks are implemented to test and control faults within the produced parts and sub-assemblies. Although this contributes negatively to the production time, it prevents inaccuracies and flaws that will, in turn, cause delays. Finally, in line with the sustainability requirements, it is important to frame the production and manufacturing such that resource waste is minimized. This involves not only material waste but also other types, such as unnecessary transportation and waiting time between stations.

Thus, strategies such as Lean manufacturing should be pursued. Lean manufacturing is a method for minimizing waste and optimizing production efficiency. It is essential in aerial vehicle design because it reduces costs, improves quality, and accelerates development. By focusing on value-added processes and eliminating waste, manufacturers can produce more reliable, cost-effective, and high-performance aerial vehicles, essential in a competitive and advanced industry.

24 | Operations and Logistics

This chapter aims to describe the operations and logistics involved in the mission. First, an operational flow diagram explaining all operations is shown in Section 24.1. Next, Section 24.2 discusses the logistical considerations relating to charging, transportation, mission, maintenance and end-of-life. Finally, a RAMS analysis is presented in Section 24.3.

24.1. Operational Flow Diagram

Although the eVTOL is airborne for only a short period, its lifecycle includes various operations such as storing, charging, transporting, maintaining, and dismantling. The flow of these operations is shown in Figure 24.1.

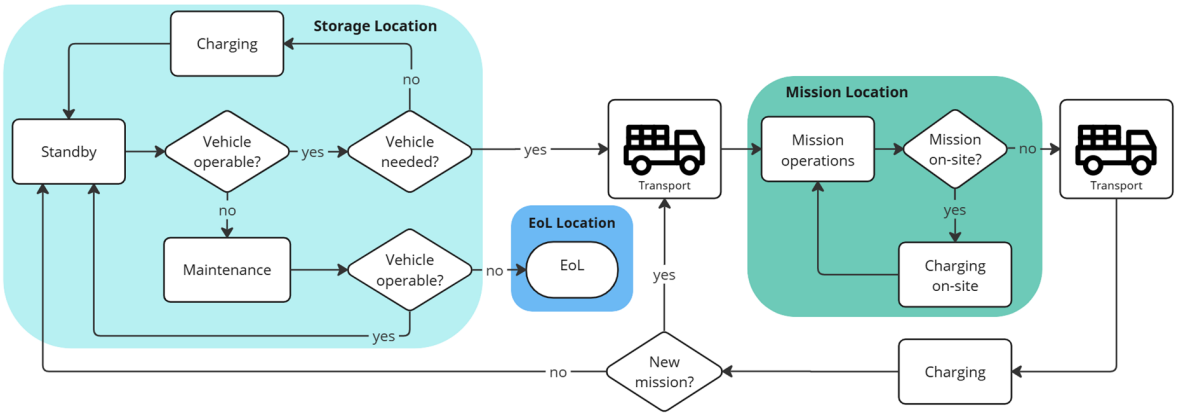

Figure 24.1: Operational Flow Diagram

Operations such as standby, charging, and maintenance occur at the storage location. If the vehicle is no longer operable, maintenance is performed. In case the vehicle is still not operable after maintenance, it transitions into the End-of-Life (EoL) phase. If the vehicle is needed, it is rapidly transported to the designated location to initialize mission operations. If another mission needs the vehicle, it is either charged on-site if it concerns the same mission location, or it is transported and charged on the go. If no new mission is initialized, the vehicle is returned to the storage location for standby.

An overview of all locations associated with the mission is shown in Figure 24.2.

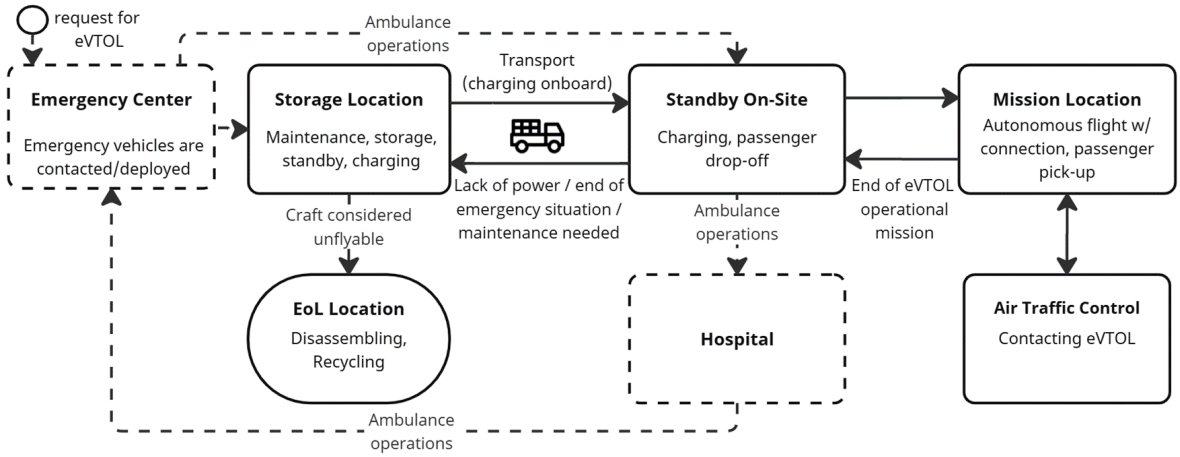

Figure 24.2: Associated Mission Locations

The dashed locations and connections represent logistical problems lying beyond the concerns tackled by the design team. Nevertheless, they mark critical on-ground ambulance infrastructure necessary for the successful execution of operations.

24.2. Logistical Considerations

Besides looking at the operational aspect, we also need to consider the logistics. In this section four different aspects are presented.

Charging

As shown in Figure 24.1, charging occurs in three different locations: the storage location, on-site and during transport. The latter is highly relevant as it eliminates the need to return to the storage location, enhancing operational efficiency. This capability offers a competitive advantage in the medical service market by enabling more missions without going back to the storage location.

As explained in Section 12.3, the vehicle can be fully charged within 20 minutes using a C-rate of 3, but it is preferred to use a C-rate of 1 resulting in a maximum charging time of 60 minutes. Since charging on-site or in the truck usually needs to be done quick due to a next mission, this will be done using a C-rate of 3, while charging in the storage location will be done using a C-rate of 1.

When not recharged, the vehicle can successfully execute a productivity mission, rescuing up to 10 passengers within a 2.4 kilometer radius from the mission location.

Transportation

Looking at the transportation, several logistical requirements are composed. First, the truck must be operable on both European and North American roads. Therefore the length, width and height of the interior of a legal truck is 13.46 $\times$ 2.4 $\times$ 2.5 m^3, as indicated by *STK-CLNT-15-MIS-1*. Looking at the environmental sustainability, an electric truck is preferred, however, this is up to the operator.

Furthermore, a maximum mass is allowed dependent on the truck selected. As the weight budget already limits the mass more than any conventional truck does, this maximum mass will not be exceeded.

Mission

The missions considered are productivity, adversity, maneuverability, altitude and range. A description of these can be found in Section 2.2. Each mission focuses on different aspects but in all of them, the vehicle is fully autonomous and has contact with both on-site emergency responders as well as air traffic control. Logistics for the payload consists of the boarding and deboarding, safety and comfort of the passenger. At the end of the mission, the vehicle arrives back at the truck, where the passenger safely deboards.

Maintenance and End-of-Life

After the vehicle is returned to the storage location, it is examined for damages. During this maintenance check, both physical as well as hardware/software are evaluated and reparations are performed when necessary. In case the maintenance check shows it is no longer possible to fix the damages, the end-of-life phase is initiated and parts are recycled. The goal is 90% recyclability as described in *Environmental Sustainability* in Subsection 21.2.2. Besides these inspections, thorough maintenance is performed every 100 flight hours.

24.3. RAMS Analysis

The aerospace industry is experiencing significant growth driven by increasing demand for both commercial and defense applications [98]. To ensure that the systems perform the mission as designed, the Reliability, Availability, Maintainability and Safety (RAMS) characteristics are analyzed.

Reliability

Reliability is defined as the probability that the system will perform its required function under given conditions for a stated time interval [99]. It is assessed to ensure that the system operates at an acceptable level of risk. It is quantified using the following relation.

$$Reliability = e^{-\frac{t}{MTBF}} \tag{24.1}$$

where t is the time and $MTBF$ is the mean time between failure.

Before determining the overall reliability, the reliability of the subsystems is assessed. The subsystems considered and their MTBF and reliability are shown in Table 24.1. The time considered is 100 hours as this is the scheduled maintenance interval.

Table 24.1: Reliability of Subsystems for 100 hours

Subsystem	MTBF [hour]	Reliability
GNSS [2x]	60464[1]	0.99835
Barometer [2x]	50000[2]	0.99800
IMU [3x]	10500[3]	0.99052
Vision Camera	40000[4]	0.99750
LiDAR Sensor	751296[5]	0.99987
Radar	1000[6]	0.90484
Airspeed Sensor [2x]	55400[7]	0.99820
Time-of-Flight Multi-Zone Ranging Sensor	667[8]	0.86071

Finally, the reliability of all subsystems is multiplied resulting in an overall reliability of 0.74668.

Availability

Availability is the probability that the design is available to perform its function when called upon. It is expressed as the ratio of the expected uptime to the total time[9].

$$Availability = \frac{Uptime}{Uptime + Downtime} \tag{24.2}$$

Some factors that influence the availability are deployment time, charging time and loiter time. As these factors are all minimized, the expected downtime is way smaller than the expected uptime, hence, the availability is expected to be high.

Maintainability

Maintainability is defined as the likelihood of effectively repairing a system within a designated time frame [100].

As explained in Section 24.2, the vehicle is inspected for external damages and the hardware/software is examined after every mission. If necessary, unscheduled maintenance is performed. Furthermore, every 100 hours a thorough maintenance check is performed.

Maintainability is quantified using the following relation.

$$Maintainability = 1 - e^{-\frac{t}{MTTR}} \tag{24.3}$$

As the mean time to repair is expected to be small, the maintainability is expected to be high.

Safety

Safety is an important characteristic of the design. It is defined as the ability to prevent injury to the passenger and avoid unacceptable consequences to materials, environment, or other aspects during its use [99].

[1] URL https://www.uavnavigation.com/sites/default/files/docs/2024-02/UAV_Navigation-GrupoOesia_GNSS_Denied_Navigation_Kit_Brochure.pdf [cited 13 June 2024]

[2] URL https://www.shipmotion.eu/barometric-pressure-sensor-smc-630.html [cited 13 June 2024]

[3] URL https://docs.novatel.com/OEM7/Content/Technical_Specs_IMU/CPT_Electrical_Environmental.htm [cited 13 June 2024]

[4] URL https://www.mech-mind.com/news/Mech-MindReachesMTBFMarkof40,000Hours.html [cited 13 June 2024]

[5] URL https://cdn.sick.com/media/pdf/7/57/657/dataSheet_LD-LRS3601_1060832_en.pdf [cited 13 June 2024]

[6] URL https://ui.adsabs.harvard.edu/abs/1983rad..symp..532D/abstract [cited 13 June 2024]

[7] URL https://www.aerocontact.com/public/img/aviaexpo/produits/catalogues/312/MD21-Datasheet.pdf [cited 13 June 2024]

[8] URL https://community.st.com/t5/imaging-sensors/reliability-for-vl53l0cx/td-p/124410?attachment-id=3114 [cited 13 June 2024]

[9] URL https://fiixsoftware.com/glossary/system-availability/ [cited 12 June 2024]

To increase the safety, redundancy is considered. For the hardware, all sensors are redundant as described in Table 17.1 in Section 17.1. For the software, a safety and redundancy layer monitors the health of the overall aircraft (Section 17.2). Furthermore, if one of the rotors fails, the vehicle is still controllable as examined in Chapter 11. However, not all components are redundant and if one of these fails, it could have catastrophic consequences. The following components are considered safety-critical functions:

- Structural main frame
- Landing gear
- Battery

To reduce the probability of failure of one of these components, contingencies are introduced as described in Chapter 20.

25 | Requirements Compliance and Design Validation

This chapter aims to describe the process of verification and validation of the proposed design. Firstly, the design is verified with respect to compliance of the requirements in Section 25.1. Secondly, it is validated by comparison with existing vehicles in Section 25.2.

25.1. Requirements Compliance

Each design must be rigorously verified for compliance with its requirements, providing critical insights to the customer on whether the proposed design meets, exceeds, or falls short of the desired performance. Table 25.1 presents all stakeholder requirements with their respective identifier. Moreover, requirement compliance was checked if the design meets it (introducing “Yes” label) or does not meet it (introducing “No” label). Due to the limited time of the project, some non-driving requirements were not considered, therefore, they are labeled as not addressed (N/A) in the table. Some remarks are written for each requirement explaining design aspects influencing the requirement compliance.

Table 25.1: Compliance matrix of the design with requirements. In the compliance column, each requirement is said to be met (Yes), not met (No) or not addressed so far in the design (N/A).

Identifier	Requirement	Compliance	Remarks
STK-CLNT-1	The vehicle shall be able to land on a 3.3 by 3.3 m platform.	Yes	• adequate choice of sensors (Section 17.1)
STK-CLNT-2	The vehicle shall be able to manoeuvre around obstacles.	Yes	• required moments and forces are generate in case of engine failure (Section 11.2) • 3m of clearance in horizontal space (Section 10.1)
STK-CLNT-3	The vehicle shall be able to fly through 8.5 m horizontal and 9.1 m vertical spaces.	Yes	• 3m of clearance in horizontal space (Section 10.1) • more than 5 meters of vertical clearance
STK-CLNT-4	The vehicle shall be fully autonomous.	Yes	• autonomous sensors (Section 17.1) • controller design (Section 16.2)
STK-CLNT-5	The vehicle shall have on-the-fly path planning.	Yes	• on-the-fly path planning sensor (Section 17.1) • controller design (Section 16.2)

Continued on next page

Table 25.1: *Continued from previous page*

Identifier	Requirement	Compliance	Remarks
STK-CLNT-6	The vehicle shall have a safety-critical design.	Yes	• choice of materials (Section 14.3) • redundancy in number of sensors and actuators (Section 17.1) • modularity of the battery (Section 12.2)
STK-CLNT-7	The vehicle shall have an electric propulsion system.	Yes	• battery as the source of energy (Chapter 12)
STK-CLNT-8	The vehicle shall be able to land on dry sand.	Yes	• rotors mounted on the top of the fuselage (Section 10.1) • skid landing gear decreasing the risk of sinking in (Section 14.1)
STK-CLNT-9	The vehicle shall be able to land on a hard surface at a 12-degree angle.	Yes	• landing gear design (Section 14.1) • Time-of-flight ranger sensor (Section 17.1)
STK-CLNT-10	The vehicle shall be able to land in half a meter of water.	Yes	• landing gear design and material choice (Section 14.1, Section 14.3) • ultrasound water sensor (Section 17.1)
STK-CLNT-11	The vehicle shall have a minimum altitude ceiling of 1000 m.	Yes	• at 1000m there is excessive power allowing for further climb (Section 7.2)
STK-CLNT-12	The vehicle shall have a range of 30 km.	Yes	• Range mission profile is executable (Section 7.3)
STK-CLNT-13	The vehicle shall be able to carry a payload of 95 kg.	Yes	-
STK-CLNT-14	The vehicle shall be able to take-off and land vertically.	Yes	• multicopter configuration (Chapter 5)
STK-CLNT-15	The vehicle shall fit on a US and EU street-legal ground transport vehicle.	Yes	• detachable rotor booms (Subsection 10.1.3)
STK-CLNT-18	The vehicle shall be deployable in 30 minutes by 2 persons.	Yes	• easy-release detachable rotor booms (Subsection 10.1.3) • battery permanently mounted (Chapter 24)
STK-CLNT-19	The vehicle shall be able to withstand wind of 6 bft.	Yes	• propulsion system sizing (Section 10.1) • counteracting moments and forces are generated (Section 11.3)
STK-CLNT-20	The cost of the vehicle shall be less than 120,000 euros.	No	• the cost is €138,169 (Chapter 18)
STK-CLNT-21	The development of the vehicle design shall not take more than 10 weeks.	Yes	-
STK-CLNT-23	The vehicle shall be operative under adverse weather conditions.	N/A	-
STK-CLNT-30	The vehicle shall be able to save at least 6 people without recharge while mantaining its maximum range.	Yes	• the vehicle can save up to 12 passenger within 2.4 km radius (Section 7.3)
STK-CLNT-31	The vehicle shall have an additional 10 minute loiter hovering.	Yes	• range mission profile includes 10 minutes for hover (Section 7.3)

Continued on next page

Table 25.1: *Continued from previous page*

Identifier	Requirement	Compliance	Remarks
STK-GP-1	The vehicle shall not disturb the public.	N/A	-
STK-PSGR-1	The vehicle shall ensure passenger comfort.	Yes	• spacious payload bay (Chapter 15)
STK-PSGR-2	The vehicle shall be easily accessible for boarding and unboarding.	Yes	• propulsion system is mounted on top of the fuselage (Section 10.1)
STK-EG-1	The vehicle shall have minimal environmental impact.	Yes	• recyclability of the materials (Section 14.3) • life cycle assessment Section 21.3)
STK-EMS-2	The vehicle shall report its state, payload status and flight path continuously to the Emergency Medical Service (EMS).	Yes	• communication and sensor architecture (Section 17.1, Section 17.3)

It should be mentioned that the design complies with all the requirements aside from *STK-CLNT-20* concerning cost. Despite the fact that the cost offset amounts to 15%, the cost of the vehicle is highly competitive when compared with other vehicles present in the aerial response market and, after consulting the customer, the cost was deemed to be satisfactory given the safety-based design philosophy. Moreover, it can be noted that non-driving requirements that were not addressed yet will be considered in the future design phase to ensure compliance.

25.2. Design Validation

This section focuses on assessing the vehicle's feasibility and validating the obtained vehicle characteristics through comparison. Given the small size of the passenger eVTOL market with the mission objective of this design aiming to close a gap in this developing market, the number of comparable vehicles is limited. This narrows the scope of statistical validation efforts.

Therefore, comparison between the designed vehicle and comparable vehicles in terms of mission, range, size and payload is chosen as a validation method. Table 25.2 presents all vehicles that are under consideration including values for the designed one. Data on payload mass, maximum take-off mass (MTOM) and cruise speed was collected allowing for the comparison of the ratio of payload mass to MTOM and cruise speed.

Table 25.2: Characteristics of Comparable Vehicles With Data on the Designed One

Vehicle	Payload mass [kg]	MTOM [kg]	Payload mass/MTOM [-]	Cruise speed [m/s]
Jetson One	95	181	0.52	28.00
Ryse Recon	114	249	0.45	18.00
FB3 Heavy-Lift Drone	100	132	0.76	30.00
Ambular 2.0	200	400	0.50	27.78
Bee Flights Bee-1	100	400	0.25	27.78
Advanced Tactics Transporter	455	1113	0.41	-
Ehang 184	100	360	0.28	27.78
Ehang 216	220	620	0.35	27.78
xpeng voyager	200	560	0.36	36.11
Cartivator SkyDrive	160	400	0.40	16.67
Esinti	80	407	0.20	31.94
Designed vehicle	94	421	0.22	33.00

Figure 25.1 presents box and whiskers plot of the ratio of payload mass to MTOM. The plot was generated for comparable vehicles and designed vehicle was compared with the resulting plot; the design is indicated by black dot on the figure. Several conclusions can be drawn from the plot. The range spanned by payload to MTOM ratio is big stemming from different application of the vehicles. The designed vehicle has the ratio below the first quartile and close to the lower end of the spectrum. The

median is located more less in the middle of the interquartile range. Given these observations, it can be claimed that the design's ratio is in the same order of magnitude as ratios of other vehicles. Nevertheless, it should be pointed out that it is lower than the majority.

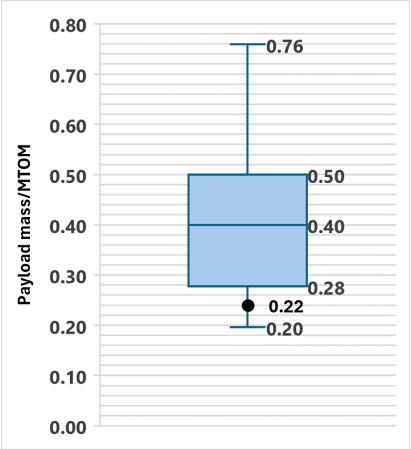

Figure 25.1: Box and whisker plot of the ratio of payload mass to the maximum take-off mass of comparable vehicles with black dot indicated the designed vehicle.

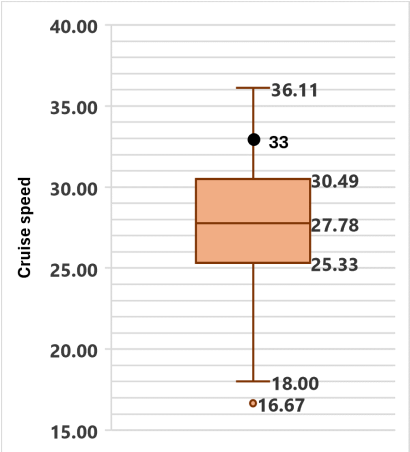

Figure 25.2: Box and whisker plot of cruise speeds of comparable vehicles with black dot indicating designed vehicle.

Figure 25.2 presents box and whisker plot of cruise speed of similar vehicles which serves as a comparison with the designed on indicated with the black dot on the figure. Similarly to the previous figure, some conclusions can be drawn about it. Firstly, the interquartile range of speed is small indicating that most of the vehicles cruise with similar speeds. Secondly, the design vehicle has a speed which is above the third quartile and close to the higher end of spectrum. Basing on that, it can be said that the design vehicle's speed is in the same order of magnitude as other vehicles. However, it is higher than majority of them.

Due to the limited data available for other vehicles, the validation is limited only to the discussed two aspects. Basing on which, it can be concluded that the proposed product is physically viable and feasible.

26 | Conclusion and Recommendations

Emergency ground responses are frequently delayed due to infrastructure issues and traffic congestion, with natural disasters aggravating these problems. Current air ambulances, while useful, are costly to operate on a large scale, require specialized personnel, and lack maneuverability in tight spaces. IUVO aims to resolve these issues, being a low-cost, single-passenger eVTOL designed for autonomous operation and agile navigation around obstacles.

To meet the mission requirements, IUVO incorporates innovative design elements that enhance flight performance. The final design features a multicopter with six high-mounted ducted rotors, which generate more thrust compared to open rotors. Each rotor is tilted at a custom angle to ensure operability under one-engine failure and to enhance maneuverability. The energy storage system utilizes modular lithium-ion batteries, emphasizing redundancy and fire prevention for enhanced overall safety. For ease of transport, the rotorcraft is designed to fit within the dimensions of US and EU street-legal vehicles. To allow for this, the rotors are detached and later assembled on-site.

Great attention is paid to the design of the rotorcraft to ensure it can meet the critical mission profile requirements. The flyer can reach a rescue location within a 15 km radius from the deployment site, cruising at a speed of 119 km/h and maintaining an altitude of 300 meters. Upon arrival, it can board a single passenger weighing up to 94.5 kg, reaching a maximum take-off weight of 421 kg, and transport them to safety, covering a maximum total distance of 30 km. Furthermore, the flyer can loiter for up to

10 minutes at cruising altitude, providing significant mission flexibility in unpredictable circumstances. IUVO demonstrates rapid response capabilities by completing the entire mission in just 35 minutes. Additionally, the battery can be recharged on-site in only 20 minutes, highlighting the rotorcraft's time efficiency and readiness for additional missions.

IUVO sets itself apart from other air ambulances with a low unit cost of only €138169. Although this is 15% above the required budget, its affordability makes it highly competitive in the current market, making it a design worth pursuing and further developing. Furthermore, its operational costs are economically viable: €80 for a single mission without transport costs, and €116 for a mission including transport via a petrol truck.

The final design can be seen in Figure 26.1, with the external layout wireframes presented in Figure 26.2. The design characteristics are summarized in Table 26.1.

Figure 26.1: IUVO: I help

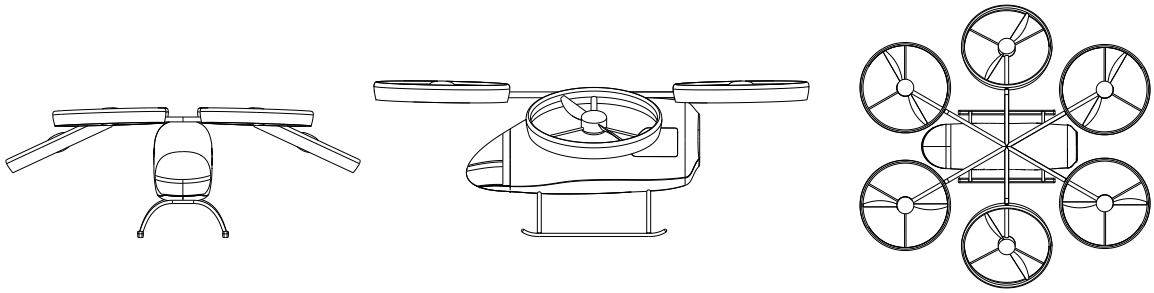

Figure 26.2: IUVO Wireframes

Table 26.1: Main characteristics of the vehicle

Parameter	Value
MTOM [kg]	421
Payload Capacity [PAX]	1
Range [km]	30
Cruise Altitude [m]	300
Cruise Speed [km/h]	120
Critical Mission Time [min]	35
Charging Time [min]	20
Unit Cost [€]	138169
Operational Cost [€]	80

Parameter	Value
Number of Rotors/Motors [-]	6
Rotor Diameter [m]	1.74
Peak Motor Power [kW]	133
Maximum Thrust [kN]	7.34
Battery Capacity [kWh]	29.4
Vehicle Width [m]	5.8
Vehicle Length [m]	6.0
Vehicle Height [m]	2.1

Recommendations

The project objective pursued by the design team is to deliver an innovative solution to rapid emergency response challenges in the span of 10 weeks. Since a detailed design would not be feasible at this time, there are some recommendations and developments that could be made in the future. This section aims to present these recommendations.

One of the most important recommendations is to perform a high-fidelity CFD aerodynamic simulation. This is important because at the moment the aerodynamic interaction effects of ducted propellers on the drag estimations could not be modeled analytically. In addition, profile and induced drag could not be modeled in the current CFD simulation, since the spinning of the propellers was not implemented. Therefore, a computational approach with manually refined and detailed mesh would be needed to estimate if the benefits that ducts bring in thrust generation offset the drag losses in cruise.

Secondly, the flight controller subsystem shows certain areas of improvement. Due to the presence of rotor tilt and 6 motors, the vehicle can produce forward force without rotation. This behavior could potentially be exploited to improve the displacement performance for smaller maneuvers. Additionally, a gain scheduler could be implemented in the control loops, to achieve the same goal.

Thirdly, the inward/outward tilt of the rotors 1, 3, 4, and 6 can be added as a third optimization variable. Furthermore, a more detailed k_{yaw} estimation can be conducted, as the AMS Margin was found to be very sensitive to this parameter.

Due to the time constraints imposed by the scope of the assignment, structural optimization for the landing gear and propeller booms is not feasible and structural design of the fuselage and ducts is not pursued. These aspects of the design should be tackled in the detail design phase. A more refined FEM model should be made to assess the structural interactions of components. Moreover a wider scope of limit load cases can be identified for these parts.

References

[1] Jonk, Y., Milkowsky, C., Croll, Z., and Pearson, K. *Ambulance Deserts: Geographic Disparities in the Provision of Ambulance Services [Chartbook]*. 2023.

[2] Fortune Business Insights. *Helicopter Market Size, Share & Industry Analysis*. https://www.fortunebusinessinsights.com/industry-reports/helicopter-market-101685. cited 03 May 2024. 2023.

[3] Smeur, E. *Project Guide Design Synthesis Exercise - GoAERO Emergency Response Flyer*. 2024.

[4] GoAERO Prize Committee. *GoAERO Fly-Off Rulebook*. Version 2024-04-11. GoAERO Prize. Apr. 2024.

[5] European Union Aviation Safety Agency. *Second Publication of Proposed Means of Compliance with the Special Condition VTOL*. Technical Report MOC-2 SC-VTOL. European Union Aviation Safety Agency, June 2021.

[6] Fortune Business Insights. *Air Ambulance Services Market Size, Share & Industry Analysis*. https://www.fortunebusinessinsights.com/air-ambulance-services-market-102577. cited 03 May 2024. 2023.

[7] Mordor Intelligence. *Air Ambulance Service Market - Growth, Trends, COVID-19 Impact, and Forecasts*. cited 03 May 2024. 2023.

[8] SkyQuest Technology. *Air Ambulance Services Market Research Report*. https://www.skyquestt.com/report/air-ambulance-services-market. cited 03 May 2024. 2023.

[9] Emergen Research. *Air Ambulance Services Market Research Report*. https://www.emergenresearch.com/industry-report/air-ambulance-services-market. cited 03 May 2024. 2023.

[10] Airbus. "Market Share of the Leading Helicopter Manufacturers Worldwide in 2020 [Graph]". In: *Statista* (2021). cited 03 May 2024.

[11] Business Jet Traveler. *Airbus Helicopters H135 T3*. https://www.bjtonline.com/aircraft/airbus-helicopters-h135-t3. cited 03 May 2024. 2023.

[12] Business Jet Traveler. *Airbus Helicopters H145*. https://www.bjtonline.com/aircraft/airbus-helicopters-h145. cited 03 May 2024. 2023.

[13] Business Jet Traveler. *Leonardo AW189*. https://www.bjtonline.com/aircraft/leonardo-aw189. cited 03 May 2024. 2023.

[14] Paramount Business Jets. *Sikorsky S-92*. 2023.

[15] Conklin & de Decker via Jet Support. *Sikorsky S-70i*. 2023.

[16] BIS Research. *Urban Air Mobility Market Analysis*. Market Analysis Report. Projected VTOL market valuation of 1.9 billion USD by 2035. 2021.

[17] McKinsey & Company. *Air Taxi Market Valuation Study*. Consultancy Report for NASA. Estimated market value for Air Taxis could reach up to 500 billion USD. 2021.

[18] IDTechEx. *Global VTOL Market Projections*. Market Forecast Report. Predicts the global market could expand to approximately 14.7 billion USD by 2040. 2021.

[19] Deloitte. *eVTOL Market Analysis*. Market Research Report. Forecast suggests a market size of 17.7 billion USD by 2040. 2021.

[20] Reports and Data. *Urban Air Mobility Market Size*. Industry Analysis Report. Documents a potential market size of 7.9 billion USD by 2030. 2021.

[21] Fortune Business Insights. *eVTOL Aircraft Market Size, Share & Industry Analysis*. https://www.fortunebusinessinsights.com/evtol-aircraft-market-106298. cited 03 May 2024. 2023.

[22] Precedence Research. *eVTOL Aircraft Market*. https://www.precedenceresearch.com/evtol-aircraft-market. cited 03 May 2024. 2023.

[23] Markets and Markets. *eVTOL Aircraft Market - Global Forecast to 2030*. https://www.marketsandmarkets.com/Market-Reports/evtol-aircraft-market-28054110.html. cited 03 May 2024. 2023.

[24] Zhong, L. *Aerodynamics Theories for Estimating Flight Profile of eVTOL Aircraft*. Tech. rep. Suwa University of Science, 2023.

[25] Maisel, M., Giulianetti, D., and Dugan, D. “The History of the XV-15 Tilt Rotor Research Aircraft: From Concept to Flight”. In: *Monographs in Aerospace History* 17.NASA SP-2000-4517 (2012).

[26] Leishmann, J. G. *Principles of Helicopter Aerodynamics*. 2nd ed. New York, USA: Cambridge University Press, 2006.

[27] Kadhiresan, A. R., and Duffy, M. J. “Conceptual Design and Mission Analysis for eVTOL Urban Air Mobility Flight Vehicle Configurations”. In: *AIAA Aviation 2019 Forum*. DOI: 10.2514/6.2019-2873. eprint: https://arc.aiaa.org/doi/pdf/10.2514/6.2019-2873.

[28] De Vries, R., Hoogreef, M. F. M., and Vos, R. “Range equation for hybrid-electric aircraft with constant power split”. In: *Journal of Aircraft* 57.3 (2020), pp. 552–557. DOI: 10.2514/1.C035734.

[29] Roskam, J. *Airplane Design Part V: Component Weight Estimation*. DARcorporation, 1999.

[30] Duffy, M., Sevier, A., Hupp, R., Perdomo, E., and Wakayama, S. “Propulsion Scaling Methods in the Era of Electric Flight”. In: *AIAA/IEEE Electric Aircraft Technologies Symposium*. Cincinnati, OH, 2018.

[31] Prouty, R. W. *Helicopter Performance, Stability, and Control*. Krieger, 2002.

[32] Schoen, A. H., Rosenstein, H., Stanzione, K., and Wisniewski, J. S. *User’s Manual for VASCOMP II: The V/TOL Aircraft Sizing and Performance Computer Program*. Report 08-0375. Boeing Vertol Company, May 1980.

[33] U.S. Government Accountability Office. *Advanced Air Mobility: Legal Authorities and Issues to Consider for Operations*. Accessed: 2024-05-24. U.S. Government Accountability Office, 2023. URL: https://www.gao.gov/products/gao-23-105562.

[34] Federal Aviation Administration. *Airworthiness Certification*. Accessed: 2024-05-24. 2023. URL: https://www.faa.gov/aircraft/air_cert/airworthiness_certification.

[35] Venckunas, V. “Who develops aircraft faster than Airbus and Boeing? | Data”. In: *Aerotime Hub* (Dec. 2020).

[36] Datta, A. *Commercial Intra-City On-Demand Electric-Vtol Status of Technology*. Tech. rep. University of Maryland, 2018.

[37] Batteiger, V., DeBreuker, R., Dedoussi, I., Delfs, J., Dinkelacker, F., Elham, A., Garcia, S. J. and Friedrichs, J. *Accelerating the path towards carbon-free aviation*. Tech. rep. Braunschweig: Niedersächsisches Forschungszentrum für Luftfahrt NFL, 2023. DOI: 10.24355/dbbs.084-202207041441-0. URL: https://leopard.tu-braunschweig.de/receive/dbbs_mods_00070904.

[38] Scholz, D., and Nita, M. “Preliminary Sizing of Large Propeller Driven Aeroplanes”. In: *Recent Research and Design Progress in Aeronautical Engineering and its Influence on Education*. Brno University of Technology. Czech Republic, 2008.

[39] Gordon Leishman, J. “Electrically-Powered Aircraft”. In: *Introduction to Aerospace Flight Vehicles*. Embry Riddle Aeronautical University, 2022. Chap. 57. DOI: 10.15394/eaglepub.2022.1066.

[40] Wang, J. *4. Weight and Performance Estimation for eVTOL aircraft*. 2022.

[41] Forster, K., Barber, T., Diasinos, S., and Doig, G. “Interactions of a counter-rotating vortex pair at multiple offsets”. In: *Experimental Thermal and Fluid Science* 86.1 (2017), pp. 63–74.

[42] European Union Aviation Safety Agency. *Certification Specifications and Acceptable Means of Compliance for Small Rotorcraft*. Tech. rep. European Union Aviation Safety Agency, 2016.

[43] Spakovszky, Z. S. *Performance of Propellers*. Tech. rep. Massachusetts Institute of Technology, 2018.

[44] Zhang, T., Barakos, A., and George, N. “High-Fidelity CFD Validation and Assessment of Ducted Propellers for Aircraft Propulsion”. In: *Journal of the American Helicopter Society* 66 (Jan. 2021), pp. 1–28. DOI: 10.4050/JAHS.66.012008.

[45] Pradeep, M., Haque, S. M., Priyanka, K. S. “Comparative Study of Ducted and Unducted Propeller”. In: *International Research Journal of Modernisation in Engineering Technology and Science* 3 (6 2021).

[46] Nathen, P., Bardenhagen, A., and Taylor, J. “Architectural performance assessment of an electric vertical take-off and landing (e-VTOL) aircraft based on a ducted vectored thrust concept.” In: (2021).

[47] Ondervan, G. J., Hoekstra, M., and Holtrop, J. “Flow Analysis, design and testing of ducted propellers”. In: *Aerospace Science and Technology* 117 (2021).

[48] Hoerner, S., and Sighard, F. “Fluid-Dynamic Drag: Practical Information on Aerodynamic Drag and Hydrodynamic Resistance”. In: (1965).

[49] Zhang, J., Söpper, M., and Holzapfel, F. “Attainable Moment Set Optimization to Support Configuration Design: A Required Moment Set Based Approach”. In: *Applied Sciences* 11.8 (2021), p. 3685. DOI: 10.3390/app11083685.

[50] Michieletto, G., Ryll, M., and Franchi, A. “Control of statically hoverable multi-rotor aerial vehicles and application to rotor-failure robustness for hexarotors”. In: (2017), pp. 2747–2752.

[51] Adkins, C. N., and Liebeck, R. H. “Design of Optimum Propellers”. In: *Journal of Propulsion and Power* 10 (1994), pp. 676–682. DOI: 10.2514/3.23779.

[52] Larrabee, E. E. “Practical Design of Minimum Induced Loss Propellers”. In: *SAE International* 88 (1979), pp. 2053–2062. DOI: 10.4271/790585.

[53] Khan, F. M. N., Rasul, M. G., Sayem, A. S. M., and Mandal, N. *Maximizing energy density of lithium-ion batteries for electric vehicles: A critical review*. 2022.

[54] Horiba, T. *Lithium-Ion Battery Systems*.

[55] Bao, Y., Dong, W., and Wang, D. “Online Internal Resistance Measurement Application in Lithium Ion Battery Capacity and State of Charge Estimation”. In: *Energies* 11.5 (2018).

[56] Pranoto, F. S., Wirawan, A., and Purnamasari, D. A. “Electrical Power Budgeting Analysis for LSA-02 UAV Technology Demonstrator”. In: *IOP Conference Series: Materials Science and Engineering* 160.1 (Nov. 2016), p. 012088.

[57] Tahir, M. U., Sangwongwanich, A., Stroe, D., and Blaabjerg, F. “Overview of multi-stage charging strategies for Li-ion batteries”. In: *Journal of Energy Chemistry* 84 (2023), pp. 228–241. ISSN: 2095-4956.

[58] Hwang, F. S., Confrey, T., Scully, S., Callaghan, D., Nolan, C., Kent, N., and Flannery, B. “MODULAR PHASE CHANGE MATERIAL (PCM) THERMAL MANAGEMENT SYSTEMS FOR CYLINDRICAL LI-ION CELLS”. In: Apr. 2020. DOI: 10.1615/TFEC2020.est.032095.

[59] Vaidyanathan, H., Kelly, W. H., and Rao, G. “Heat dissipation in a lithium ion cell”. In: *Journal of Power Sources* 93.1 (2001), pp. 112–122. ISSN: 0378-7753. DOI: https://doi.org/10.1016/S0378-7753(00)00550-4. URL: https://www.sciencedirect.com/science/article/pii/S0378775300005504.

[60] Agwu, D. D., Opara, F., Chukwuchekwa, N., Dike, D., and Uzoechi, L. “Review Of Comparative Battery Energy Storage Systems (Bess) For Energy Storage Applications In Tropical Enviroments”. In: (Sept. 2018).

[61] Lewandowski, T. A. “Additional risk assessment of alternative refrigerant R-1234yf”. In: *Gradient Corporation, July* 24 (2013), p. 2013.

[62] Hirai, I., and Gunji, T. “Relationship between Slipperiness and Coefficient of friction on the Carpets”. In: *Sen’i Kikai Gakkaishi (Journal of the Textile Machinery Society of Japan)* 53.6 (2000), T140–T146.

[63] Niu, C. *Airframe Structural Design: Practical Design Information and Data on Aircraft Structures*. Conmilit Press, 1988.

[64] Q. Wang, W. Wu, and W. Li. “Compression Properties of Interlayer and Intralayer Carbon”. In: *Polymers* 10.4 (2018).

[65] Behera, A., and Priyabrata, M. “Chapter 20 - Application of nanofibers in aerospace industry”. In: *Fiber-Reinforced Nanocomposites: Fundamentals and Applications*. Micro and Nano Technologies. Elsevier, 2020, pp. 449–457.

[66] Naresh Kumar, S., Abdul Shukur, J., Sriker, K., and Lavanya, A. “Design and Structural Analysis of Skid Landing Gear”. In: *International Journal of Current Engineering and Technology* (2014).

[67] Raymond Johnson, E. *Aerospace structures*. Virginia Tech, 2022.

[68] Hopkins, D. C., Baltis, T., Pitarresi, J., and Hazelmyer, D. “Extreme Thermal Transient Stress Analysis with Pre-Stress in a Metal Matrix Composite Power Package”. In: *Additional Conferences (Device Packaging, HiTEC, HiTEN, CICMT)* 2012 (Jan. 2012), pp. 000361–000372. DOI: 10.4071/HITEC-2012-THA25.

[69] González, F. Q., and Nuño, N. “Finite element modeling of manufacturing irregularities of porous materials”. In: *Biomaterials and Biomechanics in Bioengineering* 3.1 (Mar. 2016), pp. 1–14. DOI: 10.12989/bme.2016.3.1.001. URL: https://doi.org/10.12989/bme.2016.3.1.001.

[70] Singh, G., Singla, A., and Virk, G. “Modeling and Simulation of a Passive Lower-Body Mechanism for Rehabilitation”. In: (2016).

[71] Bae, J., Lee, J., Jang, A., Ju, Y. K., and Park, M. J. “SMART SKY EYE System for Preliminary Structural Safety Assessment of Buildings Using Unmanned Aerial Vehicles”. In: 22 (2022).

[72] K. J. Åström and H. Tore. *Advanced PID Control*. English. ISA - The Instrumentation, Systems and Automation Society, 2006. ISBN: 978-1-55617-942-6.

[73] Eastlake, C. “Aircraft Cost Analysis”. In: *General Aviation Aircraft Design*. Elsevier, 2014. Chap. 2, pp. 34–52. DOI: 10.1016/B978-0-12-397308-5.00002-7.

[74] Karamian, Y. “Spricho, an on demand energy efficient eVTOL Airtaxi”. In: (2019).

[75] Airbus. *Orders and Deliveries - January 2024*. https://www.airbus.com/sites/g/files/jlcbta136/files/2024-02/ODs-January-2024-Airbus-Commercial-Aircraft-Ib75Mn.xlsx. Accessed: 2024-05-22. 2024.

[76] Hamann, R. J., and van Tooren, M. J. L. *Systems Engineering & Technical Management Techniques: Part I*. AE3-S01. Lecture Notes, Issue 2. Delft, The Netherlands: Delft University of Technology, Faculty of Aerospace Engineering, Sept. 2006.

[77] Group 28. *GoAERO - An Emergency Response Flyer: Baseline Report*. Tech. rep. Delft University of Technology, 2024.

[78] Smith, J. R. “Aircraft Cost Analysis”. In: *Handbook of Aircraft Cost Analysis*. New York, NY: Elsevier, 2022. Chap. 2, pp. 34–53. DOI: 10.1016/B978-0-12-397308-5.00002-7.

[79] Leung, A. K. C., and Hon, K. L. “Motion sickness: an overview”. In: *Drugs in context* 8 (2019).

[80] Sweers, G., Birch, B., and Gokcen, J. “Lightning Strikes: Protection, Inspection, and Repair”. In: *AERO Magazine* 4.12 (2012), pp. 19–28.

[81] Szatkowski, G. N., Dudley, K. L., Smith, L. J., Wang, C., and Ticatch, L. A. *Open circuit resonant (SansEC) sensor technology for lightning mitigation and damage detection and diagnosis for composite aircraft applications*. Tech. rep. 2014.

[82] Kasliwal, A., Furbush, N. J., Gawron, J. H., McBride, J. R., Wallington, T. J., De Kleine, R. D., Kim, H. C., and Keoleian, G. A. “Role of flying cars in sustainable mobility”. In: *Nature Communications* 10.1 (2019), p. 1555.

[83] Pukhova, A. “Environmental evaluation of urban air mobility operation”. PhD thesis. Technical University of Munich (TUM) Munich, Germany, 2018.

[84] André, N., and Hajek, M. “Robust environmental life cycle assessment of electric VTOL concepts for urban air mobility”. In: *AIAA Aviation 2019 Forum*. 2019, p. 3473.

[85] Nicolas, A., and Manfred H. “Robust Environmental Life Cycle Assessment of Electric VTOL Concepts for Urban Air Mobility”. In: *AIAA Aviation 2019 Forum*. DOI: 10.2514/6.2019-3473.

[86] Popien, J. L., Thies, C., Barke, A., and Spengler, T. S. “Comparative sustainability assessment of lithium-ion, lithium-sulfur, and all-solid-state traction batteries”. In: *The international journal of life cycle assessment* 28.4 (2023), pp. 462–477.

[87] Mossali, E., Picone, N., Gentilini, L., Rodrìguez, O., Pérez, J. M., and Colledani, M. “Lithium-ion batteries towards circular economy: A literature review of opportunities and issues of recycling treatments”. In: *Journal of Environmental Management* 264 (2020), p. 110500. ISSN: 0301-4797. DOI: 10.1016/j.jenvman.2020.110500.

[88] EuRIC aisbl. *Metal Recycling Factsheet*. 2020.

[89] Blanco, D., Rubio, E. M., Raquel, M. and Sáenz-Nuño, M. A. “Sustainable processes in aluminium, magnesium, and titanium alloys applied to the transport sector: a review”. In: *Metals* 12.1 (2021), p. 9.

[90] Xiang, X., Xie, A., Ye, M., Yan, X., Han, X., Niu, H., Li, Q., and Huang, H. “Autonomous eVTOL: A summary of researches and challenges”. In: *Green Energy and Intelligent Transportation* 3.1 (2024), p. 100140. ISSN: 2773-1537. DOI: 10.1016/j.geits.2023.100140.

[91] Hagag, N., and Hoeveler, B. *The Feasibility of Electric Air Taxis: Balancing Time Savings and CO_2 Emissions – A joint case study of respective plans in Paris*. 2023.

[92] Priarone, P., Ingarao, G., Settineri, L., and Lorenzo, R. “On the Impact of Recycling Strategies on Energy Demand and CO2 Emissions When Manufacturing Al-based Components”. In: *Procedia CIRP* 48 (Dec. 2016), pp. 194–199. DOI: 10.1016/j.procir.2016.03.044.

[93] Shioya, M., and Kikutani, T. “Synthetic Textile Fibres: Non-polymer Fibres”. In: *Textiles and Fashion*. Woodhead Publishing, 2015. Chap. 7, pp. 139–155. ISBN: 978-1-84569-931-4. DOI: 10.1016/B978-1-84569-931-4.00007-6.

[94] TATA Steel. *Environmental Performance at a Glance*. Sept. 2023.

[95] Ghattamaneni, M. C, Wernicke, S., Hainmann, S., Sulaiman, H., and Tekkaya, A. E. “Analysis, Prediction and Reduction of Emissions in an Industrial Hot Forming Process Chain for the Manufacture of Sheet Metal Components”. In: *Key Engineering Materials* 926 (July 2022), pp. 2342–2354. DOI: 10.4028/p-g7120f.

[96] American Chemistry Council. *A Decreasing Footprint: A Review of Resin Life Cycle Assessments*. 2020.

[97] Sinke, J. “Production of Aerospace Systems (Reader)”. In: (2021).

[98] Precendence Research. *Aerospace Market Size To Reach USD 678.17 Billion By 2032*. Tech. rep. 2023.

[99] Birolini, A. “Basic Concepts, Quality & Reliability (RAMS) Assurance of Complex Equipment & Systems”. In: *Reliability Engineering*. Springer, 2017. Chap. 1, pp. 1–24. DOI: 10.1007/978-3-662-54209-5.

[100] Hottinger, B., and Kjaer Inc. “Introduction to Repairable Systems”. In: *Reliasoft System Analysis Reference*. 2024.

A | N^2 Chart

Weight and Balance		• MTOW				• CG range		• Landing gear positioning • MTOW		• MTOW • CG range	
	Aerodynamics	• Drag characteristics • Disk loading	• Drag characteristics • Propeller geometry			• Aerodynamic forces and moments				• Drag loading	
	• Tip speed	**Flight Performance**	• Tip speed • Cruise speed	• Power required • Energy required		• Manoeuvrability characteristics				• Maximum allowable load factor	
• Motors mass • Motors cg	• Disk area	• Thrust	**Propulsion system**	• Peak power required	• Number of motors	• Thrust orientation				• Thrust loading	• Motor temperature
• Battery mass • Battery cg				**Energy storage**	• Number of batteries						• Battery temperature
• Wiring mass • Voltage regulator mass • Electrical subsystem cg				• Wiring architecture	**Electrical subsytem**		• Wiring architecture • Voltage regulation architecture				
		• Manoeuvrability characteristics	• Thrust vectoring • Thrust differential	• Flight computer power consumption		**Control**					
• Avionics mass • Avionics cg				• Avionics power consumption		• Sensor readings	**Avionics**				
• Landing gear mass • Landing gear cg	• Landing gear size							**Landing gear**		• Landing gear dimensions • Landing loads	
•Payload mass • Fuselage mass • Payload cg • Fuselage cg	• Fuselage size								**Fuselage (incl. payload)**	• Payload bay sizing • Fuselage dimensions	
• Structural weight										**Structures**	
											Thermal management

Figure A.1: N^2 Chart Representing Subsystem Interfaces